



**HAL**  
open science

## Design of robust RFID chipless tags for sensor application

Florian Requena

► **To cite this version:**

Florian Requena. Design of robust RFID chipless tags for sensor application. Optics / Photonics. Université Grenoble Alpes [2020-..], 2022. English. NNT : 2022GRALT092 . tel-04129877

**HAL Id: tel-04129877**

**<https://theses.hal.science/tel-04129877v1>**

Submitted on 15 Jun 2023

**HAL** is a multi-disciplinary open access archive for the deposit and dissemination of scientific research documents, whether they are published or not. The documents may come from teaching and research institutions in France or abroad, or from public or private research centers.

L'archive ouverte pluridisciplinaire **HAL**, est destinée au dépôt et à la diffusion de documents scientifiques de niveau recherche, publiés ou non, émanant des établissements d'enseignement et de recherche français ou étrangers, des laboratoires publics ou privés.

THÈSE

Pour obtenir le grade de

**DOCTEUR DE L'UNIVERSITÉ GRENOBLE ALPES**

École doctorale : EEATS - Electronique, Electrotechnique, Automatique, Traitement du Signal (EEATS)

Spécialité : Optique et Radiofréquences

Unité de recherche : Laboratoire de conception et d'intégration des systèmes

**Conception de tags RFID sans puce, robustes, pour applications capteurs**

**Design of robust RFID chipless tags for sensor application**

Présentée par :

**Florian REQUENA**

Direction de thèse :

**Etienne PERRET**

PROFESSEUR, Université Grenoble Alpes

Directeur de thèse

**Darine KADDOUR**

MAITRE DE CONFERENCE, Université Grenoble Alpes

Co-encadrante de thèse

**Nicolas BARBOT**

MAITRE DE CONFERENCE, Université Grenoble Alpes

Co-encadrant de thèse

Rapporteurs :

**Gaetano MARROCCO**

PROFESSEUR, Univ. degli Studi di Roma 'Tor Vergata'

**Milan POLIVKA**

PROFESSEUR ASSOCIE, Ceské Vysoké Ucení Technické v Praze

Thèse soutenue publiquement le **5 décembre 2022**, devant le jury composé de :

**Hervé AUBERT**

PROFESSEUR DES UNIVERSITES, TOULOUSE INP

Examineur

**Florence PODEVIN**

PROFESSEUR DES UNIVERSITES, GRENOBLE INP

Présidente

**Arnaud VENA**

MAITRE DE CONFERENCES HDR, UNIVERSITE DE MONTPELLIER

Examineur

**Gaetano MARROCCO**

PROFESSEUR, Univ. degli Studi di Roma 'Tor Vergata'

Rapporteur

**Milan POLIVKA**

PROFESSEUR ASSOCIE, Ceské Vysoké Ucení Technické v Praze

Rapporteur

Invités :

**Nicolas BARBOT**

MAITRE DE CONFERENCE, Université Grenoble Alpes

**Darine KADDOUR**

MAITRE DE CONFERENCE, Université Grenoble Alpes





## **Abstract**

**Context :** RFID is a new identification technology that produces labels (tags) similar to the barcode using a wireless radar approach (using radio-frequency waves). In recent years, this technology has undergone considerable development in its use and the research efforts associated with it. Many RFID families have emerged in response to new issues. The RFID without chip (or chipless) is an example; the stated objective is to considerably reduce the price of the tag so it can compete with the barcode. Functionalities can be added to the chipless technology to enable new kinds of applications that its competitor cannot. We find assets related to its reading method using radio waves but also the possibility to add sensor functionalities directly in the tag. This thesis is focused on the possibility of sensing capabilities of chipless tags.

**Keywords :** chipless RFID, wireless sensor, radar, barcode.

# **Design of robust RFID chipless tags for sensor application**

by

**Florian REQUENA**

A Thesis Submitted in Partial Fulfilment  
of the Requirements for the Degree of  
Doctor of Philosophy

at

Grenoble INP - ESISAR  
January, 2023



## Declaration

I, Florian REQUENA, declare that this thesis titled, "Design of robust RFID chipless tags for sensor application", which is submitted in fulfillment of the requirements for the Degree of Doctor of Philosophy, represents my own work except where due acknowledgement have been made. I further declared that it has not been previously included in a thesis, dissertation, or report submitted to this University or to any other institution for a degree, diploma or other qualifications.

Signed: REQUENA Florian

Date: January 20, 2023





## *Acknowledgements*

I would first like to thank my thesis supervisors, PERRET Etienne, KADDOUR Darine and BARBOT Nicolas, who have accompanied and advised me during these three years of thesis.

I would like to thank MARROCCO Gaetano, POLIVKA Milan for agreeing to review this thesis and PODEVIN Florence, VENA Arnaud, AUBERT Hervé to be part of the defense's jury.

I finally thank AUBERT Hervé and LAUGA-LARROZE Estelle for accepting to be a member of the supervision committee which ensured the good progress of the thesis every year.

I would like also to thank the members of the LCIS lab. In particular : Raymundo, Ashkan, Dahmane, Caroline, Carole, Nathalie, Arthur...

I would like to thank all the PhD students I have met and exchanged with during these three years. Whether it was in Valence or Montpellier (Cedric, Benjamin, Prabir, Clément, Lauris, ..).

Finally, I would like to thank my family and friends (Jonathan, Marin, Lucile, ...) for their presence and support throughout the thesis.

To all those I have mentioned here and to those I have forgotten... Thank you.

Florian REQUENA  
January 20, 2023

# List of Publications

## JOURNALS:

- [1] **Requena Florian**, Barbot Nicolas, Kaddour Darine, and Perret Etienne. "Contactless Characterization of Metals Thermal Expansion Coefficient by a Free-Space RF Measurement." *IEEE Transactions on Antennas and Propagation*, 2020, vol. 69, no 2, p. 1230-1234.
- [2] **Requena Florian**, Gilch Michael, Barbot Nicolas, Kaddour Darine, Siragusa Romain, Costa Filippo, Genovesi Simone, and Perret Etienne. "Thermal Modeling of Resonant Scatterers and Reflectometry Approach for Remote Temperature Sensing". *IEEE Transactions on Microwave Theory and Techniques*, 2021, vol. 69, no 11, p. 4720-4734.
- [3] **Requena Florian**, Barbot Nicolas, Kaddour Darine, and Perret Etienne "Combined Temperature and Humidity Chipless RFID Sensor." *IEEE Sensors Journal*, 2022, vol. 22, no 16, p. 16098-16110.
- [4] **Requena Florian**, Barbot Nicolas, Kaddour Darine, and Perret Etienne "Orientation Sensing with a Loop Resonator based on its Re-Radiation Pattern." *submitted to IEEE Sensors Journal*, 2022.
- [5] **Requena Florian**, Barbot Nicolas, Kaddour Darine, and Perret Etienne "Robustness Improvement for Chipless RFID reading using Polarization Separation." *submitted to IEEE Sensors Journal*, 2022.
- [6] **Requena Florian**, Barbot Nicolas, Kaddour Darine, and Perret Etienne "Towards Wireless Detection of Surface modification of Silicon Nanowires by a RF Approach." *submitted to Nanomaterials*, 2022.
- [7] **Requena Florian**, Barbot Nicolas, Kaddour Darine, and Perret Etienne "Non-contact Complex Permittivity Measurement Using Resonant Scatterers and a Radar Approach." *submitted to IEEE Transactions on Microwave Theory and Techniques*, 2022.

## INTERNATIONAL CONFERENCES:

- [1] Costa Filippo, Brizi Danilo, Genovesi Simone, Monorchio Agostino, Manara Giuliano, **Requena Florian**, and Perret Etienne. "Wireless Detection of Water Level by Using Spiral Resonators

- Operating in Sub-GHz Range". *IEEE International Conference on RFID Technology and Applications (RFID-TA)* (pp. 197-200). IEEE. (2019, September).
- [2] **Requena Florian**, Barbot Nicolas, Kaddour Darine, Perret Etienne, "Chipless RFID Temperature and Humidity Sensing". *IEEE MTT-S International Microwave Symposium (IMS)* (pp. 545-548). IEEE. (2021, June).
- [3] **Requena Florian**, Barbot Nicolas, Kaddour Darine, Perret Etienne, "Increased Coding Capacity of Chipless RFID Tags Using Radiation Pattern Diversity". *European Microwave Week*. (2022, September).
- [4] **Requena Florian**, Barbot Nicolas, Kaddour Darine, Perret Etienne, "Detection of water drop volume based on Chipless RFID radar approach". submitted to *Radio Wireless Week*. (2023, January).

## **NATIONAL CONFERENCES:**

- [1] **Requena Florian**, Barbot Nicolas, Kaddour Darine, Perret Etienne, "Conception de tag RFID sans puce pour application capteur". *Congres des doctorants - Edition 2020 - UPVDOC*.
- [2] **Requena Florian**, Barbot Nicolas, Kaddour Darine, Perret Etienne, "Caracterisation sans contact du coefficient de dilatation thermique de metaux par approche RF". *XXIIemes Journees Nationales Microondes*. (2022, June).
- [3] **Requena Florian**, Barbot Nicolas, Kaddour Darine, Perret Etienne, "Capteur RFID sans puce de temperature et d'humidite". *XXIIemes Journees Nationales Microondes*. (2022, June).

# Contents

<b>Abstract</b>	<b>i</b>
<b>Declaration</b>	<b>i</b>
<b>Acknowledgements</b>	<b>ii</b>
<b>List of Publications</b>	<b>iii</b>
<b>Contents</b>	<b>v</b>
<b>1 Introduction to RFID</b>	<b>1</b>
1.1 History of RFID . . . . .	1
1.2 Current market and challenges . . . . .	3
1.2.1 Current market . . . . .	3
1.2.2 Challenges . . . . .	5
1.3 Context of the thesis . . . . .	6
1.4 Outline of the manuscript . . . . .	7
1.5 Working principle of chipless RFID tags for identification and sensing applications . . . . .	9
1.5.1 Back-scattering approach . . . . .	9
1.5.2 Read range . . . . .	12
1.5.3 Reading methods . . . . .	14
1.5.4 Re-radiation pattern . . . . .	15
1.5.5 Identification principle . . . . .	16
1.5.6 RFID sensors . . . . .	19
1.6 Conclusion of the chapter . . . . .	22
<b>2 RFID Chipless and environment sensing</b>	<b>23</b>
2.1 Characterization of thermal dilatation by RF approach . . . . .	23
2.1.1 Thermal dilatation principle . . . . .	25
2.1.2 Measurements in climatic chamber . . . . .	29
2.1.3 Results and analysis . . . . .	30
2.1.4 Incertainties . . . . .	33
2.1.5 Conclusion of the section . . . . .	34
2.2 Chipless RFID temperature sensors . . . . .	34
2.2.1 Description of the scatterer-based CPS TL . . . . .	36

2.2.2	Temperature dependence of the effective permittivity of the CPS TL-based scatterer . . . . .	37
2.2.3	Temperature extraction . . . . .	37
2.2.4	Discussion on Approximations for the determination of the temperature . . . . .	39
2.2.5	Simulations . . . . .	41
2.2.6	Evaluation of the error . . . . .	43
2.2.7	Temperature sensing in a climate chamber . . . . .	46
2.2.8	Temperature sensing in a real environment . . . . .	48
2.2.9	Thermal characterizations of a resonant scatterer-based microstrip TL . . . . .	50
2.2.10	Humidity effect . . . . .	55
2.2.11	Conclusion of the section . . . . .	56
2.3	Combined Temperature and Humidity Chipless RFID Sensor . . . . .	57
2.3.1	Theory . . . . .	59
	Relationship between resonance frequency, temperature and humidity . . . . .	59
2.3.2	Simulations . . . . .	62
2.3.3	Sensitivity of the measurement . . . . .	64
2.3.4	Parameters characterization . . . . .	64
2.3.5	Sensing in a controlled environment . . . . .	67
	Measurement setup and tag design . . . . .	67
	Results and Analysis . . . . .	68
2.3.6	Sensing in a real environment . . . . .	69
	Measurements . . . . .	69
	Results and analysis . . . . .	69
2.3.7	Discussions on the proposed approach . . . . .	70
	Discussion on measurement conditions . . . . .	70
	Time transient responses . . . . .	72
	Parameters limitations . . . . .	72
	Monte Carlo simulations . . . . .	74
2.3.8	Generalization . . . . .	75
2.3.9	Conclusion of the section . . . . .	76
2.4	Conclusion of the chapter . . . . .	76
<b>3</b>	<b>Loop scattering parameters and RFID sensors</b>	<b>79</b>
3.1	Orientation sensing using loop resonators . . . . .	79
3.1.1	Radiation pattern modeling of loop resonators . . . . .	80
3.1.2	Back-scattering expressions . . . . .	82
3.1.3	Orientation Sensing . . . . .	85
3.1.4	Uncertainty . . . . .	87
3.1.5	Simulations . . . . .	89
3.1.6	Measurements . . . . .	91
3.1.7	Generalization of the approach . . . . .	92
3.1.8	Real environment measurement . . . . .	96
3.1.9	Conclusion of the section . . . . .	102

3.2	Increased Coding Capacity of Chipless RFID Tags Using Radiation Pattern Diversity . . . . .	103
3.2.1	Principle . . . . .	103
3.2.2	Simulations . . . . .	105
3.2.3	Measurements . . . . .	106
3.2.4	Conclusion of the section . . . . .	106
3.3	Reading robustness . . . . .	108
3.3.1	Theory . . . . .	110
3.3.2	Angle estimation . . . . .	114
3.3.3	Simulations . . . . .	115
3.3.4	Measurements . . . . .	119
3.3.5	Impact of highly reflective environment . . . . .	123
3.3.6	Impact of the distance . . . . .	125
3.3.7	Case of an antenna not placed in normal incidence with respect to the tag . . . . .	127
3.3.8	Example with other resonator's shapes . . . . .	129
	Example with other resonator's shapes . . . . .	129
	Applications to resonators with ground plane . . . . .	131
3.3.9	Discussion . . . . .	133
3.3.10	Conclusion of the section . . . . .	135
3.4	Perspectives . . . . .	135
3.5	Conclusion of the chapter . . . . .	138
<b>4</b>	<b>Medium characterization using a radar approach . . . . .</b>	<b>139</b>
4.1	Wireless Detection of Surface modification of Silicon Nanowires . . . . .	139
4.1.1	Classical methods for surface analysis . . . . .	140
4.1.2	Radio-frequency approach . . . . .	141
	Principle of the radar approach . . . . .	141
	Extraction of the physical parameters . . . . .	142
4.1.3	Measurements . . . . .	143
	Results and analysis . . . . .	144
	Discussions . . . . .	146
4.1.4	Conclusion of the section . . . . .	147
4.2	Complex permittivity sensing . . . . .	149
4.2.1	Complex resonance frequency . . . . .	150
4.2.2	Permittivity extraction . . . . .	152
4.2.3	Simulations . . . . .	153
4.2.4	Measurements . . . . .	155
4.2.5	Conclusion of the section . . . . .	159
4.3	Conclusion of the chapter . . . . .	159
<b>5</b>	<b>Conclusion . . . . .</b>	<b>161</b>
<b>A</b>	<b>Nanowires fabrication, functionalization and characterization . . . . .</b>	<b>163</b>
A.1	Synthesis of silicon nanowires . . . . .	163
A.2	Silicon nanowires functionalization . . . . .	163

A.2.1	Octadecyltrichlorosilane modified silicon nanowires (SiNWs-OTS) . . . . .	163
A.2.2	Silicon nanowires functionalization with 3-azidopropyltriethoxysilane (SiNWs-N <sub>3</sub> ) . . . . .	164
A.2.3	Ethynylpyrene covalently attached to SiNWs (SiNWs-py) . . . . .	164
A.3	Results and discussion . . . . .	164
A.3.1	Characterization of SiO <sub>2</sub> -SiNWs . . . . .	164
A.3.2	Octadecyltrichlorosilane modified silicon nanowires (SiNWs-OTS) . . . . .	165
A.3.3	Formation of Azide and pyrene terminated silicon nanowires surfaces . . . . .	165
<b>B</b>	<b>Résumé en français</b>	<b>169</b>
	<b>Bibliography</b>	<b>175</b>

## Chapter 1

# Introduction to RFID

In this chapter, we will present the RFID technology from a general point of view. A brief historical review will allow us to go back over the applications and the development context of the first RFID systems until the latest advances. The different major RFID technologies will be briefly reviewed. A section on the challenges of RFID will be done to understand the enthusiasm around this technology and the context of this thesis.

### 1.1 History of RFID

RFID (for Radio Frequency IDentification) is an identification (ID) technology based on the use of radio waves. Traditional radar applications allow the detection of a target presence, position and/or velocity. Classical architectures are composed of one or several antennas able to emit an electromagnetic wave towards the target and receive the backscattered field. Backscattering RFID applications based on this principle are used for identification and sensing purposes. In such a case, the main difference with traditional radar applications is the use of a known target that has been designed for encoding information. The first application of this technology dates back to the Second World War with the identification of planes "*Friend or Foe*" [1]. This application consisted in equipping the planes with a radio frequency transponder allowing them to emit a coded signal when the plane was illuminated with an electromagnetic wave from a radar. Thus, the ground could recover this signal and compare it with a database to judge the hostility of the plane. In parallel, from the beginning of the 1900s until the cold war, Léon Theremin's works were also at the origin of the physical concepts which are still used by the RFID technology today [2]. Thusly, in the early 1900s, we find a contactless musical instrument called "Thereminvox" which uses wirelessly the position of the hand of the musician to produce a sound (see Fig. 1.1) or the passive spy system called "The Great Seal bug". The latter was offered as a gift by the USSR to the American embassy during the cold war (see Fig. 1.1). When impinged by a continuous wave (emitted outside the embassy), this passive device was able to modulate its backscattered field as a function of the audio signal present in the vicinity of the bug. Due to the planarity of the device, it remains undetected during a period of 6 years.

RFID was then democratized with consumer applications such as the anti-theft system (EAS) present in supermarkets, passport identification, access/transportation cards or even animal identification [3]. The RFID anti-theft system (EAS) in supermarkets was the first major commercial use of





**Figure 1.1:** a) Léon Theremin playing the Thereminvox. [image taken on [Theremine](#) ] b) Reconstruction of "The Great Seal bug" at the Wireless Power Week 2022 in Bordeaux.

RFID technology. Today several classes of RFID were developed to answer very specific problems [4]. We can find tags with a chip and with a battery for the remote toll, tags with a chip but without a battery in the identification of passports, or tags without a battery and chip for anti-theft systems, ... An illustration of these example is given in Fig. 1.3. Also, a brief description of the RFID solutions is given in Fig. 1.2. This manuscript will focus on the chipless technology using REP (RF Encoding Particle) presented later in Section 1.5.5.

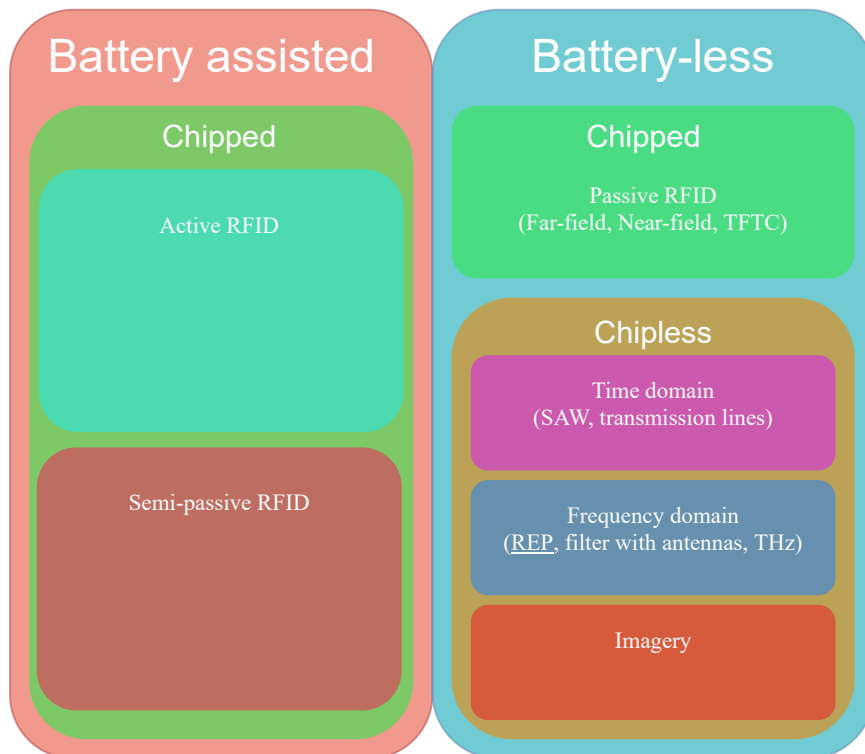


**Figure 1.2:** Brief description of RFID solutions.

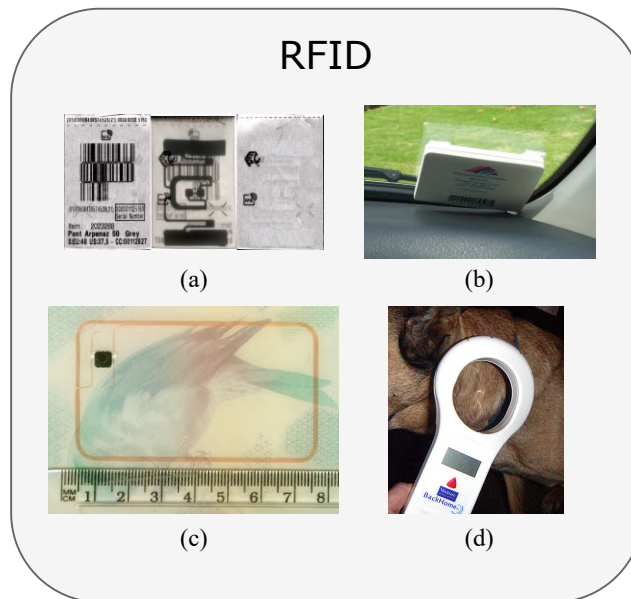


**Figure 1.3:** Example of different RFID applications : (a) Passive UHF RFID tag (Decathlon), (b) Active tag (tolls), (c) HF tags (13.56 MHz) for passport identification and (d) LF tags (136 kHz) tag for animal identification. [images taken on [RFID](#)]

## 1.2 Current market and challenges

RFID technology has exploded in recent years. This section aims to understand why such a boom has been possible by briefly looking at the issues that this technology can claim as well as its current market.

### 1.2.1 Current market

The global RFID market was valued at US \$ 2.13 billion in 2009, US \$ 10.87 billion in 2020 [5, 6] and is expected to reach US \$ 14.42 billion by 2026 and US \$ 35.6 billion by 2030 [7]. This market is composed of the sale of tags, readers but also services/software. The most common uses of RFID technology are tracking goods in the supply chain, tracking shipped objects, or for security purposes (anti-theft systems in shops or authorization badge). The second most important user of RFID technologies is the military (see Fig. 1.4). In Fig. 1.5, it is possible to see the estimated growing interest in RFID with an exponential growth in the last years. This estimation was done in 2009 [6]. In reality, printed solutions did not take off as predicted. Today, most of the growth comes from passive UHF RFID (RAIN RFID) tags.

Still, in the line with the first major commercial use of the RFID technology in the shops (with EAS) new disruptive breakouts for public habits are beginning to appear in the way of shopping and so the market might increase in the future years. Indeed, for example, companies such as Amazon are creating cashier-less shops [8] described as "a system for automatically transitioning items from a materials handling facility without delaying a user as they exit the materials handling facility". This new way of shopping uses in parallel imaging from cameras and the RFID technology [9]. This solution is an

efficient way to automatize data collection with low maintenance and an infinite lifetime of operation. In addition, the increasing adoption of RFID tags in Industry 4.0, and the Internet of Things (IoT) are expected to provide a favorable opportunity for the future growth of the RFID market.

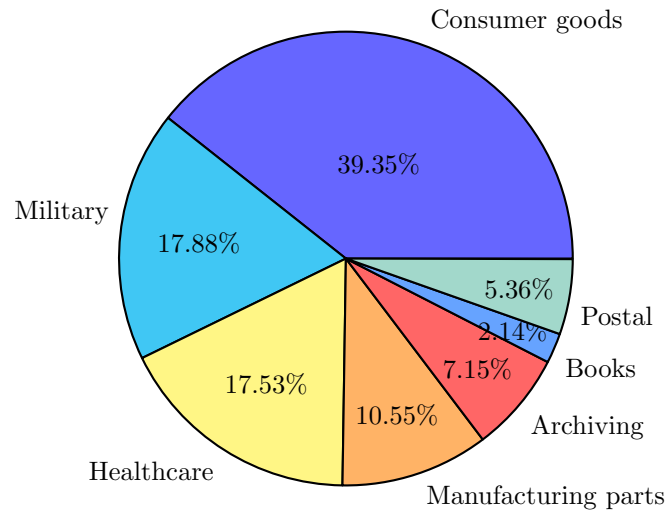


**Figure 1.4:** Distribution in value of item level RFID tag sales in 2019 [6].

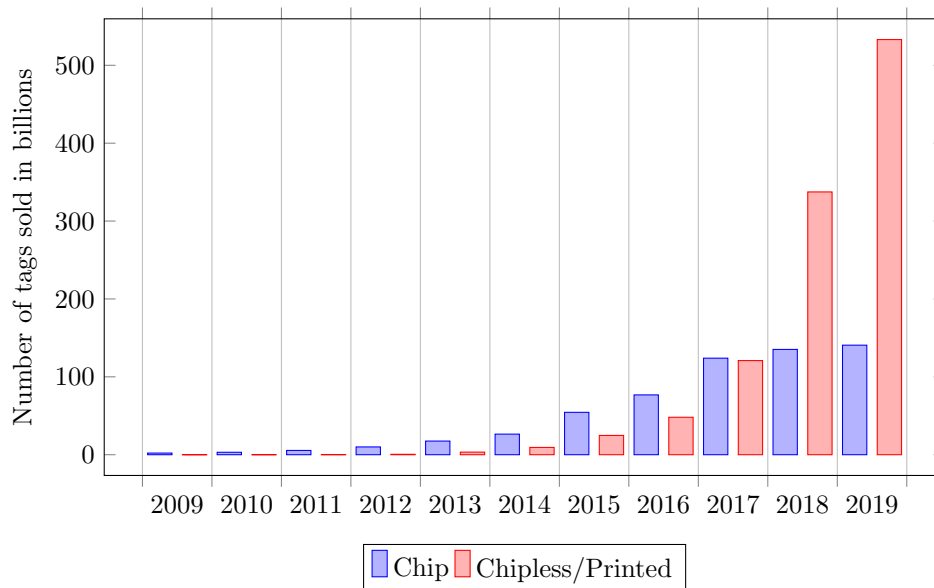


**Figure 1.5:** Number of tags sold in billions worldwide over the years [6].

While the market keeps increasing for this technology, scientific interest is also growing. As of 19/07/2022, "RFID" is a term that gives more than 720.000 results on Scholar, 135.832 patents, and 95 million results on Google. Meanwhile, specialized events such as the IEEE RFID (16 years old), RFID-TA (12 years old) conferences or the specialized journal JRFID (5 years old) started to appear as the enthusiasm grow.

## 1.2.2 Challenges

Today for the identification purpose, we can find mainly two technologies :

- the barcode - which relies on an optical approach.
- RFID - which is based on an radio-frequency (RF). approach

The term barcode is used in a general way in this report to describe any identification system based on an optical technique. Indeed, we can find different standards according to the targeted application (Code 39 for drugs, EAN for store objects, PostBar for the Canadian post office, ... ), but also different forms (1D, 2D) as illustrated in Fig. 1.6. Different standards of barcodes can be found in Table 1.1 as a reference.



**Figure 1.6:** Identification technologies : a) 1D barcode (EAN 8), b) 2D barcode (QRcode), c) RFID tags.

	EAN13	Code 39	Code 128	Data Matrix	Codabar Monarch
Dimension	20-37mm	95mm	75mm	144x144mm	-
Capacity	43bits	130bits	168bits	45kbit	-
Application	Shops	Drugs	Transport	Items marking	Blood Bank

**Table 1.1:** Comparison of different barcode standards and their applications.

Although RFID is a very present technology today, the barcode is still the most used solution for some applications. The reasons for this are its earlier appearance, its implementation in different markets such as the retail industry (all stores are equipped with barcode readers, and they have suppliers who tag the products with barcodes as soon as they are manufactured), and especially its much lower price than RFID (in particular when the price of the tag is of the same order of magnitude as that of the object tagged). But the barcode has some drawbacks : it needs direct line of sight (which imply human manipulation to orient the product with the reader), it has a limited read range, it can read a single tag reading at a time, there is no sensing applications, ... Table 1.2 summerizes the main differences between these technologies. To overcome these disadvantages, the RFID technology brings solutions to decrease its cost and increase its added values :

**Highlighting of its assets :** The RFID technology is based on a radio frequency approach which has many assets that its competitor does not have. It is for example possible to read simultaneously several RFID tags at a distance higher than the barcode and without a direct line of sight

(through certain materials). The current memories of the RFID tags allow them to offer high storage capacities. It is also possible to rewrite an RFID tag after its conception. We can also go beyond the simple identification by integrating directly in the tag sensor functionalities such as the measurement of temperature, humidity, localization, ...

**A low-cost design :** The last years have allowed to reduce the price of an RFID tag considerably limiting the gap between the two technologies. The price of RFID chips has decreased considerably. In the case of a chipless RFID, by removing the battery and the chip, the price of the tag falls drastically and reaches almost the price of the barcode. Also, today chipless tags are compatible with planar technology making it possible to print them directly with a printer in the same way as we would print a barcode.

	barcode	passive RFID (UHF)	chipless RFID
Reading range	30cm	10m	≤1m
Non line of sight reading	✗	✓	✓
Access	Reading	Reading/Writing	Reading/Writing*
Printable	✓	✗	✓
Coding capacity	depends	several kbits	depends
Sensing capability	✗	✓	✓
Writing	Impossible	Possible wirelessly and on contact	Possible on contact only
Reading of multiple ID	Impossible	Possible	Limited
Cost	0.005 €	0.2 €	0.01 €
Read through objects	If optically transparent	Possible	Possible

**Table 1.2:** Comparison of the barcode, passive UHF RFID and Chipless RFID technologies.  
\* still in the research stage [10].

Despite the advantages like the important reading distance, the tags with battery have significant drawbacks like their important size, the limited time of operation, and the cost all due to the battery. They are therefore not adapted to the problems to which the barcode answers. On contrary, the RFID tags without a battery have a cost and a reduced size (which comes from the absence of a battery), negligible maintenance but also an infinite operational life. These tags suggest many possibilities like the end of the barcode in shops [8] or new types of sensor [11]. Chipless tags reduce even more the unitary price but with a smaller reading range, less reading robustness, etc... (see Table 1.2) : they can pretend to compete with the barcode which does not give satisfaction in certain applications (for example where a reading without direct line of sight is preferred). Notice also that while chipped RFID are standardized (ISO14443 and ISO180006c for HF and UHF respectively), the chipless technology is not.

### 1.3 Context of the thesis

This thesis is part of a project currently carried out by Etienne PERRET (LCIS - Grenoble INP) : ScattererID. It is a project funded by the European Research Council. The aim of this project is : "to develop a new generation of radio-frequency identification labels, without chip, printable, recyclable and

*inexpensive. Unlike barcodes, they can be read through opaque objects or from a distance. It is also possible to implement new functionalities that are incompatible with barcode technology. Finally, since they do not include a chip or antenna, they are much less expensive than RFID tags. With costs comparable to those of a barcode, these labels should stand out by offering more functionalities than the optical approach".*

This thesis aims at taking advantage of the possible sensor applications of chipless RFID tags to extend the gap of RFID assets which the barcode. RFID technology with sensing capabilities can represent the turn-around point for the massive development of this technology or the spread of IoT. The proposed solution shares the specifications of the barcode and is not comparable to chipped RFID in particular on the reading distance as stated in Table 1.2.

It is important to notice that the developed sensor applications can be implemented on already existing chipless RFID tags but can also be used independently as a complete sensor on its own.

The sensing on top of the identification functionality can be used in the example of the Amazon shop [8]. The identification allows the shop to know which items are taken by the consumer, and manage the shelves and the expiration dates. The sensing can be added to monitor the temperature of food (protect the cold chain) and humidity (protect household appliances) as a control on the quality of the products. Shops are not the only potential beneficiaries. It could also be desirable to have the protection of sensitive infrastructures by detecting the presence of water in walls (water leakage) using the planarity of tags as well as their infinite lifetime of operation without maintenance. Finally, such sensors start to appear to the large public with for example bracelets for authorization purposes [12], toys [13, 14], gesture recognition [15], monitoring of human [16, 17, 18] ... Notice that these examples are chipped RFID with a small reading distance. In such applications, chipless tags can replace them hence the enthusiasm in this approach.

The developed sensors in this thesis can also be used without the identification paradigm. Advantages can be found in the wireless reading method, its cost, its small dimensions (planar), its infinite lifetime of operation, or its utilization in a hazardous environment where chipped sensors can not go due to the presence of electronics (too high temperature, corrosive, ...).

## 1.4 Outline of the manuscript

Chapter 2 will propose environmental sensing with a focus on temperature sensors extended to humidity sensing. This chapter will first study the thermal dilatation of metallic scatterers with no substrate. A method to characterize this dilatation using a contactless measurement of the frequency-dependant backscattered signal of a metallic resonator is presented. Then, this principle will be used in addition to permittivity thermal variations to resonators with a substrate. Unlike previous works in this domain where the thermal dependency is considered empirically, the introduced model is used to take into account all thermal effects affecting the resonant scatterers allowing to link rigorously the variations of the measured resonance frequency with the temperature without any lookup table. Eventually, we will notice that the permittivity is also sensible to other physical quantities such as humidity. The material's permittivity (impacted by these two quantities) and dilatation (impacted only by the temperature) are taken into consideration to estimate these two physical quantities independently and simultaneously using only the measurement of the resonance frequencies of two

scatterers. The sensing limitation as well as the possibility of this approach to characterize the temperature and humidity dependencies of unknown materials are also presented. No specific material, i.e. particularly sensitive to the quantities to be measured, is used for ease of implementation.

Chapter 3 presents an analytical model of the radiation pattern of a loop resonator which is frequently used as chipless RFID tags. The radiation pattern will be used in practice as a sensor to determine the orientation between the tag and the antenna in 3D for both mono-static and bi-static antenna configurations. Since the sensor is based on the radiation pattern (and so the amplitude of the signal) which is known to be less robust than the position of the resonance frequency, uncertainties will be studied with Monte-Carlo simulations. After that, the radiation pattern will be used to encode multiple peaks of resonance on the same frequency slot without interfering together. This doubles the coding capacity without increasing the frequency band of operation. Also, a method to improve the readability of a chipless tag is presented. The proposed approach permits to obtain a higher signal-to-noise ratio (SNR) of resonators whose orientation with respect to the reader is unknown and thus increasing the reading distance of the tag. It allows the separation of the resonance mode of the resonator that is connected to the identifier from other parasitic resonance modes that may appear due to possible misalignment between the tag and the antenna. A study of the improvement in the read range or harsh environments is achieved to highlight the potential of the proposed technique. This method will also be compared to state-of-art approaches.

Later on, Chapter 4 will present medium sensors. The first section suggests shows the possibility to detect the presence of grafted molecules on the surface of silicon nanowires thanks to a wireless RF radar approach based on the measurement of the backscattered signal of a resonant structure on which the nanowires are deposited. The measured resonance frequency allows the determination of the intrinsic properties related to temperature and humidity variations. Several functionalizations of nanowires have been realized and characterized. A RF approach allows the detection of significant differences related to the presence of grafted molecules on the surface of nanowires. The obtained results confirm the very good potential of the radar approach to identify the functionalization of nanowires. Also, discussions about the application of such functionalizations are made to increase the sensibility of sensors working using the radar approach. Secondly, a method to characterize the complex permittivity of dielectric is presented. The back-scattered signal from a resonant scatterer placed in contact with the dielectric is used to estimate the quantities. This method is wireless, non-destructive, with no restriction on the sample thickness, and is done using a VNA and an antenna. Discussions on the geometry of the resonator as well as the calibration step are proposed to improve the sensing capability of the approach.

Finally, Chapter 5 concludes this manuscript.

In the next section, the operating principle of chipless RFID will be presented briefly. The physical principles used to achieve the identification of chipless tags and the sensing paradigm will be introduced.

## 1.5 Working principle of chipless RFID tags for identification and sensing applications

This section briefly introduces the working principle of chipless RFID. The physical principles used to achieve a chipless tag identification will be presented with a focus on the chipless frequency approach. After that, the sensor paradigm of chipless tags is developed.

### 1.5.1 Back-scattering approach

When a target is illuminated by an electromagnetic wave, it will reflect part of the incident wave. It is this reflected wave or back-scattered wave that will be able to be captured by the reader and give an indication of the target. This is the principle of radar as illustrated in Fig. 1.7.

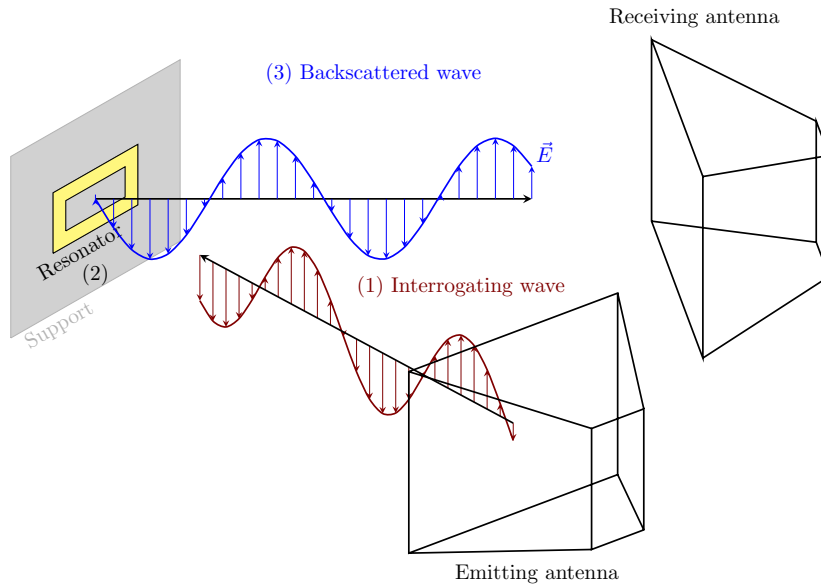


**Figure 1.7:** Illustration of the principle of re-radiation of a radar target using a bi-static antenna configuration. A transmitting antenna will emit an electromagnetic wave towards the target (1). The target will receive and reflect part of this wave (2). The reflected wave will then be able to be captured again by the receiving antenna (3).

The radar cross section (RCS) noted  $\sigma$  is the proportion of the wave reflected by the target in a specific direction compared to the incident wave. The RCS is a fictitious surface often different from the physical surface of the target. The RCS (at a given frequency in a given direction) is expressed as follows :

$$\sigma = 4\pi R^2 \frac{W_s}{W_i} \Big|_{R \rightarrow \infty} \quad (1.1)$$

where  $W_i$  is the density of the power incident on the radar target and  $W_s$  the density of the power reflected by the target at a distance  $R$ .

The RCS is characteristic of the radar target. It depends on its geometry, the illumination angles as well as the wavelength used or the nature of its constituent materials. Example of RCS values are given in Table 1.3.



**Table 1.3:** Different values of RCS [19].

Radar target	RCS (m <sup>2</sup> )
Plane	10 <sup>2</sup>
Human	10 <sup>0</sup>
Bird	10 <sup>-2</sup>
Insect	10 <sup>-5</sup>
Chipless tag with ground plane	3·10 <sup>-2</sup>
Chipless tag without ground plane	3·10 <sup>-5</sup>

On the power returned by the tag through the RCS, it is important to distinguish two contributions called "antenna mode" and "structural mode". The total RCS is the sum of the antenna mode and the structural mode :

**Structural mode :** In the case of an antenna, the structural mode is determined when there is a conjugate match between the antenna and its load. It corresponds to a reflection of the wave (optical reflection type) on the structure. Thus the structure mode is present on all objects and therefore does not code any information. The environment generates a structural mode.

**Antenna mode :** Another part of the energy will be guided, stored then re-emitted by the load. It depends on the charge connected to the antenna : it is the mode which will encode the information. While the structural mode has the same characteristics as the incident wave, the antenna mode can vary by changing the load (used in chipped RFID) or resonate only at a particular frequency (used in chipless RFID frequency domain approach). It is important to notice that the antenna mode can be not resonant but for chipless RFID applications, resonant radar target are specifically designed to have a resonant antenna mode. Then, with the design of a particular radar target, it is possible to create a "specific" radar signature by defining the resonant frequencies of the target. In this thesis, this chipless RFID frequency domain approach is used.

The re-emitted wave being the complex sum of the two modes, we can have a peak or a dip depending on the phase between the two modes as shown in Fig. 1.8. The singularity expansion method (SEM) can be used for quantifying the transient electromagnetic scattering from targets illuminated by pulsed EM radiation [20]. What interests us here is to extract the resonant mode of the target and thus the ID. The concept of SEM has been widely used in circuit theory for a long time. Let's consider the equivalent electrical model of a resonant scatterer : the RLC circuit is illustrated in Fig 1.9.

The following equation can be established :

$$\frac{dv(t)}{dt} = \left( L \frac{d^2i(t)}{dt^2} + R \frac{di(t)}{dt} + \frac{1}{C} i(t) \right) \quad (1.2)$$

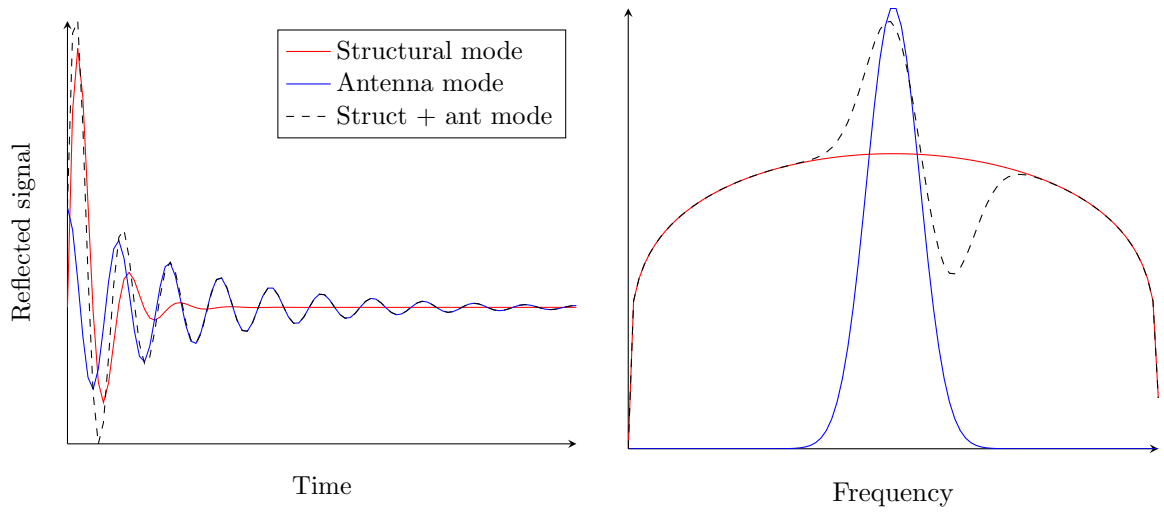


**Figure 1.8:** Time and frequency response following the illumination of a resonant radar target by a pulse wave.

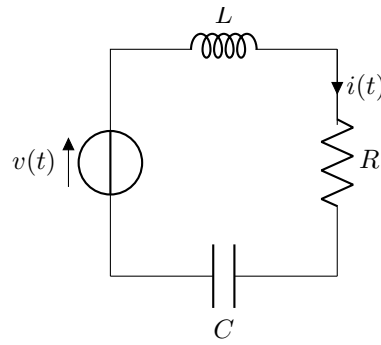


**Figure 1.9:** Electrical equivalent model of resonators.

By applying the Laplace transform to (1.2), the current can be written in the complex  $s$ -plane by [21] :

$$i(s) = \frac{Cs}{\left(\frac{s}{\omega_0}\right)^2 + \frac{1}{Q}\left(\frac{s}{\omega_0}\right) + 1} \times v(s) = y(s) \times v(s) \quad (1.3)$$

the radian resonant frequency,  $\omega_0$ , and the Q-factor at the resonant frequency,  $Q$ , are defined as :

$$\left\{ \begin{array}{l} \omega_0 = \frac{1}{\sqrt{LC}} \\ Q = \frac{1}{\omega_0 RC} \end{array} \right. \quad (1.4a)$$

$$\left\{ \begin{array}{l} \omega_0 = \frac{1}{\sqrt{LC}} \\ Q = \frac{1}{\omega_0 RC} \end{array} \right. \quad (1.4b)$$

The admittance  $y(s)$  can be developed as :

$$y(s) = \frac{A}{s-s_1} + \frac{A^*}{s-s_1^*} \quad (1.5)$$

where  $s_1 = \alpha_1 + j\omega_1$  is the complex natural resonance (CNR) of the circuit. The damping factor and resonance frequency are obtained with :

$$\begin{cases} \alpha_1 = \frac{\omega_0}{2Q} & (1.6a) \\ \omega_1 = \frac{\omega_0}{2} \sqrt{4 - \frac{1}{Q^2}} & (1.6b) \end{cases}$$

The traditional responses  $i(t)$  of resonant chipless tag is an exponentially damped sinusoidal in time and a peak in frequency as illustrated in Fig. 1.8 by "Antenna mode". This resonator damping and resonance frequency are defined by  $\alpha_1$  and  $\omega_1$  respectively. Hence, the control of  $\omega_1$  while the design of the resonator allows the ID encoding. The above discussion can be easily generalized to multi-resonant circuits. In a multi-resonant circuit, the input admittance of the circuit is expanded versus the singularity poles of the circuit as [22] :

$$y(s) = R(s) + \sum_{n=-N}^N \frac{A}{s - s_n} \quad (1.7)$$

where  $N$  is the number of the poles' resonators ( $s_n$ ) of the circuit and  $R(s)$  is the non-resonant part of the circuit.  $R$  is the quasi-optic reflection (structural mode).

A chipless RFID tag is thus a structure which, when is excited, diffuses a unique signature inherent to its geometry through the antenna mode. Therefore the information is encoded in the dimensions of the resonator and recovered from the backscattered field. With the design of a particular radar target, it is possible to create a "unique" radar signature by defining known resonant frequencies of the target. This principle will be further discussed in Section 1.5.5.

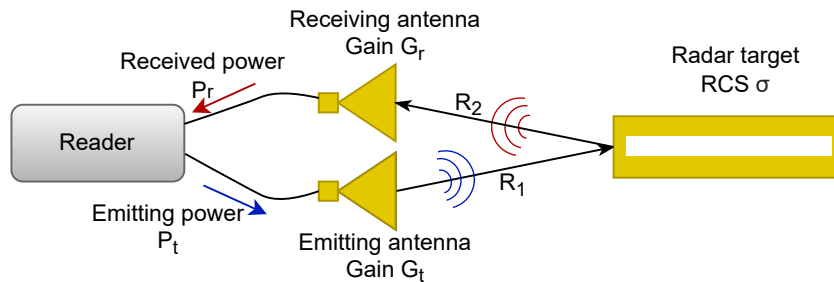


**Figure 1.10:** Illustration of a bi-static radar approach. The blue electromagnetic wave is emitted by the reader. The red electromagnetic wave is reflected by the radar target.

## 1.5.2 Read range

Fig. 1.10 represents how the electromagnetic wave reflected by the radar target, will be partially captured by the reader. For active RFID, the read range is mainly limited by the power received by the reader  $P_{rc}$ . Indeed, when the active tag powered by a battery send a signal to the reader, the only condition to be readable is the received power at the reader  $P_{rc}$  to exceed its threshold value. This

power can be computed in free-space using Friis equation assuming perfect coupling by :

$$P_{rc} = P_{tag} G_{tag} G_r \left( \frac{\lambda}{4\pi R_1} \right)^2 \quad (1.8)$$

where  $P_{tag}$  is the power sent by the tag,  $G_{tag}$  and  $G_r$  the gain of the RFID tag antenna and receiving antenna of the reader respectively. For passive and semi-passive RFID, the power received by the tag  $P_{tag}$  need to exceed the sensitivity threshold to wake up the chip [eq. (1.8)]. Then, the modulated power of the back-scattered signal  $\Delta P_r$  of the tag received by the reader need to exceed its sensitivity [23] :

$$\Delta P_r = \frac{P_t G_t G_r \lambda^2 \Delta \sigma}{R_1^2 R_2^2 (4\pi)^3} \quad (1.9)$$

where  $P_t$  and  $G_t$  are the power transmitted by the reader and the gain of its emitting antenna.  $R_1$  and  $R_2$  are the distance from the tag to the emitting and receiving antenna respectively.  $\Delta \sigma$  is the differential RCS [24]. Therefore, the emitted power, path losses, the reader/tag's chip sensitivity limits the maximum reading range. For recent chip (-22dBm activation threshold for the Impinj Monza R6) and reader (-90dBm for the ST25RU3993 reader), the read range is usually limited by the tag's chip sensitivity.

More generally in radar applications, the back-scattered power received by the reader  $P_r$  needs to be higher than its sensitivity threshold. The power  $P_r$  can be computed using the radar equation [25] :

$$P_r = \frac{P_t G_t G_r \lambda^2 \sigma}{R_1^2 R_2^2 (4\pi)^3} \quad (1.10)$$

where  $G_r$  is the gain of the receiving antenna of the reader. For chipless RFID, the limiting factor in the reading range is the environment. The maximal reading distance of chipless tags is given when the power received from the tag is higher than the one received from the environment. In the case where objects are present and reflect the electromagnetic wave, the coupling between antennas is not perfect, multipath, etc, an expression derivated in [23] can be used :

$$R = \sqrt[4]{\frac{G_t G_r \lambda^2 \sigma}{|\varepsilon(f)|^2 (4\pi)^3}} \quad (1.11)$$

where  $|\varepsilon(f)|$  is the transfer function of the residual environment. Note that, contrary to the read range extracted from (1.10), this expression does not depend on the transmitted power nor the sensitivity of the reader and is generally much lower than the one given by (1.10). This bound has been reported in Fig. 1.11 (green dashed line) for a dipole scatterer and a residual environment of -60 dB at a frequency of 915 MHz in the configuration  $R_1 = R_2 = R$  along to other RFID solutions in term of read range.

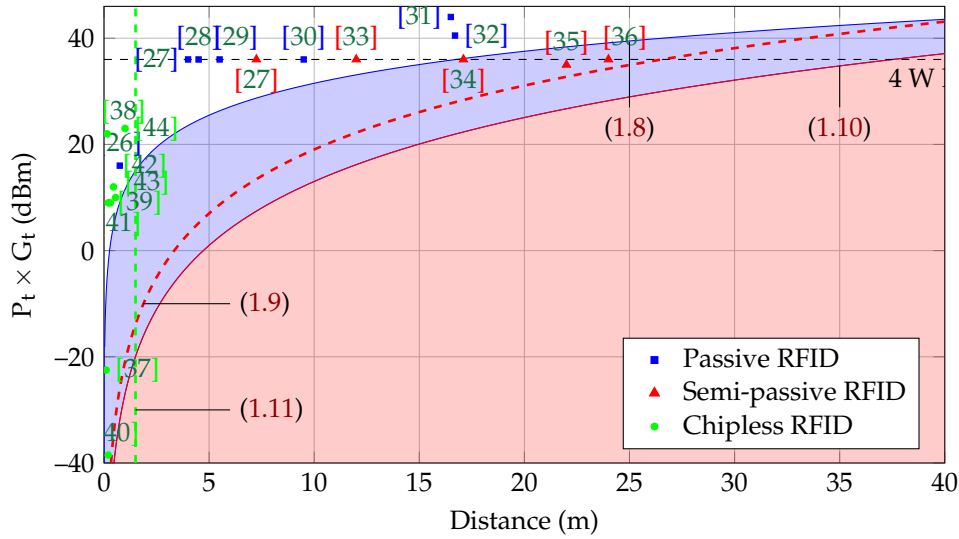


**Figure 1.11:** Theoretical read range versus EIRP for passive and semipassive at 915 MHz in free space and their associated measured read range. Chipless RFID performance is identical to semipassive RFID in free space. Dashed lines correspond to (1.9) and (1.11) [23].

### 1.5.3 Reading methods

To interrogate a tag, a reader sends a signal toward the tag and measures the backscattered response to estimate the resonant frequencies. The signal sent by the reader could be a frequency sweep (such as a VNA-based measurement - frequency-modulated continuous-wave radar) or a time pulse (pulse radar). The antenna configuration is either a bi-static antenna configuration (as illustrated in Fig. 1.10) or a mono-static antenna configuration (only one antenna is present). As previously explained, in chipless RFID, the interrogation process is affected by the clutter present in the environment hence different reading methods have been proposed to enhance the tag readability :

**The subtraction of the environment** (sometimes called empty measurement) is very common in chipless RFID works. This is a very simple way to subtract the effect of the environment to make the tag easier to read [45, 46]. An initial measurement  $S_e$  of the environment called “empty” (with objects present but without the tag) is done first. Then, the tag is added and a second measurement  $S$  is done. In this case, the tag response  $S_t$  can be approximated by :

$$S_t \simeq S - S_e \quad (1.12)$$

In real application this method is difficult to implement when the tag is printed on the package since tag and package can not be easily separated. This is not usable especially when the environment contains objects that move over time.

**Time-Gating** uses the time response of the tag to reduce the clutter. The time response is obtained via inverse Fourier transform from a measurement done with a VNA for example. As illustrated in the Fig. 1.8, the mode of interest is the resonant antenna mode. The clutter response is the initial pulse of Fig. 1.8. Due to its high-quality factor, the antenna mode is long-lasting. By taking a time window where the clutter response is null but the antenna mode still resonating,

it is possible to only have the tag response. The frequency response is obtained by the Fourier transform of this time window. Notice that it is possible to have several clutters due to multiple reflections/multipath. This technique is very efficient in the presence of a ground plane where the initial peak is very strong. The major drawback is that it does not exist analytical formula to determine the time window to use. Also, if an object is present at a distance larger than the tag, the method cannot be used easily. The time-gating approach can combine time and frequency in representation such as a spectrogram [45].

**Pole residue techniques** are methods to extract the complex poles of a chipless tag response as presented in Section 1.5.1. Algorithms such as the Short-Time Matrix Pencil [47, 48] or numerical fitting of the damped time response illustrated in Section 1.5.1. This technique is also used on the time response.

**Polarization filtering** is also common in chipless RFID works. The idea is that most ordinary objects do not depolarize the electromagnetic wave and therefore can not reflect it in cross-polarization since, around us, objects are mostly positioned vertically or horizontally and we do the same for the orientation of the reader. Induced currents on radar targets used for chipless RFID backscatter the wave in a preferred direction. This direction can induced cross-polarization when using special resonators shapes [46, 49] or by positioning the resonators with an angle (usually  $45^\circ$ ) from the co-polarization axis [50, 51]. The major drawback of this approach is that not all the power is received in cross-polarization, a part of the power is still in co-polarization hence lower signal levels. Also, relative orientation between the reader and the tag needs to be known a priori.

The configuration illustrated in Fig. 1.7 is simulated in CST MW using the time domain solver and a plane wave excitation. The probe is positionned 1 meter from the loop resonator. A dielectric of 5mm and permittivity 20 is placed 20mm behind the loop resonator to create a reflexion (environment). The raw simulated backscatterer signal is compared to the other approaches in Fig. 1.12. Notice that for the loop at  $45^\circ$ , a wide peak at 2.5GHz is present which is not linked to the loop resonator's behavior. This peak is a parasitic mode of resonance exhibit in Section 3.3. A more complete comparison of these approaches is done in Section 3.3.

#### 1.5.4 Re-radiation pattern

The concept of re-radiation pattern will be presented in this section and be used in Chapter 3. The re-radiation pattern is a representation of the back-scattered power of a target in space usually in its far-field region (distance  $R$  with  $R < 2D^2/\lambda$  where  $D$  is the largest dimension of the target) - similar to the RCS. Indeed, backscattered signals are not emitted with the same amount of power in the different directions of space, some regions are privileged. An example of common chipless RFID resonators' radiation patterns can be found in Fig. 1.13. In Fig. 1.13, red regions are the directions with the maximum power reemitted while blue regions are the regions with the lowest power.

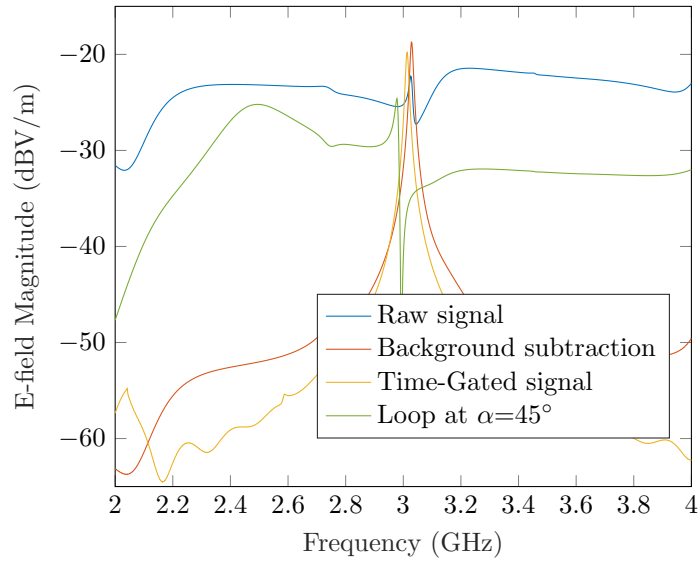


**Figure 1.12:** Different reading methods for chipless RFID applied on a simulated loop resonator placed in front a dielectric of 5 mm and permittivity 20 placed 20 mm behind the loop.

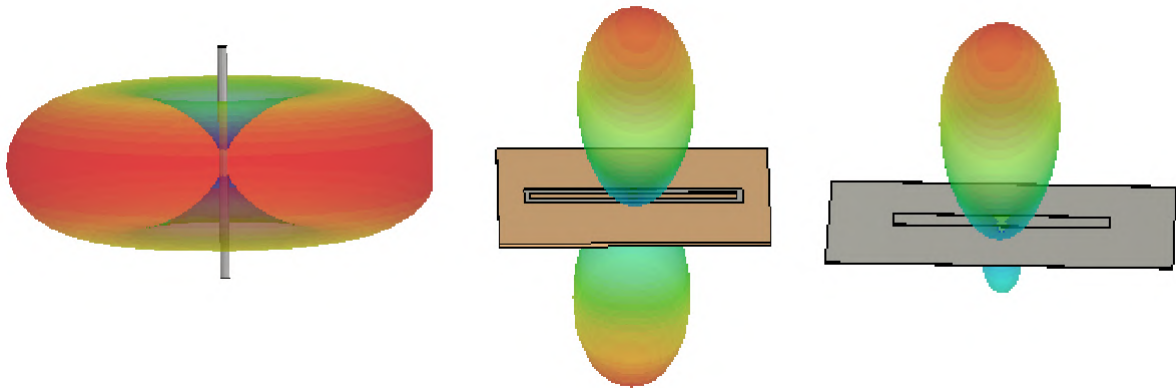


**Figure 1.13:** Radiation pattern of a (a) dipole, (b) a loop and (c) dipole over ground plane resonators at their fundamental resonance frequency. For the dipole, the plane wave excitation is on the side coming towards the dipole. For the loop and the dipole over ground plane, the plane wave is above the tag coming towards the resonator.

### 1.5.5 Identification principle

To encode the information in RFID chipless tags, it is necessary to encode the ID on a physical parameter since no electronics/chips are present to establish a communication protocol. The reader will detect these physical variations to identify the tag. We find various approaches which were proposed during the development of the RFID chipless : time domain (using delay transmission lines) [52, 53], frequency (using the position, the amplitude or the phase at certain resonance frequencies) [54, 55, 56], using a radar image [57, 58] or a combination of several of the preceding methods. A recent comparison of the data encoding of different approaches is presented in [59] and is summarized in Table. 1.4.

**Table 1.4:** Comparison of coding capacity in chipless RFID [59].

Technique	Type of tag	bit/cm <sup>2</sup>	Operating frequency (GHz)
Time domain	SAW [60]	<1	2.44
	TDR [61]	0.17	3.1 - 10.6
Frequency domain	Slot [62]	<4.2	3.1 - 10.6
	Spiral [63]	0.61	3.1 - 7
	C-shape [64]	1.14	2 - 4
Hybrid	Frequency-phase [65]	2.86	2.5 - 7.5
	Frequency-angle [66]	0.52	1.8 - 2.2
	Frequency-Magnitude [59]	3	2 - 5
Spatial-domain	SAR [67]	2	-
	INSAR, SAR [68]	1.6	-
Polarization	Split ring [69]	3	-

We will focus on the frequency approach since it is the one used for this thesis. The frequency approach is today the most attractive compared to the others. Currently, this approach allows obtaining high coding capacities with compact tag geometries.

The frequency approach in chipless RFID consists in coding the information by creating peaks/dips on the amplitude of the backscattered signal of the tag at certain frequencies. For this reason, the vast majority of frequency tags require a very large frequency band to operate and are therefore subject to FCC (in the USA) or ECC (in Europe) legislation [70, 71]. Chipless RFID technology can work in the ultrawideband range (3.1–10.6 GHz). UWB frequency masks defined by FCC and ECC are presented in Fig. 1.14. This impose low and limited emission powers from the reading system. Notice that it is not required to measure the RCS of the tag but S-parameters sufficient [72]. Frequency chipless tags can be classified into two categories :

**Planar filter tag :** It consists of two antennas connected by a transmission line coupled to resonators.

One antenna acts as a receiver and the other as a transmitter. Often, the two antennas are oriented at 90° to each other to avoid crosstalking. Planar filter tag with only one antenna also exists. Each resonator will act as a notch filter. Thus in the frequency response, the presence of a resonator at a frequency  $f_i$  will appear as a notch/peak on the signature of the backscattered wave represented as a function of frequency (see Fig. 1.15). If we want to encode a '1', we can short-circuit the resonator which has the effect of translating the notch in higher frequencies outside the operating frequency of the tag.

**REP (RF Encoding Particle) :** The REPs are resonant elements that backscatter the wave comprising a receiving antenna, a filter/generation of the ID and a transmitting antenna all-in-one. There are several types of resonators performing these functions : dipole, patch, SRR, C-shaped, L-shaped, loop, ... Some resonators are also independent of the polarization of the incident wave.



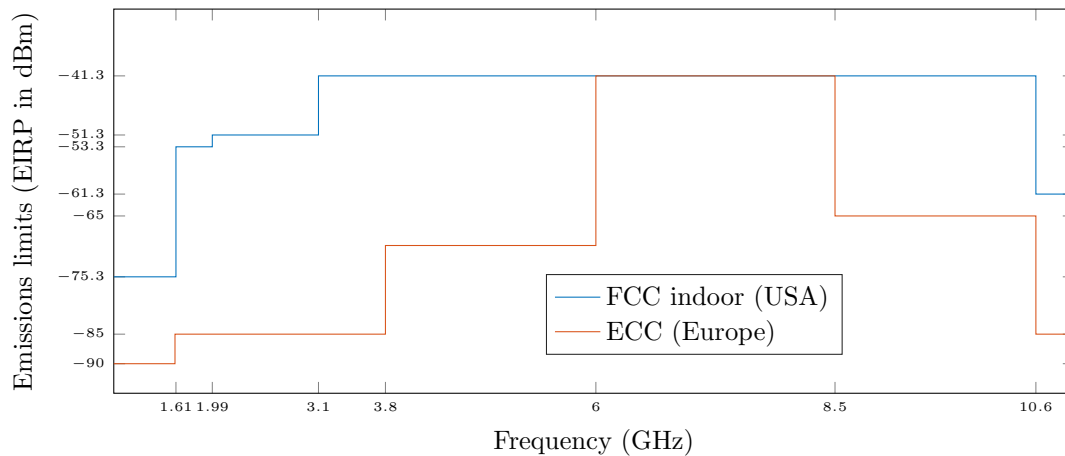


**Figure 1.14:** European UWB mask and FCC UWB indoor mask.

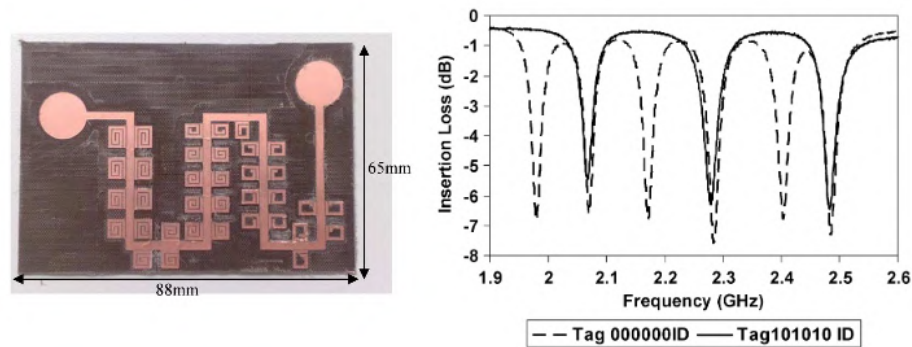


**Figure 1.15:** Planar filter tag used in [73] and its frequency response.

Their geometry intrinsically allows a resonance mode at a given frequency. REPs are very attractive thanks to their compactness. Therefore, they are at the center of this thesis work.

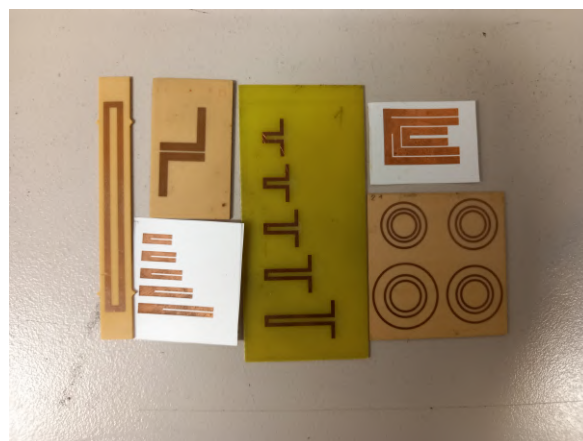


**Figure 1.16:** Different shapes of REP.

Finally, frequency tags have also been realized in the THz frequencies. The identifier is encoded in

the arrangement of layers in a Fabry-Perot type structure. Its operation is thus similar to Fabry-Perot cavities where the reflected wave depends on the permittivity of each layer and their thickness [74].

Frequency coded chipless tags are composed of several resonators as illustrated in Fig. 1.17 with dipoles resonators. When an incoming electromagnetic wave illuminates a tag, resonators will backscatter some energy at their resonance frequencies. Since each resonator has its own resonance frequency (the frequency where the resonator dimension is  $\lambda/2$  - see Fig. 1.17), it is possible to differentiate each resonator individually. Based on this principle, diverse data encoding schemes have been proposed. A conventional encoding scheme is the On-Off Keying modulation : a frequency band will be chosen and divided into sub-frequency slots. Each frequency slot is associated with a bit of data. In Fig. 1.17, a resonance peak is present in a frequency slot if the corresponding resonator is present, then the bit is set to '1'. If no peak is present (the corresponding resonator is absent), the bit is set to '0'. The simplicity and robustness of this encoding scheme explain its widespread.

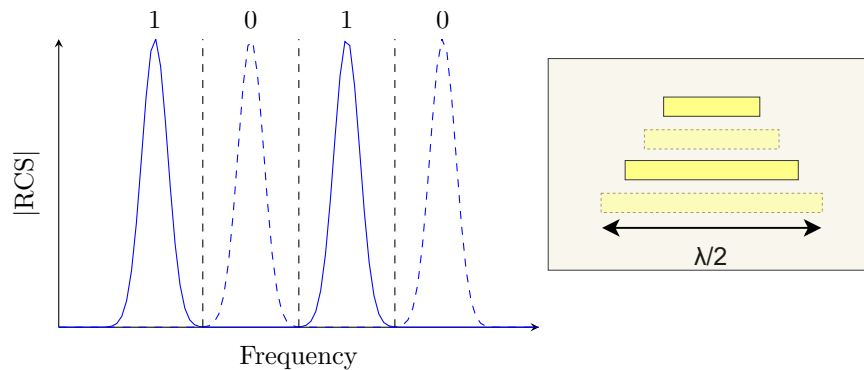


Figure 1.17: REP approach using dipoles [75] and OOK encoding.

### 1.5.6 RFID sensors

To position the chipless RFID sensors, it is interesting to go back to what can be done in RFID (chipped and chipless). RFID technology has become very popular in both identification and sensing applications. The technology is widely used driving demand for low-power, low-cost and wireless utilization. RFID sensors are energy efficient, small, and easy to use, and meet various needs of IoT. The use of innovative materials and manufacturing techniques combined with increasingly sophisticated data collection techniques makes RFID sensors even more attractive for IoT applications that require sensing capabilities. Additionally, each RFID sensor has a unique identification number to disambiguate data collection from the sensor. Finally, RFID has significant advantages over other sensing and identification technologies because it does not require a line of sight, and can collect data from multiple sensors simultaneously in real-time. A comparison of sensor solutions can be found in Table 1.5.

For these reasons, RFID sensors are of great interest not only in the world of scientific research, but also in industry. We see many advanced and practical applications today - see Table 1.18.

Chipped RFID tags are now a mature technical solution, continuously increasing their presence in the market and multiple application scenarios [13, 12]. Battery-powered sensors have obvious

	Wired Sensors	Wireless Sensors	RFID Sensors	Chipless RFID Sensors
Installation cost	High	Low	Low	Low
Maintenance cost	Low	High	Low	Low
Scalability	Low	High	High	High
Sensor accuracy	High	High	Medium	Medium

Table 1.5: Comparison of sensor technologies [11].









RFID Sensors							
Healthcare	Food Quality	Agriculture	Automotive	Structural Health Monitoring	Space	Wearable & Implantable	Localization & activity monitoring
							
<ul style="list-style-type: none"> <li>Body temperature monitoring</li> <li>Blood glucose monitoring</li> <li>Activity and gesture sensing</li> <li>Sleep disorders</li> </ul>	<ul style="list-style-type: none"> <li>Meat, fish, vegetable freshness monitoring</li> <li>Expiration date monitoring</li> </ul>	<ul style="list-style-type: none"> <li>Soil moisture monitoring</li> <li>Precision irrigation</li> <li>Agro-food supply chain monitoring</li> <li>Vineyard monitoring</li> <li>Cold chain monitoring</li> </ul>	<ul style="list-style-type: none"> <li>Automatic production monitoring</li> <li>Security of infants</li> <li>Tire pressure sensors</li> <li>Vehicles road distance</li> </ul>	<ul style="list-style-type: none"> <li>Metal and concrete crack monitoring</li> <li>Structural damage detection</li> <li>Monitoring of structural movements</li> <li>Corrosion monitoring</li> </ul>	<ul style="list-style-type: none"> <li>Temperature monitoring</li> <li>CO<sub>2</sub> monitoring</li> <li>Battery level monitoring</li> </ul>	<ul style="list-style-type: none"> <li>human movements</li> <li>Heart &amp; breath frequency monitoring</li> <li>monitoring body areas and vascular prosthesis</li> </ul>	<ul style="list-style-type: none"> <li>human movements</li> <li>Heart &amp; breath frequency monitoring</li> <li>monitoring body areas and vascular prosthesis</li> </ul>
Examples of practical applications							

Figure 1.18: RFID sensors: application fields and examples of practical applications [11].

advantages for long-distance data transmission, but the use of batteries increases system complexity, maintenance issues, and shortens system life (they must be replaced every few days) limiting the environmental capabilities (temperature, humidity, corrosion, etc.). Battery-less tags can also exist powered by either the reader or the environment. A possible architecture is shown in Fig. 1.19. The sensor resides on the tag and interacts with the [76] chip or is integrated into the chip [77]. Some bits of the ID code can be used to transmit the value of the detected parameter. Another solution is to integrate a sensor mechanism on top of the antenna (see Fig. 1.19).

In contrast, chipless RFID detection is a relatively new paradigm with the potential to become a disruptive solution in the market but further research in this area is needed to adapt it for use in specific scenarios. Various elements make the tag sensitive to their environment limiting their application. This sensitivity can be used to make sensors. An example of the change in losses or permittivity due to ambient variation can be seen in the frequency response as shown in Fig. 1.20. The losses impacts the amplitude of the resonance frequency while the permittivity impacts its position. In practice, detection can be achieved by many radio frequency properties, such as dielectric constant/loss changes [78], tag geometry changes [79], and wave polarization conversions [80]. In this work, we present several sensors that use these different properties. By eliminating the chip and

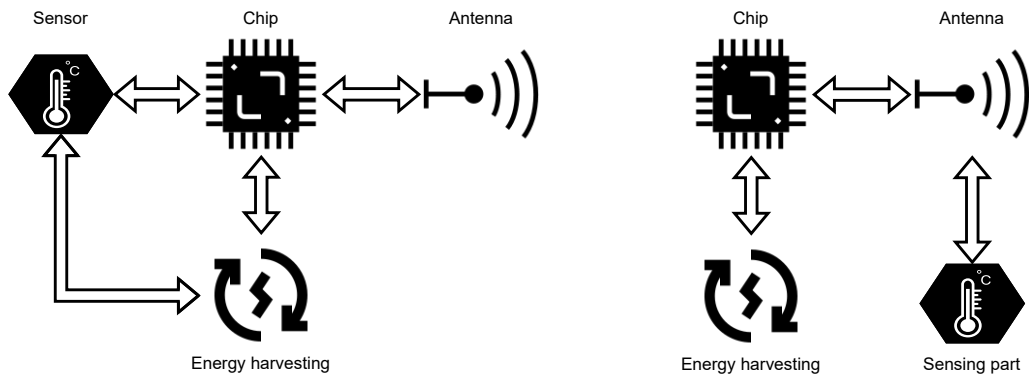


Figure 1.19: Chipped RFID sensors architectures.

battery, the cost of the sensor can be greatly reduced, and theoretically, infinite service life can be achieved. With no electronics, chipless RFID sensors can be suitable for harsh environments where chipped tags can not go (high temperature, corrosion, ...).

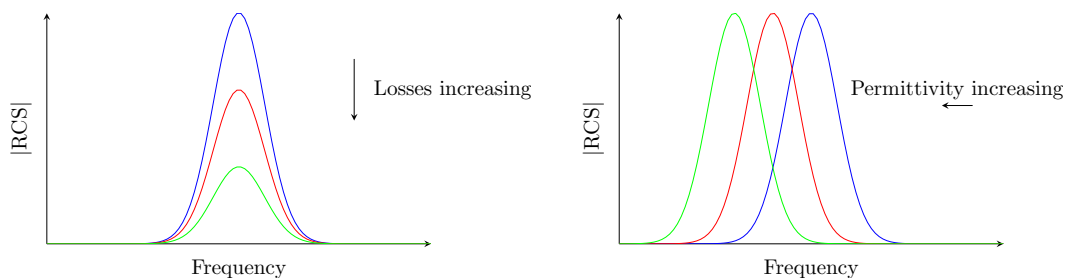


Figure 1.20: RCS variation of resonant chipless tags following environment changes.

As it was presented in Table 1.1, the unitary price of a chipless RFID sensor is lower than the price of UHF RFID which is also lower than the price of an electronic sensor. The price chart as a function of the number of sensors brought is shown in Fig. 1.21. RFID technologies present an initial offset due to the acquirement of a reader which is a one-time purchase.

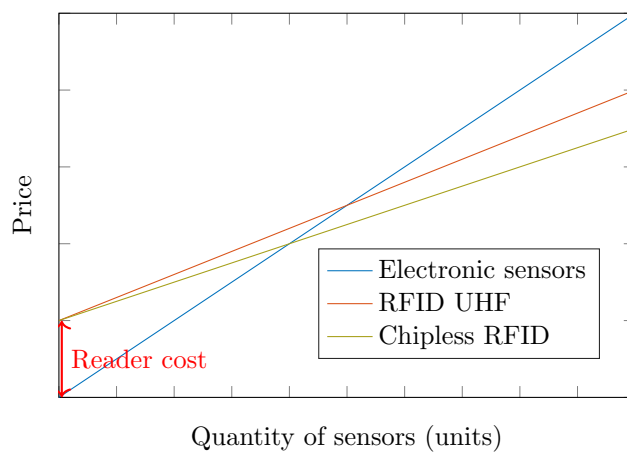


Figure 1.21: Price chart as a function of number of sensors.

This sensor functionality can be added to current frequency chipless RFID tags at no additional expense while maintaining their identification capabilities keeping the traditional interrogation procedure. Indeed, such small shifts as illustrated in Fig. 1.22 in their resonance frequencies do not impact the chipless RFID identification scheme and do not reduce the coding capacity of the tag. We will see later in the manuscript that for example variation of 1°C leads to a shift of 64kHz which is negligible compared to the width allocated to the frequency slots for the identification (100 MHz).

Finally, concerning sensors in the general case, two types exist:

**Threshold sensor** These sensors are more easily achievable and often not expensive. It does not allow measuring precisely physical quantities but allows us to know if this one exceeded a certain threshold value. Because of these characteristics and its simplicity, it is of interest in applications such as food distribution with the monitoring of the cold chain.

**Absolute sensor** These sensors are more delicate to realize in practice but allow to have a value and not an indication of a value overtaking.

We can make an analogy with digital signals. The first type of sensor would be digital with discrete values that indicate whether the value being measured has exceeded a threshold or not. The second type of sensor would be an analog with continuous values. In this manuscript, the work focuses on absolute sensors.

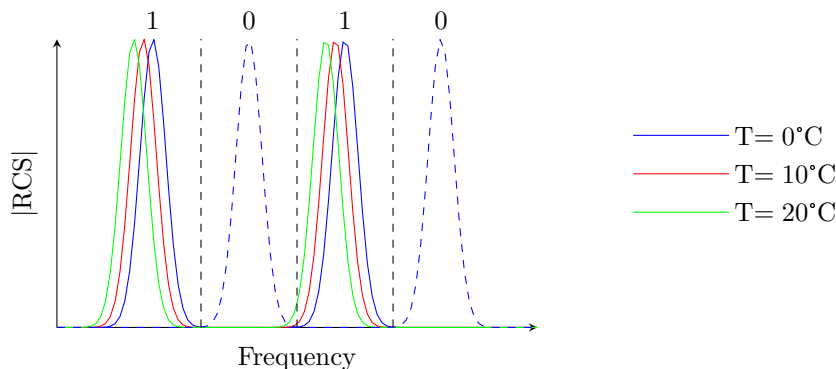


**Figure 1.22:** Illustration of temperature sensing  $T$  added on top of the identification purpose of chipless RFID tags.

## 1.6 Conclusion of the chapter

In this chapter, the history of RFID technology from the Thereminvox to the latest advancements was introduced. A comparison between the barcode and RFID was presented to understand its assets and the enthusiasm around this new identification technology. A focus was done on chipless RFID to explain the context behind this thesis work. The working principle of such tags was presented with the back-scattering approach and its radar configuration, the reading methods used to read chipless tags, and how the information is encoded in the back-scattered signature. Finally, a brief section explaining the interest and a working example of chipless frequency sensors was introduced. The next Chapter will continue on the idea of sensors with temperature and humidity sensors.

## Chapter 2

# RFID Chipless and environment sensing

In this chapter we will focus on the relation between thermal considerations and the radio-frequency domain. Firstly, we will focus on the phenomenon of thermal dilatation. This study will lead to the creation of a novel test-bench to characterize thermal dilatations of metals. A second section will focus on the temperature measurement using classical chipless RFID scatterers. The sensing will be achieved through the thermal dilatation of the tag as well as the permittivity variation of its substrate due to changes in temperature (both with and without dielectric resonators will be studied). It will be shown that the selectivity of this sensor is not perfect since other physical quantities can also affect the response of the sensor. For this reason, a final section will present a method to isolate and sense multiple physical quantities with an example on combined temperature and humidity sensing.

### 2.1 Characterization of thermal dilatation by RF approach

Thermal expansion coefficient is a crucial parameter for applications in the field of civil engineering or semiconductor industries. We can see in the literature that many different experimental approaches have been used. This significant diversity comes from the great variety of techniques that exist to measure displacement. We can cite purely mechanical approaches, or the very wide variety of optical approaches (interferometry, optical imaging, X-rays diffraction...) [81]. Thus, to extract the thermal expansion of a material, examination of the literature reveals for example mechanical dilatometers such as capacitance dilatometers [82] which consist of two parallel plates with one stationary and one that can move. The thermal expansion moves the free plate and so, shifts the gap between the plates. By measuring the capacitance, the thermal expansion coefficient can be extracted. Push-rod dilatometer [83] can also be found, where a rod of the material under-test expands and transfers its expansion to a pressure gage measuring the displacement. This method is widely used for many reasons. For example, it is compatible with most materials. However, one of the main drawbacks of this test benches comes from the fact that the material under test is in contact with the bench, so particular attention must be paid to thermally isolate the bench from the heated sample. Specific materials are needed to fabricate the test bench, and reference samples can be used to reduce the uncertainty. For this reason, contactless methods have been widely studied. To develop more precise test bench, several optical approaches have been used to measure CTE [84]. Compared to dilatometry, significantly

greater accuracy can be obtained. For example, optical dilatometers using an interferometer can have resolution of 0.1% [85, 86]. However, the main limitation of these techniques, such as interferometry, is a maximum temperature of measurement above 700°C. Other drawbacks of these methods are the cost of optical setup, the need of alignment accuracy as well as a strict control of the environment (the use of a vacuum chamber for the effect of the refractive index of the atmosphere on the wavelength of light, strict control of the wavelength of the laser...). Another optical method consists in a digital microscope to picture the expansion as a function of temperature and an optical mire to convert pixel to length [87]. For some materials such as crystals, X-ray diffraction can be used to measure the crystal lattice parameter as a function of the temperature in order to extract its thermal expansion [88]. From the state of the art, each experimental approach has advantages and disadvantages depending on multiple factors such as the uncertainty, the sample size or shape, the sample preparation time, or the temperature range required. Note also that most of these test methods have been standardized for general use [89, 90, 91]. A brief summary of the general advantages and disadvantages of some approaches is given in Table 2.1. Multiple other CTE measurement benches exist and have been listed in [81].

In the first row of Table 2.1, the uncertainty of the different methods is compared based on some references in order to give examples of the error that can be reached. However, even if the CTE of various materials are listed in a large number of reference books, the uncertainty is seldom reported. Due to the fact that these values are averaged over large ranges of temperature in most sources, the uncertainty at ambient temperature can be increased. Another reason why reference books could not be accurate enough is relating to the fact that metals are rarely pure, so CTE can vary from manufacturer to manufacturer. Note also that all these different experimental approaches require dedicated and optimised test benches that are generally not commercially available or not easy to access to non-expert in the field of materials engineering. For all these reasons, an easy approach to implement CTE measurement technique is required. Contrary to most existing techniques, the one presented here requires no calibration or sample of reference. It is based on a very simple analytical model that everyone can implement. Moreover, the bench is composed of commercially available off-the-shelf RF equipment. Last but not least, this novel test bench can be easily replicated by any expert in the field of RF in order to measure the CTE of his own material.

Despite the very large number of test benches developed for the measurement of CTE, to our knowledge, none is based on an RF principle. However, since the beginning of the 19th century [2], it has been shown that by sending an electromagnetic wave towards a specific target, and by receiving the backscattered field, many physical quantities can be sensed wirelessly. A striking example of such back-scattering application can be traced back to the early 1900's with Leon Theremin's work [2]. This work includes the contactless musical instrument called 'Thereminvox' which uses the position of the hand to produce a sound, or the passive listening device called 'The Great Seal bug' [2]. Since then, numerous works have been done to wirelessly sense physical quantities using this back-scattering principle such as mechanical displacement of the order of 100  $\mu\text{m}$  [92], strain [93], small variations due to the fabrication randomness of the tag for authentication [94], or even permittivity [49]. The closeness between RF and thermal domain has been also used to develop RF temperature sensors by using, for example, temperature dependence of permittivity [95] or dilatation of a 3D structure [96].

Here, a free-space measurement of the resonance frequency of a resonator is used to characterize the thermal coefficient of metals. Specific planar resonant scatterers fabricated with several metals under characterization have been introduced for this purpose. The scatterer's shape is simple enough to be modeled with an analytical expression and also to fabricate. With this model, the derivation of the CTE does not require any advanced computation, any RF solver or even a lookup table as it is generally the case when one seeks to capture a physical quantity by using the principle of back-scattering because of the complexity of the problem. The measurement technique is essentially based on the resonator which has been designed to meet precise specifications: the resonator is made entirely of metal, in one layer and has a high resonating behavior. As described below, these two characteristics are essential for the measurement of CTE using RF waves.

**Table 2.1:** Advantages and disadvantages of existing methods

	Mecanical (push-rod)	Optical (microscope)	Optical (interference)	X-ray	This method
Error on CTE	4% [97]	6% [87]	<1% [98]	6% [99]	6%*
Materials adaptability	Very good	Good	Good	Only crystals	Only metals
Contactless	No	Yes	Depend	Yes	Yes
Alignment accuracy	Not needed	Needed	Needed	Needed	Not needed
Sample preparation	Minimal	-	Depend	Extensive	Medium
Equipment cost	Low	Medium	High	High	Medium
Standard	[89]	No	[90]	No	No

\* Maximum error observed on the data set.

### 2.1.1 Thermal dilatation principle

The thermal expansion of a material is defined as the modification of its volume with a temperature variation at a constant pressure. If we consider a 1-dimension object of length  $l_1$  at temperature  $T_1$  (Fig. 2.1), this object will expand with an increase of temperature, and the final length at a temperature  $T_2$  is :

$$l_2 = l_1 + d_l = l_1(1 + \alpha_{CTE}(T_2 - T_1)) \quad (2.1)$$

where  $d_l$  is the variation in length due to the increase in temperature [81] and  $\alpha_{CTE}$  the coefficient of thermal expansion (CTE) of the material.  $T_2 - T_1$  will be written  $\Delta T$  in the rest of the manuscript.

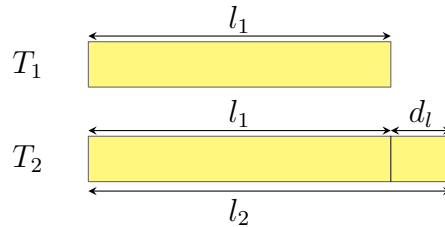


**Figure 2.1:** Expansion of a 1D object due to temperature variation.



In this work, the thermal expansion coefficient  $\alpha_{\text{CTE}}$  is supposed to be temperature-independent in the considered temperature range which is usually the case for metal on wide temperature ranges (e.g. for temperature in the range  $0^\circ\text{C}$  and  $100^\circ\text{C}$ ). Note that this coefficient is positive for almost all materials. In addition, this thermal effect affects a real 3D object in all directions which means that if the material is not isotropic for this phenomenon, the CTE can be different in the different directions ( $x$ ,  $y$ , and  $z$ ). Example of CTE for different metals can be found in Table 2.2.

**Table 2.2:** Coefficient of thermal expansion at  $25^\circ\text{C}$  of different materials [100].

Material	CTE [ $^\circ\text{C}^{-1}$ ]
Zinc	$31 \times 10^{-6}$
Copper	$17 \times 10^{-6}$
Titanium	$8.5 \times 10^{-6}$
Nickel	$13 \times 10^{-6}$
Aluminium	$23 \times 10^{-6}$
Bronze	$17 \times 10^{-6}$
Tungsten	$4.5 \times 10^{-6}$

In this section, a loop resonator is considered as the scattering device and its thermal expansion is studied (Fig. 2.2). The resonator is only composed of one layer of metal to remove the substrate thermal influence since the dilatation of the resonator is the under-characterization phenomenon. The thickness of the metal is sufficiently important (around  $500\mu\text{m}$ ) to ensure a good rigidity of the pattern. The case where the resonator is placed on a substrate will be studied in the next section. With this loop shape, the resonance frequency can be considered to be related only with its larger dimensions. So the extracted CTE is in the direction of the notch characterized by its length  $l$  (along  $x$  axis) as illustrated in Fig. 2.2. In the rest of the manuscript, a physical quantity with subscript 1 (respectively 2) is considered at temperature  $T_1$  (respectively  $T_2$ ).

The measurement principle based on free-space measurement is illustrated in Fig. 2.3. When a loop is illuminated by an incoming electromagnetic-field, the maximum energy back-scattered at a temperature  $T_1$  occurs at its resonant frequency  $f_1$  defined by [101]:

$$f_1 = \frac{c}{2\sqrt{\epsilon_{\text{eff}}}(l_1 + 2\Delta l_1)} = \frac{c}{2\sqrt{\epsilon_{\text{eff}}}L_1} \quad (2.2)$$

where  $c$  is the speed of light in vacuum,  $\epsilon_{\text{eff}}$  is the effective permittivity seen by the loop,  $l_1$  is the length of the notch and  $\Delta l_1$  is the additional length taking into account the presence of short circuit (SC) discontinuities (see Fig. 2.2). Indeed the loop resonator can be considered as a transmission line section terminated at both ends by a SC [101]. Note that the effective length  $L_1 = l_1 + 2\Delta l_1$  will be used for the rest of the manuscript. Note also that if the loop is used without any substrate, so  $\epsilon_{\text{eff}}$  is equal to 1.

As mentioned, the physical length of the resonator  $l_1$  follows (2.1) but  $2\Delta l_1$  which physically corresponds to an interconnection realized by a conductor does not necessarily follow the same

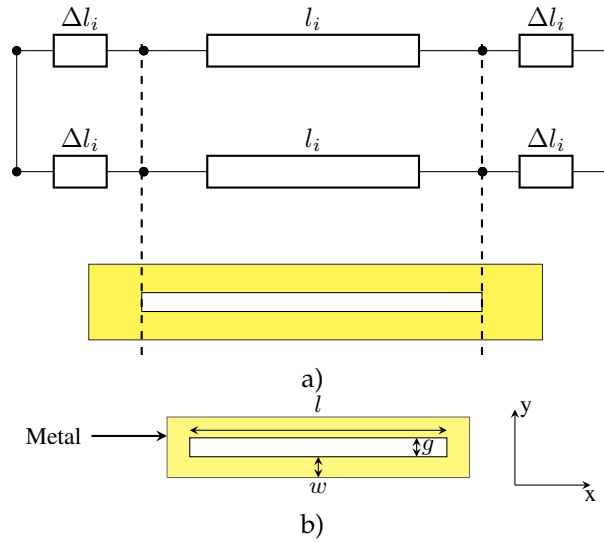


**Figure 2.2:** a) Equivalent transmission line model of a loop resonator [101]. b) Nominal dimensions of the fabricated loop (i.e. values used for the fabrication):  $l = 50.83\text{mm}$ ,  $g=2.07\text{mm}$  and  $w=1.43\text{mm}$ .

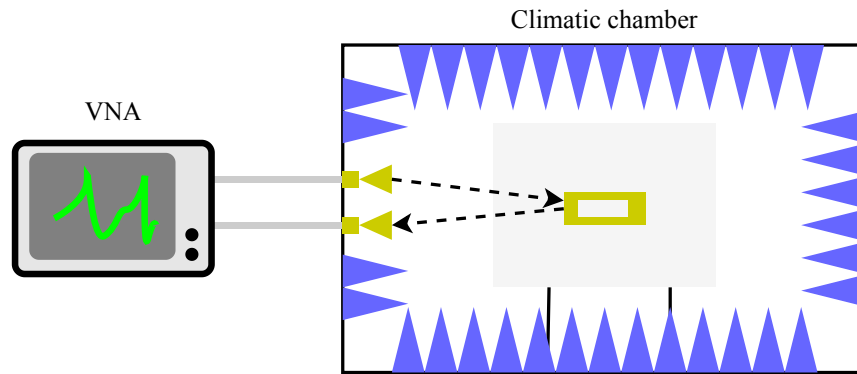


**Figure 2.3:** Principle of the measurement method used to extract the CTE.

dependence with temperature. Indeed, the shape of this conductor is not only along the  $x$  axis but also the  $y$  axis. At a temperature  $T_2 > T_1$ , the effective length  $L_1$  will increase and its expression  $L_2$  can be written as :

$$L_2 = l_1(1 + \alpha_{\text{CTE}}\Delta T) + 2\Delta l_1(1 + K\alpha_{\text{CTE}}\Delta T) \quad (2.3)$$

with a constant coefficient  $K$ , where in the proposed model, describes the specific dilatation of the SC discontinuities. Therefore, the resonant frequency  $f_2$  for a temperature  $T_2 > T_1$  will be shifted to lower frequencies and can be written as :

$$f_2 = \frac{c}{2\sqrt{\epsilon_{\text{eff}}}L_2} = \frac{c}{2\sqrt{\epsilon_{\text{eff}}}L_1(1 + \alpha_c\Delta T)} \quad (2.4)$$

where  $\alpha_c$  is introduced as the equivalent expansion coefficient for the effective length  $L_1$ . The expression of  $\alpha_c$  is deduced from (2.3) and (2.4) and is :

$$\alpha_c = \alpha_{CTE} \frac{l_1 + 2K\Delta l_1}{l_1 + 2\Delta l_1} \quad (2.5)$$

In order to study the effect of K, electromagnetic simulations of a loop resonator in vacuum with dimensions given in Fig. 2.2 have been carried out using the software CST MW. The quantity  $2\Delta l_1$  has been determined so that the effective length in (2.4) matches the simulated resonance frequency for  $T=0^\circ\text{C}$ . The frequency response of the resonator has been extracted for different temperatures in the range  $0-60^\circ\text{C}$  based on (2.1). Fig. 2.4 presents the variation of the simulated resonant frequency versus temperature.

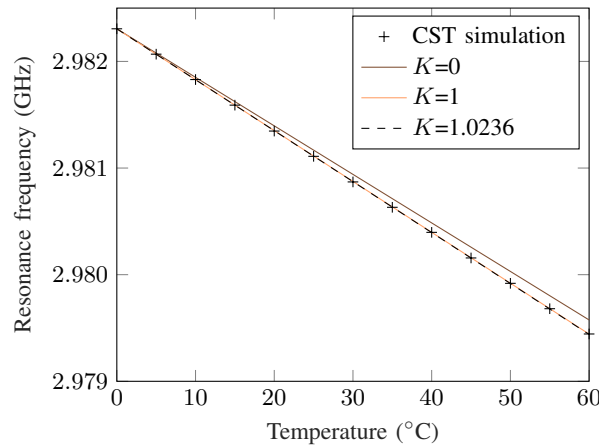


**Figure 2.4:** Resonance frequencies of a loop versus the temperature. Comparison between simulations results and the introduced model (2.5) for different values of the coefficient K.

To illustrate the effect of K, with the use of (2.5), two cases were plotted:  $K = 0$  ( $\Delta l_1$  doesn't expand with temperature) and  $K = 1$  (both lengths are affected in the same way). We can see that the case ( $K=0$ ) leads to the maximum error with the simulations while the case ( $K=1$ ) gives better results. However, the optimal result is obtained when  $K=1.02$  leading to an equivalent expansion coefficient :

$$\alpha_c = 1.01\alpha_{CTE} \quad (2.6)$$

The quantity K is a geometry dependant parameter of the scatterer and  $\Delta l_1$  is a function of the effective permittivity as expressed in [101]. Simulations with different loop lengths  $l$  show that K can have different values (for example,  $K=1.60$  is found for  $l=39\text{mm}$ ) which makes (2.6) necessary to obtain a good accuracy on the extracted CTE. A study of the influence of K on the accuracy of the measurement is presented later in Section 2.1.4.

In simulation, it has been noticed that different resonator lengths lead to different K values. Thus two resonators of the same metal - same  $\alpha_{CTE}$  - have two different  $\alpha_c$  values. We will see in more details in the next section that this conclusion offers a significant advantage.

When temperature increases, the effective length  $L_1(1 + \alpha_c \Delta T)$  increases leading to a lower value of the resonant frequency as described by (2.4). If the substrate permittivity is assumed temperature-independent, the value of  $\alpha_c$  can be extracted with the measurement of two resonant frequencies ( $f_1, f_2$ ) at different temperatures ( $T_1, T_2$  respectively) and then the value of  $\alpha_{\text{CTE}}$  can be extracted using (2.6). Indeed, based on (2.4) we can write for two temperatures  $T_1, T_2$  with a reference length  $L_0$  at temperature  $T_0$  :

$$L_1 = L_0(1 + \alpha_c(T_1 - T_0)) = \frac{c}{2\sqrt{\epsilon_{\text{eff}}}f_1} \quad (2.7)$$

$$L_2 = L_0(1 + \alpha_c(T_2 - T_0)) = \frac{c}{2\sqrt{\epsilon_{\text{eff}}}f_2} \quad (2.8)$$

Considering (2.7) and (2.8), the CTE can be extracted using the following formula:

$$\alpha_c = \frac{f_1 - f_2}{f_2 T_2 - f_1 T_1 - (f_2 - f_1)T_0} \quad (2.9)$$

Note that (2.9) is independent of  $L_0$  and also of the effective permittivity  $\epsilon_{\text{eff}}$ . With this method, the CTE can be extracted with a good accuracy without a prior knowledge on the length  $l_0$  and effective permittivity of the scatterer. For the rest of the manuscript, the reference temperature  $T_0$  is set to  $0^\circ\text{C}$  to be able to compare our results with the data given by the metal's provider (Table 2.4). In this case, (2.9) can be simplified:

$$\alpha_c = \frac{f_1 - f_2}{f_2 T_2 - f_1 T_1} \quad (2.10)$$

Another solution to extract  $\alpha_c$  is to develop (2.7) and (2.8) using Taylor series of first order and to note that the frequency shift  $\Delta f$  caused by a variation of the temperature is equal in first approximation to

$$\Delta f \simeq f_1 \alpha_c (T_2 - T_1) \quad (2.11)$$

So if we have several measurements at different temperatures, this linear expression can be used to extract  $\alpha_c$ .

## 2.1.2 Measurements in climatic chamber

Tags made of different metals have been realized to validate the approach. Tag dimensions are given in Fig. 2.2. The measurement configuration setup and the fabricated tags used to determine the CTE are illustrated in Fig. 2.5. As shown in Fig. 2.3, tag support is polystyrene with an effective permittivity close to 1. Based on results described previously, a value of  $K = 1.02$  was considered to extract the CTE [see (2.6)].

A climatic chamber VC0018 by Votsch is used to control the temperature. Absorbers are placed inside the chamber to reduce the reflection level (see Fig. 2.5). A bi-static antenna configuration is used to increase the isolation. The protocol followed to do the measurements is the following: the temperature in the climatic chamber is first set. When the temperature is stabilized, the  $S_{21}$  parameter is measured using a VNA. The exact measurement of the temperature of the loop is then determined using a thermal camera (Infrared Thermal Camera TC-1). We used this method to be sure of the extracted temperature because of the thermal inertia of the different materials inside the climatic

chamber. The measurements have been smoothed in order to remove any residual measurement noise that may impact the search for the maximum and thus induce an error on the frequency extraction. Raw and smoothed measurements are plotted in Fig. 2.6-b.

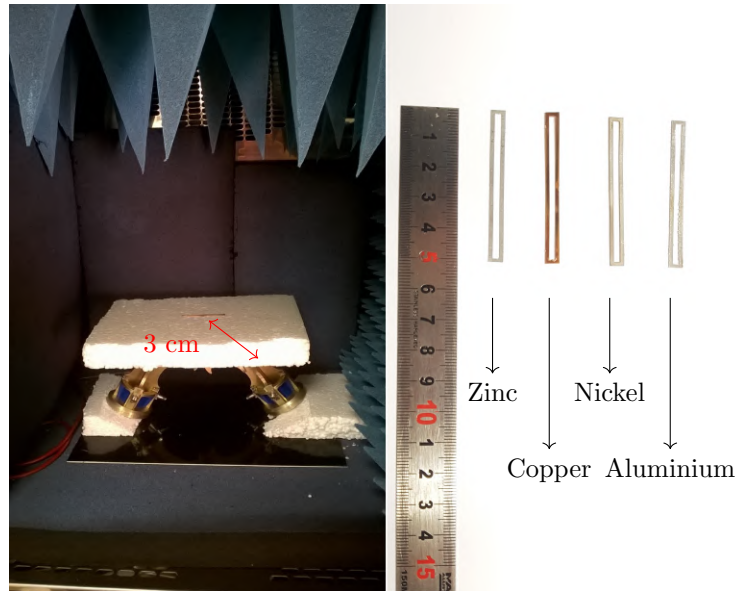


**Figure 2.5:** Setup configuration. a) Bi-static configuration inside the climatic chamber. b) The loop resonators made with different metals.

**Table 2.3:** Technical information of the climate chamber [102].

Technical informations		
Temperature range	°C	-10°C à 90°C
Humidity range	%RH	10 à 98
Temperature fluctuation over time	°C	±0.1°C à ±0.5°C
Temperature difference in space	°C	1 à 2
Fluctuation of the hygrometry in time	%RH	±1 à ±3
Heating	°C/min	0.6
Cooling	°C/min	0.3

### 2.1.3 Results and analysis

The loop of the same geometrical dimensions presented in Fig. 2.2 has been realized with 4 different metals (Zinc, Nickel, Copper, and Aluminum). High purity metals have been chosen for the fabrication (more than 99% purity). The CTE of these metals is given by the manufacturer following ASTM or DIN (international standards test-methods) [100] presented in Table 2.4 and compared to our measurements. Note that aluminium is coming from a different provider and its CTE is given with a precision of ±5%.

The zinc loop resonator has been measured for several temperatures from 27.2°C to 56.2°C. The measured  $S_{21}$  parameters are plotted in Fig. 2.6-a. Simulation results are also given for comparison. Note that a notch  $l$  equal to 51.1mm at  $T=27.2^\circ\text{C}$  has been considered in simulation to perfectly fit the data with the measurement results.

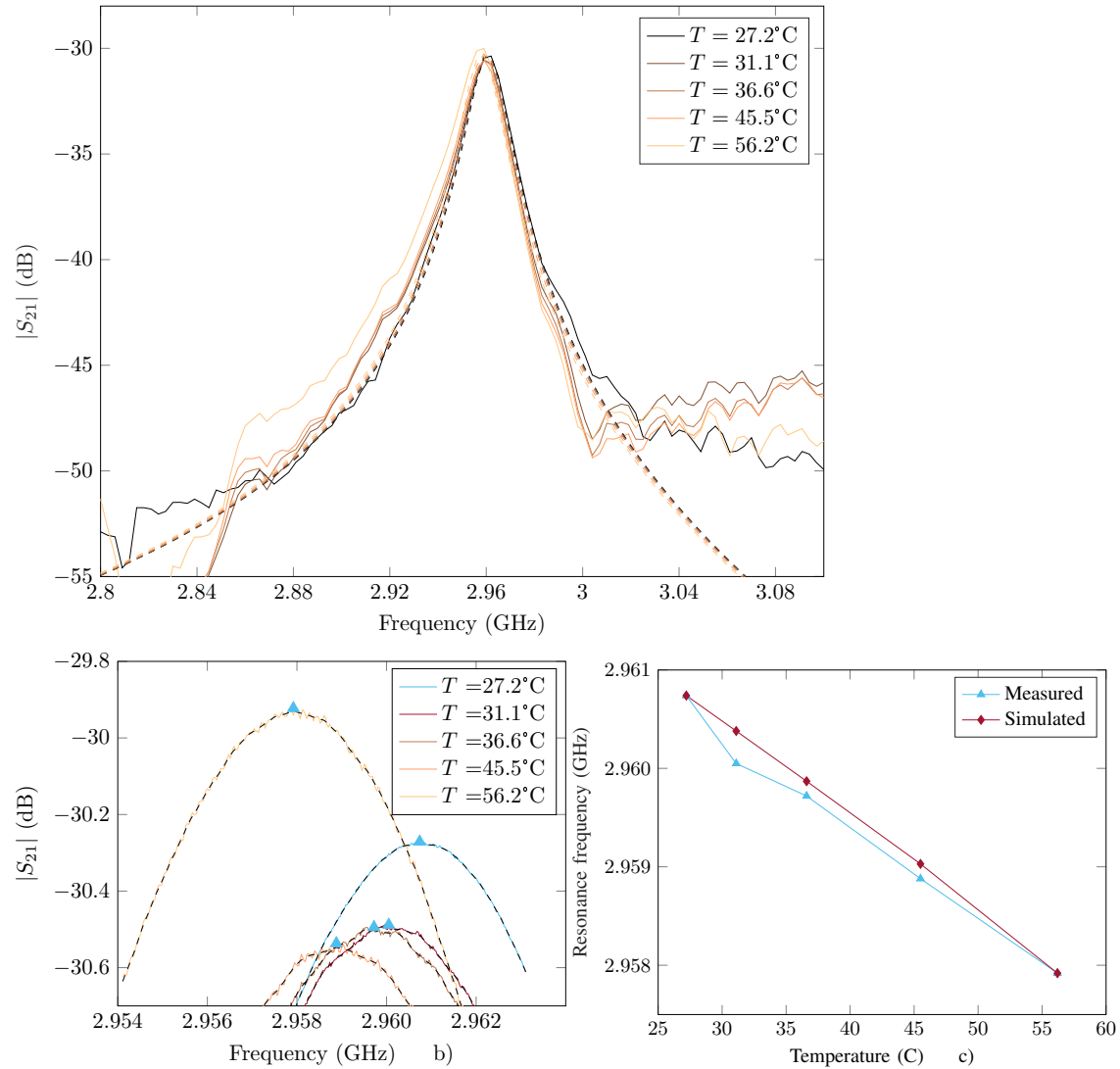


**Figure 2.6:** a) Measured and simulated  $S_{21}$  response for a zinc loop as a function of frequency for several temperature values - Measurement (solid line) and simulation (dashed line). b) Measured and smoothed  $S_{21}$  response for a zinc loop - Smoothed measurement (dashed line) and raw data (solid line). c) Smoothed and simulated resonant frequencies extracted.

As shown in Fig. 2.6-a, simulations and measurements are in good agreement for the considered temperature range. A maximum error of 0.3 MHz can be observed at 31.1°C. Fig. 2.7 plots the measured frequency shift versus temperature for the different metals. With the exception of this temperature the measured resonance frequencies tend to a linear evolution as obtained in simulation and stated by (2.11).

By applying the protocol described previously, the CTE of zinc can be extracted using (2.6). By

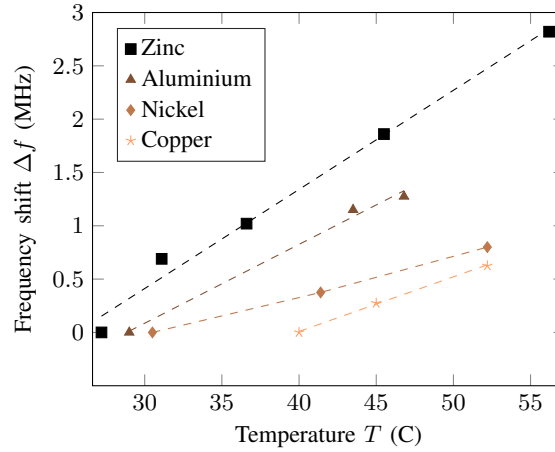


**Figure 2.7:** Measured frequency shift versus temperature for the different metals.

considering only the minimum and maximum temperature values, a CTE of  $31.08 \times 10^{-6} \text{C}^{-1}$  is computing using (2.10). A linear fitting based on the five different temperatures and by using using (2.11) leads to a value of  $31.03 \times 10^{-6} \text{C}^{-1}$  presenting thus a relative error of 0.09 % when compared to the value provided by the manufacturer.

The same measurement protocol has been applied for the three other metals (Copper, Nickel, Aluminium). Results are presented in Table 2.4. The extracted CTE exhibits a good agreement with the value provided by the manufacturer. For Copper and nickel, both the fitting technique and the linear extraction give the same value for the CTE. The error compared to the provider value is higher for nickel which presents the lowest CTE value. The lower is the CTE, the smaller is the expansion, and thus, accuracy is lower. For the lowest CTE (Nickel), an error of 6% is obtained while Zinc and Copper provide a better agreement with an error less than 1%.

**Table 2.4:** CTE comparison ( $\alpha_{\text{CTE}}$ ) between RF measurements and the provider's data.

Metal	Provider	Estimated CTE ( $\times 10^{-6} \text{C}^{-1}$ )		Difference in % with the provider's data	
		with (2.11)	with (2.10)	with (2.11)	with (2.10)
Zinc	31.0	31.03	31.08	0.09	0.25
Copper	17.0	16.96	17.13	0.2	0.76
Nickel	13.3	12.43	12.45	6	6
Aluminium	22-25	22.1	22.07	-	-

The relation between the measured expansion in length of the loop  $\Delta l$  due to an increase of temperature is plotted in Fig. 2.8. It is interesting to note that we can extract from this figure that the approach is accurate enough to measure the dimension variation of  $\Delta l = 3.6 \mu\text{m}$ . This is observable for aluminium between  $43^\circ\text{C}$  and  $46^\circ\text{C}$ . This value can be compared with the  $25 \mu\text{m}$  of variation in length already detected based on a RF backscattering wave approach in [94]. It can be noticed that the extraction of the conductor expansion coefficient seems rather robust against the precision of the resonator dimensions. Indeed, the precision of the resonator cutting is about  $100 \mu\text{m}$  while the studied

variations are about  $0.1\mu\text{m}$  or 1000x smaller. Fig. 2.8 shows the high sensitivity to length variation of the proposed approach which is requested to extract with high accuracy the CTE of different metals. In Fig. 2.7 the measured frequency of the different metals as a function of temperature is plotted. Note that, in such representation, the slope of the measured frequency shift is equal to  $f_0\alpha_c$  as stated by (2.11).

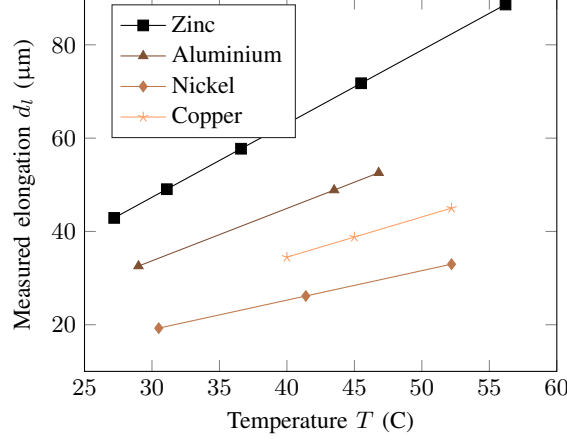


**Figure 2.8:** Measured length elongation versus temperature for the different metals from the reference temperature  $T_1=0^\circ\text{C}$ . The measured elongation is obtained using the fitted  $\alpha_c$  of Fig. 2.7 and (2.11).

An analysis of the evaluation of K on the extracted CTE can be done to check the criticality of this parameter. We can calculate the CTE( $\alpha_{\text{CTE}}$ ) using (2.5). Using this equation, we can vary the value of K to evaluate its effect on the extraction of  $\alpha_{\text{CTE}}$ , for example if a constant value of K is used for several dimensions of the loop. If we vary the value of K from 0.6 to 1.6, we find that an error of 2% is obtained in the worst case if K is equal to 1.6. This means that an error of 56% on K only introduces an error of 2% on the measured CTE.

#### 2.1.4 Incertainties

The theoretical uncertainty of the method can be estimated. From (2.6) and (2.10), the error on  $\alpha_{\text{CTE}}$  can be written as

$$1.01\Delta\alpha_{\text{CTE}} = \left| \frac{f_2(T_2 - T_1)}{(f_2T_2 - f_1T_1)^2} \right| \Delta f_1 + \left| \frac{f_1(T_1 - T_2)}{(f_2T_2 - f_1T_1)^2} \right| \Delta f_2 + \left| \frac{f_1(f_1 - f_2)}{(f_2T_2 - f_1T_1)^2} \right| \Delta T_1 + \left| \frac{f_2(f_2 - f_1)}{(f_2T_2 - f_1T_1)^2} \right| \Delta T_2 \quad (2.12)$$

This sensibility study shows that in order to have a better precision for CTE extraction, a higher variation in temperature is required. The higher is the difference, the higher is the resolution on the extracted CTE. Also (2.12) can be applied to evaluate the uncertainty on the extracted value. If a lower precision is required, the temperature variation range during the measurements can be increased.



### 2.1.5 Conclusion of the section

In this section, a new method based on a non-contact measurement approach to extract metal CTE is presented. This method allows to extract this coefficient with a better accuracy than the one used to fabricate the planar resonator. This approach allows a non-contact measurement without the need of any calibration. Resonator loops on several metals such as zinc, nickel, copper and aluminum have been made and tested. The extracted values for the coefficient of thermal expansion are in good agreement with the values provided by the manufacturer, highlighting the potential of the radio frequency measurement approach for characterizing the coefficient of thermal expansion.

This work brings interests for the characterization of the thermal expansion coefficient of conductive material since :

1. It proposes a new approach that offers many advantages over existing techniques. Contrary to mechanical approaches, the measurement bench is not in direct contact with the temperature source and therefore it does not expand causing errors on the measurement. Compared to optical approaches, the strict control of the environment (such as air) is not required. Also, the proposed approach is simpler to implement and less expensive.
2. This is also the first CTE measurement by a radio-frequency approach.

A perspective of improvement of this work can be the characterization of dielectrics' thermal dilatation. Indeed, dielectric resonator also exhibit a resonance frequency linked to their geometry hence possibly extending the present approach to non metallic materials [103, 104].

## 2.2 Chipless RFID temperature sensors

In this section, a reflectometry approach is used to develop a thermal modeling of a transmission line (TL) based resonant scatterer by introducing the temperature dependence in the line effective permittivity, as well as in its physical length. The resonators are considered as coplanar strip (CPS) or microstrip (MS) lines with specific boundary conditions. With this approach, the introduction of the temperature dependence is straightforward: thermal expansion of metals and temperature dependence of the substrate permittivity (which are physical quantities directly linked to the scatterer resonance frequency) can be added in common TL formulas such as the ones describing CPS or microstrip line. In this way, physical insight into the origins of the thermal dependency is kept. Note that this approach is different from the classical one used to model thermal variations in TL [105, 106], where a thermal dependency is considered on the inductive reactance and the series resistance of the transmission line. Contrary to that, the proposed approach uses as inputs the coefficient of thermal expansion (CTE) and the thermal dependency of the substrate which are two physical quantities that are generally provided by manufacturers.

Based on the reflectometry approach, all the measurements are done remotely using one or two antennas and a VNA. Based on the analytical formulas introduced, an approach to extract the temperature is also described demonstrating how the designed scatterers can be used as temperature sensors. The extracted temperature will be compared with the one directly measured with a thermometer for demonstrating the accuracy of the proposed model. Numerous works have been

done in the field of chipless RFID for temperature sensing (see Table 2.5). For example, the use of a resonator composed of a substrate with thermal dependent electrical parameters has been widely investigated [107, 95, 108]. The variation of electrical conductivity can also lead to the measurement of the temperature [109, 110].

**Table 2.5:** Different Approaches Used in Chipless RFID for Temperature Sensing

	[95]	[108]	[110]	[96]	[111]	*
Thermal effect investigated	Change in permittivity	Change in permittivity	Change in conductivity	Dilatation of 3D structure	Change in permittivity	Change in permittivity and dilatation
Sensor design information	Planar shape PCB design	Planar shape PCB design	Planar shape Ink-jet printed	3D cantilever Clean room	Fully dielectric machined	Planar shape PCB design
Presence of ground plane	Yes	No	No	No	No	Depends on the resonator used
Materials considered in the study	Stanyl polyamide	Stanyl polyamide	Polymer carbon nanotube composite ink	Gold and silicium cantilever	Ceramic cylinder	Metallic resonator on a substrate
Measurements in real environment	No	Not mentioned	No	Yes	Yes	Yes
Measurements through obstacles	No	No	No	No	No	Yes
Resonance frequency	0.7GHz	6GHz	2.4GHz	22GHz	2.9GHz	3GHz
Frequency shift / Temperature variation	0.04 GHz / 50°C	Not mentioned	36.9% of RCS amplitude	1.7 GHz / 250°C	0.1 GHz / 220°C	3 MHz / 30°C

\* this work.

However, none of these studies has developed an accurate model to link rigorously the measured resonance frequency to temperature variations by taking into account all the different temperature-dependent RF phenomenon. In this section, an accurate thermal model of the effective permittivity and line elongation of a CPS and MS line is presented. This model takes into account material expansion and permittivity dependency on the temperature of the substrate while showing that other thermal effects can be neglected. The link among the resonance frequency, the line elongation, and the TL effective permittivity is presented and the temperature dependence is exposed. The variation of the scatterer dimensions and its electrical parameters due to a change in temperature causes a shift of its resonance frequency which can be monitored remotely using a reflectometry approach. Then the use of such a model and scatterers can be applied to the measured resonance frequency for temperature sensing.

The section is organized as follows : first analytical expressions used to model the CPS TL effective permittivity and the resonance frequency of the scatterer with temperature are introduced. Then the validation in simulation and measurement of the model for application in temperature sensing is presented. Finally, model of the microstrip resonant scatterer and discussion on the humidity impact on the temperature sensing are made.

### 2.2.1 Description of the scatterer-based CPS TL

The first step to model the temperature effect on a scatterer, as previously explained, consists of treating a resonant scatterer as a TL. The rectangular loop is a good candidate, because an analogy between this simple geometry and a CPS TL section terminated at both ends by a short circuit (SC) can be done [101]. Fig. 2.9 presents the topology of a classical rectangular loop resonator. In this simple configuration, the resonator is only composed of one layer of metal, without any ground plane or substrate. The geometrical dimensions ( $l$ ,  $g$ ,  $w$ ) illustrated in Fig. 2.9-a are the nominal dimension used for the fabrication. The metal is thick enough  $100\mu\text{m}$  for the loop to be rigid. The resonator can also be placed on the top of any support, like planar dielectric substrates. Note that in this last configuration, the structure is similar to a more practical CPS TL short-circuited at both ends. With such a metal loop and the possibility to place it on top of any substrate, it is possible to dissociate the effect of temperature on the metallic part of the TL (which will characterize the TL length variation), from the ones relating to the presence of the dielectric. So, based on this, the following methodology will be used: 1) the dilatation of the loop alone will be first characterized. The formula describing the TL length elongation due to temperature variation will be obtained based on the detection of the loop resonant frequency shift. 2) a more complex configuration will be considered: dielectric support with a thermal dependent permittivity will be added to the loop to derive the formula of the TL effective permittivity with temperature dependence. For ease of characterization, the metal loop resonator can be placed on a specific dielectric as already mentioned, or the resonator can also be fabricated like a classical PCB. This second type of fabrication will also be considered for its ease of fabrication.

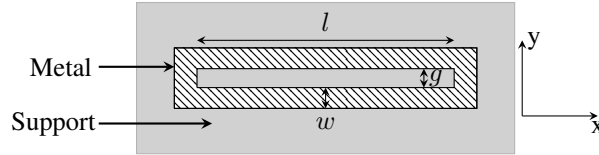


**Figure 2.9:** Nominal dimensions of the fabricated loop (i.e. values used for the fabrication):  $l=50.83\text{mm}$ ,  $g=2.07\text{mm}$  and  $w=1.43\text{mm}$ . The polarisation of the electric field used to excite the resonator is along  $y$ . Contrary to Section 2.1, a substrate is also considered. No ground plane is present.

When a loop at a temperature  $T$  is illuminated by an incoming electromagnetic-field, the maximum energy backscattered occurs at its resonant frequency  $f_r(T)$  defined in Section 2.1 by (2.2). When a temperature dependant substrate is present, this resonance frequency can be written as :

$$f_r(T) = \frac{c}{2\sqrt{\varepsilon_{\text{eff}}(T)}(l(T) + 2\Delta l(T))} = \frac{c}{2\sqrt{\varepsilon_{\text{eff}}(T)}L(T)} \quad (2.13)$$

where  $\varepsilon_{\text{eff}}(T)$  is the effective permittivity seen by the loop and depends on the substate on which the loop is placed. The thermal dependency of the permittivity will be developed in the following part. Please refer to the previous section (Section 2.1) for the thermal dilatation consideration.

### 2.2.2 Temperature dependence of the effective permittivity of the CPS TL-based scatterer

For the loop, the effective permittivity can be modeled by considering again the resonator as a slot line terminated at both ends by SC as illustrated in Fig. 2.2. Thus, the effective permittivity of the loop resonator  $\epsilon_{\text{eff}}$ , on a single substrate layer, can be expressed as [112] :

$$\epsilon_{\text{eff}} = 1 + \frac{\epsilon_r - 1}{2}q \quad (2.14)$$

where  $\epsilon_r$  is the permittivity of the substrate. The parameter  $q$  is dependent on the thickness of the substrate and the geometry of the resonator as described by the analytical expression given in [112, eq. (21)]. In our case, the permittivity of the support is considered to vary with the temperature following the relation  $\epsilon_r(T) = \epsilon_r(1 + \sigma T)$  where  $\sigma$  is the thermal-dependency of the substrate that can be obtained from material datasheets. Equation (2.14) can be rewritten as:

$$\epsilon_{\text{eff}}(T) = 1 + \frac{\epsilon_r(1 + \sigma T) - 1}{2}q \quad (2.15)$$

Like previously for the effective length  $L_2$  in (2.1), the effective permittivity can be expressed as:

$$\epsilon_{\text{eff}}(T) = \epsilon_{\text{eff}}(1 + \alpha_p^{\text{CPS}}T) \quad (2.16)$$

where the thermal dependency of the effective permittivity ( $\alpha_p^{\text{CPS}}$ ). The coefficient  $\alpha_p^{\text{CPS}}$  can be expressed as a function of the thermal-dependency of the dielectric substrate  $\sigma$  by using (2.15), (2.16) and [112, eq. (21)] as:

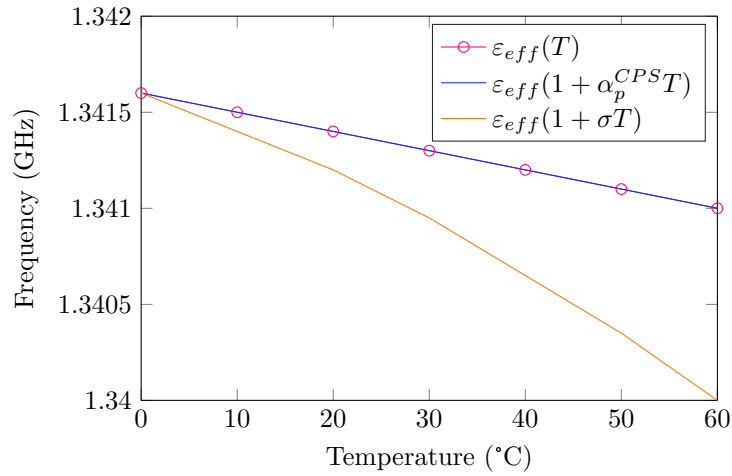
$$\alpha_p^{\text{CPS}} = \frac{\sigma q \epsilon_r}{2 + (\epsilon_r - 1)q} \quad (2.17)$$

Fig. 2.10 shows the error if considering  $\sigma$  instead of  $\alpha_p^{\text{CPS}}$  with as an example a simulation of a dielectric of 1mm. Concerning the validity range in frequency of the model, it depends on the analytical expressions of the TL used in the approach. Note that (2.14) can be used up to 100 GHz [112] which shows that the model is compatible with the UWB band (3.1 GHz - 10.6 GHz) which is usually used in chipless RFID. However, the sensitivity of the approach is also related to the value of the quality factor (Q-factor) of the resonators. The higher the Q-factor, the more accurate the extraction of the resonant frequency and therefore the temperature estimation. Also, as the Q-factor decreases with increasing frequency [113, 114], the best results will be obtained for the lowest frequencies of the considered band.

### 2.2.3 Temperature extraction

The equation of the thermal dependence of the loop resonance frequency can be obtained by injecting (2.5) and (2.16) in (2.13). Thus, the resonance frequency  $f_r$  at a temperature  $T$  is :

$$f_r(T) = \frac{c}{2\sqrt{\epsilon_{\text{eff}}(1 + \alpha_p^{\text{CPS}}T)L(1 + \alpha_c T)}} \quad (2.18)$$



**Figure 2.10:** Resonance frequency depending on the effective permittivity temperature dependent model.

Where  $\alpha_p^{\text{CPS}}$  is the thermal-dependency of the effective permittivity and  $\alpha_c$  the coefficient of effective dilatation of the loop. Linearizing (2.18) using a Taylor series for small value of  $\alpha_i T$  (since  $\alpha_p^{\text{CPS}} T$  and  $\alpha_c T$  are in the order of  $10^{-5}$  and  $T < 100^\circ\text{C}$ ). The following equation can be derived :

$$f_r(T) \simeq \frac{c}{2\sqrt{\epsilon_{\text{eff}}L}} \left[ 1 - (\alpha_c + \alpha_p^{\text{CPS}}/2)T \right] = \frac{c}{2\sqrt{\epsilon_{\text{eff}}L}} (1 - \alpha T) \quad (2.19)$$

where  $\alpha$  is defined by

$$\alpha = \alpha_c + \alpha_p^{\text{CPS}}/2 \quad (2.20)$$

Note that  $\alpha$  depends on thermal proprieties of the conductor, the substrate dielectric and the scatterer shape as shown in (2.20). Fig. 2.11 shows the error done in the approximation of (2.19) for different metals.

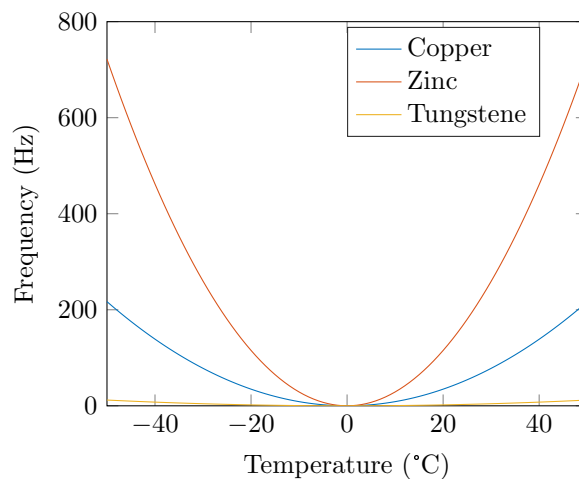


**Figure 2.11:** Error done in the approximation of (2.19) for different metals.

Using (2.19), the relation between the resonance frequencies  $f_r(T_1)$  and  $f_r(T_2)$  for respectively two temperatures  $T_1$  and  $T_2$  is:

$$f_r(T_2) = f_r(T_1) \frac{1 - \alpha T_2}{1 - \alpha T_1} \quad (2.21)$$

Note that (2.21) gives the relation between tag's resonance frequencies (obtained from measurement) and the coefficient  $\alpha$  (known value depending on the scatterer shape and the material used) and the considered temperatures  $T_1$  and  $T_2$ . So, a simple approach to use this resonant scatterer as a temperature sensor consists in characterizing  $T_1$  and  $f_r(T_1)$  one time. Then the measurement of  $f_r(T_2)$  will allow to extract  $T_2$  using (2.21).

It is interesting to note that when the current temperature  $T_2$  has been extracted, all the characteristics of the line can be directly obtained at the temperature under test. Indeed the computation of the effective permittivity  $\varepsilon_{\text{eff}}(T_2)$  of the TL is computed using (2.16) with  $\varepsilon_{\text{eff}}$  defined by (2.14). Then the physical TL length  $l_2$  is extracted using (2.5) and (2.21).

Moreover, one can also remark that the length of the loop does not appear in (2.21), which means that the approach is valid regardless of the length of the loop and so of the operating frequency from the moment the structure resonates. It is therefore possible to miniaturise the tag by working at higher frequencies if necessary.

This equation permits to explain the different influences of the parameters such as the dependency on the metallic conductor chosen to do the resonator, the dielectric parameters such as thickness, permittivity, thermal dependency, the resonator shape, etc ... It can be used to find optimal parameters to increase the sensibility of a potential sensor: the initial resonance frequency, a conductor who expands more, dielectric who varies more, etc ..

## 2.2.4 Discussion on Approximations for the determination of the temperature

Temperature variation has a lot of consequences on RF parameters even for the simple TL-based scatterer under study. It is why only the main contributions have been taken into account in the model introduced above. This means that several approximations have been made in order to obtain this model, and the objective of this subsection is to discuss these assumptions. Some of them will be evaluated in simulation in the next section and the entire model will be confronted with measurements to validate its accuracy in the rest of the section.

### Thermal Expansion of Dielectric

Like for the metal part, the substrate volume is not constant with the temperature variation. Dielectrics generally expand with an increase of temperature, and this is observable in the three spatial directions. For needs of mechanical robustness, particularly to ensure temperature robustness, materials used in the realization of any item must have similar thermal expansion constants. Otherwise, the object may deform irreversibly or even break. This applies to the manufacture of PCB and electronic packaging. For example the Rogers RO4003C has CTE of 11, 14, 46 ppm/°C respectively in the x, y, z-axis. The CTE of copper is 17 ppm/°C. Our model integrates the mechanical deformation of the line as a function of temperature. However its origin could be related to the metal as well as

to the dielectric. What is important here is to take into account a CTE value representative of this deformation. Taking that of the metal (the latter being slightly higher than the dielectric) leads to results in accordance with the experiments shown in Section VII. This was also confirmed by our approach of treating the metal loop alone and then with the dielectric. It is the same when the loop is simply placed on the dielectric or attached as is the case when the resonator is manufactured as a PCB.

Dielectric elongation can also impact the substrate thickness. In such a case, almost all device parameters are modified like  $q$  or even  $\Delta l$ . However, in the considered temperature range, the thickness variation is low in comparison with the other effects. In the case of Rogers RO4003C,  $q$  varies from 0.5828 to 0.5830 for a substrate expansion caused by a temperature variation of 60°C. In this case,  $\alpha_p^{\text{CPS}}$  goes from 23.738 ppm to 23.744 ppm which is negligible.

### Electrical conductivity variation with temperature

It is also well-known that the electrical conductivity of any metal varies with temperature. This phenomenon has not been considered in this work for two reasons. In first approximation, electrical conductivity variation will affect only the TL losses and not the TL electrical length. Effects of temperature on losses are not considered in this section since only the resonance frequency shift is taken into account. Note that the resonance frequency shift can be measured with high accuracy. This is not the case of the magnitude of the signal at the resonance which can be impacted by the presence of surrounding objects around the scatterer.

To characterize TL losses variations with temperature, a simple approach like the one in [105, 106] can be used. The temperature dependence of the line effective resistance can be taken into account using a formula similar to (2.1) (linear dependence of the resistance with the temperature).

The second reason is due to the fact that in the temperature range under study, the variation of the electrical conductivity is small. It will be decreased by a factor of 2 - 3 for an increase of 100°C. These small variations in the electrical conductivity will lead to variations of the magnitude of the RCS that are not significant in relation to the measurement accuracy.

### Approximations linked to $\Delta l(T)$ and $\alpha_c$

As explained in Section 2.1.1, for a metal loop a more general relation between  $\alpha_c$  and  $\alpha_{\text{CTE}}$  is given by (2.5). When the scatterer is printed on a dielectric, the relative permittivity has also to be considered in the computation of  $\Delta l_1$ . This dependency is given by the following formula [101] :

$$\Delta l(\epsilon_{\text{eff}}) = \frac{\Delta l}{\sqrt{\epsilon_{\text{eff}}}} \quad (2.22)$$

So (2.5) can be rewritten considering the presence of the dielectric. The study of the influence of  $K$  on the temperature extraction presented in Section 2.1.4 and in Section 2.2.5 (with or without dielectric) shows that the introduced errors lead to a very small variation which is negligible. Indeed, the measurement errors of the resonance frequencies have higher errors contributions in the extraction of the temperature as shown in Section 2.2.5. Later in this section dedicated to temperature sensing, loop geometry are used to match the condition  $K=1$ , so  $\alpha_c$  and  $\alpha_{\text{CTE}}$  are considered to be equal.

### 2.2.5 Simulations

CST thermal and mechanical solvers are first used to impose the desired temperature on each point of the loop given in Fig. 2.9-a by considering a constant ambient temperature. The initial loop dimensions given as input in the simulation are the ones noted in the caption of Fig. 2.9-a. These dimensions are considered to correspond to temperatures in the range 0°C-60°C with a 5°C step. Then, a simulation in CST MW with a plane wave excitation and the Time Domain Solver is used with the loop dimensions extracted from the mechanical solver. The loop is in free space and is made with copper (no dielectric) so that  $\alpha = \alpha_c = 17 \times 10^{-6} \text{C}^{-1}$ . The simulated RCS is plotted in Fig. 2.12. By increasing the temperature, the TL length increases so the resonance frequency decreases as stated by (2.19). A total frequency shift of 3MHz is observed for the 60°C variation with an initial resonance frequency of around 2.98 GHz at 0°C. Fig. 2.13-a presents the evolution of the resonance frequency versus the simulated temperature. By applying (2.21) on the simulated resonant frequencies  $f_r$ , we can plot the extracted temperature as a function of the one imposed in simulation (Fig. 2.13-b). Extracted temperature is very close to the imposed one with a maximum error below 0.1°C over the 0°C-60°C temperature range.

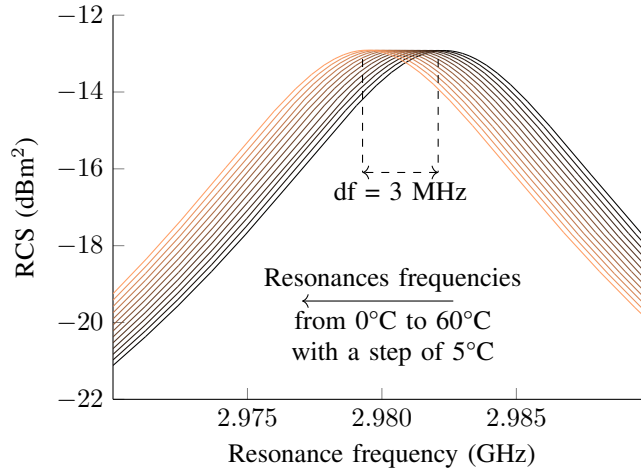


**Figure 2.12:** RCS as a function temperature for the simulated copper resonator without substrate in vacuum for temperature ranging from 0°C to 60°C with a 5°C step.

To study the effect of  $K$  on the extracted temperature, a loop of dimensions  $l=38\text{mm}$  is considered. Following Section 2.1, this loop is characterized by a value of  $K$  equal to 0.91. If we approximate  $K=1$  to simplify the expression of  $\alpha_c$ , the extracted temperature using (2.19) is plotted in Fig. 2.14. The error is less than 0.5°C on a 0-60°C temperature variation. The linearity in the error comes from the error in the linear coefficient of (2.20) since  $K$  was approximated in  $\alpha_p^{\text{CPS}}$ . In this case, due to the approximation  $K=1$  (rather than considering the exact value 0.91), the maximum error introduced on the estimated temperature is only of 0.03°C. So, compared to the resonator used in this section ( $l=51\text{mm}$  and  $K=1.02$  without any approximation), the difference between  $K=0.9$  and 1 is higher and so introduces more errors than the case used in practice. For these reasons the approximation  $K=1$  was assumed to be suitable for the application and for the loop resonators.

The case of a non-thermal dependent support ( $\sigma = 0, \epsilon_{\text{eff}} \neq 1$ ) has also been studied to see the



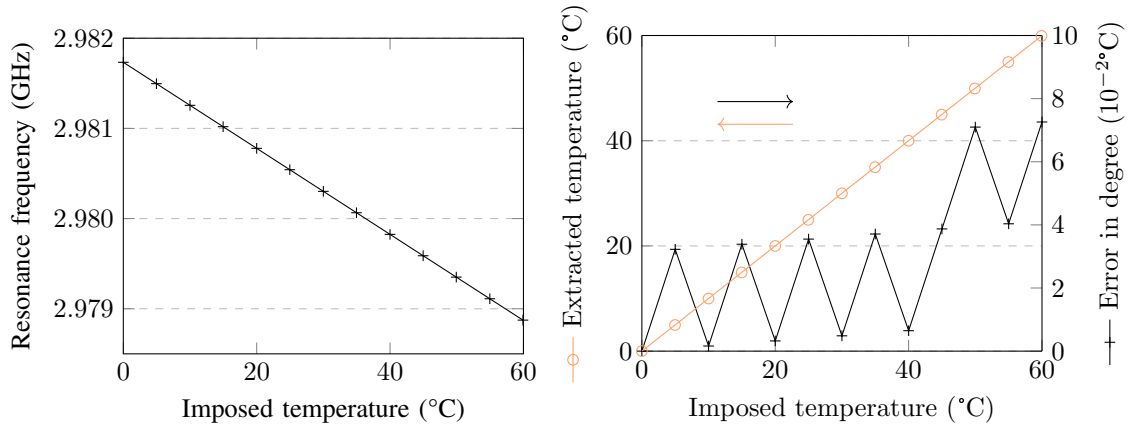


**Figure 2.13:** (a) Resonance frequency in GHz of the copper loop resonator in vacuum as a function of temperature. (b) Extracted temperature using (2.21) and error in °C.

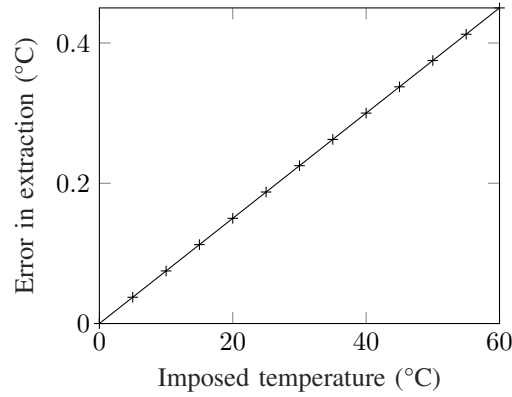


**Figure 2.14:** Error between the extracted temperature using (2.21) and the simulated temperature when the approximation  $K=1$  is used.

effect of the permittivity of the support on the extracted temperature. The same loop described in Fig. 2.9 is simulated on a 50 mm thick dielectric of permittivity constant  $\epsilon_r$  ranging from 1 to 5. Fig. 2.15 plots the error between the extracted temperature and the simulated one. The coefficient  $\alpha_c$  is calculated with  $K = 1.02$ ,  $\epsilon_{\text{eff}}$  is obtained with [112] and  $\Delta l(\epsilon_{\text{eff}}) = \frac{\Delta l}{\sqrt{\epsilon_{\text{eff}}}}$ . The error on the extracted temperature is very low (less than 0.2°C) thus validating the possibility to use a substrate in the presented model.

Finally, the general case of a support with a temperature dependency of the dielectric constant has been studied to validate that both conductor and dielectric thermal effects were correctly considered in (2.19). In this last configuration, the simulated temperature sensor tag is supposed to be fabricated with PCB technology. The loop is in copper ( $\alpha_{\text{CTE}} = 17 \times 10^{-6} \text{ } ^\circ\text{C}^{-1}$ ) on a RO4003C substrate with a dielectric constant of 3.55 with thermal dependency  $\sigma = 40 \times 10^{-6}$ . The substrate thickness is 1mm which leads to a value  $q = 0.58$  [112]. Simulation results are plotted in Fig. 2.16.

The extracted temperature is in good agreement with the imposed temperature with an error of less than 0.7°C. The linearity in the error comes from an error in the linearity in (2.21) on the value

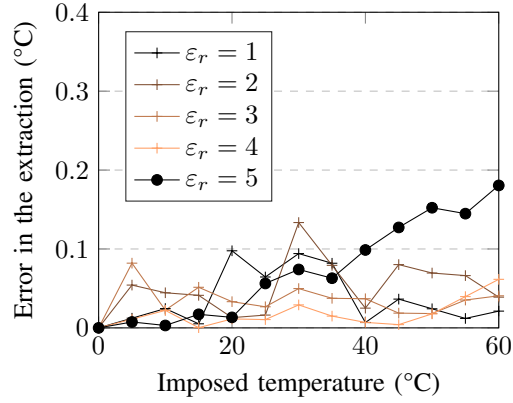


**Figure 2.15:** The error in the extracted temperature of (2.21) in °C as a function of the simulated temperature with 0°C as a reference measurement for a copper resonator on a 50mm thick support whose permittivity is ranging from  $\epsilon_r = 1$  to 5.

of  $\alpha$ . The calculated  $\alpha$  using (2.21) is  $25.5 \times 10^{-6} \text{ } ^\circ\text{C}^{-1}$  while a value of  $25 \times 10^{-6} \text{ } ^\circ\text{C}^{-1}$  (equivalent to  $q = 0.53$ ) leads to lower error of less than  $0.45^\circ\text{C}$ . Henceforth, these results demonstrate that (2.19) is accurate enough to model thermal effects on the resonance frequency of the loop.

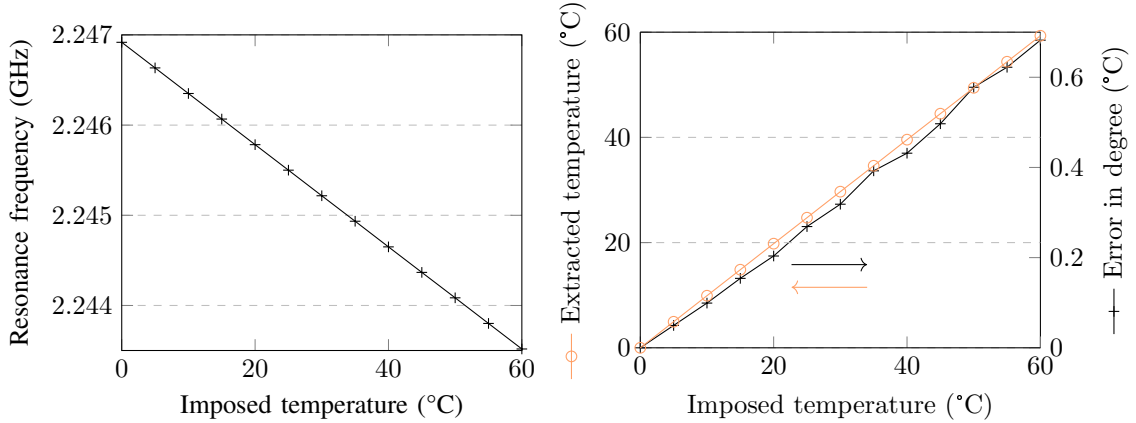


**Figure 2.16:** (a) Resonance frequency of the copper loop on a temperature dependent support (RO4003C) of 1mm thickness ( $q=0.58$ ) as a function of temperature. (b) Extracted temperature with (2.21) and error in °C.

## 2.2.6 Evaluation of the error

### Uncertainty

The uncertainty of the method can be estimated with (2.21) using :

$$\Delta T = \left| \frac{\partial T}{\partial f(T_1)} \right| \Delta f(T_1) + \left| \frac{\partial T}{\partial f(T_2)} \right| \Delta f(T_2) + \left| \frac{\partial T}{\partial \alpha} \right| \Delta \alpha \quad (2.23)$$

with  $\Delta f = 10\text{kHz}$  (VNA accuracy) and  $\Delta \alpha = 1 \times 10^{-5}$  (corresponding to 5% error on the calculated  $\alpha$ ).

If we do the numerical application where  $T$  is given by (2.21) using  $\Delta f = 10\text{kHz}$  and  $\Delta\alpha = 10^{-5}$ , we can see that errors in the measured frequencies  $\Delta f_i$  introduce uncertainties 10 times bigger than error  $\Delta\alpha$  on the coefficient  $\alpha$  but overall, the uncertainty is low (around  $3^\circ\text{C}$ ) which explains the good agreement with our results in practice. In practice since each resonator can estimate the temperature, sensing and averaging on all the resonators can increase the robustness of the sensor without impacting the identification functionality.

### Sensitivity of the sensor

The resonance frequency shift due to temperature at the  $n$ -th harmonic of a resonator can be computed using (2.19) and is

$$df_n = \alpha\Delta T \frac{nc}{2\sqrt{\epsilon_{\text{eff}}}L} \quad (2.24)$$

Thus, to improve the sensibility of our sensor, we have to increase the frequency shift. To achieve this, we can :

- Increase the coefficient  $\frac{c}{2\sqrt{\epsilon_{\text{eff}}}L}$  which results in a more compact resonator resonating at only higher frequencies.
- Increase the factor  $n$ . We can keep actual dimensions for the ID functionality and do a measurement on a harmonic for the sensor functionality (see Fig. 2.17). In blue are represented temperature independant resonance frequencies and in red, real resonance frequencies temperature dependant. The measurements of harmonics shifts  $df_n$  introduces bigger variations easier to measure leading thus to a better resolution.
- Increase the factor  $\alpha$  which means use a metal that expands more (like zinc) and/or a support whose permittivity is more affected by thermal variation  $\sigma$ . A totally different geometry of resonator can also contribute in increasing  $\alpha_p$  and so  $\alpha$  as shown in Section 2.2.5.

The frequency shift  $df$  due to temperature for a given resonance frequency can be computed using (2.24) and compared with previous simulation results. In the case of the copper loop, the calculated shift is  $3\text{MHz}$  which is in good agreement with the simulation results shown in Fig. 2.12.

Note that the frequency shift due to temperature is small enough to be compatible with the use of this type of scatterer to realize chipless RFID tags for identification purposes [63]. This numerical application shows that the sensing capability can be added to this type of chipless RFIDs tag without any compensation. Indeed this frequency shift has no impact on the ID capability of a chipless RFID tags that encodes data using a frequency position technique [63] where a frequency band of few tens of MHz is generally allocated to each code. Thus sensing capability can be added without reducing the coding capacity.

As mentioned in the introduction, several papers have been published using the variation in permittivity to sense the temperature (see Table 2.5). However, this approach does not consist in proposing a model of the thermal phenomenon but rather a lookup table that allows linking the measured resonance frequency to a temperature value. This lookup table is obtained after a first practical characterization, in temperature, of the tag. With the proposed approach it is possible to

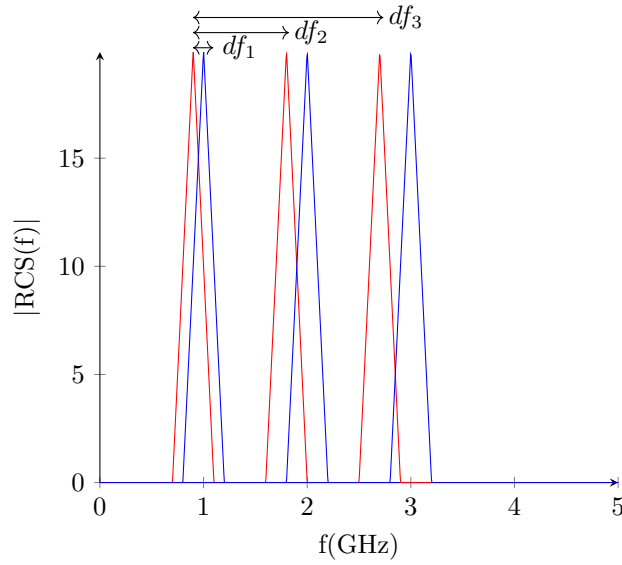


**Figure 2.17:** Utilization of harmonics to increase the frequencies shift. In blue, temperature independent resonance frequency. In red, real resonance frequencies temperature dependant.

dissociate the variation coming from the dielectric permittivity change from the variation coming from the material elongation. Contrary to what is claimed in most chipless RFID papers on this topic (see Table 2.5 – planar / PCB configurations) where only the contribution of the permittivity variation is considered, it should be noted that it is not possible to neglect the contribution of the elongation of the metallic parts as a function of temperature. This is particularly true for scatterer-based CPS TL, and also true to a lesser extent for scatterer-based microstrip TL as it will be discussed in Section X. Equations (2.20) and (2.24) show that the shift in frequency is due to the factor  $[1 - (\alpha_c + \alpha_p/2)\Delta T]$ .

Since both terms  $\alpha_c$  and  $\alpha_p$  usually have the same magnitude, the shift in frequency caused by the metal dilatation is twice more important than the shift caused by a change in permittivity since it is divided by 2. This is amplified if the support is of small thicknesses. In this case, the coefficient  $q$  used to calculate  $\alpha_p^{\text{CPS}}$  is around 0.5 so the thermal dielectric effect can be divided by 4. For example, the factor  $\alpha$  of a zinc loop resonator with support with no thermal dependency is  $\alpha = \alpha_c = 31 \times 10^{-6}$  while a copper loop resonator on a 1mm thermal dependent dielectric like Rogers RO4003C has a factor  $\alpha = \alpha_c + \alpha_p^{\text{CPS}}/2 = 29 \times 10^{-6}$ . Hence, a single metallic resonator with no support can have more thermal sensibility than a resonator with a thermal dependent substrate. Most of the time, material elongation is neglected in existing works. Current studies are essentially focused on the choice of a dielectric that is as sensitive as possible to temperature, i.e. with the highest coefficient  $\sigma$ .

### Impact of the distance

To conclude on the evaluation of the errors related to the implementation of this reflectometry-based approach, we will study in this section the impact of the measurement distance on the temperature extraction. The resonator was placed on a guiding rail in an anechoic chamber. The S-parameters were measured with a VNA for different spacings between the tag and the antenna (bi-static configuration). Fig. 2.18-a shows the impact of the distance between the tag and the antennas on the resonance

frequency. A resonance frequency shift of 0.4 MHz is measured for a distance variation from a 3 cm to 1 m as illustrated in Fig. 2.18-b. By using (2.24), this frequency shift corresponds to a change of around 4°C. This error of 4°C can have two origins. First when the distance increases, the backscattering signal becomes lower, and it is possible that part of the variation is due to the measurement itself. The second origin can be explained by the variation of the temperature inside the anechoic chamber due to the presence of an operator who has to enter into the chamber to change the position of the tag. Considering this second effect, we can admit that an error on the temperature extraction of 3°C, as computed in Section VII.A, can still apply for a measurement range from 3 cm to 1 m. This possible error of 4°C will have no effect on the measurement. Indeed, in (2.21), the reference measurement will act as a calibration so if the tag is not moved during measurement, no additional error will be added. This idea will be demonstrated in practice using different reading ranges.

First the measurement benches used to validate the temperature extraction are described. The first set of measurements focuses on the validation of the model developed in this section for various tags configuration in a controlled environment. The second measurement emphasizes the sensor application where a low-cost traditional PCB design is used in a real environment to sense temperature.

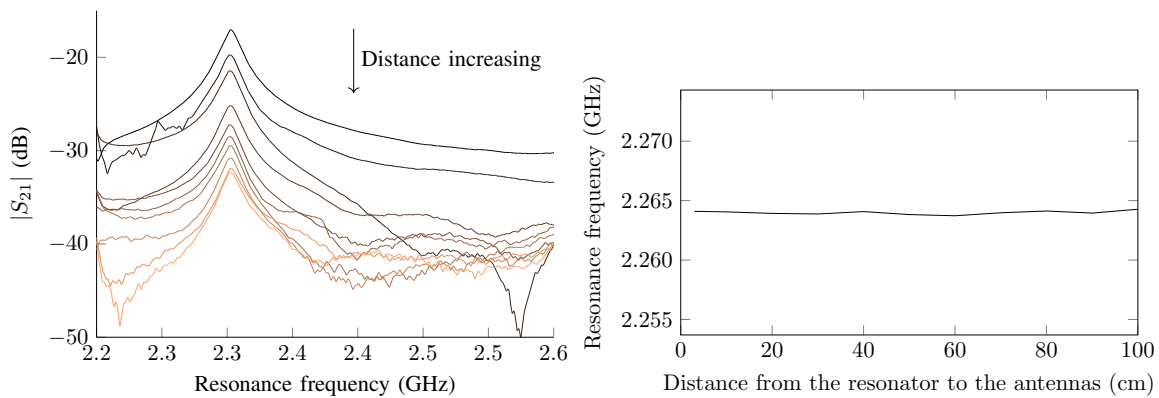


**Figure 2.18:** (a) Effect of the distance on the S-parameters amplitude. (b) Effect of the distance on the resonance frequency.

### 2.2.7 Temperature sensing in a climate chamber

The model developed in (2.19) will be first validated in a controlled environment. Like in Section 2.1.2, several resonators with the same geometric dimensions presented previously in Fig. 2.9-a have been fabricated using different metals such as Zinc, Copper, and Nickel. In such configuration no dielectric support is used. CTE of these different metals provided by our metals' provider Goodfellow [100] for a temperature range 0°C-100°C following ASTM or DIN test methods are reported in Table 2.2. Copper resonators on a Rogers RO4003C dielectric and a zinc loop put on a high temperature-dependent dielectric (K50) have been also fabricated to take into account the support thermal dependence. The dielectric and thermal properties of RO4003C and K50 are listed in Table 2.6. The main characteristics of the Rogers RO4003C substrate are given in [115]. It can be seen that the evolution of the dielectric constant is linear regarding the temperature over the range -50° to 150°C. For K50, the characteristics can be found in [116]. This panel of 5 resonators has been selected to prove the validity of (2.19) for different materials and with or without support.

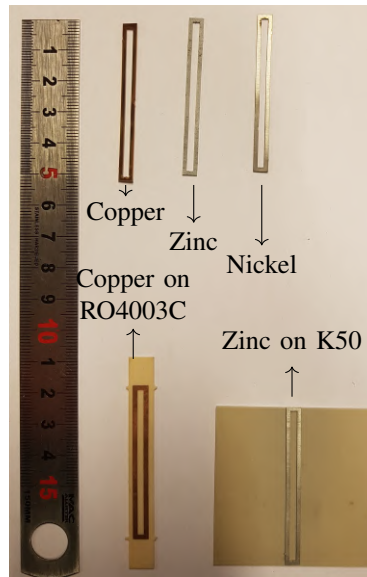


**Figure 2.19:** The fabricated loop resonators made with different metals and substrates.

### Measurement setup

The measurement setup used in a climate chamber and the fabricated scatterers operating as temperature sensors are illustrated in Fig. 2.19. The measurement protocol is the same as Section 2.1.2. The resonance frequency of each temperature is extracted and (2.21) is applied to determine the temperature based on the RF measurements.

### Results and analysis

**Table 2.6:** RF and Thermal Characteristics of RO4003C (Rogers) and K50 (National Magnetics Group) Dielectrics

Dielectric	RO4003C	K50
Permittivity	3.55	50
Permittivity thermal dependance ( $\sigma$ )	$40 \times 10^{-6}$	$-700 \times 10^{-6}$
Thermal dilatation ( $10^{-6} \text{ } ^\circ\text{C}^{-1}$ )	X=11, Y=14, Z=46	9.7

With (2.21), the temperature can be extracted from the measured resonance frequency. The extracted temperature and the error with the temperature measured with the infrared thermal camera (noted expected temperature in the following) are plotted in Fig. 2.20 for the zinc resonator without dielectric. We can see that the maximum error is  $1.8^\circ\text{C}$  at  $31^\circ\text{C}$ . Everywhere else the error is lower than  $1^\circ\text{C}$ .

Temperature extraction using (2.21) is applied for the rest of our 5 scatterers and results are shown in Table 2.7. The highest error is for the zinc loop with an error of  $1.8^\circ\text{C}$ . On average, the

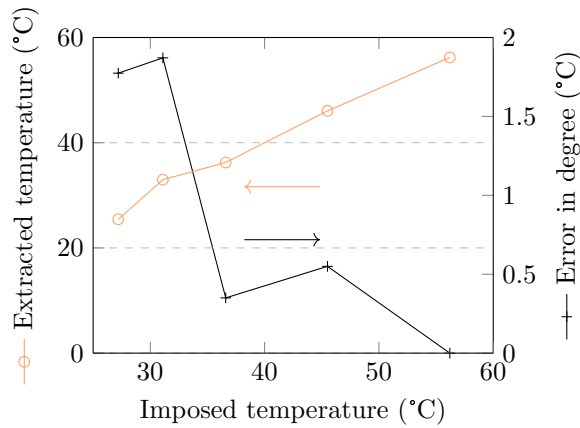


**Figure 2.20:** Extracted temperature using (2.21) in measurement on the zinc resonator and the error done with the measured temperature in the climatic chamber - the reference temperature is  $T_1 = 56.6^\circ\text{C}$ .

extracted temperature error is lower than  $1^\circ\text{C}$ . Copper resonator has the best results both with respect to the maximum error and the average error.

**Table 2.7:** Temperature Extraction using (2.21) for Different sets of Measurements

Set	Max error ( $^\circ\text{C}$ )	Average error ( $^\circ\text{C}$ )
Zinc	1.8	0.9
Copper	0.24	0.15
Nickel	1.39	0.46
Zinc on K50	1.60	0.58
Copper on RO4003C	0.89	0.44

## 2.2.8 Temperature sensing in a real environment

The PCB scatterer composed of a copper loop on a RO4003C substrate is the one considered in this section. For this resonator, the loop is realized by etching on a RO4003C substrate laminated on one side by a copper layer. The resonator photo is shown in Fig. 2.19-b. The presence of a thermal dependent dielectric increases the frequency shift (so the accuracy as mentioned in Section VII.B).

### Measurements

Four test-benches in a real environment were built and used to validate the potential of the scatterer for temperature sensing applications (Table 2.8). The principle of the test-bench is illustrated in Fig. 2.21. The PCB tag is placed on a support of thickness  $t$  at a distance  $d$  from the antenna(s). Both monostatic and bi-static antenna configurations were tested. Measurements were performed in different places such as in corridors, offices. Some places were air-conditioned, some were not. The support was either polystyrene ( $\epsilon_r \simeq 1.1$ ) to simulate a spacing with air or wood/glass when the measurement was done between two-rooms for example. All these parameters are summarized in

Table 2.8. A program running on a computer was measuring every minute the S-parameters of the VNA. The computer was controlling also the measurement of the temperature using an integrated temperature sensor (TES 1365). Measurements through a window glass and a wooden door were achieved from one room to another. The test-bench used with the wooden door is shown in Fig. 2.22 as an example. For the wooden door and glass measurements, a spacer in polystyrene of 2cm was used between the tag and the object (see Fig. 2.21). An empty measurement of the environment is first done. After that, we subtract this empty measurement to the next measurements to remove as much as possible the environment noise (door impact, glass impact, ...). In all cases during the temperature monitoring, the first measurement was used as a calibration (measurement at  $T_1$ ) and the tag was not moved during the measurement. For the wooden door and glass measurements, a spacer in polystyrene of 2cm was used between the tag and the object (see Fig. 2.22). This spacing isolates the tag from the object so that the two elements are not coupled. Therefore, the evolution of the resonance frequency, particularly as a function of temperature, remains independent of the object on which the tag is placed. Indeed, from [112] it is possible to calculate the thickness of the separation layer (spacer) allowing a sufficient isolation between the tag and the object on which the tag is attached. For example, if we consider the following constraining case, namely the stacking of layers: 1) tag dielectric support, 2) metallic layer, 3) air spacer of 5mm and 4) an unknown object (door) potentially of infinite thickness. In this case, the coefficient that multiplies the dielectric permittivity of the different layers  $q$  can be computed, and as a result, the effective permittivity is composed at 96% of the first layer dielectric constant (air in this example), and 4% of the second (object on which the tag is attached). So, the influence of an object like a door (in wood or in plastique) will be negligible compared to the others dielectrics. This result is confirmed in practice.

**Table 2.8:** Parameters of the four test-benches

Measurement set	Antenna configuration	d	t	Support type
1	mono-static	0cm	3cm	Polystyrene
2	bi-static	0cm	12cm	Polystyrene
3	bi-static	10cm	4cm	Wooden door
4	bi-static	10cm	5mm	Glass

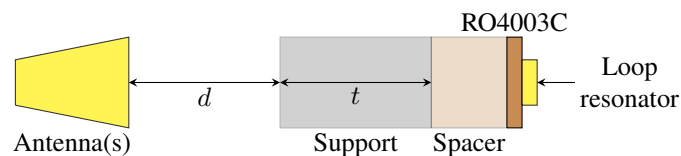


**Figure 2.21:** Principle of the measurement setup in a real environment.

### Results and analysis

Extracted temperature results are plotted on Fig. 2.23 to Fig. 2.26. For the four test-benches, the temperature using the integrated temperature sensor and the one extracted from the loop resonator response with (2.21) are in good agreement.



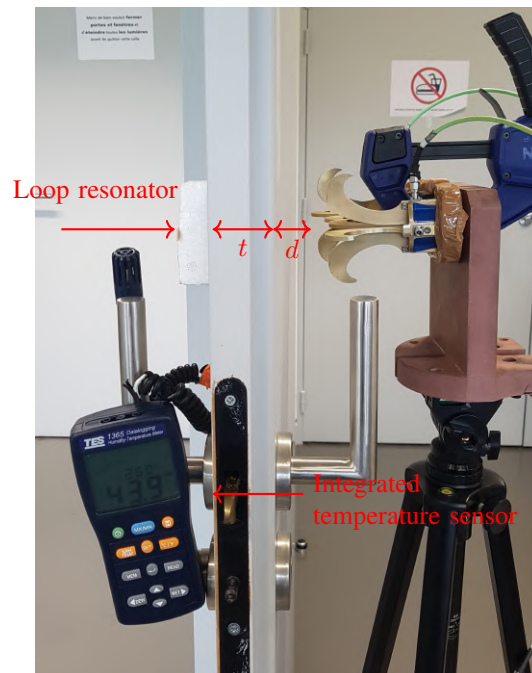


**Figure 2.22:** Principle of the measurement setup in a real environment through a wooden door from a room to another.

In Fig. 2.23, temperature variations corresponding to daytime/nighttime can be seen. The maximum difference between both measurements is around  $2^{\circ}\text{C}$  on the 3 days measurement duration. To increase the isolation between the incident and reflecting wave and to reduce the error, bi-static measurements are then considered. Bi-static measurements through 12cm of polystyrene and through a wooden door give a maximum error of  $0.5^{\circ}\text{C}$  (Fig. 2.24 and 2.25). Bi-static measurement through a window glass gives a higher error of  $1.5^{\circ}\text{C}$  (see Fig. 2.26).

In Figs. 2.23 and 2.25, we can see in practice the effect of the distance on the measurements : the distance variation is not impacting the accuracy of the temperature extraction.

Another noticeable point is the importance of the frequency resolution (number of points for a given frequency span) for the sensor sensitivity. For test-benches with polystyrene (test-bench n°1 and n°2), a frequency resolution of 10kHz was used. This value corresponds to a temperature sensitivity of  $1/9^{\circ}\text{C}$  as stated by (2.24) which is observable in the results. For measurements from one room to another (test-bench n°3 and n°4), a lower frequency resolution of 30kHz was used. The corresponding temperature sensibility is  $1/3^{\circ}\text{C}$  as stated by (2.24) which is also what was measured in practice. This result points out a limiting factor in temperature sensing with this RF approach which is a temperature resolution directly linked to the frequency resolution of the RF equipment used for the measurement.

### 2.2.9 Thermal characterizations of a resonant scatterer-based microstrip TL

The same concept can be applied to different types of scatterers. In this section resonant scatterer-based microstrip TL is considered. In its simplest form, the scatterer is a metallic strip (a dipole)

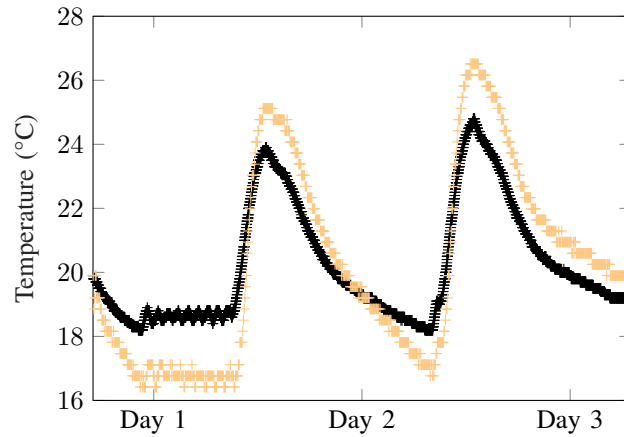


**Figure 2.23:** Comparison between the temperature measured with an integrated sensor in black and using the loop resonator in yellow during a period of 3 days for the test-bench n°1.

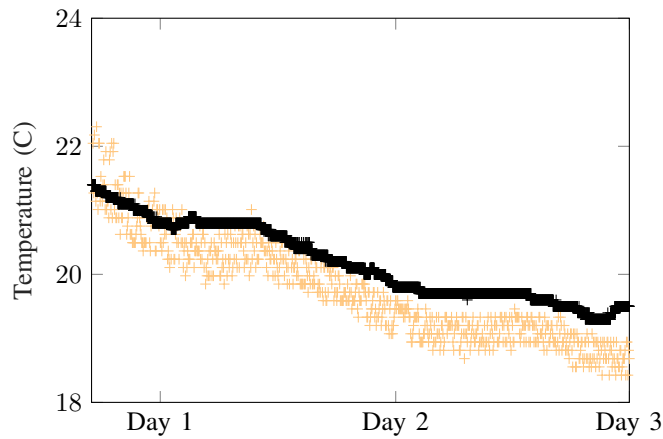


**Figure 2.24:** Comparison between the temperature measured with an integrated sensor in black and using the loop resonator in yellow during a period of 3 days for the test-bench n°2.

above a ground plane. This scatterer can be considered as a microstrip TL section terminated at both ends by an open circuit (OC). This resonator is illustrated in Fig. 2.27. This resonator offers multiple advantages for temperature sensing. Indeed, the presence of a ground plane confines the electromagnetic fields in the substrate (Fig. 2.27). We will see that in such a case the sensitivity of the sensor can be increased compared to scatterer-based CPS TL when a temperature-dependent substrate is used. Moreover, the ground plane isolates the scatterer from its direct environment, so a spacer as the one used in Fig. 2.22 is not needed. The major drawback of this resonator is its lower Q-factor compared to the loop, leading to a wider peak resonance which makes it harder to find the peak apex corresponding to the resonance frequency. About the thermal dependency of the resonance frequency, the expansion due to temperature can be modeled exactly like the loop. So (2.16) can be used such as the equality between  $\alpha_c$  and  $\alpha_{CTE}$ . The thermal-dependency of the effective permittivity  $\alpha_p^{MS}$  can be obtained following the same approach introduced in Section 2.2.2, i.e. in this case by modeling the dipole over a ground plane as a microstrip line. Note that this line is similar to a patch antenna which has been widely studied in the literature [25]. So the classical expression

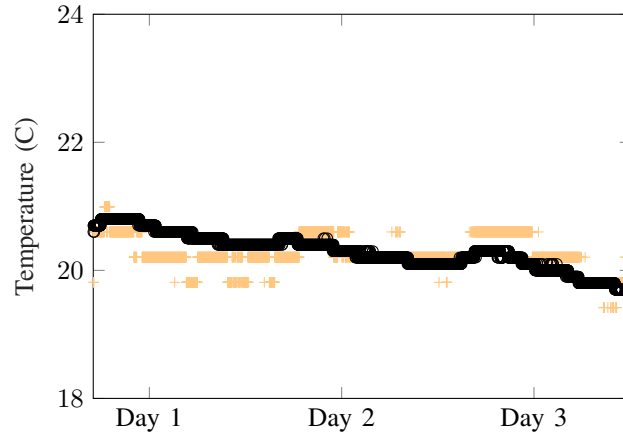


**Figure 2.25:** Comparison between the temperature measured with an integrated sensor in black and using the loop resonator in yellow during a period of 3 days for the test-bench n°3 (Wooden door).

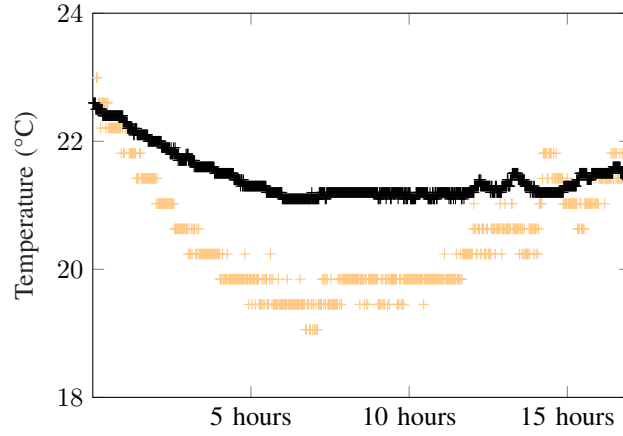


**Figure 2.26:** Comparison between the temperature measured with an integrated sensor in black and using the loop resonator in yellow for the test-bench n°4 (Glass).

of its effective permittivity can be used and the dependence with temperature can be added. The coefficient  $\alpha_p^{MS}$  can then be expressed as:

$$\alpha_p^{MS} = \frac{\frac{\epsilon_r \sigma}{2} \sqrt{1 + 12 \frac{h}{W}}}{\frac{\epsilon_r + 1}{2} + \frac{\epsilon_r - 1}{2} \sqrt{1 + 12 \frac{h}{W}}} \quad (2.25)$$

where  $h$  is the thickness of the substrate and  $w$  the width of the dipole as shown in Fig. 2.27. Considering the scatterer-based microstrip TL geometry given in Fig. 2.27, a value of  $\alpha_p^{MS} = 23.6 \times 10^{-6}$  is obtained with (2.25) using the same Rogers RO4003C.

Note that in the case of the scatterer-based CPS TL shown in Fig. 2.9, where  $\alpha_p^{CPS} = 22.4 \times 10^{-6}$  was obtained with (2.17) for the same substrate,  $\alpha_p^{MS}$  has a higher value. This is due to the presence of a higher confinement of the EM fields in the thermal-dependent substrate for the dipole (see Fig. 2.27).

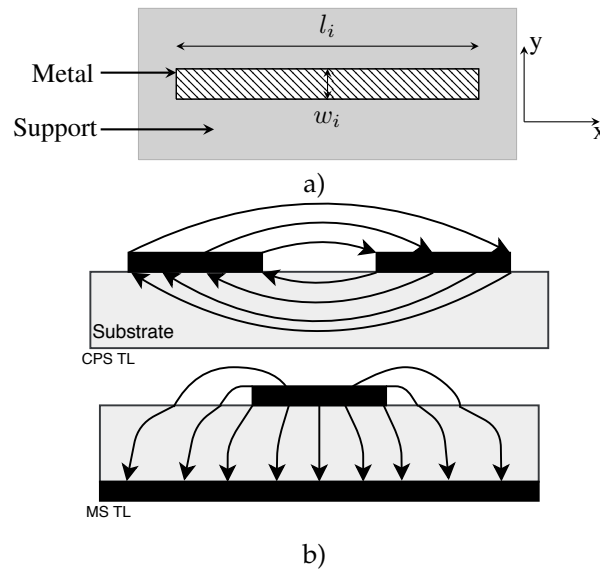


**Figure 2.27:** (a) Resonant scatterer-based microstrip TL. Below the dielectric support of height  $h$  a ground plane is placed. Nominal dimension are  $w=2\text{mm}$ ,  $l_1=2.5\text{cm}$ ,  $l_2=2.2\text{cm}$  and  $l_3=2\text{cm}$  for the three resonators respectively. The polarisation of the electric field used to excite the resonator is along  $x$ . (b) Electric field configuration for the two different TL resonators.

So, by using the same metal and same substrate as the loop, the dipole over the ground will have a greater frequency shift. Even in this TL configuration, the coefficient  $\alpha_c$  is not negligible in the frequency shift response to temperature and should be considered as stated in Section 2.2.6.

**Table 2.9:** Comparison of resonators with and without ground plane.

	With ground plane	Without ground plane
Working on metallic object	✓	Difficult
Support independent	✓	✗
Cost	Higher	Lower
Ease to produce	Harder	Easier

### Measurements

In this measurement, a chipless RFID tag composed of three dipoles over a ground plane is studied [63]. This measurement will show that the proposed model can be generalized to other types of the resonator, as well as the possibility to implement the temperature sensing to existing chipless RFID tags without impacting their identification capability. The measurement protocol is the same as in Section 2.2.7 and test-bench is shown in Fig. 2.28. A cross-polarisation measurement is done. The 3 microstrip dipoles have respectively a resonance frequency of 3.1, 3.7 and 4.1GHz.

### Results and analysis

Extracted temperature results are plotted in Fig. 2.29 alongside the integrated sensor results in black. Extracted temperature using (2.21) and (2.25) is in good agreement with the one measured with the

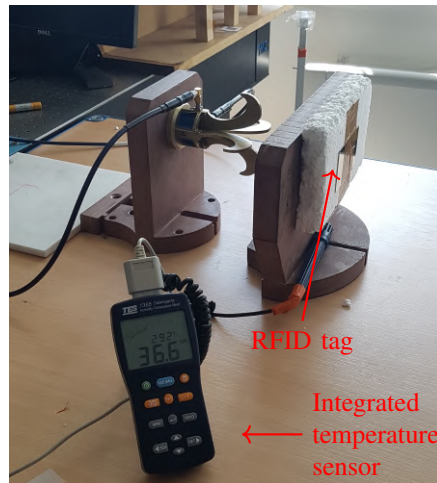


**Figure 2.28:** Principle of the measurement setup for a chipless RFID tag composed of three dipoles over a ground plane thought a wooden object.

integrated sensor. The highest error is of 2°C for the resonator n°2 during the whole measurement validating the analytical thermal model proposed in this section.

We can also see in Fig. 2.29 that having multiple resonators permits to have multiple independent temperature extraction that can be averaged to increase the robustness of the temperature sensor compared to the utilization of a single resonator. An error of 2.7% is obtained when the averaging temperature is considered.

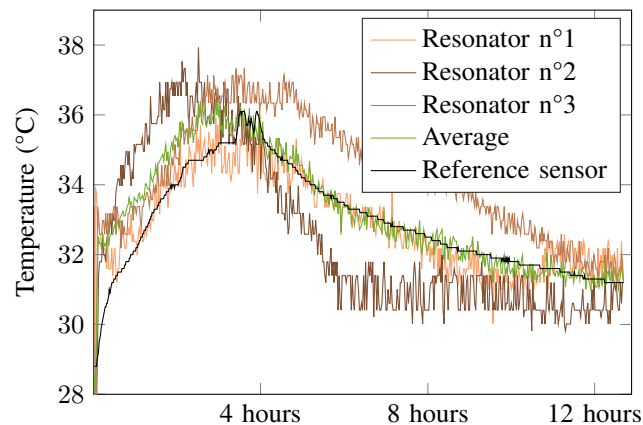


**Figure 2.29:** Comparison between the temperature measured with an integrated sensor in black and using the different resonators that compose the RFID tag.

If we compare the temperature extraction errors between the two types of resonators used (the scatterer-based CPS TL and MS TL), we observe that despite the relation  $\alpha_p^{MS} > \alpha_p^{CPS}$  we obtain similar errors in practice. This can be explained by the fact that the measurement accuracy is also related to the quality factor of the resonators. Indeed, as said earlier, the higher the quality factor, the more accurate the extraction of the resonance frequency and therefore the temperature will be. Here, at the considered frequencies, the quality factor of the scatterer-based MS TL resonator is lower than the CPS TL resonator resulting in a better and more robust measurement of the resonance frequency

(maximum of the S-parameter curve) for the CPS TL resonator. The measured CPS resonator Q-factor is of 148 while the MS resonator has a Q-factor of 48 (3 times lower).

It is also important to note that the shift in frequency is not only linked to  $\alpha$  but also to the resonator length  $L$ , the substrate permittivity and other parameters as shown in (2.24). A figure of merit based on (2.24) can be introduced to better illustrate the temperature sensitivity of the resonators under study:

$$\frac{2Ldf_n}{cn\Delta T} = \frac{\alpha}{\sqrt{\epsilon_{\text{eff}}}} \quad (2.26)$$

This figure of merit can be used to compare different resonator shapes working at the same frequency (same  $L$ ). If we consider a CPS and a MS TL-based scatterer, we can compute (2.26) for different dielectric heights  $h$  and dielectric constant  $\epsilon_r$  to see which one is more sensitive to the temperature. This figure of merit is plotted in Fig. 2.30. We can see that the sensitivity of the sensor  $\frac{\alpha}{\sqrt{\epsilon_{\text{eff}}}}$  is actually lower for the scatterer-based MS TL-based scatterer than for the scatterer-based CPS TL in our configuration ( $h$  and  $\epsilon_r$ ) while presenting  $\alpha_p^{\text{MS}} > \alpha_p^{\text{CPS}}$ . The MS TL has a figure of merit of  $5.9 \times 10^{-6}$  while the CPL TL has a figure of merit of  $1.7 \times 10^{-5}$  (almost 3 times higher).

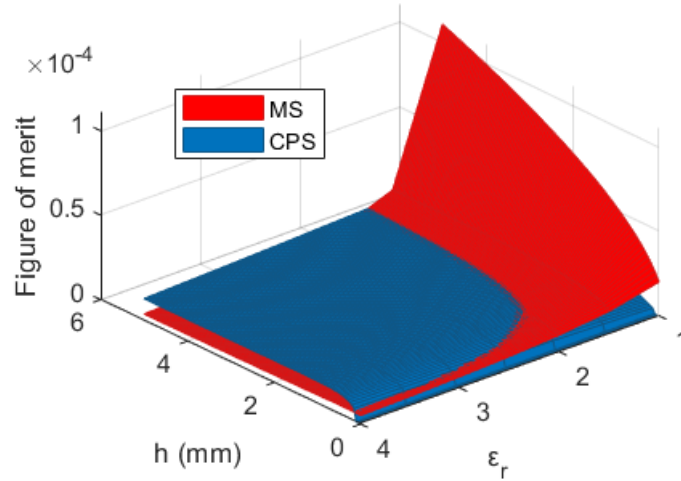


**Figure 2.30:** Figure of merit  $\frac{\alpha}{\sqrt{\epsilon_{\text{eff}}}}$  for the CPS and the MS TL-based scatterer as a function of the substrate height  $h$  and permittivity  $\epsilon_r$ .

### 2.2.10 Humidity effect

Temperature variation in the environment can also significantly change the relative humidity. Such humidity variation can have an impact on the temperature extraction using the proposed model. Indeed, as water's real part of permittivity is around 80 near 3GHz, a higher humidity can lead to a lower resonant frequency due to the increase of the effective permittivity seen by the resonator.

First measurements were done in a climatic chamber where the humidity was maintained constant. These measurements results allowed to validate the introduced thermal behavior. Secondly measurements were done in a real environment where humidity varied during the measurement. These variations (not taken into account in the model) impacted the temperature extraction by adding

errors to it. However, it is possible to investigate the humidity impact for a possible real environment application of this type of tag sensors where the humidity effect is not considered. Note that in Section 2.3 a more general model (taking into account both the temperature and the humidity) will be introduced to further increase the extraction accuracy of the temperature for example.

By using the climatic chamber presented above, a variation of humidity from 40%RH to 60%RH at constant temperature 20°C was performed to characterize the humidity impact on the measured resonance frequency. The measurement results are plotted in Fig. 2.31.

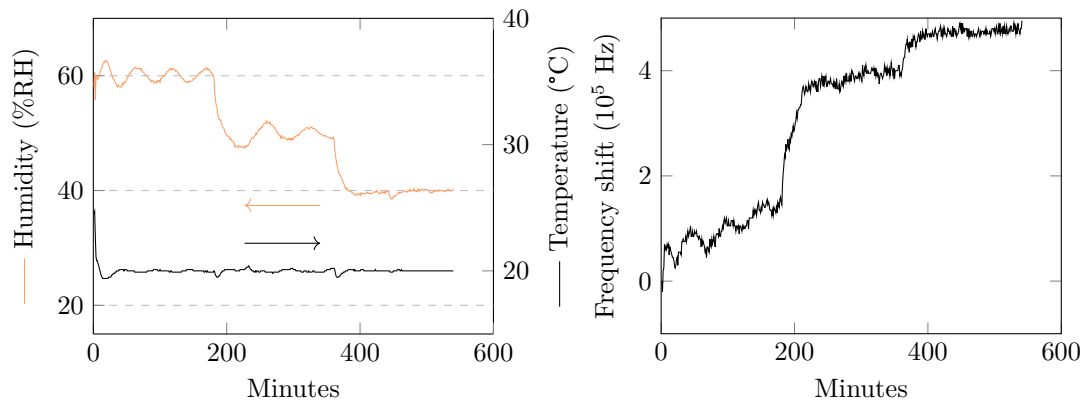


**Figure 2.31:** With significant humidity variation (around 15%RH of change). (a) Measured temperature and humidity. (b) Corresponding resonance frequency variations.

We can see that a 20% relative humidity variation (from 40%RH to 60%RH) leads to 0.5 MHz shift on the resonance frequency. So by using (2.24), this shift (linked to a change of 20% of the relative humidity) can be seen as a variation of  $0.25^{\circ}\text{C}/\%RH$ . Always based on results given in Fig. 2.31, the introduced error by considering a variation from 50%RH to 40%RH is lower: the shift is only of 0.1MHz which corresponds to a variation of  $0.1^{\circ}\text{C}/\%RH$ . Indeed, as shown in [117], the higher the relative humidity, the more the resonance frequency varies. We can extrapolate an error of  $0.06^{\circ}\text{C}/\%RH$  for the humidity range 40%-30%RH and  $0.0033^{\circ}\text{C}/\%RH$  for the range 30%-20%RH. Concerning the highest humidity values we had during our measurement in real environment, a variation between 40%RH and 42%RH was observed, hence an error of  $0.1^{\circ}\text{C}/\%RH$  can be considered in such a case. So, the error on the temperature due to the variation of humidity can be estimated to a maximum of  $0.2^{\circ}\text{C}$ . In the other measurements, a relative humidity lower than 40%RH (even lower than 30%RH in some) was observed, hence the introduced errors are even smaller. However, we will see in the next Section 2.3 that more important errors on the temperature can occur. Also, in these configurations, a more complete model integrating the effect of humidity on the permittivity can resolve the the problem.

### 2.2.11 Conclusion of the section

This section introduced an analytical thermal frequency behaviour of resonant scatterers by modelling them as transmission lines. This approach can be generalized to a large variety of resonators as long as their shape can be analytically described using Scattering Matrix concatenation method. The model permits to rigorously link the variations of the measured resonance frequency with the

temperature without any lookup table. Several resonators configurations have been tested (different metals, different substrates, different types of resonator) to validate the equations. Unlike previous works in this domain where the thermal dependency is considered empirically, the introduced model is used to take into account all thermal effects affecting the resonant scatterers allowing to link rigorously the variations of the measured resonance frequency with the temperature without any lookup table.

As previously presented, the humidity also impact the sensor functionality. It was shown that a controlled humidity variation was necessary to achieve good temperature sensing. In the following section, a generalization of the sensing approach for temperature extraction will be presented. This new approach will permit to sense temperature and humidity at the same time allowing to dissociate both impacts (and so reduce errors) as well as measuring more physical parameters.

## 2.3 Combined Temperature and Humidity Chipless RFID Sensor

Several chipless RFID humidity sensors have been published [118, 119, 120]. In these works, dedicated substrates with permittivities sensitive to humidity are used. In this case, a humidity variation will cause a variation of the permittivity detected by resonators resulting in a shift of their resonance frequencies. These frequency shifts are used to compute the ambient humidity around the resonator. At the same time, multiple chipless RFID temperature sensors have been made [95, 107, 108, 79] based on the same idea, i.e. temperature variations induce a shift on the resonance frequency which can be detected by the reading system. The link between the resonant frequency and temperature involves two physical phenomena. The first studied mechanism is the thermal expansion of the material. In this case, when the temperature varies, the physical dimensions of the resonator will change resulting in a variation of the resonance frequency. The second mechanism is the change of the dielectric constant of the substrate with the temperature. Similar phenomena is observed for humidity. One of the advantages highlighted with this remote reading approach is the possibility to retrieve the tag identifier (ID) along with the temperature even through some everyday objects, such as through a wall or a door [79]. A summary of recent works is presented in Tab. 2.10.

An important limitation of these works is that these sensors can only estimate a single physical parameter while the other has to remain constant (and known). However, in a real-life application, both temperature and humidity will vary and impact the resonance frequency which is used as a sensor but also to decode the tag identifier. This is due to the fact that most of these studies are not based on an analytical model. Indeed they use an empirical approach, which makes it impossible to separate the effects of temperature and humidity. Note that these two variables have an impact on the resonance frequency, which is generally the only quantity that is measured and therefore used to recover the information related to these two independent quantities. Then, when humidity is studied for example, temperature variation can be wrongly interpreted introducing errors on the extracted humidity. Therefore, the real-world applicability of these sensors is debatable. Also, contrary to the majority of works on chipless sensors where specific materials are used to obtain the desired function, the introduced approach is based on an analytical model and can be simply applied to tags previously introduced for identification applications. These tags do not contain any specific material, i.e. particularly sensitive to the quantities to be measured and they have the advantage of being



simple to manufacture. An undeniable advantage over other works is the ability to simultaneously retrieve three independent information sources : the tag identifier, the surrounding temperature and humidity. This section redrafts the problem definition from a theoretical point of view and goes as far as showing the potential and the limits of this approach through several practical experiments. Thus, this section shows how to measure two physical quantities at the same time without the addition of any specific material, with a very accurate physical model that predicts the evolution of the resonance frequency of resonators when the tag is subjected to both temperature and humidity variations. Measurements in a real environment; a study of repeatability on the extraction of the physical quantities and their limiting range, as well as Monte-Carlo simulations are achieved in this section. A method to characterize the temperature and humidity dependencies of unknown materials is also proposed. This section focuses on the estimation of temperature and humidity based on the chipless RFID technology. The study of the remote sensing principle through obstacles (wood, glass, walls...), reading distance or resonator geometry has already been presented in detail in Section 2.2. As the obtained results showed good performance in reading, these studies have not been repeated here.

The section is organized as follows : first the expressions used to extract the temperature and humidity from the measured S-parameters are introduced. Then simulations and measurements in a controlled and in a real environment respectively are presented. Moreover a method to estimate the model coefficients, a repeatability study and the estimation of the errors and the uncertainties of the method using Monte-Carlo simulations were done. Finally, a conclusion is drawn.

**Table 2.10:** Comparison of chipless and antenna-based temperature or humidity sensors

Article	Sensing parameter	Effect investigated	Materials considered	considered	Measurements in real environment	Sensor design
[95]	Temperature	Change in permittivity	Stanyl polyamide		No	Planar shape – PCB design
[108]	Temperature	Change in permittivity	Stanyl polyamide		Not mentioned	Planar shape – PCB design
[110]	Temperature	Change in conductivity	Polymer nanotube composite ink	carbon	No	Planar shape – inkjet printed
[96]	Temperature	Dilatation of 3D structure	Gold and silver cantilever		Yes	3D cantilever – Clean room
[111]	Temperature	Change in permittivity	Ceramic cylinder		Yes	Fully dielectric machined
[121]	Humidity	Change in permittivity	Kapton polyamide	HN	Yes	Planar shape – inkjet printed
[118]	Humidity	Change in permittivity	PVA polymer		No	Planar shape
[119]	Humidity	Change in permittivity	PET film		No	Planar shape – inkjet printed
[117]	Humidity	Change in permittivity	Silicon nanowires		No	Planar shape – PCB design
*	Temperature & Humidity	Change in permittivity & dilatation	Metallic resonator on a RO4003C substrate without materials particularly sensitive to T & RH		Yes	Planar shape – PCB design

\* this work

### 2.3.1 Theory

#### Relationship between resonance frequency, temperature and humidity

As previously said in the introduction, the substrate dependence of humidity is unknown. A rare case where the humidity is characterized by its provider is presented in Fig. 2.32 with Kapton HN dielectric. In the most general case, by considering small variations of humidity around a specific value  $RH_0$ , where RH denotes the relative humidity (in %) seen by the resonator, it is possible to linearize the resonator substrate permittivity  $\epsilon_r$  with:

$$\epsilon_r(T, RH) \simeq \epsilon_r(RH) \times (1 + \sigma T) \simeq \epsilon_r(RH_0) \times (1 + \sigma T) \times \left[ 1 + \frac{\epsilon_r'(RH_0)}{\epsilon_r(RH_0)} (RH - RH_0) \right] \quad (2.27)$$

where  $\sigma$  is the thermal dependence of the substrate often characterized by the provider.  $\epsilon_r'(RH_0)$  is the derivative of  $\epsilon_r$  according to the variable RH. Equation (2.27) can be rewritten as:

$$\epsilon_r(T, RH) = \epsilon_r(RH_0) \times (1 + \sigma T) \times (1 + [a + \eta RH]). \quad (2.28)$$

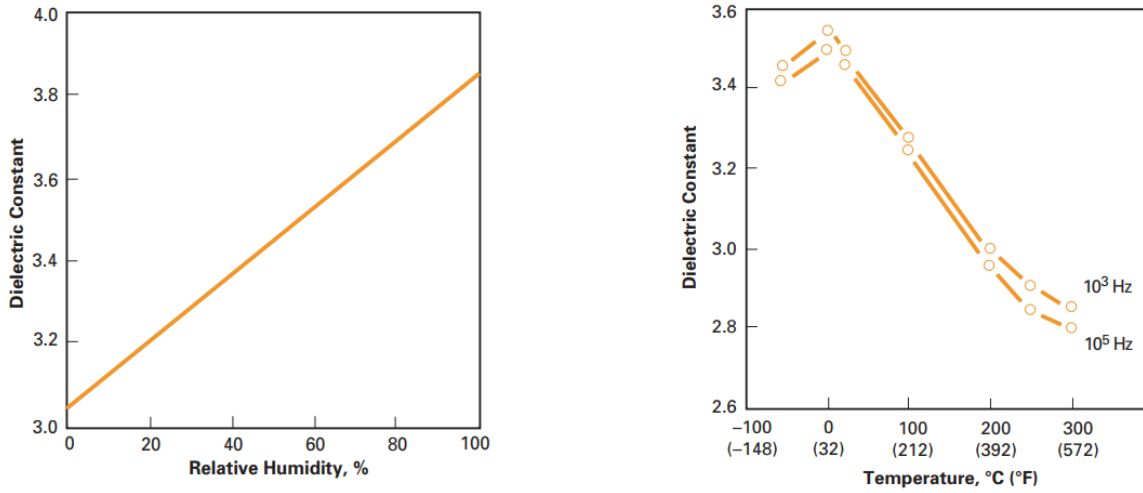


**Figure 2.32:** Temperature and humidity characterization of Kapton HN dielectric by its provider.

The coefficients  $a$  and  $\eta$  represent the humidity dependence of the substrate. For the loop, the effective permittivity can be modelled by considering the resonator as a slot line terminated at both ends by a SC. Thus, the effective permittivity of the loop resonator  $\epsilon_{eff}$ , on a single substrate layer, can be expressed as [112]:

$$\epsilon_{eff}(T, RH) = 1 + \frac{\epsilon_r(1 + \sigma T) \times (1 + [a + \eta RH]) - 1}{2} q \quad (2.29)$$

where  $\epsilon_r$  is the permittivity of the substrate at  $T = 0^\circ\text{C}$  and  $RH = RH_0$ . The parameter  $q$  is dependent on the thickness of the substrate and the geometry of the resonator as described by the analytical expression given in [112, eq. (21)] which leads to:

$$\epsilon_{eff}(T, RH) \simeq \epsilon_{eff}(0, RH_0) \times (1 + \alpha_p T) \times (1 + a' + \gamma RH) \quad (2.30)$$

with :

$$\alpha_p = \frac{\sigma q \epsilon_r}{2 + (\epsilon_r - 1)q} \quad (2.31)$$

and

$$\gamma = \frac{\eta q \epsilon_r}{2 + (\epsilon_r - 1)q} \quad (2.32)$$

and

$$a' = \frac{a q \epsilon_r}{2 + (\epsilon_r - 1)q} \quad (2.33)$$

In this case, (2.1) can be rewritten as :

$$f(T, RH) = \frac{c}{2\sqrt{\epsilon_{\text{eff}}(1 + \alpha_p T)(1 + a' + \gamma RH)L_0(1 + \alpha_c T)}} \simeq F \times (1 - \alpha T - \frac{1}{2}[a' + \gamma RH]) \quad (2.34)$$

with

$$\alpha = \alpha_c + \alpha_p/2 \text{ and } F = \frac{c}{2\sqrt{\epsilon_{\text{eff}}L_0}} \quad (2.35)$$

Notice that the thermal and humidity dependence on the permittivity is expressed by the coefficients  $\alpha$ ,  $a'$  and  $\gamma$  in (2.34). For this reason, the value of  $\epsilon_{\text{eff}}$  in (2.34) is a constant which does not depend on the temperature nor on the humidity. Please also note that for the remainder of this section, we will consider the values of  $\alpha$ ,  $a'$  and  $\gamma$  to be known. A method for the extraction (used in the measurement part of this section) of these coefficients will be described later.

The principle of the sensor introduced is based on the use of two resonators of the same topology. Rectangular loop resonators are studied for their good EM performance. As illustrated in Fig. 2.33, the resonators present two different lengths  $l_1$  and  $l_2$  (associated to their resonance frequencies  $f_1$  and  $f_2$ ) for respectively resonators 1 and 2. Based on (2.34), and considering two loops, we can write the following equations:

$$-\begin{pmatrix} F_1 & F_2 \end{pmatrix} \begin{pmatrix} \alpha_1 & \frac{\gamma}{2} \\ \alpha_2 & \frac{\gamma}{2} \end{pmatrix} \begin{pmatrix} \Delta T \\ \Delta RH \end{pmatrix} = \begin{pmatrix} \Delta f_1 \\ \Delta f_2 \end{pmatrix} \quad (2.36)$$

where  $\Delta T = T - T_{\text{ini}}$ ,  $\Delta RH = RH - RH_{\text{ini}}$  with  $T_{\text{ini}}$  (respectively  $RH_{\text{ini}}$ ) the initial temperature (respectively relative humidity) at time  $t_0$ ,  $T$  (respectively  $RH$ ) the temperature (respectively relative humidity) at time  $t$  ( $t > t_0$ ).

The quantity  $F_n$  (independent of temperature and humidity) can be extracted using an initial measurement and (2.34). Indeed, by measuring the temperature  $T_{\text{ini}}$  and humidity  $RH_{\text{ini}}$  of the first measured resonance frequency  $f_{\text{ini}}^n$  of the resonator  $n$ , we have:

$$F_n = \frac{f_{\text{ini}}^n}{(1 - \alpha_n T_{\text{ini}} - \frac{1}{2}[a' + \gamma RH_{\text{ini}}])} \quad (2.37)$$

As the set of terms appearing in the second part of (2.37) is known, it is possible to calculate  $F_n$ . If the criterion  $\alpha_2 \neq \alpha_1$  is respected, (2.36) allows a unique expression for both temperature and humidity

as follows :

$$\left\{ \begin{array}{l} T = T_{\text{ini}} - \frac{1}{F_1 F_2 (\alpha_1 - \alpha_2)} (F_2 \Delta f_1 - F_1 \Delta f_2) \end{array} \right. \quad (2.38a)$$

$$\left\{ \begin{array}{l} RH = RH_{\text{ini}} - \frac{2}{\gamma F_1 F_2 (\alpha_1 - \alpha_2)} [F_1 \alpha_1 \Delta f_2 - F_2 \alpha_2 \Delta f_1] \end{array} \right. \quad (2.38b)$$

If the resonators are placed on the same substrate, they will present the same values for  $\gamma$  and  $a'$  and  $\alpha_p$  as well. However, even if scatterers are designed on the same substrate and the same metal for the resonator's pattern, the value of  $\alpha_c$  so  $\alpha$  varies with the resonator length (see [122]). Thus the fact of considering two different lengths means that we have  $\alpha_1$  not equal to  $\alpha_2$  in a vast majority of cases and especially in the case that will be presented next.

By doing a initial measurement of the resonance frequency  $f_{\text{ini}}^n$  for both resonators at a known temperature  $T_{\text{ini}}$  and humidity  $RH_{\text{ini}}$ , we can then calculate  $F_n$  using (2.37). To extract  $T$  and  $RH$  at time  $t$ , (2.38a) and (2.38b) will be applied on the measured resonance frequencies of the two resonators  $f_1$  and  $f_2$ . As previously said, coefficients  $\alpha$ ,  $\gamma$  and  $a'$  are supposed to be known using (2.31), (2.32) and (2.33) for known tag materials and geometry or can either be obtained by measurement (described later). In the present section, Rogers RO4003C will be used as a substrate. Note that its humidity dependence is not characterized by its provider. So, the procedure detailed later was first used to extract missing coefficients.

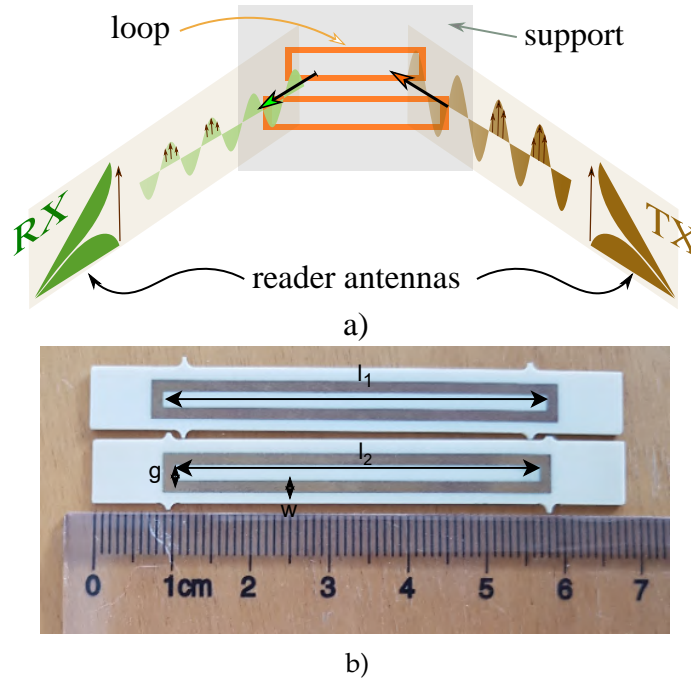


**Figure 2.33:** a) Principle of the measurement of the scatterer's resonance frequency used to sense temperature and humidity. When the tag is placed in a climatic chamber, the temperature and humidity can be controlled in order to characterize the accuracy of the sensor function implemented. Real environment measurements are done in office-type environments. b) Resonators used for the measurements. The first resonator has  $g = 2$  mm,  $w = 1$  mm and  $l_1 = 49$  mm. The second resonator has the same  $g$  and  $w$  but  $l_2 = 46$  mm. The substrate is Rogers RO4003C.

### 2.3.2 Simulations

Prior to that, EM simulations using CST were achieved to make a proof of the sensor concept presented above. Figure 2.33 shows the tag, which is made up of two loop scatterers. For simulation, zinc and copper metals with corresponding thermal dilatations of  $\alpha_c^{\text{copper}} = 17 \times 10^{-6} \text{ }^\circ\text{C}^{-1}$  and  $\alpha_c^{\text{zinc}} = 31 \times 10^{-6} \text{ }^\circ\text{C}^{-1}$  are used.  $g = 2.07 \text{ mm}$ ,  $w = 1.43 \text{ mm}$ , and  $l_1 = 47.97 \text{ mm}$  are the dimensions of the first copper resonator. The second zinc resonator has the same  $g$  and  $w$  values but a different length  $l_2 = 38.38 \text{ mm}$ . The permittivity of the simulated support is  $\epsilon_r(T, \text{RH}) = 3(1 + 40 \times 10^{-6}\text{RH})(1 + 10 \times 10^{-6}\text{T})$  where  $T$  and  $\text{RH}$  will fluctuate following  $0 < T < 60 \text{ }^\circ\text{C}$  and  $0 < \text{RH} < 100\%$ . The dielectric support is supposed linear with humidity so  $a = 0$ . A plane wave excitation and a Transient Solver are considered. The physical parameters used for the simulation are summarized in Table 2.11. RCS simulation results are plotted in Fig. 2.34 for different temperature and humidities values. Equations (2.38a) and (2.38b) are then applied to the extracted resonance frequencies : 2.36 GHz and 2.91 GHz are the values obtained for the resonator 1 and 2 respectively.

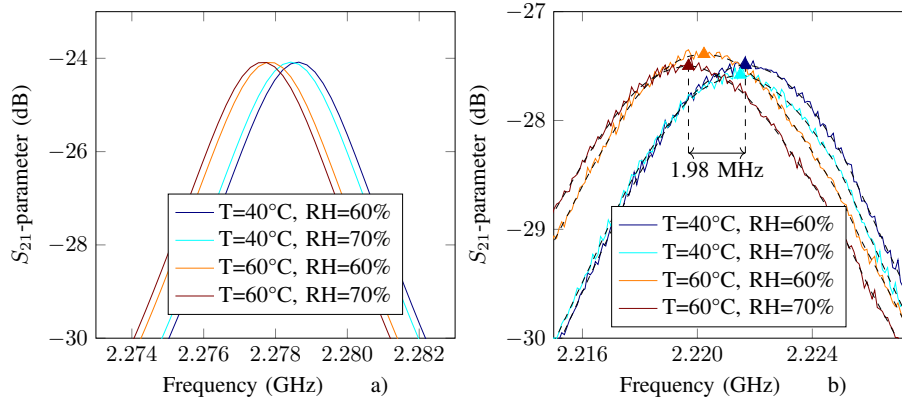


**Figure 2.34:** a) Simulated RCS response of a resonator for different temperatures and humidities values. b) Smoothed measurement (dashed line) and raw data (continuous line) for  $S_{21}$  response at different temperature and humidity values. A gaussian smoothing using a moving window is used. The window is 200 frequency points width on a measurement of 10.001 points.

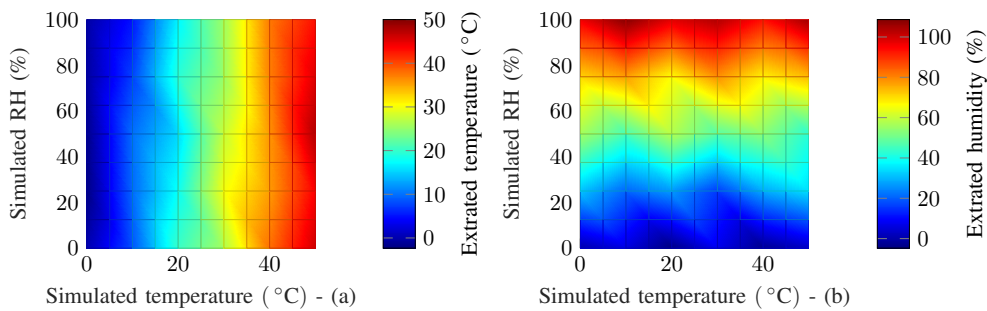


**Figure 2.35:** a) Extracted temperature using (2.38a). b) Extracted relative humidity using (2.38b). The simulated chipless tag is shown in Fig. 2.33. The permittivity of the support is  $\epsilon_r = 3(1 + 40 \times 10^{-6}\text{RH})(1 + 10 \times 10^{-6}\text{T})$ .

Fig. 2.35a and b plot respectively the extracted temperature and relative humidity using (2.38a)

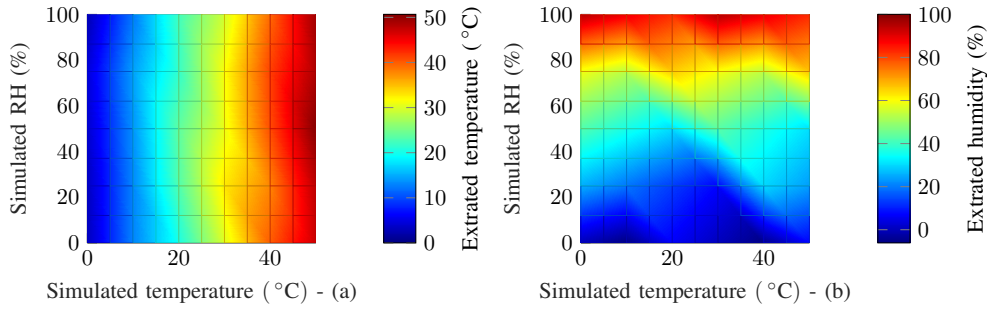


**Figure 2.36:** a) Extracted temperature using (2.38a). b) Extracted relative humidity using (2.38b). The simulated chipless tag is shown in Fig. 2.33. The permittivity of the support is  $\epsilon_r = 3.55(1 + 20 \times 10^{-6}\text{RH})(1 + 40 \times 10^{-6}\text{T})$ .

and (2.38b) with the simulated resonance frequencies. The axes in Fig. 2.35 correspond to the temperature and humidity values imposed in the simulation. It can be seen that the extracted physical quantities are independent, which shows that the system of equations (2.36) can be solved.

The extracted temperature in Fig. 2.35a is in good agreement with the simulated temperature with an average error of 2°C (and a maximum of 6°C). With humidity, a slightly larger error with 3%RH on average (and a maximum of 9%RH) is observed.

A second simulation has been done where the previous parameters still apply except for the permittivity which is now described by  $\epsilon_r(T, \text{RH}) = 3.55(1 + 20 \times 10^{-6}\text{RH})(1 + 40 \times 10^{-6}\text{T})$ . The goal of this simulation is to demonstrate the concept which is the importance of the substrate for the humidity extraction. The humidity dependence has been lowered compared to the value used in the previous simulation (a reduction of  $\eta$  from 40 to 20). For temperature,  $\sigma$  was increased from 10 to 40. Extracted temperature and humidity are plotted in Fig. 2.36. The extracted temperature is in good agreement with the simulated temperature with a maximum error of 4°C and 2°C on average. For humidity, a maximum error of 22%RH and 10%RH on average are observed. We can confirm that by increasing the thermal dependence  $\sigma$ , hence the frequency shift, it is easier to estimate the correct temperature. Meanwhile, by reducing the humidity dependence  $\eta$  and so its frequency shift, higher errors on the humidity extraction are observed. Also, we can see that the behaviour between the temperature and humidity is not symmetrical since a low value of  $10 \times 10^{-6}$  on  $\sigma$  does not increase significantly errors compared to  $\eta$ . This behaviour appears since the temperature extraction is also impacted by the thermal dilatation of the resonator while humidity extraction is only impacted by the permittivity.

These simulations confirm the trends in extraction, but they do not allow to estimate very precisely the error to be expected when using (2.38a). Indeed, despite a very dense mesh, and therefore a very long simulation time, the numerical accuracy obtained in the simulation remains relatively low and induces significant errors which will not be present in measurement. It is the experimental study that will allow us to better characterize the errors obtained on the extraction of temperature and humidity.

**Table 2.11:** Physical parameters used for the simulations.

Parameter	Simulation 1	Simulation 2
$\alpha_c^1$ ( $^{\circ}\text{C}^{-1}$ )	$17 \times 10^{-6}$	$17 \times 10^{-6}$
$\alpha_c^2$ ( $^{\circ}\text{C}^{-1}$ )	$31 \times 10^{-6}$	$31 \times 10^{-6}$
$\sigma$ ( $^{\circ}\text{C}^{-1}$ )	$10 \times 10^{-6}$	$40 \times 10^{-6}$
$\eta$ ( $\%RH^{-1}$ )	$40 \times 10^{-6}$	$20 \times 10^{-6}$
$\epsilon_r$	3	3.55
$g_1$ (mm)	2.07	2.07
$g_2$ (mm)	2.07	2.07
$w_1$ (mm)	1.43	1.43
$w_2$ (mm)	1.43	1.43
$l_1$ (mm)	47.97	47.97
$l_2$ (mm)	38.38	38.38

### 2.3.3 Sensitivity of the measurement

The choice of the substrate which makes up the resonator is important for the accuracy of the sensor, especially for humidity. Temperature extraction is impacted by both the substrate and the metal part of the resonator [see (2.35)] while humidity can only be sensed by the substrate.

To increase the resolution of the sensor, the frequency resolution of the VNA has to be low. Indeed, the resonance frequency shift  $\Delta f$  due to temperature and humidity can be computed with [79]:

$$\Delta f = \frac{c}{2\sqrt{\epsilon_{\text{eff}}}L} (\alpha\Delta T + \frac{1}{2}\gamma\Delta RH) \quad (2.39)$$

Using typical values for  $\alpha$  and  $\gamma$  (given in the next section), we can find that an increase of  $1^{\circ}\text{C}$  leads to a frequency shift of 64kHz. The frequency step on the VNA during our measurements is 6kHz. Thus, the estimated temperature is discretized by steps of  $1/11^{\circ}\text{C}$ . Moreover, an error in the research of the curve maximum of only 11 frequency steps can lead to an error of  $1^{\circ}\text{C}$ . Therefore, increasing the number of frequency points during the measurement would reduce this error and this discretization.

Note that loop resonators are considered in this section but other tag geometries can also be used. For example, in Section 2.2, (2.1) is also used for dipole over ground plane resonators. In this case, the expression of  $\alpha_p$  and also the transformation from  $\eta$  to  $\gamma$  is different and must be updated.

### 2.3.4 Parameters characterization

Substrate temperature variations are often given by providers in the data sheet but humidity response is often not characterized. This section will show how to characterize the coefficients  $a'$ ,  $\alpha$  and  $\gamma$  with an example of Rogers RO4003C substrate. The time transient response as well as the limiting range of (2.34) will also be studied for this dielectric.

By normalizing the measured resonance frequency  $f$  in (2.34) by (2.37), we have :

$$\frac{f}{F} = 1 - \frac{a'}{2} - \alpha T - \frac{\gamma}{2} RH \quad (2.40)$$

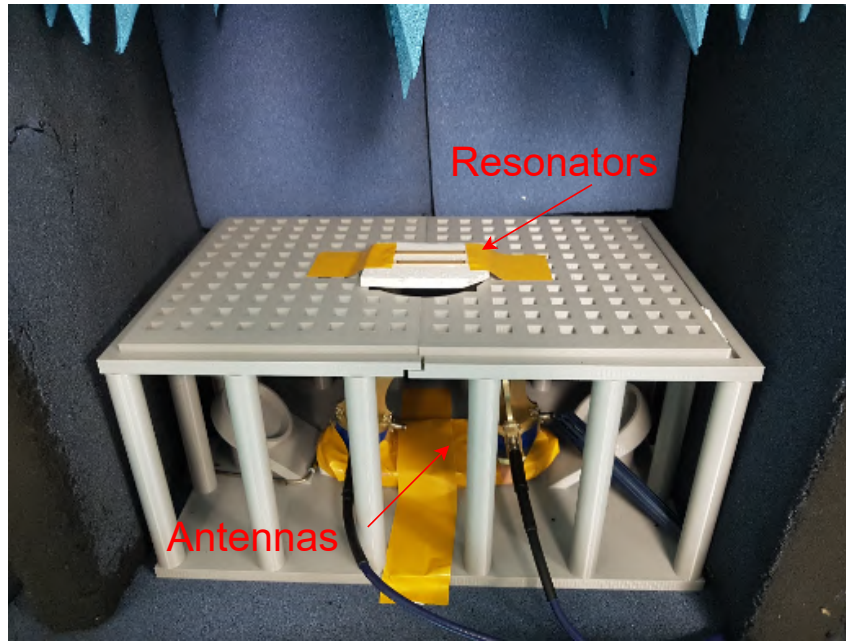


**Figure 2.37:** Photo of the measurement bench and tags inside the climatic chamber.

By considering  $f_{ini}$  as the first measured resonance frequency at time  $t_0$ , as the coefficients  $a'$ ,  $\alpha$ ,  $\gamma$  are small compared to one (see Table 2.12), one can simplify (2.37). From this, we can rewrite (2.40) as follows. Note that this simplifying assumption will be validated later.

$$\frac{f}{f_{ini}} \simeq 1 - \frac{a'}{2} - \alpha T - \frac{\gamma}{2} RH \quad (2.41)$$

From (2.41) it is possible to extract the coefficients  $a'$ ,  $\alpha$  and  $\gamma$  by linear regression applied on measurement. Indeed, it is possible to have the resonance frequencies corresponding to a set of different values of temperature and humidity. The set of measurements presented earlier, as long as we have measured at the same time the temperature and the humidity with an independent electronic sensor can be used to make this extraction.

Measurements in the climatic chamber with temperature and humidity profiles such as the one shown in Fig. 2.38-a have been used to extract the three coefficients. Indeed, once the frequencies  $f$  were measured alongside the temperature  $T$  and humidity  $RH$ , a fit of all the realized measurements was done based on (2.41) to find the values of  $\alpha_n$ ,  $\gamma$  and  $a'$  and is illustrated in Fig. 2.38-b. This extraction was repeated three times. For each measurement, the entire test bench was disassembled and put back in place. Extracted coefficients are listed in Table 2.12. The measurement in a real environment is also used to estimate these coefficients and the obtained results are added in Table 2.12. Fig. 2.39 shows a comparison between the normalized resonance frequency and (2.41) using the measurements obtained in real environment. We can see that the fitting is in good agreement for different humidity and temperature variations.



**Table 2.12:** Fitting coefficients of (2.41) for different measurements using the same resonator.

	Measure 1	Measure 2	Measure 3	Real environment
$\alpha$	$3.852 \times 10^{-5}$	$4.624 \times 10^{-5}$	$4.165 \times 10^{-5}$	$4.131 \times 10^{-5}$
$\gamma$	$2.658 \times 10^{-5}$	$3.108 \times 10^{-5}$	$2.926 \times 10^{-5}$	$2.836 \times 10^{-5}$
$a'$	0.004	0.006	0.006	0.004

We can see that the extracted coefficients in the climatic chamber (for a sensing range of 40°C-60°C and 60%RH-70%RH) are very close to each other, reflecting a good repeatability of the measurement. In comparison to the real environment estimation, we can see that the setup has a limited impact on the extraction. Also, in the real environment the measurement was done in the range of 20°C-25°C and 25%RH-40%RH as shown in Fig. 2.43. It means that the linear approximation of humidity made for the Rogers RO4003C (which is uncharacterized in terms of humidity) seems a good approximation for the whole 25%RH-70%RH range. This range of validity for our substrate and the limits of the approach will be discussed later.

Some of the extractions presented here were also done using the same approach (linear regression on a set of measurements made at different times for different values of temperature and humidity) applied on (2.40), i.e. before the simplification indicated above. The results obtained are close to those presented in Table 2.12, with an error of less than 10% on each coefficient. This value of 10% will be taken into consideration to calculate the uncertainty and the error induced on the extraction of temperature and humidity. However, the extraction from (2.40) is more difficult to implement. Indeed, it has been seen in practice that this extraction is strongly dependent of the initial values given to  $a'$ ,  $\alpha$  and  $\gamma$  since  $F$  also depends on these parameters as stated in (2.37). This is not the case with (2.41) where the obtained results are independent from the initial values given to these coefficients. This is the reason why only the extracted values obtained with (2.41) are used in this section.

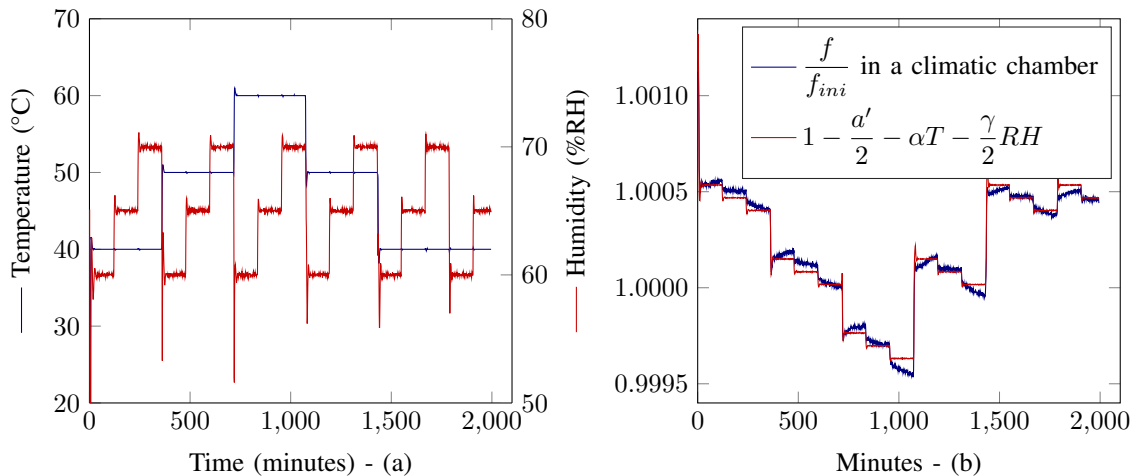


**Figure 2.38:** a) Temperature and humidity measured with an electronic sensor. b) Measured normalized resonance frequency in a climatic chamber in blue and (2.41) using estimated parameters in red with  $\alpha = 4.165 \times 10^{-5} \text{C}^{-1}$  and  $\gamma = 2.926 \times 10^{-5} \%RH^{-1}$  (see Table 2.12).

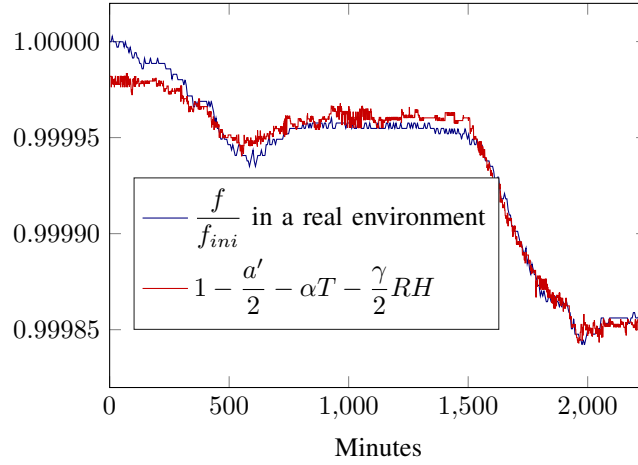


**Figure 2.39:** Measured normalized resonance frequency in a real environment in blue and (2.41) using estimated parameters in red with  $\alpha = 4.131 \times 10^{-5} \text{C}^{-1}$ ,  $\gamma = 2.836 \times 10^{-5} \% \text{RH}^{-1}$  and  $a' = 0.004$  (see Table 2.12). Temperature and humidity variations of this measurement are presented in Fig. 2.43.

### 2.3.5 Sensing in a controlled environment

The introduced approach is mainly based on the measurement of scatterer resonance frequencies. This information can be obtained from the measurement of the RCS of the scatterer [123], a quantity that can be easily obtained in simulation. In practice, it is not necessary to have the RCS, the measurement of the  $S_{21}$  parameter in bi-static configuration and in frequency is sufficient. Indeed, the resonance frequencies are intrinsic to the scatterers and do not depend on the measurement setup like the distance between the antennas and the tag or the antennas themselves [124].

#### Measurement setup and tag design

Fig. 2.37 presents the measurement setup and the fabricated tags used are shown Fig. 2.33. Experimental measurements are performed using a VNA (Agilent 5222A). The source power of VNA is equal to 0 dBm. The frequency sweep ranging from 2 to 3 GHz with 10001 points is used. A co-polarization bi-static configuration with Satimo (QH2000) quad ridged open boundary antennas (2–32 GHz) is used. During the VNA experiments, an IF bandwidth of 10kHz was also used.

Temperature and humidity are controlled using a Votsch climatic chamber VC0018. The measurement protocol is the same the one described in Section 2.1.2.

In practice, a standard PCB chipless tag was measured. On a Rogers RO4003C substrate, the tag is made up of two copper resonators (see Fig. 2.33b). By using different resonator lengths, the requirement  $\alpha_1 \neq \alpha_2$  is respected (see Section 2.1). The humidity dependency for this substrate is not indicated by the provider. As a result, we have extracted the values of  $\gamma$  and  $a'$  first as presented earlier. A variation of temperature from 40°C to 60°C with a 10°C step is achieved as well as a variation of the relative humidity from 60%RH to 70%RH with 5%RH steps. The temperature and humidity profiles are shown in red in Fig. 2.40a. Both resonators are placed at the same time side by side (as shown in Fig. 2.37) for the measurement and were not moved during the whole monitoring. Example of measured S-parameters can be found in Fig. 2.34.

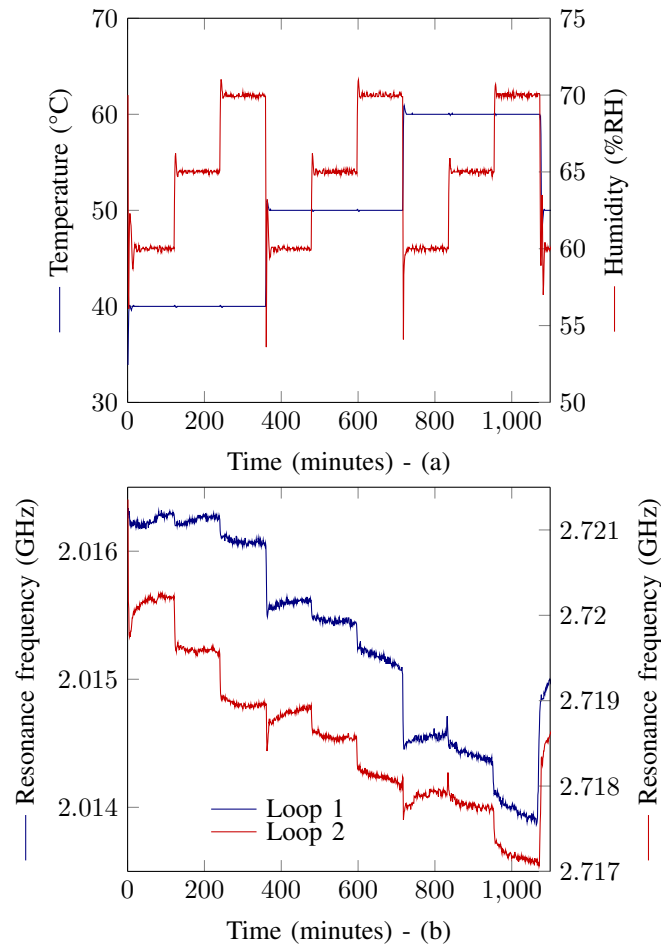


**Figure 2.40:** a) Temperature and humidity measured inside the climatic chamber by an electronic sensor as a function of time. b) Measurement of the resonance frequency of the two resonators as a function of time.

### Results and Analysis

The measured resonance frequencies are plotted in Fig. 2.40b. Variations of 20 °C and 20%RH are achieved and (2.38a) and (2.38b) are applied. The results of the extraction are shown in Fig. 2.42 alongside the temperature and humidity measured by the electronic sensor.

The highest difference with the electronic temperature sensor is of 2.8 °C and 0.95°C on average. For humidity, the highest difference is very localized near 700min and equals to 7.2%RH. On average, an error of 2.1%RH was made with the electronic sensor. We can see that humidity is estimated with more errors than temperature. Indeed, as presented earlier, the humidity impact tends to be lower than the temperature one since it is only sensed by one physical mechanism (the substrate variation) and so induces smaller shifts which are harder to measure. This is the case for copper resonators on Rogers RO4003C. Investigations on substrate properties will be presented later and Table 2.12.

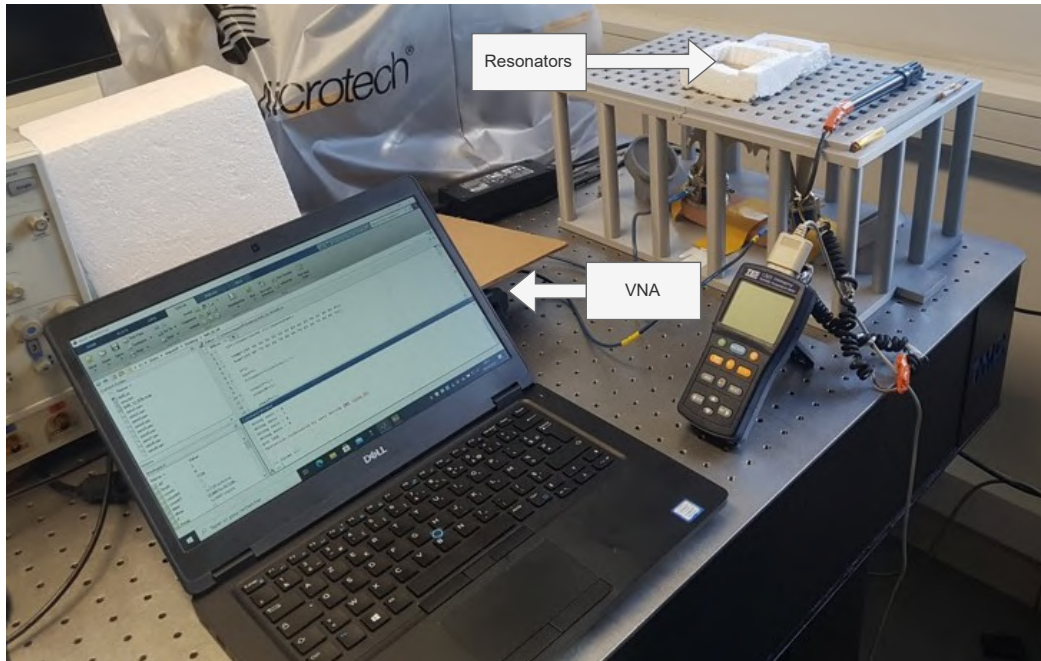


Figure 2.41: Photo of the measurement bench and tags.

### 2.3.6 Sensing in a real environment

#### Measurements

Measurements were done in a real environment to validate the sensing approach. The measurement setup is shown in Fig. 2.41 and the tags used in practice are presented in Fig. 2.33. The bistatic antenna configuration is kept to increase the isolation. A computer is connected to a VNA and an electronic temperature and humidity sensor. Each minute, the computer triggers measurements on the VNA and the sensor. Temperature, humidity and the S-parameters are saved on the computer. The measured S-parameters have been smoothed to remove any residual measurement noise that may impact the search of the resonance frequency and thus induce an error on the frequency extraction. The tag was not moved during the whole monitoring.

#### Results and analysis

The recorded temperature and humidity during the measurement are shown in Fig. 2.43 in red. The measurement lasted 2200 minutes. Equations (2.38a) and (2.38b) are applied and the estimated temperature and humidity are shown in Fig. 2.43 in blue alongside the electronic sensor in red. We can see that the two quantities are in good agreement with an error lower than 1°C and 5%RH on the estimated quantities. In Fig. 2.43 the estimated temperature which can be sensed using a traditional chipless RFID temperature sensor is also plotted in brown. As said in the introduction, if the humidity effect is not considered, a higher error of 2°C on the extracted temperature can be observed. The 2°C error is obtained for relatively low humidity values (around 30%), and would be even greater if humidity increases. This approach shows how it is possible with (2.38a) to reduce the errors in the estimation of temperature as well as enabling to sense more physical quantities (here humidity).

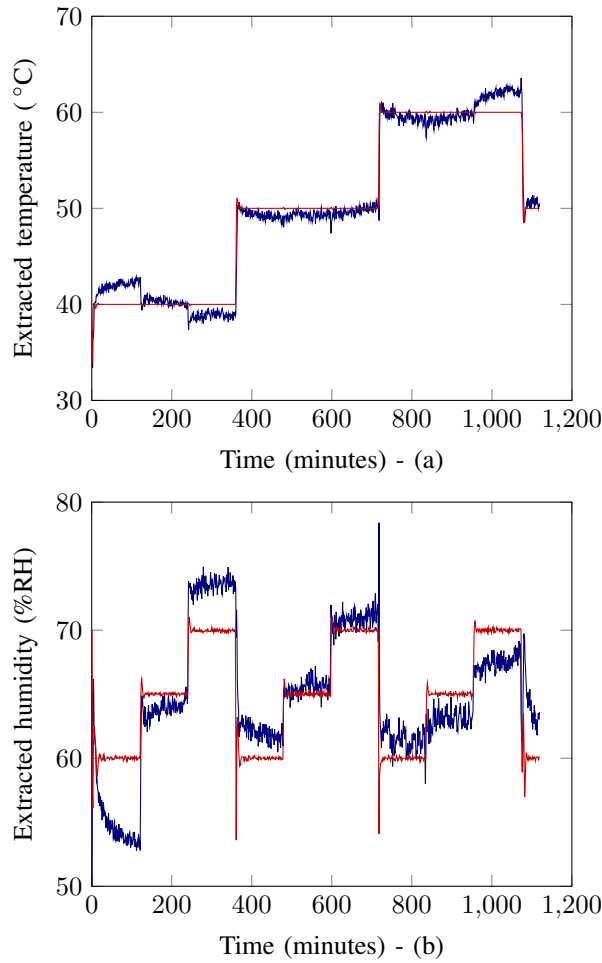


**Figure 2.42:** a) Extracted temperature in blue using (2.38a) and measured temperature with the electronic sensor in red. b) Extracted relative humidity using (2.38b) in blue and measured with the electronic sensor in red. The test-bench is shown in Fig. 2.37.

### 2.3.7 Discussions on the proposed approach

#### Discussion on measurement conditions

The introduced tags allow to perform an identification and a sensor function (temperature, humidity) simultaneously. It should be noted that the measurement conditions associated with these two functions are quite different from each other. Indeed, for the identification function, the objective in application is to be able to retrieve information in the most constrained environments, potentially in motion, and an interesting example to illustrate this type of measurement condition is when the tag is held in the hand. To this end, several approaches have been introduced to make the measurement as independent as possible of the environment, even if the tag is coupled with the unknown object on which it is placed [64, 125]. The measurement in connection with the sensor functionality is quite different and requires to further constrain the measurement conditions [122, 79]. This also means that it will always be possible to obtain the tag identifier when reading in sensing mode, whereas the reverse is not true. In identification, we can allow a margin of 80 MHz on the detection of the

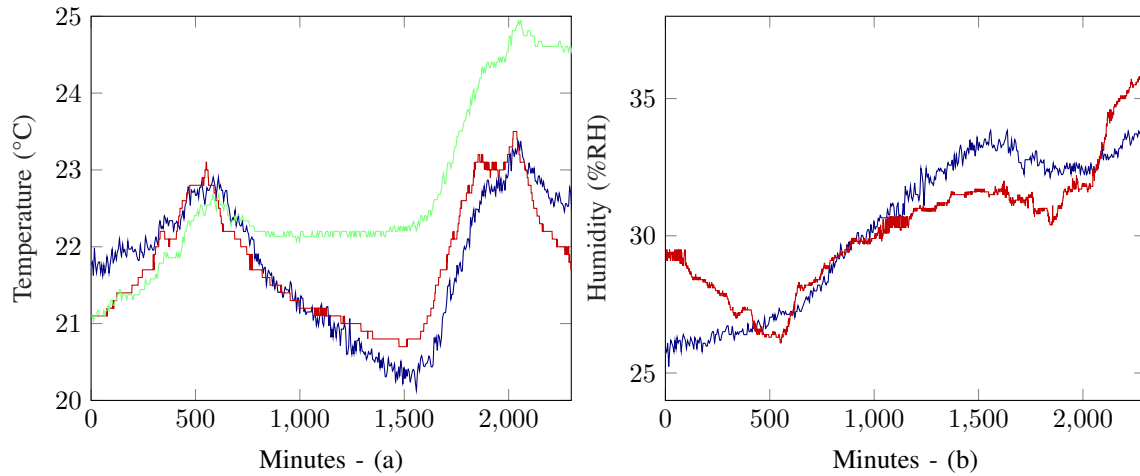


**Figure 2.43:** a) Extracted temperature in blue using (2.38a), measured temperature with the electronic sensor in red and temperature sensing only in green. b) Extracted relative humidity using (2.38b) in blue and measured with the electronic sensor in red. The test-bench is shown in Fig. 2.41.

resonant frequency for the decoding of the information, in sensor, we will try to measure the smallest variations of the resonance frequency and we must therefore make sure that this variation is linked to the physical parameters that we are measuring and not to the changing environment. As an example, a variation of 0.8 MHz (i.e. 100 times less than for the identification mode) is equivalent to a change of 6°C in temperature for the tags presented. Therefore, the results presented are only possible if the environment (excluding temperature and humidity variations) and the measurement system have an effect on the resonant frequency of less than 0.1 MHz (64kHz for 1°C of error as discussed earlier). To illustrate that, it is important to note that in an environment where nothing moves in the vicinity of the tag (i.e. within a radius of one meter centered on the reading zone), the action of taking the tag and replacing it strictly in the same place implies a modification of the resonance frequency of around 0.8 MHz. This figure shows that 1) the error due to the environment on the tag's resonance frequency can be reduced very significantly when the environment is perfectly stationary, 2) any displacement of the tag, even if very small, leads to significant errors for the sensor function. This is why the measurement conditions implemented in the article impose a fixed environment around the tag and a fixed tag that is not moved during the measurement [79]. The person carrying out the measurements stands at a distance of at least one meter from the tag and most of the measurements are carried out without any person in the room where the experiment takes place. In terms of measurement methodology, the principle of extraction is based on 1) the initial measurement of the resonance frequency (at time  $t_0$ ) as well as the temperature and humidity, 2) successive measurements at time  $t$  of the resonance frequency under the same conditions as the measurement at  $t_0$  where only the humidity and temperature vary over time. The difference in resonance frequency  $\Delta f = f(t) - f(t_0)$  obtained thus contains information on the effects of the variation of the physical parameters on the resonator, effects which are modeled and given by (2.36). Note that the fact of imposing not to move the tag or the environment in contact to the tag during the measurement is not incompatible with applications, we can give the example of a sensor fixed in a building and positioned far from human activities. Under these conditions, temperature and humidity can be extracted remotely with simple

resonators manufactured with classical PCB manufacturing techniques. Note also that we do not use any specific materials that are particularly sensitive to humidity or temperature for the sensor function (the RO substrate is known to be relatively insensitive to humidity variations). Also, depending on the application, it is always possible to select another substrate to reduce the reading constraints specified here.

### Time transient responses

The measurement done to identify the parameters in the climatic chamber in Fig. 2.38 permits to find the same coefficients as the ones obtained with the measurement in a real environment. We also note that the measurement in the climatic chamber offers additional information on the time response of the sensor. Indeed, since we can change temperature and humidity more quickly in the climatic chamber, we can see in Fig. 2.38 the transient response of the sensor, i.e. the time response of the Rogers RO4003C substrate in regard to humidity variations. According to the estimated humidity in the previous subsection, as well as the comparison with the real environment fitting where this time response was not taken into account, we can neglect this effect for this particular substrate. Indeed, fitting the measured frequency to (2.41) using the end of humidity steps only (where the transient time is nearly over), leads to  $\alpha = 4.190 \times 10^{-5} \text{C}^{-1}$  and  $\gamma = 3.710 \times 10^{-5} \% \text{RH}^{-1}$  instead of  $\alpha = 4.165 \times 10^{-5} \text{C}^{-1}$  and  $\gamma = 2.934 \times 10^{-5} \% \text{RH}^{-1}$  when considering the whole response. This measurement correspond to measure n°3 in Table 2.12. For measurements every minute, we can notice that the impact on temperature response time is negligible and the impact on humidity is low confirming the results previously presented.

### Parameters limitations

Unlike temperature dependence of the permittivity, which can often be considered linear for classical materials used for tag fabrication in a range that could be around 0-100 °C, the linearization of humidity dependence in (2.27) is only valid for a limited range of humidity around a specific value. However, to increase this range of definition, it is possible to use a model with more parameters [compared to (2.27)] describing a nonlinear variation of the permittivity with humidity. This model can be based on a polynomial fitting of order 2 or 3 for example.

Furthermore, some materials such as Kapton dielectrics, have been characterized in both humidity and temperature variations [126]. The thermal and humidity dependencies are linear and are valid on 0°C-200°C and 0%RH-100%RH ranges. With similar materials, the linear assumption is valid for the whole 0-100 %RH sensing range. In reality, close to 100 %RH, the presented approach will not work since water droplets will start to form on the surface of the tag. The presence of water will heavily impact the resonance frequency of the resonator due to its high permittivity ( $\epsilon_{\text{water}} \simeq 80$ ). Measurements with different humidity values have been done in order to determine this limitation for the dielectric used in this section (Rogers RO4003C). An example of normalized resonance frequency used to extract the coefficient  $\gamma$  is plotted in Fig. 2.44. The estimated  $\gamma$  for different humidity ranges are presented in Table 2.13. The 25%RH-40%RH range was the one considered during the measurement in a real environment. The last measurement (measurement n°3) was done from 60%RH to 95%RH and divided in sub-domains. Between these measurements, the test-bench was completely

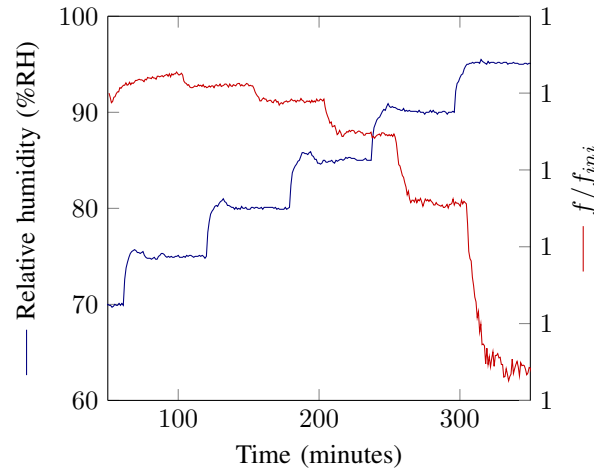


**Figure 2.44:** a) Measured humidity with an electronic sensor in the climatic chamber with a constant temperature of 40°C. b) Normalized resonance frequency  $f/f_{ini}$  for the different humidity values used to extract  $\gamma$ .

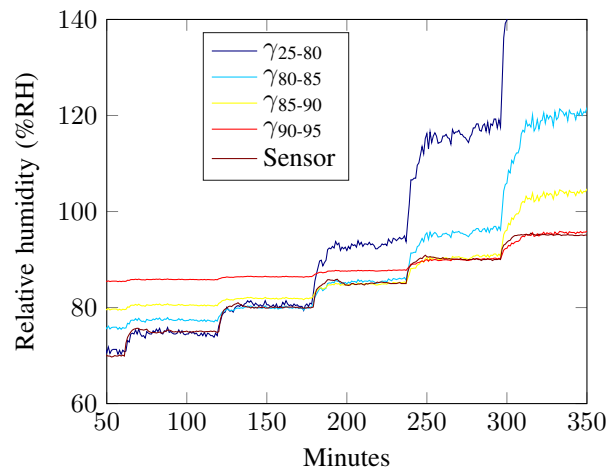


**Figure 2.45:** Extracted humidity using different  $\gamma$  compared with the real humidity measured with a reference sensor (noted sensor in the figure) for a constant temperature of 40°C.

disassembled and put back together. We can see that  $\gamma$  is quite constant for humidity values lower than 75 %RH. For higher values,  $\gamma$  significantly increases with the humidity and the linear model cannot be used to extract the relative humidity on the total humidity range considered here. At 85 %RH, the value of  $\gamma = 2.8 \times 10^{-5} \%RH^{-1}$  does not describe well the humidity dependence of the resonator and so can be considered as a limitation of (2.34) here this linear approximation model is considered on this wide range. In Fig. 2.45 are plotted the extracted humidity values using a value of  $\gamma_{25-80} = 2.8 \times 10^{-5} \%RH^{-1}$ , which corresponds to the 25-80 %RH extraction range and a value of  $\gamma_{90-95} = 33.5 \times 10^{-5} \%RH^{-1}$ , which corresponds to the 90-95 %RH extraction range. We can see that using a constant  $\gamma_{25-80}$  for the linear approximation allows a good extraction until 80 %RH but does not describe well a higher humidity range. At the same time,  $\gamma_{90-95}$  only permits to have the correct value in the 90-95 %RH range with 10 %RH error for a real humidity of 70 %RH.



**Table 2.13:** Fitting coefficient  $\gamma$  of (2.41) for different humidity range.

	Relative humidity range	Estimated $\gamma$ by fitting
Measure n°1	25-40 %	$2.836 \times 10^{-5} \%RH^{-1}$
Measure n°2	60-70 %	$2.926 \times 10^{-5} \%RH^{-1}$
Measure n°3	60-70 %	$2.934 \times 10^{-5} \%RH^{-1}$
Measure n°3	70-75 %	$2.876 \times 10^{-5} \%RH^{-1}$
Measure n°3	75-80 %	$2.808 \times 10^{-5} \%RH^{-1}$
Measure n°3	80-85 %	$7.524 \times 10^{-5} \%RH^{-1}$
Measure n°3	85-90 %	$13.754 \times 10^{-5} \%RH^{-1}$
Measure n°3	90-95 %	$33.5 \times 10^{-5} \%RH^{-1}$

### Monte Carlo simulations

Monte Carlo simulations have been made to estimate the error done on the estimation of the humidity and temperature as well as uncertainties. The RCS curves of Fig. 2.34 have been used with a SNR of 40dB which is a coherent value measured in practice. Resonators were chosen to have  $f_1 = 3\text{GHz}$ ,  $\alpha_1 = 16 \times 10^{-6} \text{C}^{-1}$ ,  $f_2 = 3.2\text{GHz}$ ,  $\alpha_2 = 32 \times 10^{-6} \text{C}^{-1}$  and  $\gamma = 40 \times 10^{-6} \%RH^{-1}$ . Monte-Carlo simulations show no particular behavior which means that the estimation is without bias (not shown here). Errors are quite low with less than  $1^\circ\text{C}$  on the temperature and less than 0.5% on the humidity. Uncertainties are  $2.6^\circ\text{C}$  for temperature and 1.5% for humidity. To increase the temperature and humidity accuracy and sensibility, dielectrics with higher temperature and humidity dependencies (like Kapton [126]) as well as a resonator made of metals with higher dilatation coefficients (like zinc) should be used. By doing so, coefficients  $\alpha_1$  and  $\alpha_2$  in (2.34) will increase, resulting in higher frequency shifts which are easier to measure. Also, by looking at (2.38a) or using (2.38b), one can notice that the temperature and humidity resolution are immediately linked to the frequency steps used for the measurements. Hence having a lower frequency step increases the resolution of the measurands.

Uncertainties on the parameters  $\alpha$  and  $\gamma$  in (2.38a) and (2.38b) can also impact the estimation, so we also studied the errors and uncertainties resulting from an error on these parameters. Results are plotted in Fig. 2.46 and Fig. 2.47. We can see that the errors and uncertainties introduced on the extracted temperature and humidity are higher than the ones coming from an error from the measurement of the resonance frequency. We can also notice a tendency in which the uncertainty increases for the estimated temperature as temperature increases and the uncertainty for the estimated humidity increases when temperature or humidity increase.

It is notable that (2.38a) does not depend on  $\gamma$  and so the error on the estimated temperature only increases as T increases. Meanwhile, (2.38b) does depend on both  $\alpha$  and  $\gamma$  and so the error increases as T or RH increases.

Overall, even with high uncertainty, the sensor functionality remains possible as demonstrated in the measurements. Indeed, a high uncertainty means that the estimated quantities are in an interval of  $\pm 10\%RH$  for humidity as an example for  $\Delta T = 80^\circ\text{C}$  and  $\Delta RH = 80\%$ . But the error stays low for both estimated quantities so on average, the estimated quantities are close to the real quantities. This average is easy to do on a measurement by using the average functionality of the VNA.

It is reminded that the sensitivity of the measurement is directly related to the accuracy of the measuring device. The use of a VNA is perfectly suitable with a high dynamic of measurement and the resolution in frequency essential to implement the introduced approach.

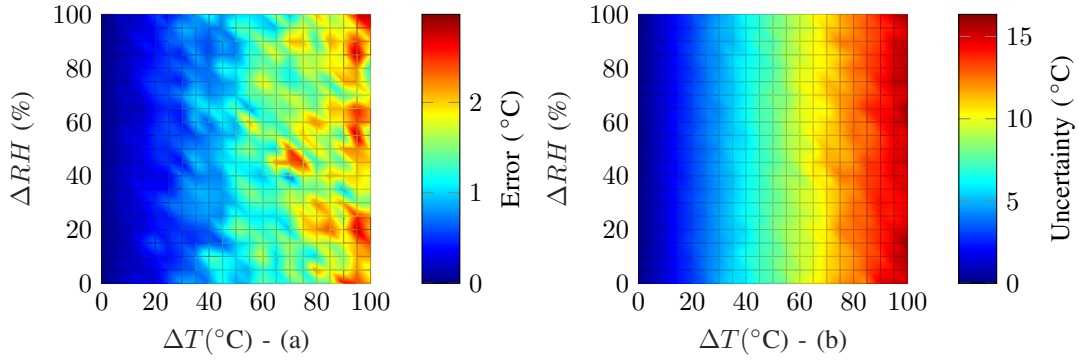


**Figure 2.46:** a) Errors and b) uncertainties on the estimated temperature as a function of real values of temperature and humidity with an uncertainty of 10% on  $\alpha, \gamma$ .

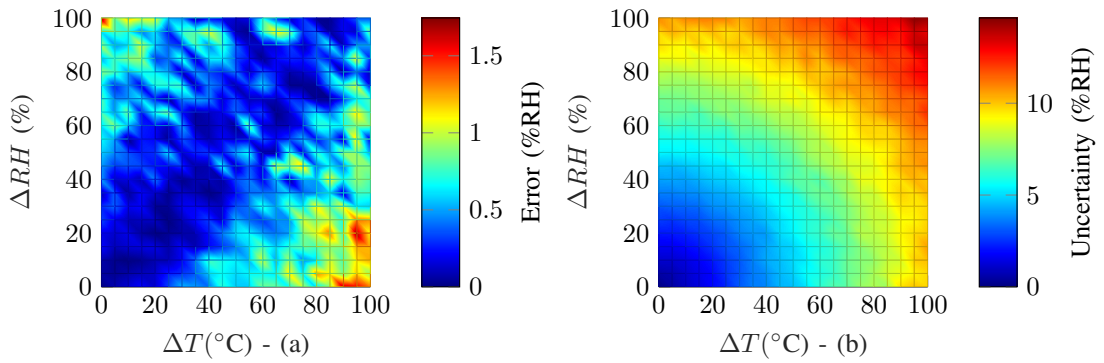


**Figure 2.47:** a) Errors and b) uncertainties on the estimated humidity as a function of real values of temperature and humidity with an uncertainty of 10% on  $\alpha, \gamma$ .

### 2.3.8 Generalization

In real environment, during our measurements, temperature and humidity can both vary and impact the resonance frequency. In a more complex environment, other physical quantities can also impact the resonance frequency. We can imagine having a substrate whose dielectric constant is also sensible to several gases. In this case, the model presented in this section can be generalized to  $n$  parameters using  $n$  resonators with :

$$\begin{pmatrix} \alpha_1 & 1 & 1 & 1 \\ \alpha_2 & 1 & 1 & 1 \\ \alpha_3 & 1 & 1 & 1 \\ \alpha_4 & 1 & 1 & 1 \\ \dots & & & \end{pmatrix} \begin{pmatrix} T \\ \gamma RH + a' \\ \zeta Gas_1 + b' \\ \chi Gas_2 + c' \\ \dots \end{pmatrix} = \begin{pmatrix} 1 - f_1 \frac{2L_1 \sqrt{\epsilon_{eff}}}{c} \\ 1 - f_2 \frac{2L_2 \sqrt{\epsilon_{eff}}}{c} \\ 1 - f_3 \frac{2L_3 \sqrt{\epsilon_{eff}}}{c} \\ 1 - f_4 \frac{2L_4 \sqrt{\epsilon_{eff}}}{c} \\ \dots \end{pmatrix} \quad (2.42)$$

where  $\alpha$ ,  $\sigma$  and  $\gamma$  follow the same equation presented in Section 2.2 for their respective dependencies. The advantage of such an approach is significant in an environment where multiple gases can be present and vary for example. Thus, it is important to consider their contributions to isolate the estimated quantities and remove their interdependency on the resonance frequency which is the only measurand used to make the sensor application.

### 2.3.9 Conclusion of the section

A combined temperature and humidity sensor for RFID chipless applications is described in this section. It is shown that two physical quantities such as temperature and humidity can be extracted independently using only the measurement of resonance frequencies of resonators positioned on a label and interrogated remotely using a radar approach. We also note that these two quantities are obtained simultaneously and that the tags used do not include any specific materials which makes them very accessible. Simulation and real-life measurements are used to validate the sensor model. The linear approach for a Rogers RO4003C substrate was determined to work up to 80%RH with errors of 1°C and 5%RH in the real environment and 1°C and 2%RH in an anechoic climatic chamber. It was demonstrated that there is no hysteresis for Rogers RO4003C substrate.

## 2.4 Conclusion of the chapter

In this second chapter, we linked the resonance frequency of resonators used classically in chipless RFID to physical ambient quantities such as temperature, and humidity. We started by characterizing the thermal dilatation of the metallic part of resonators. This work led to a new type of test bench to measure the CTE of metals offering advantages to the current state-of-art methods. After that, we studied temperature sensing by including the permittivity variation on the resonator's response. This section was focused on temperature sensing but also its real-life application with investigation towards the reading range, and different possible real environment cases, ... Equations were also extended to different resonators with an example of a MS resonator. Lastly, we showed how to incorporate all ambient physical quantities that can be sensed on the length of the resonator or change in permittivity with the example of combined temperature and humidity sensing. This section provides for the first time an analytical equation to rigorously link these quantities to the resonance frequency of a resonator. These not only permit to achieve multi-sensing but also reduce the errors on the estimated quantities (since they all impact the resonance frequency which is the only measurand). These errors were characterized using numerical Monte-Carlo simulations. Finally, this last section enables the characterization of dielectric to numerous physical quantities as it is mostly reserved today for temperature variation using the presented test bench.

This chapter presents some perspectives :

1. In the same way as the CTE testbench was established, a similar protocol can be developed with dielectrics resonators to characterize the dilatation of dielectrics. Indeed, dielectric resonator also exhibit a resonance frequency linked to their geometry hence possibly extending the present approach to non metallic materials.

2. During this thesis, measurements were done to characterized Rogers RO4003C sensitivity to CO<sub>2</sub>. It was measured that 1°C variation had more impact than nearly 100% variation of CO<sub>2</sub> hence this substrate is not appropriate to gas sensing. Various dielectrics can be characterized using the protocol presented in Section 2.3 to find a more suitable dielectric to achieve a proper gas sensor using (2.42).



## Chapter 3

# Loop scattering parameters and RFID sensors

In this chapter, several chipless RFID sensors will be presented. These sensor will not use the value of the resonance frequency to sense physical quantities but rather its amplitude. Indeed, the loop scattering parameters (radiation pattern of the loop resonator as well as its polarization) will permit to develop new approaches. Since the amplitude is less robust to the environment compared to the resonance frequency, each sensor will be studied with Monte-Carlo simulations and with real life measurements to exhibit its working application in real environments. The first section will be dedicated to the modelling of the loop resonator radiation pattern. This radiation pattern will then be used to measure the loop rotation in 3-dimensions. The potential of the radiation pattern to increase of the coding capacity of RFID chipless tags will then be demonstrated. Finally, the polarization of the resonator will be studied to improve its RFID reading robustness.

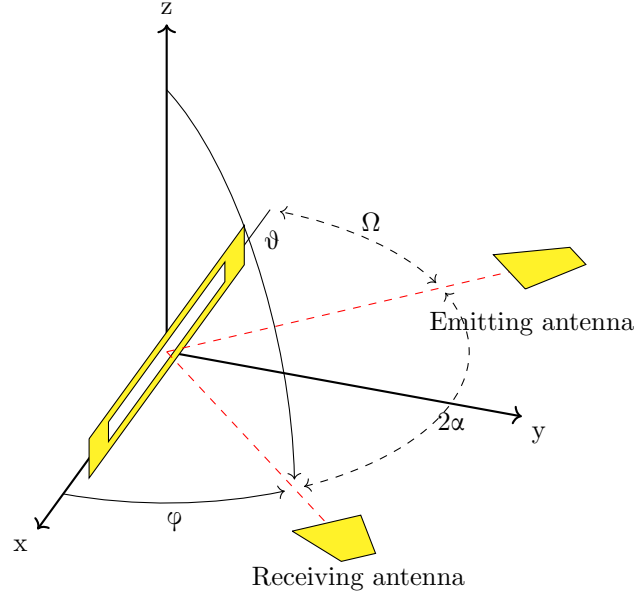
### 3.1 Orientation sensing using loop resonators

In this section, a rectangular loop known to have a high Q-factor [101] is considered [see Fig. 3.1]. A simple model based on array antennas is introduced to model the radiation pattern of this loop resonator. The model is based on the study of the current distribution in the loop resonator allowing one to determine the orientation of the resonator in the 3D space.

The coordinate system used in this chapter is illustrated in Fig. 3.1. Note that the loop is positioned in the  $xOz$  plane. The objective in this section is to estimate the angle  $\varphi$  between the loop and the receiving antenna placed in the  $xOy$  plane when the resonator rotates around the  $z$ -axis (azimuthal angle). Note that the angle  $\Omega$  is defined as the angle between the loop and the emitting antenna. The angle  $\alpha$  is the angle between both antennas. If a mono-static antenna configuration is used then  $\alpha = 0$ . Finally,  $\vartheta$  is the angle between the  $z$ -axis and the direction of propagation of the incident and reflected field (these fields depend on the position of the transmitting and receiving antennas). In other words, it is the inclination (or polar angle) in the spherical coordinate system of reference.

### 3.1.1 Radiation pattern modeling of loop resonators

When impinged by a plane wave along the  $y$  direction, significant currents are induced along the small arms of the loop at the fundamental frequency and harmonics. The approach introduced is based on the use of the first two resonance modes of the loop.



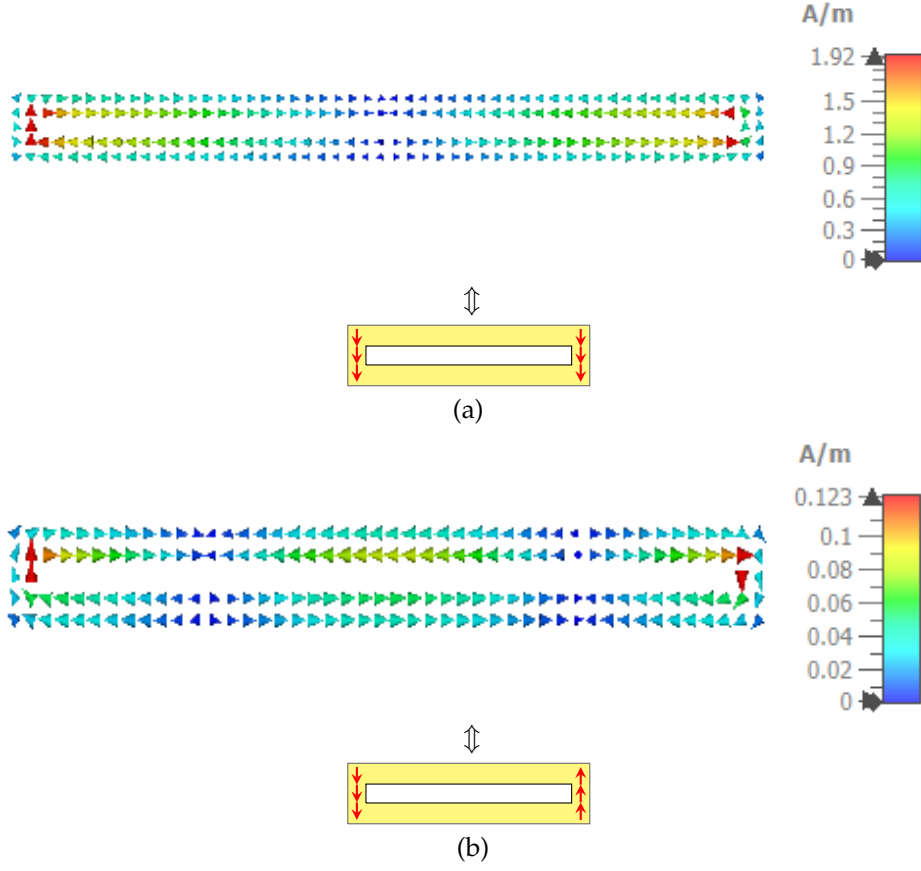
**Figure 3.1:** Loop scatterer, coordinate system and notations. The angle under study  $\varphi$  is between the resonator and the receiving antenna. Emitting and receiving antennas are positioned at the same angle  $\vartheta$  both in monostatic ( $\alpha = 0$ ) and bistatic ( $\alpha \neq 0$ ) configurations.

Fig. 3.2 presents the electromagnetic simulation done using CST MW to illustrate the surface current distribution at resonance on the loop for the fundamental and first harmonic. These currents are in phase at the fundamental frequency and for odd harmonics while they are in opposition of phase for even harmonics. Surface currents are also induced in the top and bottom arms of the loop but they are always in phase opposition. Since the top and bottom arms are close to each others, the radiated field caused by them is nearly cancelled out. For this reason, these currents are not taken into account. As a result, we can model the loop resonator as two small dipoles of length  $L$  and spaced  $\lambda/2$  apart in the  $z$  direction as illustrated in Fig. 3.3.

If we consider the two dipoles with the same current  $I_0$ , the total radiated electric field  $\vec{E}_s$  is the complex summation of the two electric fields radiated by the two dipoles. This quantity  $\vec{E}_s$  can be obtained using the array-factor (AF) from the array-antenna theory knowing the electric field radiated by a single infinitesimal dipole  $\vec{E}_d$  as [25] :

$$\vec{E}_s = \vec{E}_d \times AF = \left( j\eta \frac{kI_0 L e^{-jkr}}{8\pi r} \sin(\vartheta) \vec{e}_\vartheta \right) \times \left( \frac{\sin(kd \sin(\vartheta) \cos(\varphi) + \beta)}{2 \sin(0.5(kd \sin(\vartheta) \cos(\varphi) + \beta))} \right) \quad (3.1)$$

where  $k$  is the wavenumber,  $d$  and  $\beta$  are respectively the distance and the phase difference between the dipoles.  $I_0$  the uniform current flowing through a dipole with length  $L$  and  $r$  is the distance



**Figure 3.2:** Surface current obtained from simulation with a plane wave excitation at (a) the fundamental resonance frequency (even mode) and at (b) second resonance frequency (odd mode).

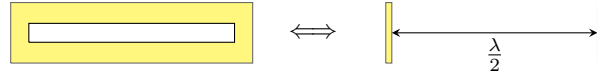


**Figure 3.3:** Equivalent model of the loop resonator. The loop is replaced by two small dipoles spaced  $\lambda/2$  apart with  $\lambda$  taken at the fundamental resonance frequency of the loop  $f_1$ .

between the center of the coordinate system and the observation point of the E-field.

Hereafter, a subscript will indicate the integer  $n$  relative to the resonance mode considered. At the fundamental frequency ( $n = 1$ ), we have  $kd = n \frac{2\pi}{\lambda} \cdot \frac{\lambda}{2} = \pi$  and  $\beta = 0$ . The total radiating field  $E_s(f_1)$  amplitude ( $\vec{E}_s$  is along the z-axis) is :

$$E_s(f_1) = E_d \times AF_1 = k_1 T_1 \sin(\vartheta) \frac{\sin(\pi \sin(\vartheta) \cos(\varphi))}{\sin\left(\frac{\pi}{2} \sin(\vartheta) \cos(\varphi)\right)} \quad (3.2)$$

where

$$T_1 = \frac{\eta I_1 L}{16\pi r} e^{-jkr} \quad (3.3)$$



Using the same procedure, for the first harmonic ( $n = 2$ ), we have  $kd = n \cdot \frac{2\pi}{\lambda} \cdot \frac{\lambda}{2} = 2\pi$  and since it's an odd harmonic  $\beta = \pi$  [see Fig. 3.2]. The total radiated field amplitude  $E_s(f_2)$  at the first harmonic can be written :

$$\begin{aligned} E_s(f_2) &= E_d \times AF_2 \\ &= k_2 T_2 \sin(\vartheta) \frac{\sin(2\pi \sin(\vartheta) \cos(\varphi) + \pi)}{\sin(\pi \sin(\vartheta) \cos(\varphi) + \frac{\pi}{2})} \\ &= 2k_2 T_2 \sin(\vartheta) \sin(\pi \sin(\vartheta) \cos(\varphi)) \end{aligned} \quad (3.4)$$

where

$$T_2 = \frac{\eta I_2 L}{16\pi r} e^{-jkr} \quad (3.5)$$

The expressions of the total fields  $|E_s(f_n)|$  are compared with the ones retrieved from a CST MW simulation in Fig. 3.4 and Fig. 3.5. In CST simulations, the loop is excited by an incoming plane wave with linear polarization (the wave propagates in the direction of the resonator and the electric field is along the z-axis) and the scattered E-fields have been normalized for the comparison. In Fig. 3.4, the simulated radiation pattern of the loop at the second harmonic in the plane  $\varphi = \pi/2$  is plotted and compared to the analytical model. In Fig. 3.5, the radiation pattern of the loop for different harmonics in the plane  $\vartheta = \pi/2$  is plotted for both CST simulation and analytical model. We can see that the simulated radiation pattern of the loop and the one obtained with the introduced equivalent model are in good agreement. Note that contrary to the model, the full wave simulation used for the comparison takes into account all EM effect, such as coupling. However, since the results are almost identical, the analytical model can be used.

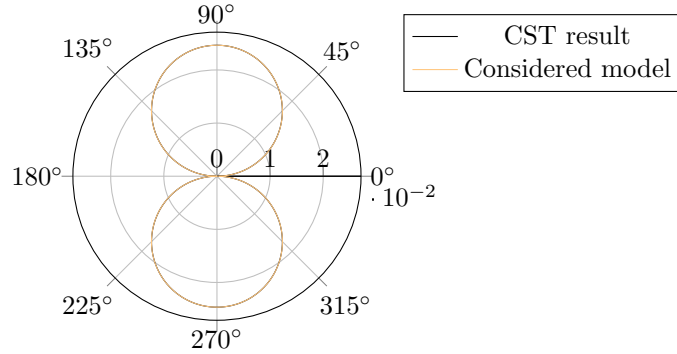


**Figure 3.4:** Magnitude of the E-field (V/m) radiated by the loop with  $\varphi = \pi/2$  and  $\vartheta \in [0^\circ; 360^\circ]$  at the second harmonic ( $n = 3$ ). The wave propagates in the direction of the resonator and the electric field is along the z-axis.

### 3.1.2 Back-scattering expressions

We are now interested in the expression of the induced current on the loop in order to be able to compute  $T_1$  and  $T_2$ . The classical electrical equivalent model of a dipole in the receiving mode is shown Fig. 3.6.

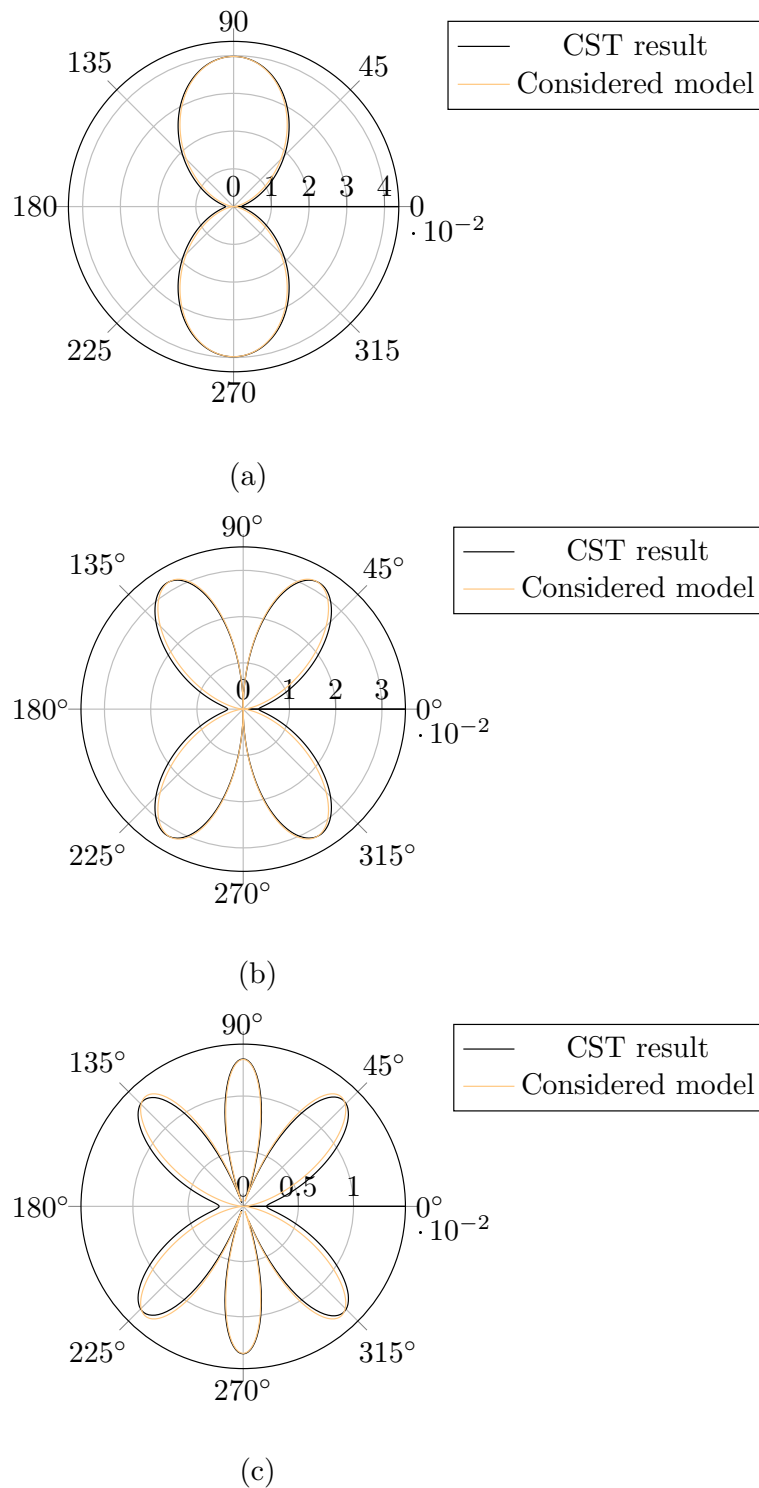


**Figure 3.5:** Magnitude of the E-field (V/m) radiated by the loop with  $\vartheta = \pi/2$  and  $\varphi \in [0^\circ; 360^\circ]$  at (a) the fundamental frequency, (b) the first harmonic and (c) the second harmonic. In black the CST simulation and in yellow the expressions obtained from the loop model. The wave propagates in the direction of the resonator and the electric field is along the z-axis.

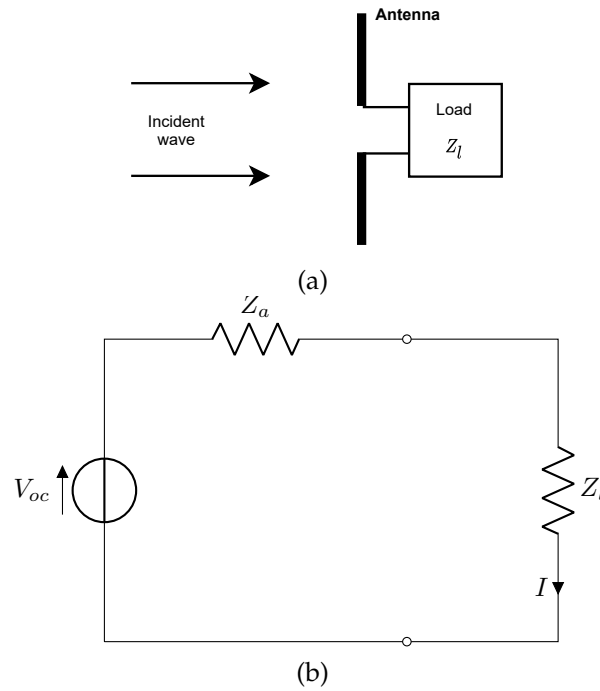


**Figure 3.6:** (a) Antenna in the receiving mode and (b) its electrical equivalent model where  $Z_a$  is the antenna impedance,  $Z_l$  the load impedance and  $V_{oc}$  the open circuit voltage appearing across the antenna's terminals.

The effective length of a dipole antenna is defined by [127] :

$$L_{eff} = V_{oc}/E_i \quad (3.6)$$

where  $V_{oc}$  is the open circuit voltage appearing across the antenna's terminal and  $E_i$  is the incident electric field on the antenna surface. Therefore, the current on the dipole  $I$  is :

$$I = \frac{V_{oc}}{Z_a + Z_l} = \frac{V_{oc}}{Z_a} = \frac{E_i \times L_{eff}}{Z_a} \quad (3.7)$$

where  $Z_a$  is the antenna impedance and  $Z_l$  the load impedance which is considered to be equal to zero as the dipole is in short circuit. It should be noted that the effective length is also a far-field quantity and it is related to the far-zone field  $E_a$  radiated by the antenna, with current  $I$  in its terminals, by :

$$E_a = -j\eta \frac{kI}{4\pi r} L_{eff} e^{-jkr} \quad (3.8)$$

After identification with (3.2) and (3.8) considering the same current on the dipole and the same frequency, we have :

$$L_{eff-n} = \frac{L}{2} \sin(\vartheta) \times AF_n \quad (3.9)$$

Thereafter, the ratio  $T_2/T_1$  can be expressed using (3.7) and (3.9) as :

$$\frac{T_2}{T_1} = \frac{I_2}{I_1} = \frac{L_{\text{eff-2}} \times Z_a(f_1)}{L_{\text{eff-1}} \times Z_a(f_2)} = \frac{Z_a(f_1) AF_2(\Omega)}{Z_a(f_2) AF_1(\Omega)} \quad (3.10)$$

Since we are consider the received power, the angle that needs to be used in the array factor is  $\Omega$ , i.e. the angle between the resonator and the emitting antenna. The value of  $\Omega$  can be calculated using Fig. 3.1 and is equal to :

$$\Omega = \pi - \alpha - \varphi \quad (3.11)$$

The expression of the impedance  $Z_a$  of the antenna to be considered corresponds to the half-loop, i.e. the vertical part (of length  $L$ , modeled until now by an infinitesimal dipole) as well as the two horizontal bars, each of length  $d/2$ . Although these horizontal parts do not participate in the radiation, they are at the origin of the imaginary part of the antenna impedance  $Z_a$ . However, at the resonant frequency of the loop, this imaginary part is zero. Therefore, for the rest of the demonstration, only the real part of  $Z_a$  was considered. The latter is obtained by considering, as before, that the radiation of the antenna is linked to the vertical part of the loop modeled by an infinitesimal dipole and its expression is given by [127, p. 179] :

$$R_a = 80\pi^2 \left( \frac{L}{\lambda} \right)^2 \quad (3.12)$$

Thus, the coefficient  $\frac{Z_a(f_1)}{Z_a(f_2)}$  is a constant that is equal to :

$$\frac{Z_a(f_1)}{Z_a(f_2)} = \left( \frac{\lambda_2}{\lambda_1} \right)^2 = \frac{1}{4} \quad (3.13)$$

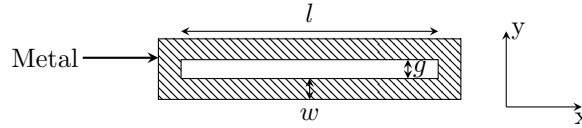


**Figure 3.7:** Loop resonator used for the orientation extraction. Dimensions :  $d = 47.97$  mm,  $g=2.07$  mm and  $w=1.43$  mm. The resonance frequency for this dimension is 3GHz.

Equation (3.10) can be compared to full-wave simulation results. Using CST MW, the maximum value of the electric-field is measured under different incidence angles  $\Omega$  of the emitting antenna with the loop resonator with the same dimensions as the ones given in the legend of Fig. 3.7. The results are plotted in Fig. 3.8. We can observe that the model and the simulation are in good agreement which validates the model.

### 3.1.3 Orientation Sensing

For orientation sensing, most of the studies have been focused on the detection of the tag's rotation in the plane perpendicular to the propagation vector using co-polarization [128, 129] or cross-polarization [130, 131, 132, 133] measurements. All these methods permit to determine the orientation

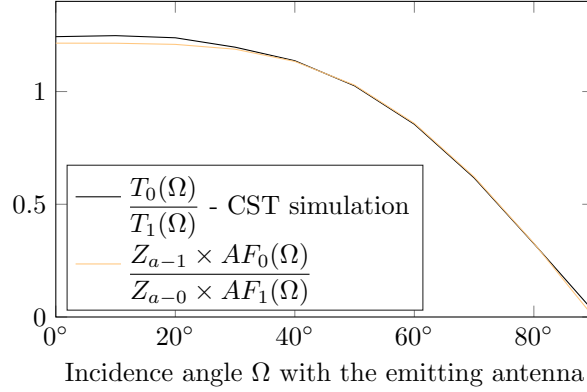


**Figure 3.8:** Comparison between  $T_1(\Omega)/T_2(\Omega)$  extracted from CST simulation and (3.10).

of the chipless tag from the magnitude of the received signal and are often based on a reference measurement which has to be done at the same distance and in a known orientation. It can also be noted that it is possible with a radar approach to detect yaw and pitch change with the help of a dedicated designed transponder [134].

In this section, a novel approach is introduced to determine the roll orientation of a loop resonator tag, i.e. its inclination and azimuthal angles when considering a spherical coordinate system. This approach is based on an analytical model of the radiation pattern of the loop resonator and is significantly different from the EM polarization based methods described in the literature. The proposed approach is derived to be independent from the reading distance, the loop tag geometry and does not depend on a reference measurement.

### Azimuthal angle determination

From (3.2), (3.4), (3.10) and (3.13), it is possible to measure the azimuthal angle  $\varphi$ , i.e. the rotation of the loop resonator around the z-axis ( $\varphi$ ) as shown in Fig. 3.1. By dividing (3.2) and (3.4), we have :

$$\frac{E_s(f_2)}{E_s(f_1)} = 2 \frac{k_2}{k_1} \frac{T_2(\Omega)}{T_1(\Omega)} \sin\left(\frac{\pi}{2} \sin(\vartheta) \cos(\varphi)\right) \quad (3.14)$$

Finally, by replacing (3.10) and (3.13) :

$$\begin{aligned} \frac{E_s(f_2)}{E_s(f_1)} &= 4 \frac{k_2}{k_1} \frac{Z_a(f_1)}{Z_a(f_2)} \sin\left(\frac{\pi}{2} \sin(\vartheta) \cos(\varphi)\right) \times \sin\left(\frac{\pi}{2} \sin(\vartheta) \cos(\Omega)\right) \\ &= 2 \sin\left(\frac{\pi}{2} \sin(\vartheta) \cos(\varphi)\right) \times \sin\left(\frac{\pi}{2} \sin(\vartheta) \cos(\pi - \alpha - \varphi)\right) \end{aligned} \quad (3.15)$$

Equation (3.15) is particularly interesting as it is independent of the geometric quantities describing the resonator or the distance  $r$  between the scatterer and the antennas. It is thus possible to use this equation to derive the angles without any calibration step or knowledge on the distance  $r$ , which is very different from the angle measurement approaches already introduced in chipless RFID. In practice, by using a VNA, we will only be able to measure S-parameters. With the radar equation, the incoming power  $P_y$  on the port  $y$  of the VNA and the emitted power  $P_x$  on the port  $x$  and the

definition of S-parameters, we have:

$$|S_{xy}|^2 = \left| \frac{P_y}{P_x} \right| = \frac{G_t(\vartheta, \varphi) G_t(\vartheta, \Omega) G G' \lambda^4}{(4\pi)^4 R_0^2 R_1^2} \times (1 - |\Gamma|^2) \times (1 - |\Gamma'|^2) \quad (3.16)$$

where  $G$  and  $G'$  are the gain of the emitting and receiving antennas respectively,  $R_0$  and  $R_1$  the distances between the emitting and receiving antennas with the resonator,  $\Gamma$  and  $\Gamma'$  the reflection coefficients respectively for emitting and receiving antenna.  $S_{xy}$  can correspond to a mono-static configuration with  $S_{11}$  or  $S_{22}$  or to a bi-static configuration with  $S_{21}$  or  $S_{12}$ .  $G_t$  is the gain of the resonator. In case of the loop resonator with the model previously presented, it is possible to analytically calculate its gain with [127, p. 155] :

$$G_t = 4\pi \frac{\frac{r^2}{2\eta} |E|^2}{\int_0^{2\pi} \int_0^\pi \frac{r^2}{2\eta} |E|^2 \sin(\vartheta) d\vartheta d\varphi} \quad (3.17)$$

where  $\eta$  is the intrinsic impedance of the medium and the radiated E-field  $E$  can be computed using (3.2) or (3.4) for example. We have :

$$G_t(\vartheta, \varphi, f_i) = a(i) \times \sin(\vartheta)^2 \times AF_i(\vartheta, \varphi)^2 \quad (3.18)$$

where we can calculate for the first two resonances using (3.17) :

$$a(i) \simeq \begin{cases} \frac{4\pi}{14.20'} & \text{for } i = 0 \\ \frac{4\pi}{16.47'} & \text{for } i = 1 \end{cases} \quad (3.19a)$$

$$(3.19b)$$

By dividing (3.16) for the first two harmonics ( $f_1$  and  $f_2$ ), we obtain (3.20) which is an equivalent relation to (3.15) using S-parameters.

$$\begin{aligned} \left| \frac{S_{xy}(f_2)}{S_{xy}(f_1)} \right| &= 0.86 \times \sqrt{\frac{G(f_2)G'(f_2)}{G(f_1)G'(f_1)}} \times \sqrt{\frac{1 - |\Gamma(f_2)|^2}{1 - |\Gamma(f_1)|^2}} \times \sqrt{\frac{1 - |\Gamma'(f_2)|^2}{1 - |\Gamma'(f_1)|^2}} \\ &\times \sin\left(\frac{\pi}{2} \sin(\vartheta) \cos(\varphi)\right) \times \sin\left(\frac{\pi}{2} \sin(\vartheta) \cos(\pi - \alpha - \varphi)\right) \end{aligned} \quad (3.20)$$

In our case, QH2000 antennas are used in practice with the antenna gain and matching  $\Gamma$  provided by the manufacturer [135]. So, (3.20) and (3.15) can be translated into S-parameters to :

$$\left| \frac{S_{xy}(f_2)}{S_{xy}(f_1)} \right| = 2.42 \sin\left(\frac{\pi}{2} \sin(\vartheta) \cos(\varphi)\right) \times \sin\left(\frac{\pi}{2} \sin(\vartheta) \cos(\pi - \alpha - \varphi)\right) \quad (3.21)$$

### 3.1.4 Uncertainty

A Monte-Carlo simulation was done in order to estimate the robustness of the proposed method and explain behaviors exhibit in simulation/measurements. Both mono-static and bi-static configurations

have been studied. Simulation results are plotted in Fig. 3.9. The true angle  $\varphi$  varies from  $0^\circ$  to  $90^\circ$  and the estimated angle  $\hat{\varphi}$  is extracted with an SNR of 40 dB which corresponds to the classical noise observed in measurement.

To achieve such results, first CST simulations have been realized for different angle values (from  $0^\circ$  to  $90^\circ$  as shown in Table 3.2). The corresponding S-parameters have been then exported to Matlab. A white gaussian noise with a standard deviation corresponding to a SNR of 40 dB has been added to both real and imaginary parts of the 10.000 S-parameter points. Then (3.23) or (3.26b) has been applied to the S-parameters with noise and the uncertainty information have been extracted from the obtained estimated angles using Matlab dedicated functions. When measurements are corrupted by noise, this noise impacts the estimators by two different ways: a bias, which is a systematic error between the estimated value and the true orientation of the tag (characterized by the mean of the estimator); and a random error, which can be characterized by its standard deviation. With this method, both the errors and the uncertainties are presented in the manuscript.

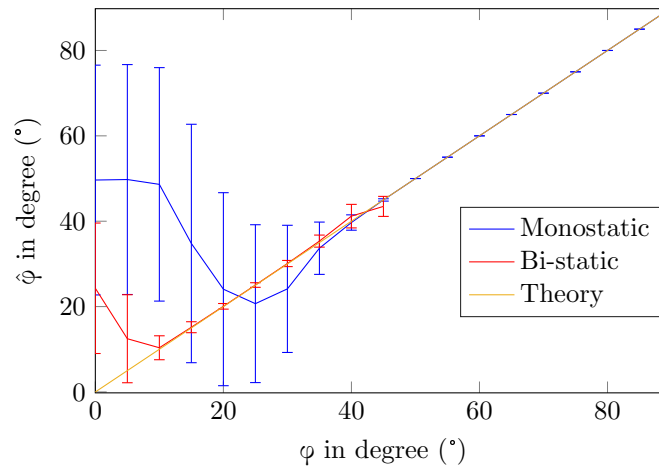


**Figure 3.9:** Monte-Carlo simulation : the uncertainty of the extracted angle  $\hat{\varphi}$  as a function of the real angle  $\varphi$  is plotted for both configurations. The bi-static configuration uses a value of  $\alpha = 45^\circ$ . Vertical bars represent the standard derivation on  $\hat{\varphi}$ . The considered SNR is 40dB.

We can see with this simulation that the bi-static is more robust than the mono-static configuration. Also, we can notice that for low  $\varphi$  angle values, the mono-static approach has high uncertainties below  $40^\circ$  and cannot be used for  $\varphi$  angles below  $15^\circ$  with an error lower than  $< 7^\circ$ . Indeed, the instantaneous estimation in mono-static for a value of  $\varphi$  between  $15^\circ$  and  $40^\circ$  can have an error of  $15^\circ$  but on average, the error is very low beyond an angle of  $15^\circ$ . Note that common VNAs natively implement average functionalities allowing to use this approach as low as  $15^\circ$  for the mono-static case for this given SNR. These remarks will be further illustrated in the measurement part. In the Monte-Carlo simulation [see Fig. 3.9], the residual environment is modeled by additive gaussian noise and considering that the variance is a function of the distance.

This simulation can be used to maximize the correctness of the sensor in bi-static configuration where an optimal setup can be obtained when  $\alpha = 54^\circ$ .

Mono-static and bi-static approaches have been studied because they both bring their own advantages and disadvantages and the model described previously can be used to characterize the performance of both approaches. The cost of a mono-static measurement is lower since only one antenna is required compared to a bi-static approach. Additionally, a mono-static measurement gives one solution of  $\varphi$  while the bi-static gives two solutions due to the periodicity of (3.15) as a function of  $\alpha$ . Furthermore, the bi-static introduces errors in practice because the angle  $\alpha$  need to be determined while this parameter does not exist for the mono-static configuration. Besides these disadvantages, the bi-static offers advantages like a higher precision on the extracted angle, a lower uncertainty and the possibility to sense very low angles. Last but not least, a setup with two antennas can be used to take advantage of both configurations. Starting by measuring  $S_{11}$  (mono-static approach) only one solution will be found. After that, a  $S_{21}$  measurement (bi-static approach) can be done to extract the angle with a higher precision and lower uncertainty. Two solutions will be found with the periodicity of (3.15) but the correct one can be found since it will be the closest to the one measured with  $S_{11}$ . A comparison between both mono-static and bi-static antenna configurations is provided in Table 3.1.

**Table 3.1:** Comparison of mono-static and bi-static configurations

	Mono-static	Bi-static
Cost	Lower cost (1 antenna)	Higher cost (2 antennas)
Uncertainties	Higher	Lower
Precision	Lower	Higher
Theoretical number of solution ( $\varphi \in [0^\circ-90^\circ]$ )	1	2
Theoretical lowest measurable angle with SNR 20dB and $< 7^\circ$ error	$15^\circ$	$5^\circ$

### 3.1.5 Simulations

Simulations have been carried out using CST MW to validate the introduced approach to estimate the orientation  $\varphi$  of a loop. The transient solver with a plane wave excitation was used. So the azimuthal angle  $\varphi$  is extracted using (3.15), and the backscattered E-field  $E_s$  is obtained using far-fields probes in the simulator. The loop dimensions also used in the measurement part are given in Fig. 3.7. Results are given in Table 3.2 and Table 3.3. We see that the estimated angle  $\hat{\varphi}$  is in good agreement with the simulated angle  $\varphi$ . Both mono and bi-static antenna configurations were simulated and validated, allowing thus the possibility to use the desired one as a final application. A noticeable point is the obtained measurable range : in bi-static the estimated angle is accurate down to  $0^\circ$ , but for the mono-static configuration the estimated angle cannot go lower than  $30^\circ$  limiting the measurable range to  $[30^\circ; 90^\circ]$ . The reason behind this limitation has been discussed and is illustrated in Fig. 3.10. In the mono-static case, when the incidence angle  $\varphi$  is small, antenna aperture of the loop is small both for the wave reaching the loop and for the wave backscattered to the antenna. This case is different in bi-static, where it is clear that the receiving antenna is positioned in a favorable direction, namely at the main lobe of the loop antenna. It is for this reason that in a mono-static configuration below  $30^\circ$ , the estimated angle is constant because the backscattered E-field is equal to the noise floor. Notice



that the higher uncertainty and error of the mono-static approach are predicted by the Monte-Carlo simulation [see Fig. 3.9].

**Table 3.2:** Simulation (CST) in mono-static ( $\alpha = 0^\circ$ )

$\varphi$	$0^\circ$	$10^\circ$	$20^\circ$	$30^\circ$	$40^\circ$	$50^\circ$	$60^\circ$	$70^\circ$	$80^\circ$	$90^\circ$
$\hat{\varphi}$	$28^\circ$	$26^\circ$	$21^\circ$	$27^\circ$	$40^\circ$	$51^\circ$	$61^\circ$	$70^\circ$	$80^\circ$	$88^\circ$

**Table 3.3:** Simulation (CST) in bi-static ( $\alpha = 90^\circ$ )

$\varphi$	$0^\circ$	$10^\circ$	$20^\circ$	$30^\circ$	$40^\circ$	$50^\circ$	$60^\circ$	$70^\circ$	$80^\circ$	$90^\circ$
$\hat{\varphi}$	$0^\circ$	$11^\circ$	$20^\circ$	$30^\circ$	$40^\circ$	$50^\circ$	$56^\circ$	$70^\circ$	$80^\circ$	$90^\circ$

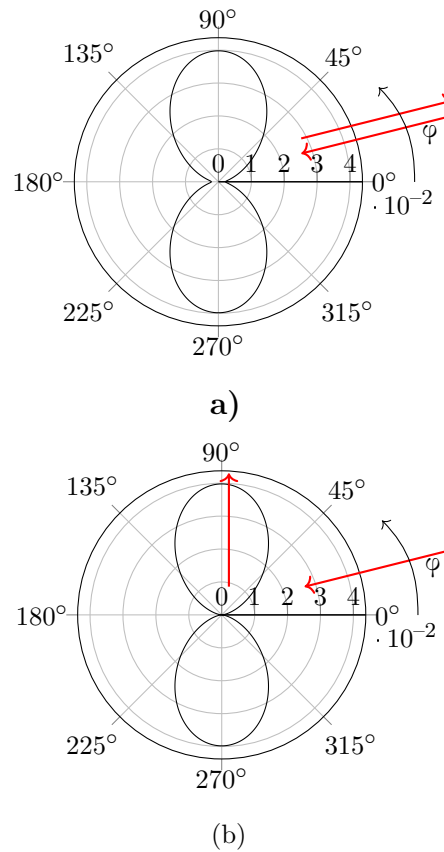


**Figure 3.10:** (a) Path followed by the electromagnetic wave when the incidence  $\varphi$  is small in a mono-static case and (b) in a bi-static case.

To improve the measurable range and precision, we can use a bi-static configuration or even higher harmonics. Indeed, by looking at the radiation pattern of the second harmonic in Fig. 3.5c, we can see that we have a maximum of power around  $45^\circ$  allowing thus a higher back-scattering power for small values of  $\varphi$ . Indeed, this second harmonic  $E_s(f_2)$  for example, can be used instead of the first

harmonic in (3.15) with the following equation to extend the measuring range :

$$\frac{E_s(f_3)}{E_s(f_1)} = \frac{1}{3} (2 \cos(\pi \cos(\varphi)) - 1) \times (2 \cos(\pi \cos(\Omega)) - 1) \quad (3.22)$$

### 3.1.6 Measurements

Now that the extraction of the loop orientation is validated in simulation, real measurements are considered both in mono and bi-static configuration. Measurements for the mono-static configuration were done following the test bench shown in Fig. 3.11. For the bi-static configuration, the same setup is used but with a second antenna placed at  $\alpha = 90^\circ$  from the first one. The tag is placed on top of a rotating pillar (about 15 cm away using a piece of foam to isolate the loop from the pillar which is very reflective). The protocol used for the measurement is the following : the S-parameters are measured using the VNA (Keysight P9375A) for the tag being rotated from  $5^\circ$  to  $90^\circ$  in relation to the antenna with a  $5^\circ$  step (the antenna is perpendicular to the loop for  $\varphi = 90^\circ$  as described in Fig. 3.1). If we place the antenna at  $\vartheta = 90^\circ$ , (3.21) can be simplified to:

$$\left| \frac{S_{xy}(f_2)}{S_{xy}(f_1)} \right| = 2.42 \sin\left(\frac{\pi}{2} \cos(\varphi)\right) \times \sin\left(\frac{\pi}{2} \cos(\pi - \alpha - \varphi)\right) \quad (3.23)$$

For each angle, (3.23) is used to determine  $\hat{\varphi}$ . A first measurement without the resonator is subtracted to the other measurements (with the resonator) to remove the response of the environment [45, 72, 136]. Raw measurements directly measured with the VNA are used without any post-processing.

#### Mono-static configuration

The mono-static configuration offers several advantages, such as the fact that it is easier to implement as presented in Table 3.1. For these reasons, the mono-static configuration (case  $\alpha = 0^\circ$ ) is first considered. Measurements were done following the test bench described in Fig. 3.11 and the results are given in Fig. 3.12. The resonator is 20 cm away from the antenna.

The obtained results are in good agreement with those previously described in the simulation : the mono-static configuration can be used with a very good accuracy for angles higher than  $40^\circ$ . Indeed, in the simulation, the limit angle was equal to  $30^\circ$ , in practice due to a higher noise floor, this angle is near  $40^\circ$ . Overall, the estimated angle is in good agreement with the real angle validating the potential of this approach. In the range  $40^\circ$ - $90^\circ$ , the maximum error measured is  $2.6^\circ$  when the real angle is equal to  $55^\circ$ . Below a real angle of  $40^\circ$ , measured errors are getting higher with almost  $10^\circ$  for a real angle of  $\varphi = 30^\circ$  as predicted by Monte Carlo simulations. Below  $30^\circ$ , errors were too high to extract any angle.

#### Bi-static configuration

Fig. 3.13 presents the estimated angle  $\hat{\varphi}$  alongside the real angle  $\varphi$  with a bi-static configuration. We can see that the extracted angle  $\hat{\varphi}$  is in good agreement with the real value  $\varphi$ . The highest error is

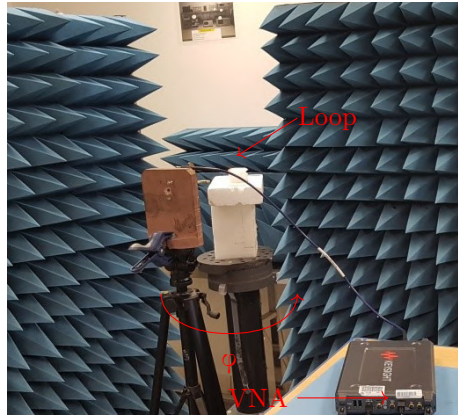


**Figure 3.11:** Setup used for the extraction of  $\varphi$  - mono-static configuration ( $\alpha = 0^\circ$ ).

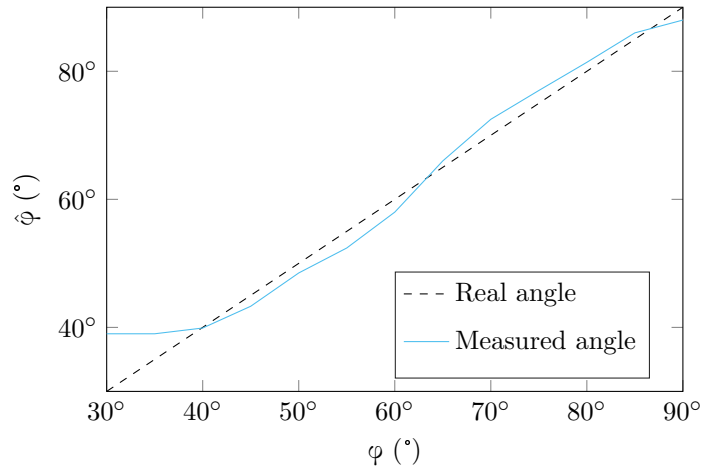


**Figure 3.12:** Measurement in mono-static configuration ( $\alpha = 0^\circ$ ). The estimated angle  $\hat{\varphi}$  is plotted as a function of the real angle  $\varphi$ .

obtained at  $50^\circ$  with a difference of  $5^\circ$ . As the Monte-Carlo showed, the measured quantities are in very good agreement with the real angle with value as low as  $\varphi = 10^\circ$ .

### 3.1.7 Generalization of the approach

Before, we have considered  $\vartheta = 90^\circ$  but the proposed model is more general and allows the estimation of both the inclination  $\vartheta$  and the azimuthal  $\varphi$  angles. If we consider a configuration with two antennas where both antennas have the same inclination  $\vartheta$  (as illustrated in Fig. 3.1), with (3.21), we can have by measuring  $S_{11}$  :

$$\frac{S_{11}(f_2)}{S_{11}(f_1)} = 2.42 \sin\left(\frac{\pi}{2} \sin(\vartheta) \cos(\varphi)\right)^2 \quad (3.24)$$

By using the  $S_{22}$  parameter, we can also have :

$$\frac{S_{22}(f_2)}{S_{22}(f_1)} = 2.42 \sin\left(\frac{\pi}{2} \sin(\pi - \alpha - \vartheta) \cos(\varphi)\right)^2 \quad (3.25)$$

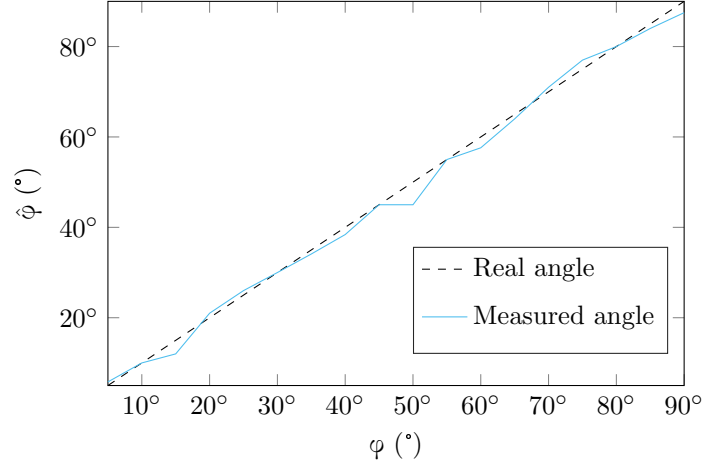


**Figure 3.13:** Measurement in bi-static configuration with  $\alpha = 90^\circ$ . The estimated angle  $\hat{\varphi}$  is plotted as a function of the real angle  $\varphi$ .

Thus, by solving the system of equations composed of (3.24) and (3.25), the following equations can be obtained :

$$\left\{ \begin{array}{l} \varphi = \arccos \left( \frac{1}{\sin(\vartheta)} \frac{2}{\pi} \arcsin \left( \sqrt{\frac{S_{11}(f_2)}{2.42S_{11}(f_1)}}} \right) \right) \\ \vartheta = \cot^{-1} \left( \csc(\alpha) \left[ \frac{\arcsin \left( \sqrt{\frac{S_{22}(f_2)}{2.42S_{22}(f_1)}}} \right)}{\arcsin \left( \sqrt{\frac{S_{11}(f_2)}{2.42S_{11}(f_1)}}} \right)} - \cos(\alpha) \right] \right) \end{array} \right. \quad (3.26a)$$

$$(3.26b)$$

Note that (3.26b) can be used to estimate  $\vartheta$ . After that,  $\hat{\vartheta}$  can be injected in (3.26a) to estimate  $\varphi$ . Note also that  $S_{21}$  parameter means signal coming from antenna 2 to antenna 1 but both antennas share the same polarization axis (along the resonator arms).

### Simulations

Simulations have been done in order to validate this approach. The simulated configuration is the same as previously but now, both  $\vartheta$  and  $\varphi$  can change simultaneously and (3.26a) is applied on the simulated results. Results are plotted in Table 3.4. We can see that extracted quantities are in good agreement with the expected ones. Errors increase as angles values decrease with a maximum error of  $8^\circ$  on  $\hat{\varphi}$  at  $\varphi = 60^\circ$  and  $\vartheta = 50^\circ$ .

### Measurements

A semi anechoic environment (MVG StarLab) has been used to validate the determination of both  $\vartheta$  and  $\varphi$  in measurement. The setup is illustrated in Fig. 3.14. The loop resonator is horizontally placed on top of the central pillar. The pillar can rotate along its axis resulting a variation of the angle

**Table 3.4:** Estimated angles ( $^{\circ}$ ) of the emitting antenna using (3.26a) in simulation for (a)  $\vartheta$  and (b)  $\varphi$  in simulation.

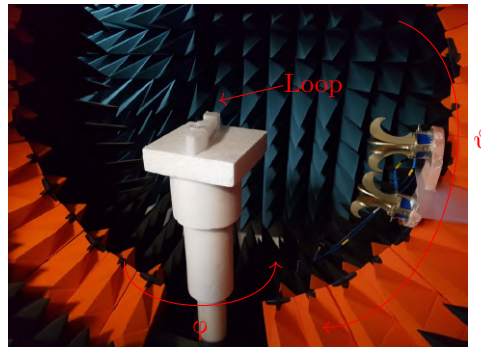
$\vartheta \backslash \varphi$	80	70	60
90	90	90	90
80	79	79	80
70	69	71	68
60	59	57	56
50	52	45	53

(a)

$\vartheta \backslash \varphi$	80	70	60
90	80	70	60
80	80	70	60
70	80	68	59
60	79	68	57
50	79	66	52

(b)

$\varphi$  between the loop and the antennas. Also, the orange arch can rotate resulting in a variation of the angle  $\vartheta$  of the tag with the antennas. Due to the StarLab configuration, the measuring range is limited to  $60^{\circ} < \varphi < 80^{\circ}$  with a step of  $10^{\circ}$  and  $60^{\circ} < \vartheta < 70^{\circ}$  with a step of  $3^{\circ}$ . An averaging on 36 samples on the VNA is used to lower the noise floor. The resonator is placed 45 cm away from the antenna. The angle  $\alpha$  is equal to  $30^{\circ}$ . An example of measured S-parameters is presented in Fig. 3.15. Equation (3.26a) is used and results are plotted in Table 3.5. The angle  $\hat{\varphi}$  is well estimated with a maximum error of  $4^{\circ}$  for  $\varphi = 60^{\circ}$  and  $1.5^{\circ}$  on average. The angle  $\hat{\vartheta}$  is estimated with higher errors and a maximum error of  $9^{\circ}$  ( $2.8^{\circ}$  on average).

**Figure 3.14:** Measurement setup in semi anechoic environment to determine the orientation of the antenna (extraction of  $\vartheta$  and  $\varphi$ ). The angle  $\alpha = 30^{\circ}$ .**Table 3.5:** Estimated angles ( $^{\circ}$ ) of the emitting antenna using (3.26a) in practice for (a)  $\vartheta$  and (b)  $\varphi$  in practice.

$\vartheta \backslash \varphi$	80	70	60
60	57	62	56
63	63	52	52
66	64	66	64
70	74	79	69

(a)

$\vartheta \backslash \varphi$	80	70	60
60	78	68	56
63	79	69	58
66	78	69	59
70	78	68	56

(b)

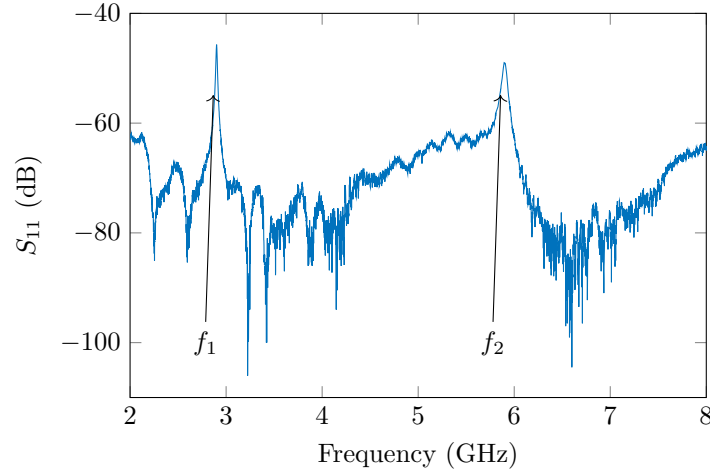


**Figure 3.15:** Measured S-parameters where the empty measurement has been subtracted for a value of  $\varphi = 70^\circ$  and  $\vartheta = 84^\circ$  in the Starlab for a distance resonator-antenna of 45cm.

### Monte-Carlo simulations

Monte Carlo simulations have been done on (3.26a) and (3.26b) in order to estimate errors and uncertainties on the extracted quantities  $\hat{\varphi}$  and  $\hat{\vartheta}$  and results are plotted in Fig. 3.16 and Fig. 3.17 for  $\hat{\varphi}$  and  $\hat{\vartheta}$  respectively. We can see that for  $\hat{\varphi}$ , errors and uncertainties are quite low except when  $\vartheta > 60^\circ$  and  $\varphi < 20^\circ$ . Elsewhere, the errors are below  $1^\circ$  and uncertainties are below  $1^\circ$  when  $\varphi > 40^\circ$  but increase up to  $15^\circ$  for  $20^\circ < \varphi < 40^\circ$ . For  $\hat{\vartheta}$  errors are lower than  $1^\circ$  except when we are close to  $\varphi = 90^\circ$  or  $\vartheta = 90^\circ$ . In practice, due to the StarLab limitations, measurements were done in the range of  $60^\circ < \varphi < 80^\circ$  and  $60^\circ < \vartheta < 70^\circ$  which, according to the Monte-Carlo simulation results, corresponds to a favorable configuration.

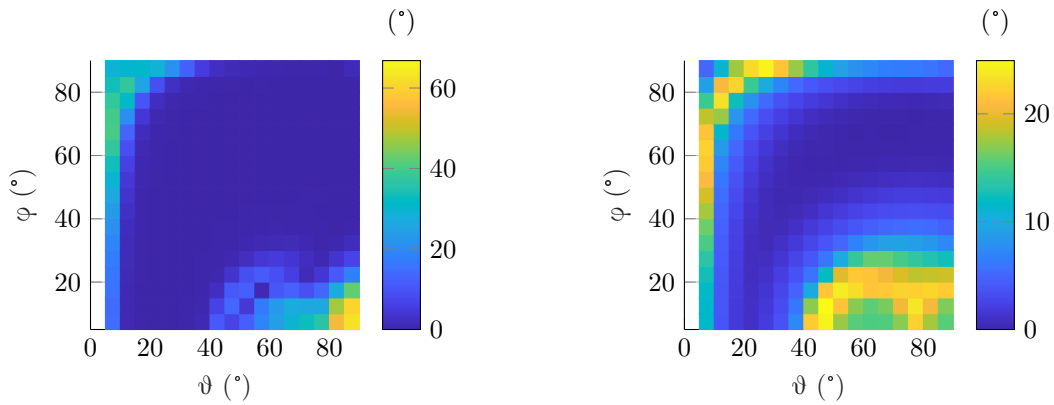


**Figure 3.16:** (a) Errors and (b) uncertainties on the estimated angle  $\hat{\vartheta}$  as a function of real values of  $(\vartheta, \varphi)$  with a SNR of 40dB.

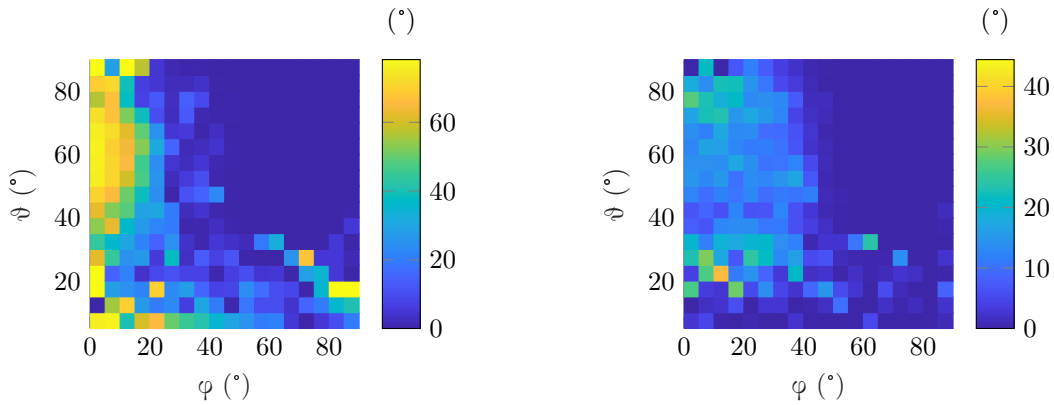


**Figure 3.17:** (a) Errors and (b) uncertainties on the estimated angle  $\hat{\varphi}$  as a function of real values of  $(\vartheta, \varphi)$  with a SNR of 40dB.

### 3.1.8 Real environment measurement

In this section, we want to show potential applications of the proposed approach. These applications have in common that they are implemented in a real environment, namely in an office-type room. In the first part, we will focus on the accuracy of measurement obtained in this type of environment. We will be particularly attentive to the undesirable effects linked to the presence of objects near the tag. These effects will be quantified by characterizing the limitation induced on the reading distance as well as the angular range of the sensor. The second part will present application examples in a more constrained environment (resonator placed on a plastic card moved by hand in front of the reader). We will see that despite the presence of these objects near the tag, it is possible to use the proposed solution to track in real time the movements of a plastic card. Indeed, we will see that for this type of application, it is not necessary to have a very good precision in the extraction of the angles but rather to be able to extract the information from a method that is very inexpensive in terms of calculation time. Table 3.6 summarizes the informations of the different setup configurations used in this section.

**Table 3.6:** Different setup configurations used in this section.

Setup illustration	Fig. 3.18	Fig. 3.22	Fig. 3.25
Distance antenna-loop	Variable	20cm	<10cm
Antenna configuration	monostatic	monostatic	Mono and bi-static
Antenna model	QH2000 & QH800	QH2000	QH2000
Frequency band	2-7GHz	2-7GHz	2-7GHz
Number of points	2001	2001	100
IF bandwidth	10kHz	10kHz	10kHz
Time-gating	No	No	No
Averaging	No	No	No
Empty measurement	Yes	Yes	Yes
Loop geometry	Fig. 7	Fig. 7	Fig. 7
Support	Polystyrene	Plastic box	Credit card

### Limitation in real-life environments

Previous measurements were done in semi-anechoic environment. This section is dedicated to real environment measurements. The measurement setup of Section IV-A (mono-static configuration) is repeated in an office (approximately  $8\text{m}^2$ ) without any anechoic walls and for different resonator-antenna distances. The test bench is illustrated in Fig. 3.18; an example of measured S-parameters is presented in Fig. 3.19. The extracted  $\varphi$  angles are given in Fig. 3.20 where in plain line, the angle estimation in the office is done for different distances. The angle estimation done in Section IV with a semi anechoic environment is also presented (dashed red) for comparison. We can see that in a real environment, the lower bond of the measuring range angle increases as the distance resonator-antenna increases. This can be explained by the Monte-Carlo simulation [see Fig. 3.9] and the link between distance and SNR [23]. Indeed, the minimum measurable backscattered signal amplitude can be seen in Fig. 3.19. The measured resonant frequency peak apex can not be lower than -60dB and as shown in (3.16) the signal levels are a function of the distance between the tag and the antenna. Thus, it is possible to relate Fig. 3.19 to a Monte Carlo study (Fig. 3.21) where the error has been calculated for different SNR values. Comparing the two figures, it is very clear that increasing the reading range reduces the SNR and therefore increases the measurement error and more significantly reduces the range of use of the sensor by limiting the angles for which measurement is possible. We can notice in Fig. 3.21, that errors start to appears for  $\varphi = 90^\circ$  (first harmonic should be zero) when the SNR decreases but also the lower bond of the measuring range increases (when the fundamental and the first harmonic come close to zero) which was confirmed in practice in Fig. 3.20. We can also see in Fig. 3.20 (black line) that by using an antenna with a higher directivity (QH800 [135]), the measuring range is increased by 30cm. Indeed, the higher is the gain, the lower is the residual environment [23] but also the backscattered signal from the loop is higher meaning a higher SNR. Note that the Monte-Carlo simulations are a good way to predict the measurable range in practice for a given environment knowing its SNR. Moreover, the introduced formulas are not sensitive to the distance variation between the tag and the antennas nor to the geometry of the loop. Indeed, the formulas can be applied without any indication on the distance between the resonator and the antennas. However, in practice, the SNR is a function of the distance, which is a limiting factor. This is why the measurement distances are those classically found in chipless applications. The measurement noise is also linked to the environment, typically to the presence and the variation over time of objects placed near the tag. In practice, we observe a measurement distance of around 50 cm in a controlled real environment (no or few objects near the tag), this distance can be reduced to 20 cm if the environment near the tag changes during the measurement. Monte-Carlo simulations can be performed to estimate the measuring range knowing the SNR of the environment.

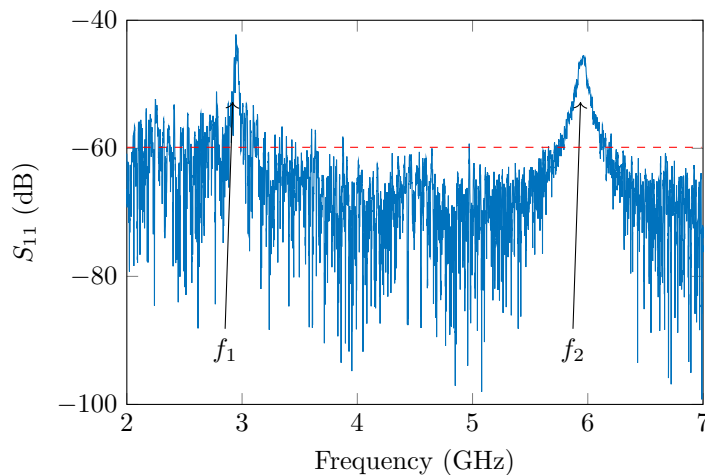
Measurements through a lossy object have also been carried out. A plastic box was used as a container as showed in Fig. 3.22. The distance between the resonator and the antenna is 20cm. The resonator was either placed inside the box or on its side and estimations are presented in Fig. 3.23. We can see that the response is similar to the previous case without any obstacle between the resonator and the tag [see Fig. 3.20]. So the plastic had a limited impact of the estimation. The sensor functionality seems more viable when the resonator is placed on the side of an obstacle if an obstacle is present. Again by using an antenna with a higher gain, the measuring range is improved as illustrated in



Fig. 3.24.



**Figure 3.18:** Test bench configuration for the mono-static measurement in an office.



**Figure 3.19:** Measured S-parameters with the empty measurement for a value of  $\varphi = 70^\circ$  and  $\vartheta = 90^\circ$  in the office for a distance resonator-antenna of 20cm. An averaging of 5 samples is used.

### Real time angular tracking application

Two examples of real-time applications in real-life are presented below as a proof of concept of this approach. To see concretely the achievable performances for a real time application, two videos have been made [137, 138]. In these videos, the loop angular sensor is used to allow a user to interact with an electronic equipment (the chipless reader). The loop is fixed on a plastic card in credit card format. The reader is composed of one or two antennas (depending on the reading mode recommended, i.e. extraction of information on one [137] or two angles [138]), a VNA for the measurement of the S parameters and a computer that performs the calculations and controls the VNA. The real time information of the angular position of the card is displayed on the PC screen. A user holds in his hand

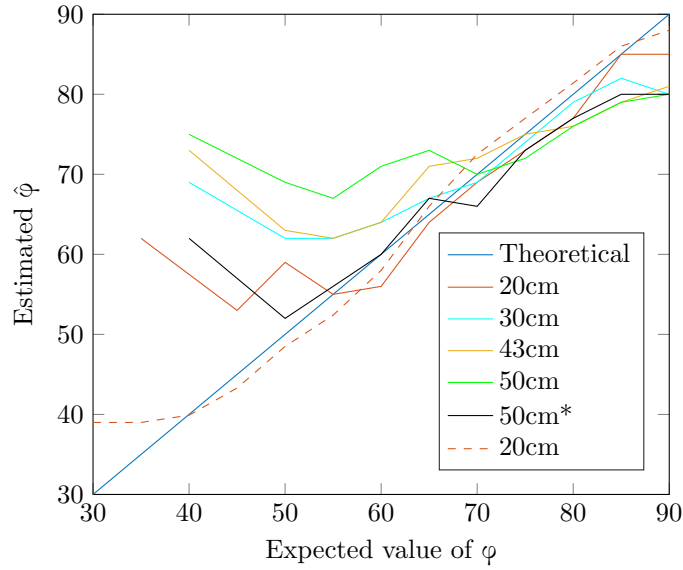


**Figure 3.20:** Estimated value of  $\varphi$  in an office for different distances between the tag-antenna. In dashed line, the measurements done in Section IV in semi-anechoic environment. The estimation in black annotated by '\*' is done with a different antenna (higher gain - QH800 [135]).

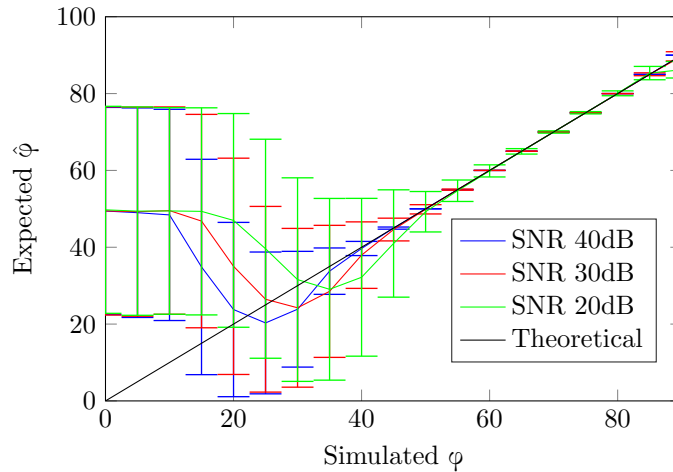


**Figure 3.21:** Monte Carlo simulations for different values of SNR for a mono-static configuration as a function of  $\varphi$  while  $\vartheta = \pi/2$ .

the plastic card. When he puts the card above the antenna [see Fig. 3.25] the reader detects the angle of the loop and displays it in real time on a computer screen (using Matlab). Note that in these two examples, measurements are done in a real environment with the presence of humans nearby as well as scattering objects (human hand, plastic card). No alignment (such as calibration measurements) between the antenna and the resonator is performed, the user just place its card above the antenna.

The video [137] presents the mono-static configuration [see Fig. 3.25a], where only the azimuth angle is detected [see (3.23)]. In the video [137], on the left is shown the hand holding the resonator in front of the antenna (QH800). On the right is presented the real time estimated azimuth angle on

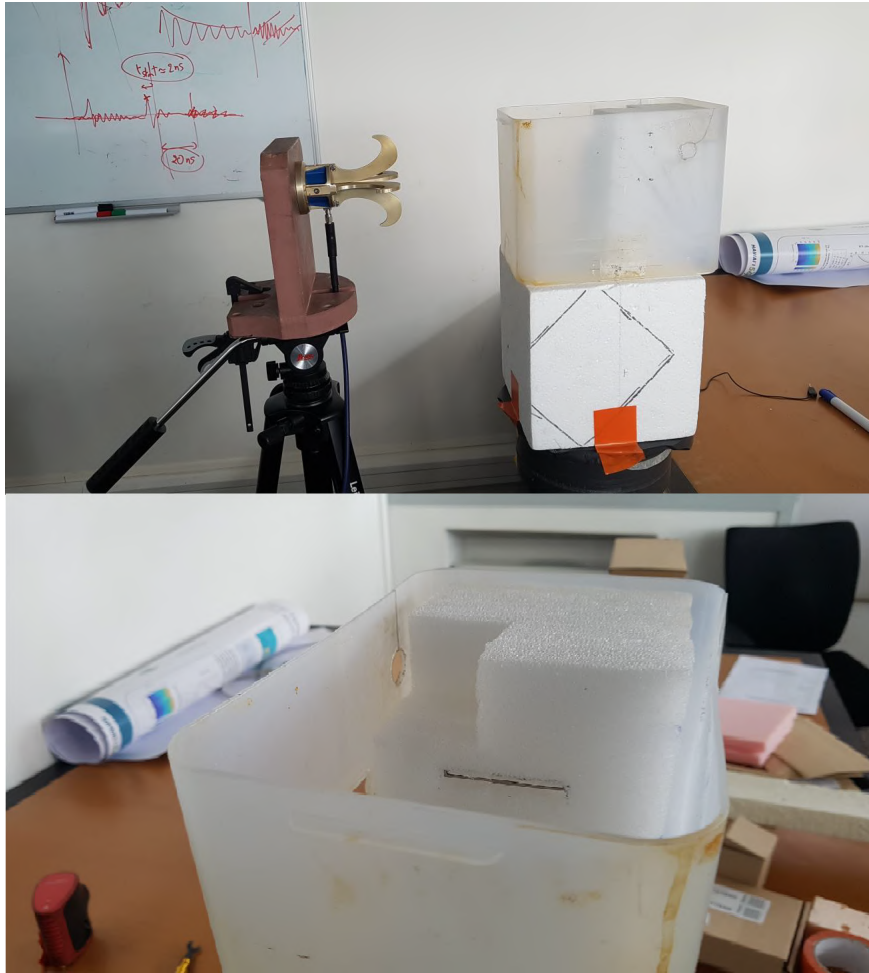


**Figure 3.22:** Test bench configuration for the mono-static measurement in an office through a plastic box.

a Matlab figure. The fixed green arrows represent the coordinate system. The black line corresponds to the loop resonator. The red arrow is orthogonal to the loop resonator showing the direction in which the resonator aims. In this experiment, several distances between the tag and the antenna were recorded. Also, the measurement is done in a real environment with the presence of humans nearby as well as scattering objects (humans hand, credit card, ...). No alignment (such as calibration measurements) between the antenna and the resonator is performed, the user just place its card above the antenna. We can see that the estimated angle (given in the top of the left window) is in good agreement with the movement of the user.

A second video was recorded [138] in a bi-static configuration [see Fig. 3.25b], where both the elevation and azimuth angles are extracted [see (3.26a) and (3.26b)]. The setup configuration is the same as before except the use of two antennas (QH2000) here. Due to the presence of the human and his hand near the resonator, it is not possible to obtain displacements as regular as those obtained in the monostatic configuration. However, it is possible to detect different positions of the tag. In the video, we can see that the user switches the card between two positions and the estimated angles

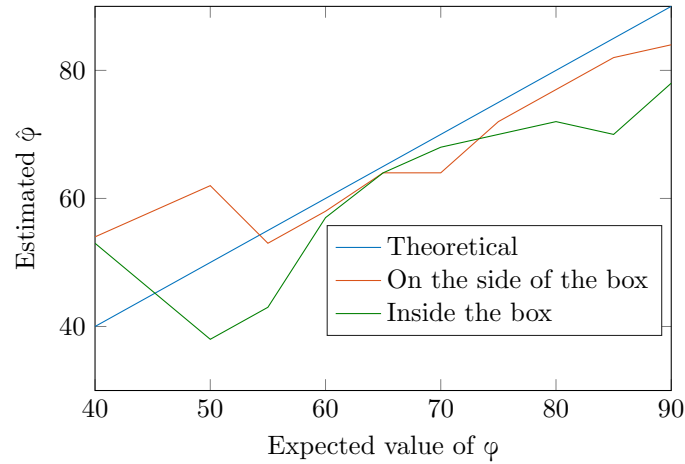


**Figure 3.23:** Estimated value of  $\phi$  when the resonator is placed inside a plastic box or on its side. The measurement bench is shown Fig. 3.22. The loop to antenna distance is 20cm. The antenna is the QH2000 from MVG [135].

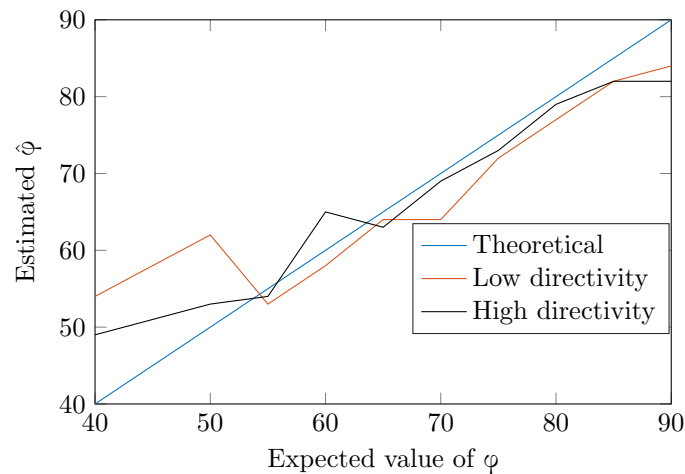


**Figure 3.24:** Estimated value of  $\phi$  when the resonator is placed on the side of the plastic box for a low or high directivity antenna (respectively QH2000 and QH800 from MVG [135]). The measurement bench is shown Fig. 3.22. The loop to antenna distance is 20cm.

relating to these positions are correctly detected.

Note that these two examples were recorded in real time using a computer with normal specifications. We can see that the real environment as well as the human or hand/card presence does not affect too much the sensing. In the end, the detection is compatible with this type of application. We also notice that in our case, no 'artificial intelligence', 'learning algorithm' is necessary since the resolution is done analytically on the basis of perfectly determined physical quantities. This allows to reduce the computational cost as much as possible and to be able to present angular tracking results in real time without any specific work. A few examples of practical applications can be found in the field of wireless joystick, human-computer interface, or for gesture recognition. Indeed, the main interest here is the possibility to detect without any electronic device (obviously without battery) the

angular displacement of a small object (that can also be identified) that a user would move to interact with an electronic equipment, and this at short distance. This approach based on a sensor without chip literally breaks with the solutions currently proposed which in the vast majority requires a battery to operate. This work is therefore in line with the idea of providing innovative solutions that are environmentally friendly while providing a much sought-after functionality in many applications. More precisely, we can quote for example a use to make gaming, sign language, virtual manipulation, daily assistance, or even human robot interaction.

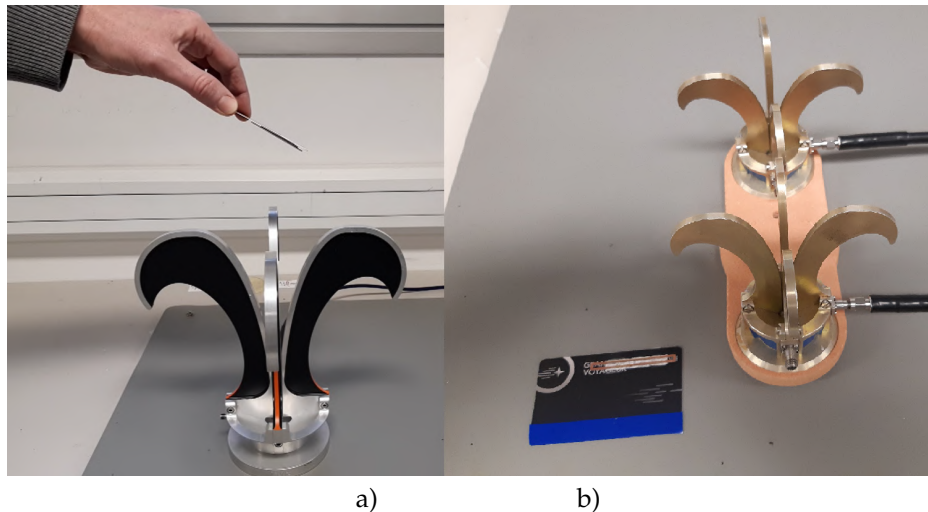


**Figure 3.25:** Real time application: example of angular tracking. Above the reader, a user holds the resonator attached to a plastic card. Equation (3.23) is used to extract the angles from the measurements done by the VNA which is connected to the antennas. The result is displayed in real time on the computer screen to visualize the displacements generated by the user. a) Mono-static configuration, azimuth angle detection only, b) bi-static configuration, elevation and azimuth detection.

### 3.1.9 Conclusion of the section

In this section, a model of the radiating pattern of a loop resonator has been developed. This radiation pattern was then used to determine the orientation of the loop with respect to the positions of the antennas. Simulations and measurements have been done to validate the proposed method and the derived expressions. This approach can estimate the azimuthal angle of the chipless tag with an error less than  $2.6^\circ$  (one dimension angle extraction). In the case where one seeks to extract at the same time the azimuthal angle and the inclination, errors were on average lower than  $3^\circ$  for both estimated angles (for the rather favorable directions). Moreover, the analytical expressions are not sensitive to the distance variation between the tag and the antennas nor to the geometry of the loop. It can be applied without indication on the distance resonator-antennas but depending on the SNR in practice, the measuring range can be reduced. Monte-Carlo simulations can be performed to estimate the measuring range knowing the SNR of the environment. Unlike chipless approaches which at best can extract a unique rotation angle, the introduced method does not require any special calibration measurements. Finally, the identification functionality of the tag (for example if we consider a tag composed by several loops similar to the one presented here) can be remained untouched so that identification and sensing can be combined to address a new kind of applications.

### 3.2 Increased Coding Capacity of Chipless RFID Tags Using Radiation Pattern Diversity

In this section, a method to increase the coding capacity of chipless RFID tags by encoding multiple resonance peaks into a single frequency slot is proposed while keeping a constant total frequency range. The proposed method is based on the spatial diversity which can be compared to imaging technique similar to [67] allowing a tag to be made with several resonators having the same resonance frequency. However the approach introduced is not based on imaging. The novelty is the use of different radiation patterns to achieve this new reading method. This radiation pattern diversity will be achieved using the loop resonators and its different harmonics.

#### 3.2.1 Principle

Fig. 3.26 presents a schematic of long and short rectangular loops considered in this study. Fig. 3.27 presents the measurement setup principle. The coordinate system used in this section is given in Fig. 3.27. The loops are positioned in the xOz plane centered around the origin of the coordinate system. The antenna n°1 is positioned at normal incidence to the tags. The angle  $\varphi$  is between the loops and the antenna n°2.

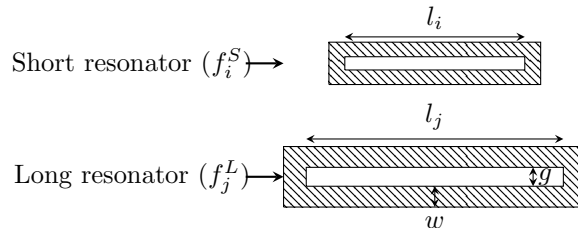
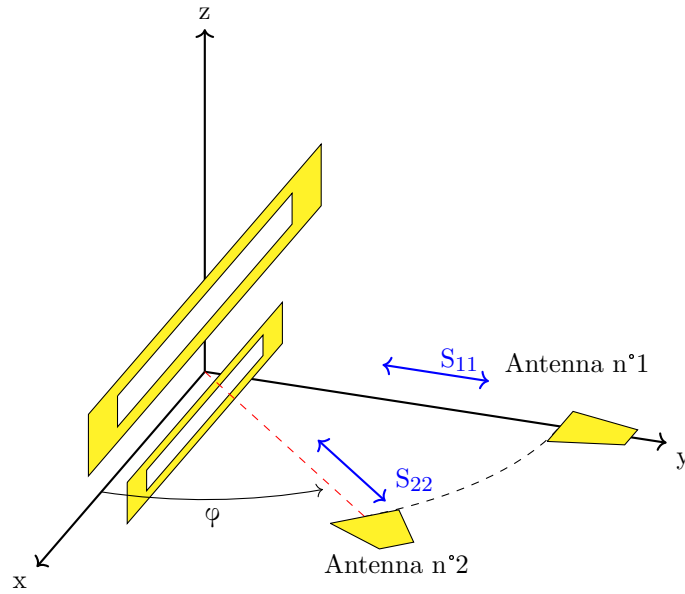
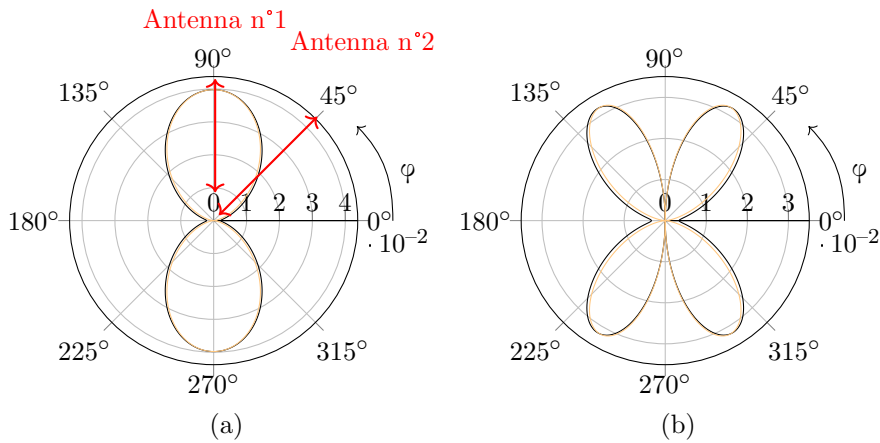


Figure 3.26: Schematic of the long and short loop resonators used in this study.

Equations (3.2) and (3.4) are used to plot the radiation pattern of the loop resonators for the fundamental and the first harmonic frequencies in Fig. 3.28. We can notice that with this resonator more data can be encoded using blind spots of the radiation pattern if harmonics are used. Indeed, if we place an antenna at  $\varphi = 90^\circ$ , long loop resonators working at their fundamental frequencies ( $f_1^L$ ) can be seen according to their radiation patterns (see Fig. 3.28a) but short loop resonators working at their first harmonic ( $f_1^S$ ) can not be seen (see Fig. 3.28b). Now, if a second antenna is placed at  $\varphi \neq 90^\circ$ , both resonators can be seen according to their radiation patterns. The idea in this section is to use a long and a short resonator working at the same frequency (sharing a frequency slot) and being able to read both of them to increase the coding capacity. An illustration of the requested frequency band is presented in Fig. 3.29. Note that first resonance (for small loop) and second resonance (for long loop) can lie outside the operating frequency band of the reader. These peaks do not impact the proposed method since chipless tags are linear time-invariant systems. The protocol to read both modes of resonance (even at the same resonance frequency  $f_1^S = f_1^L$ ), is based on two measurements using 2 antennas (see Fig. 3.27) : First, a  $S_{11}$  measurement at  $\varphi = 90^\circ$  has to be done with antenna n°1. This measurement gives the response of loop resonators working at their fundamental frequencies only. Then, a  $S_{22}$  measurement needs to be done with antenna n°2 at the angle  $\varphi$  (see Fig. 3.27).



**Figure 3.27:** Loop scatterers, coordinate system and notations considered in this section. Antenna n°1 is aligned with the y-axis while antenna n°2 is oriented along the  $\varphi$  angle.



**Figure 3.28:** Magnitude of the E-field (V/m) radiated by the loop for  $\varphi \in [0^\circ; 360^\circ]$  at (a) the fundamental frequency and (b) the first harmonic. In black the CST simulation and in yellow the expressions obtained from [80].

Since the response of resonators operating at their fundamental frequency is known (using  $S_{11}$ ), it is possible to remove its contribution from  $S_{22}$  to only have the resonators response operating at their first harmonic. Indeed, using (3.2) and (3.4), we can evaluate the value of the contribution of resonators working at their fundamental is reduced at an angle  $\varphi$ .

In conclusion, resonance frequencies of resonators working at their fundamental frequency  $M^L$  can be obtained using :

$$M^L = S_{11} \quad (3.27)$$

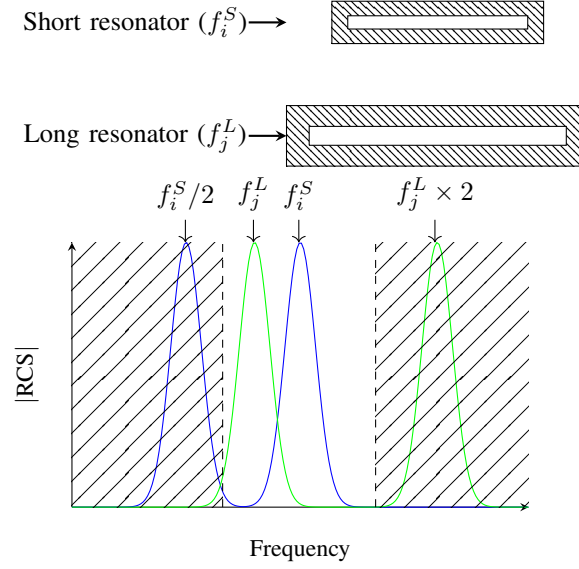


**Figure 3.29:** Frequency band considered where some resonators work at their fundamental frequencies  $f_j^L$  and some work at their first harmonic  $f_i^S$ . The hatched areas are not used to encode information.

For resonators operating at the first harmonic, the frequencies can be obtained from the following  $M^S$  signal :

$$M^S = S_{22} - S_{11} \times \sin\left(\frac{\pi}{2} \cos \varphi\right)^2 \quad (3.28)$$

Using a configuration with two antennas and the first two modes of resonance it is possible to realize the reading of the short resonator and the long resonator independently. This procedure actually double the coding capacity since it is now possible to encode 2 bits per frequency slot (one related to loops operating in their fundamental resonance frequency and one to loops operating in their first harmonic).

### 3.2.2 Simulations

Simulations have been carried out using CST MW to validate the approach. Four loop resonators, as illustrated in Fig. 3.30, were designed such as 2 of them operate at their fundamental mode of resonance while 2 others work at their first harmonic mode of resonance between 3GHz and 3.4GHz. Furthermore, one resonator at the fundamental frequency and one at the first harmonic have been chosen to share the same resonance frequency (frequency slot) at 3GHz. Simulated E-fields corresponding to  $S_{11}$  and  $S_{22}$  parameters are plotted in Fig. 3.31 for a second antenna placed at  $\varphi = 60^\circ$ . We can see on Fig. 3.31 that for  $S_{11}$ , only the two resonators working at their fundamental frequency are visible. Now with an angle of  $\varphi = 60^\circ$  ( $S_{22}$ ), we can notice that both modes of resonances are present. Using (3.28), we can successfully remove the fundamental response of resonators from  $S_{22}$ , leaving only the first harmonic mode. By doing so, one can encode data using the fundamental and harmonics on the same frequency slots.



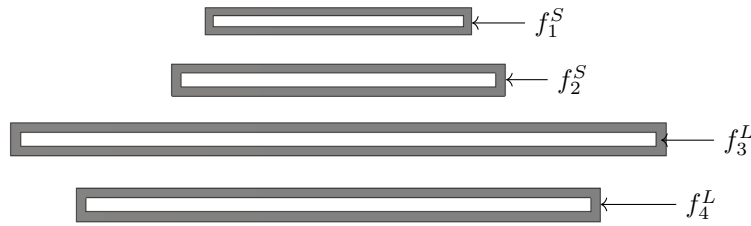


**Figure 3.30:** Configuration of 4 loop resonators used for the simulation. The loops have the same  $g = 2\text{mm}$  and  $w = 1.4\text{mm}$ . Lengths are  $l_1 = 42.2\text{mm}$ ,  $l_2 = 47.97\text{mm}$ ,  $l_3 = 87\text{mm}$  and  $l_4 = 77\text{mm}$ .

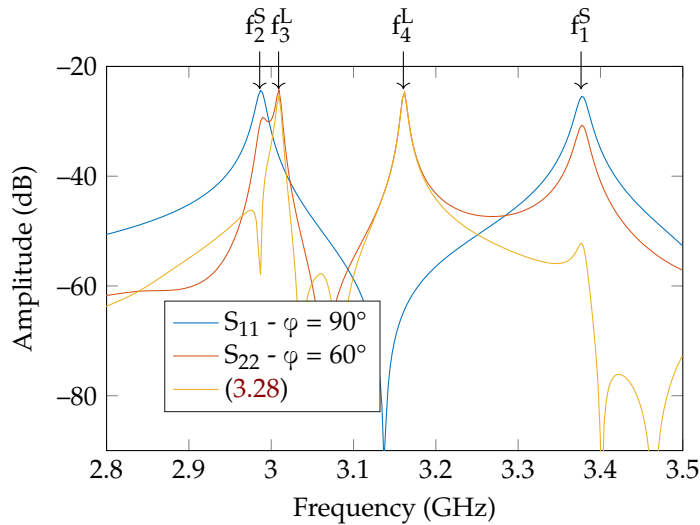


**Figure 3.31:** Simulated E-fields response corresponding to  $S_{11}$  and  $S_{22}$  parameters for the 4 loop resonators illustrated in Fig. 3.30.

### 3.2.3 Measurements

Measurements in a semi-anechoic chamber inside a StarLab from MGW were achieved as shown in Fig. 3.33. A configuration with two antennas is used where antenna  $n^{\circ}1$  is placed at  $\varphi = 90^{\circ}$  and antenna  $n^{\circ}2$  placed at  $\varphi = 60^{\circ}$ . The two resonators working at 3 GHz (on their fundamental and first harmonic) on the same frequency slot (dimensions are obtained from the simulation) have been cut in an aluminium sheet as shown in Fig. 3.32. S-parameters have been measured and (3.28) has been applied. We can see that (3.28) allows to make the distinction between the two loops having the same resonance frequency. This results shows the potential of this new approach to increase the coding capacity by a factor 2.

### 3.2.4 Conclusion of the section

In this section, a method to increase the coding capacity with a constant frequency bandwidth of chipless tag was proposed. This approach is based on the radiation pattern diversity of same resonator topology but different modes of resonance. Simulations and measurements have shown the increase in the coding capacity using conventional loop resonators. We note that it is also possible



**Figure 3.32:** The loop resonators used for the measurement. The first resonator has  $g = 2$  mm,  $w = 1.4$  mm and  $l_1 = 47.97$  mm. The second resonator has the same  $g$  and  $w$  but  $l_2 = 97$  mm.

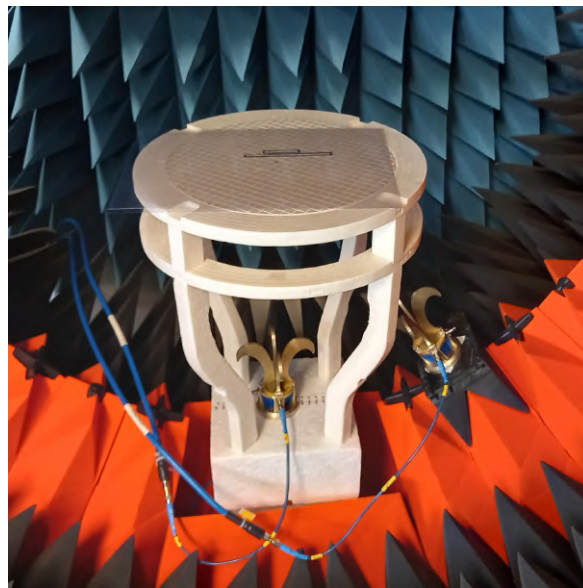


**Figure 3.33:** Test bench inside the semi-anechoic chamber StarLab from MGV.

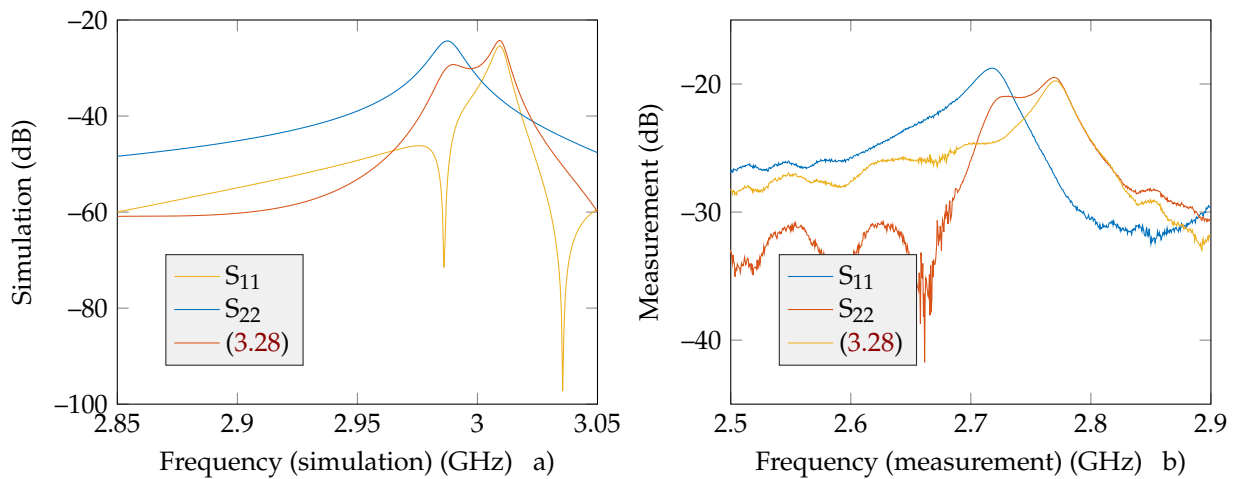


**Figure 3.34:** S-parameters measured for the loop resonators shown in Fig. 3.32 in a) simulations and b) measurements.

to use the same principle with different families of resonators, for example by mixing loops with C shape resonators.

### 3.3 Reading robustness

RFID was democratized with consumer applications such as anti-theft systems in supermarkets, passport identification, access/transport cards, or even animal identification [3, 4]. The RFID anti-theft system (EAS) in supermarkets was the first major commercial use of RFID technology. The goal of the chipless RFID technology is to provide more functionalities than a barcode at a comparable price. One of the direct drawbacks of this approach is the deterioration of the tag readability for example in term of reading range compared to a UHF RFID tag. By removing the chip and the load modulation used in classical RFID systems, chipless tag reading is lower and clearly less robust in real environment. However a certain level of robustness is needed to correctly read the tag, as well as to improve the reading distance. In addition, today chipless RFID applications do not only include the identification functionality but also sensing capabilities [139, 140, 141, 142, 143]. This sensing approach often relies on the remote measurement of a shift in the resonance frequency of a resonator. Such shifts can be as low as 25 kHz [140, 122], hence a certain level of robustness of reading is highly expected for practical applications of chipless RFID technology.

A large number of resonators of different shapes have been introduced for use in RFID chipless [144, 145]. Contrary to the previous generation of tags that included one or two antennas and a transmission line on which the resonators were positioned [139], the REP approach allows to realize tags where only resonant structures are present [146]. These simpler structures have shown better performances in terms of compactness but also in terms of reading distance in real environments [147, 45, 146]. Also, as previously indicated, these resonant forms are compatible with reading techniques based on time gating or the polarization of the reading system to significantly increase their performance. Contrary to the so-called time-domain chipless RFID tags [148, 149], the reading principle of the REP tags is based on the resonance frequency of the geometrical shape that composes the tag. Also, strictly speaking, the information is not obtained from the structure mode and the antenna mode [150] of the tag as for the time-domain tags [149] but in the extraction of the resonance modes of the tag [151, 152, 48, 45, 153]. Most often, in the operational frequency band of the tag, only one resonance mode per elementary form is present, so the temporal expression of the backscattered electric field is none other than a damped sinusoidal to which a term is added corresponding to the non-resonant part of the backscattered field and which, from a temporal point of view, is present only in the early-time response of the tag [151, 152, 48, 45, 153]. It can be seen from this example that this representation of the electric field is not the one used to describe loaded antennas [150] which means that the terms “structure mode” and “antenna mode” are not strictly adapted to describe the operation of a REP tag. For ease of implementation (especially for sensor applications) and to reduce the price of the tag, REP tags without a ground plane are very interesting [147, 146]. Techniques allowing to take into account the frequency shifts observed when such a tag is placed on different supports have been introduced and allow to use these tags in a large number of configurations [154]. We note that the rectangular loop resonators [101], which have a RCS twice as high as the C-loops [101, 146, 154, 145], are particularly interesting shapes because they have a high quality factor (of the order of 130 at 3 GHz), comparable to resonators with a ground plane [155, 144]. On the other hand, the main drawback that limits the use of these structures is the impossibility of reading them in cross-polarization (in this case the loop must be rotated by  $45^\circ$  compared to a classic co-polarization reading). This is directly linked to the fact that a rectangular loop has two resonance modes, namely a

weakly resonant mode (parasitic mode) which is located a few MHz before the loop mode, the later one is resonant enough to be used to encode information. It is therefore particularly expected to be able to read these loops with a new approach that will allow to isolate the polarization that contains the information, thus reducing a significant part of the amplitude of the backscattered field (namely the parasitic mode, but more generally the contribution of the reflection oriented in the direction of this mode) which behaves as noise in the measurement of a REP chipless tag. Subsequently this method is general and allows to improve the reading of all the REP type tags.

Several works have been done to improve the robustness reading of chipless RFID. We can cite for example [156, 157] where authors have shown that the arrangement of the resonators on the tag can improve its robustness. Others works are based on the polarization of electromagnetic waves. Indeed, the environment does not usually depolarize electromagnetic waves. For this reason, de-polarizing tags such as in [147, 158] or resonators placed at  $45^\circ$  in relation to the orientation of the antennas have been studied to send a signal with a polarization in a different direction from the environment's response (cross polarization measurements). The drawback of such methods is that only a part of the signal is depolarized by the tag and arrives at the receiving antenna positioned at an angle of  $90^\circ$  regarding the transmitting antenna. Hence the received signal is reduced and so its readability distance (for example, 6dB is lost when a resonator is placed at 45 degrees with respect to the same measurement in co-polarization with an angle 0 with respect to the antennas). Also, placing resonators at  $45^\circ$  can excite parasitic modes of resonances which can pollute the final electromagnetic response of the resonator. Moreover, in all these measurement approaches, the tag orientation must be known prior to the measurement. This is why measurement techniques independent of the orientation of the tag have recently been introduced from the reader part [159, 160] or the tag part [161]. However, these techniques do not separate the wave reflected by the environment from the one linked to the tag and therefore its identifier [162]. Moreover, numerous approaches based on the postprocessing of the time response of a resonator have been proposed to increase the robustness. We can cite for example methods based on time gating [48, 45, 153]. Even if this method is very effective and allows to significantly improve the performance of reading chipless tags, unfortunately, as with cross-polarization readings, cutting off the signal (early time part) also contributes to not using a significant portion of the energy that continues the tag identifier. In addition to that possible different attenuation coefficient of resonators on the same tag due to their different working frequencies or their Q-factors as well as the empirical way to obtain the needed parameters (such as  $t_{\text{start}}$  and  $t_{\text{stop}}$  to select the part of the time signal to be retained) are majors drawbacks of this technique. Most of the time, these parameters need to be characterized by the user based on the measurement responses.

In this section, a method based on incident wave polarization is proposed. The presented approach is able to isolate orthogonal modes of resonance from the measurement and to detect 100% of the useful signal for the detection while keeping a low environment response. In addition, it does not require any knowledge about the tag orientation. This method can be applied to different resonators but loop resonators which are resonators commonly used in chipless RFID [63] are considered in this section. Indeed, these scatterers can exhibit a strong parasitic mode of resonance and so are a good example for such approach. This work will show how the polarization filtering can remove this parasitic mode for identification application.

### 3.3.1 Theory

The loop resonator illustrated in Fig. 2.2-a is a resonator commonly used in chipless RFID. In this study the resonator is a metal loop with no substrate. The thickness of the metal is sufficient to give good rigidity to the structure which allows it to be handled and used on different substrates. These loops are widely used in RFID chipless systems because they have no ground plane (only one metal layer) and their geometry allows them to have a high quality factor (above 120 for frequencies around 3 GHz), which is comparable to many ground plane resonators. However, their main disadvantage is that this scatterer have to be read in co-polarization with a precise orientation with respect to the reader's antenna. Indeed, the preferred direction is when the incident field is perpendicular to the length of the loop (see Fig. 2.2). The identification of the loop will be possible in this configuration with at least a misalignment of a few degrees. When the loop is illuminated by an incoming electromagnetic field, the maximum energy backscattered occurs at its resonant frequency  $f$  defined by (2.2).

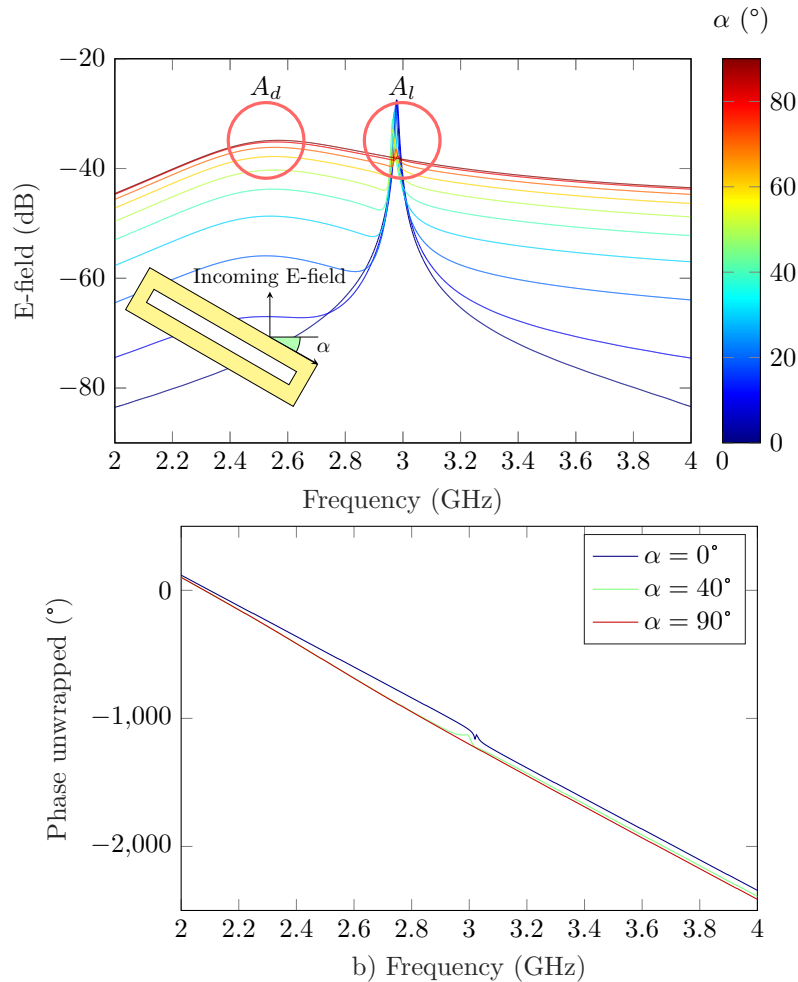


**Figure 3.35:** a) Simulated E-farfields corresponding to  $S_{11}$  parameter of a loop for different values of  $\alpha$  in amplitude and b) in phase. The incoming E-field according to the resonator is shown in Fig. 3.35. The angle  $\alpha$  goes from  $0^\circ$  to  $90^\circ$  with  $10^\circ$  step.

To improve the robustness reading of this resonator, it is important to notice that depending on the incident E-field orientation this resonator can present two modes of resonance: a dipole-like mode  $A_d$  and a loop-like mode  $A_l$ . So, in the general case (when the tag is not aligned with the antenna), both modes can be excited and the total measured radiated field will be the complex summation of the two. To illustrate this, the loop resonator with the dimensions given in Fig. 2.2-a is simulated using CST MW and the transient solver. The resonator is first oriented at  $40^\circ$  to the incoming electric field. Simulation results are plotted in Fig. 3.35. A wide peak can be seen at 2.5 GHz corresponding to the dipole mode  $A_d$  and a sharper peak at 3 GHz from the loop mode  $A_l$ . We will see that polarization filtering introduced here will permit to remove the parasitic mode to facilitate the extraction of the information contained in the tag, whatever its orientation in relation to the reader. It can also be seen for  $\alpha = 0^\circ$  the tag is easily detectable (only the resonance mode  $A_l$  linked to the identifier is present) and for  $\alpha = 90^\circ$  it is not possible to catch the resonance frequency. The further away from the condition  $\alpha = 0^\circ$  the more difficult the reading, which shows a significant limitation.

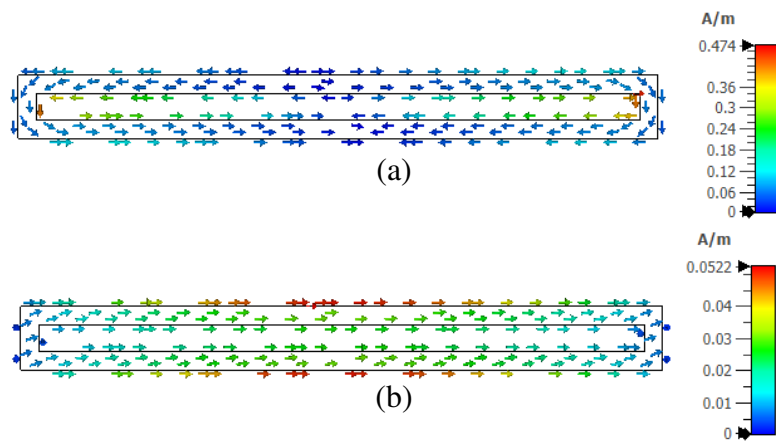


**Figure 3.36:** (a) Current distribution on the loop resonator for the loop mode  $A_l$  at 3GHz and (b) the dipole mode  $A_d$  at 2.5GHz.

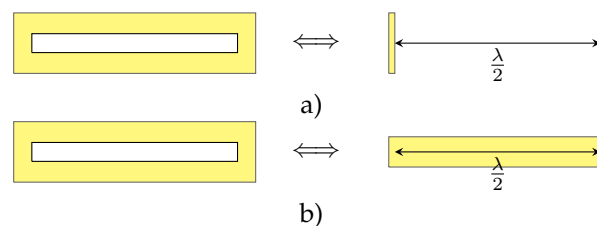


**Figure 3.37:** (a) Equivalent model of the loop resonance for the  $A_l$  mode. The loop is modeled by two infinitesimal short circuited dipoles spaced by  $\lambda/2$  with  $\lambda$  corresponding to the notch  $l$  length. (b) Equivalent model of the dipole resonance for the  $A_d$  mode. The loop is modeled by one short circuited dipole of length  $\lambda/2$  with  $\lambda$  corresponding to the total length of the resonator  $l + 2w$ .

It has been shown in [79] that the loop mode  $A_l$  scattering phenomenon is associated to the induced current on the extremities of the resonator. This phenomenon can be confirmed by the simulated current distribution at the resonance of the loop mode (see Fig. 3.36-a). The loop resonator can then be modeled as two infinitesimal dipoles spaced by  $\lambda/2$ . This equivalence is illustrated in

Fig. 3.37-a. For this resonance mode, the radiation pattern but also the polarization of the backscattered wave can be determined using [79]. The Q-factor associated to this mode is high as seen by the sharp peak in the S-parameters (see Fig. 3.35). Due to its sharpness, this mode is the one wanted in chipless RFID when using loop resonators for identification or sensing applications.

The second mode of excitation is when the currents are induced on the whole resonator as shown in Fig. 3.36-b. The scattering mechanism is closer to a single short circuited dipole (without ground plane) as illustrated by its equivalent model in Fig. 3.37-b. Here, the radiation pattern but also the polarization of the backscattered wave by a dipole are known in the literature [163]. It should be noted that the two resonance frequencies are very close to each other (relative to distances  $l$  and  $l + 2w$  respectively) and cannot be suppressed simply by design or even with time gating. Thus, as illustrated Fig. 4, the two modes of resonance of the loop resonator can be associated to dipoles which are orthogonal to each other. This orthogonality can be used with a polarization filtering approach as discussed below to extract the parasitic mode of resonance. Indeed, by filtering the two modes using the polarization of the backscattered wave, the parasitic signal can be removed but also the peak prominence is improved.

We will also see that the method proposed here is not limited to the suppression of the dipole mode of the loop, but in a more general way will allow to subtract all the reflections coming from the environment which are 1) excited by the incident wave (direction of port 1) and 2) whose polarization of the backscattered signal is aligned with the direction of the dipole  $A_d$ . This is why the interest of this method is not limited to the dipole resonator (even if it is a very good example because of the presence of the dipole mode) but applies whatever the scatterer is. The demonstration will be done considering that the environment reflects a wave in the direction of the dipole mode  $A_d$  and we will treat the case of a completely different resonator (resonator with ground plane) for which the method can also be applied with a notable gain on the robustness of reading. Unlike a cross-polarization measurement, we will see that this method does not reduce the influence of the environment in the  $A_l$  direction. However, without this property, we will see that it is possible to use this method with a notable improvement in the read distance even when the tag without ground plane is in the presence of a large reflecting object as well as for tags with ground plane (where time gating can be combined with the proposed approach).

A dual-polarization antenna (2-ports) will be used for the study. The coordinate system and the preferred directions to excite the loop modes are illustrated in Fig. 3.38. When the resonator is rotated by the angle  $\alpha$ , the polarization scattering matrix  $S$  (Sinclair matrix) which relates the scattered electric field vector  $E_s$  to the incident field vector  $E_i$  is [164] :

$$S(\alpha) = \Omega \times S(0^\circ) \times \Omega^T \quad (3.29)$$

with

$$S(0^\circ) = \begin{pmatrix} A_l & 0 \\ 0 & A_d \end{pmatrix}, \quad \Omega = \begin{pmatrix} \cos \alpha & \sin \alpha \\ -\sin \alpha & \cos \alpha \end{pmatrix} \quad (3.30)$$

and  $T$  denotes the transpose.  $A_n$  denotes the contribution of the resonance in the direction of mode  $E_n$ . S-parameters coefficients for the angle  $\alpha$  can there be written :

$$\begin{cases} S_{11}(\alpha) = \sin(\alpha)^2 A_d + \cos(\alpha)^2 A_1 + E_{11} \\ S_{21}(\alpha) = \sin(\alpha) \cos(\alpha) A_d - \sin(\alpha) \cos(\alpha) A_1 + E_{21} \end{cases} \quad (3.31)$$

where  $S_{xy}$  corresponds to the environment response (without the loop) in the direction of the  $xy$ -port of the antenna. So both modes are given by :

$$\begin{cases} A_1 = [S_{11}(\alpha) - E_{11}] - \tan(\alpha) [S_{21}(\alpha) - E_{21}] \\ A_d = [S_{11}(\alpha) - E_{11}] + \cot(\alpha) [S_{21}(\alpha) - E_{21}] \end{cases} \quad (3.32)$$

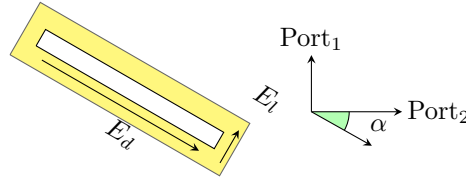


**Figure 3.38:** Coordinate system. Port<sub>1</sub> and Port<sub>2</sub> are the ports of the dual-polarization horn antenna. The rotation  $\alpha$  is between the Port<sub>2</sub> and the direction of  $A_d$ .

An initial measurement without the resonator is done to get  $E_{11}$  and  $E_{21}$  and then the tag is placed. If the rotation angle of the loop  $\alpha$  is known as well as  $S_{11}(\alpha)$  and  $S_{21}(\alpha)$ , (3.32) can be used directly to extract only  $A_1$  (and so the tag ID), removing the parasitic mode  $A_d$ . If the rotation of the loop  $\alpha$  is unknown, a numerical resolution can be done in order to estimate this angle. More information about this resolution can be found in Section 3.3.2. This second approach allows to correctly apply the presented method as well as to add a rotation sensor capability to the existing identification functionality of the chipless RFID tag. Notice that this approach can be used to improve the readability of a loop resonator without indication of its position but also as an orientation sensor following the first remark. This ability to read a tag regardless of its orientation is also a way to improve reading robustness in real applications [159].

Notice that for  $\alpha=0^\circ$  or  $\alpha=90^\circ$ , (3.32) does not grant solutions. Indeed, for these values the mode is not excited or not received (orthogonal to the antenna ports) hence this result. It is possible however to use  $S_{22}$  and  $S_{21}$  in such cases to remove this problem since these ports are orthogonal to  $S_{11}$  and  $S_{12}$ , they will excite and receive the modes.

It is clear from the second part of (3.32) that this method suppresses the dipole mode of the loop  $A_d$  but also the contribution of the environment which is aligned with the direction of the loop  $A_d$ . Previously, we have considered the term  $A_d$  as the dipole mode of the loop resonator. However, in a more general case,  $A_d$  represents the total contribution of the backscattered field perpendicular to the preferred reading direction ( $E_l$ ) of the tag by the rotating target, a target consisting of the tag and any support that would rotate or not with the tag. Indeed in this term  $A_d$ , we can take into account both the presence of a parasitic mode (example specific to the loop), or the quasi-optical mode of the tag or the contribution of the support on which the tag is attached (we have chosen to illustrate the method on a loop insofar as with this parasitic mode, this structure alone has a significant contribution in



this specific direction  $E_d$ ). Like the parasitic mode of the loop, depending on the angle of this target in relation to the reading antenna,  $A_1$  is directly involved in the measured signals  $S_{11}$  and  $S_{21}$  [see (3.31)] and therefore negatively impact the tag reading by adding to the signal a contribution not including the ID of the tag which necessarily reduces the ratio between the useful signal and the total signal measured and thus results in the end in a reduction of the reading distance. Thus, as we will see in practice, this possibility to remove a part of the environment which does not include useful information on the tag will allow a significant increase in the reading distance. A practical case study will be discussed in Section 3.3.6. We note, however, that this approach does not overcome the unknown contribution of the environment or the quasi-optical mode of the tag in the preferred reading direction ( $E_1$ ). This is for example the case when a large metal plate is positioned behind the loop (see Section 3.3.5) or when tags with a ground plane are used. Since these two configuration are commonly used in practice, in Section 3.3.5 and 3.3.8 a modified version of the approach introduced here will be applied. It will be shown through these examples that the approach is general and allows a reading improvement for any chipless tag based on the use of resonators, with or without ground plane and this in different environments.

Last but not least, 100% of the useful signal of  $A_1$  is captured using (3.32) whereas only 1/4 is captured when only measuring  $S_{21}$  with a tag at  $45^\circ$  as it is done today hence improving the SNR and so the maximum reading range.

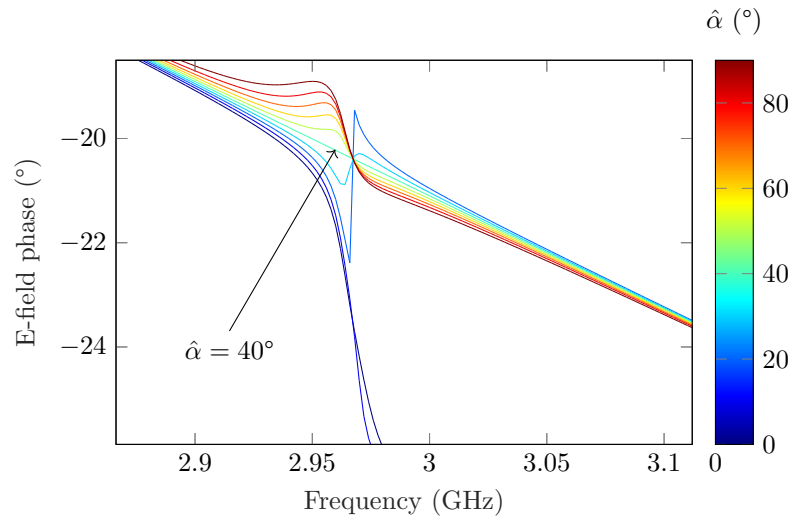


**Figure 3.39:** Unwrapped phase of the dipole mode  $A_d$  computed with (3.32) when the resonator is oriented at  $\alpha = 40^\circ$  for different values of estimated  $\hat{\alpha}$ .

### 3.3.2 Angle estimation

Lets consider the loop resonator of Fig.3.38. The polarization axis of  $A_1$  is along the  $E_1$  axis. If the antenna polarization port 1 matches the  $A_1$  axis, 100% of the resonance is received by the port 1 and none on the port 2. Now, if the resonator is rotated at  $45^\circ$ , 50% is received on port 1 and 50% on port 2. So, if we tell that 100% on the resonator is received on 1 port and 0% on the other port, we know

that the coordinates system of Port1/Port2 is aligned with the resonator. We are using this principle to estimate the angle rotation.

Using (3.32), we have a rotating coordinate axis. If we rotate the coordinate system to match the  $A_1$  axis, the port 1 of the coordinate system have 100% of the power while the port 2 of the rotating axis have 0%. To estimate if no signal is received on port 2, we can look at the phase at resonance of  $A_1$ . Indeed, at resonance, a jump on the phase is present due to the resonant behavior.

Hence to estimate the rotation of the resonator, the following algorithm is implemented in Matlab :

```

1  [S11,F]=extract('S11.txt','re_im');
2  S21=extract('S21.txt','re_im');
3
4  best_alpha=zeros;
5  best_norm=1e9;
6
7  for alpha=-180:1:180
8      Ad= S11 + cotd(alpha)*S21;
9
10     [~,S]=polyfit(F, unwrap(angle(Ad)),1);
11     if(S.normr < best_norm)
12         best_norm=S.normr;
13         best_alpha(ID) = alpha;
14     end
15 end
16 disp(['Estimated alpha :' num2str(best_alpha)])

```

**Listing 3.1:** Matlab implementation to estimate  $\alpha$ .

The numerical resolution tries all the angle from  $-180^\circ$  to  $180^\circ$  until port 2 no longer have a phase jump at the  $A_1$  resonance: so the rotating axis port 1 is aligned with the resonator. The value of  $\hat{\alpha}$  which gives no phase jump is the one with the lowest norm of the residuals of a fitting with linear function (line 10 of the algorithm). An illustration is given in Fig. 3.40 where a loop resonator is simulated at  $\alpha = 45^\circ$ . The phase of  $\hat{A}_d$  for  $\hat{\alpha} = 35^\circ$  and  $\hat{\alpha} = 45^\circ$  are presented with their respective linear fitting. Since the loop is place at  $\alpha = 45^\circ$  and  $A_d$  is orthogonal with  $A_1$ , no phase jump due to resonance is present for  $\hat{\alpha} = 45^\circ$  on the phase of  $\hat{A}_d$ .

### 3.3.3 Simulations

Simulations have been carried out using CST MW to validate the proposed approach. A plane wave excitation along the direction noted Port<sub>1</sub> in Fig. 3.38 was used. The loop dimensions for the simulation part but also for the loop used in measurements are shown in Fig. 2.2. E-farfield probes at 1meter from the loop, relating to the directions Port<sub>1</sub> and Port<sub>2</sub> in Fig. 3.38, and thus corresponding to  $S_{11}$  and  $S_{21}$  parameters have been extracted when the tag rotates as illustrated in Fig. 3.38. These two quantities are plotted in Fig. 3.35a and Fig. 3.41 respectively. At  $\alpha = 0^\circ$ , only the  $A_1$  mode can be excited and received by Port<sub>1</sub>, as demonstrated in Fig. 3.35a. At  $\alpha = 90^\circ$ , only the  $A_d$  mode can be excited and received by Port<sub>1</sub>; this is also confirmed in Fig. 3.35a. Between  $\alpha = 0^\circ$  and  $\alpha = 90^\circ$ ,

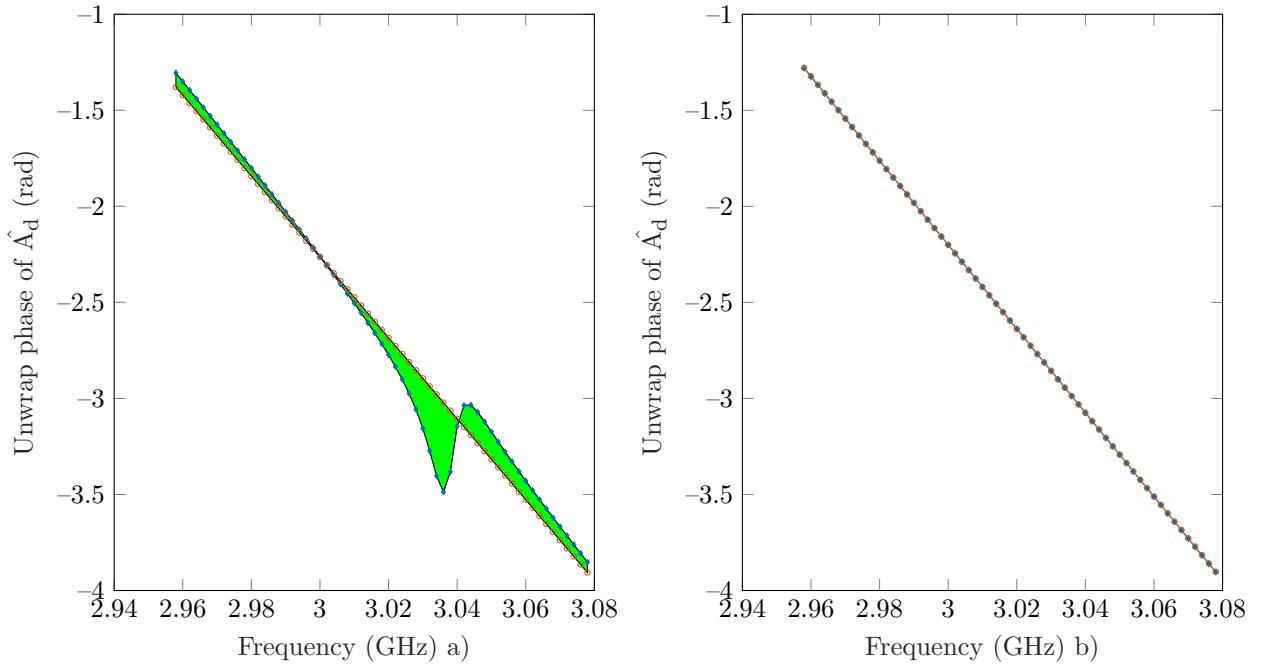


**Figure 3.40:** Phase of  $\hat{A}_d$  in red and its linear fit in blue for a)  $\hat{\alpha} = 35^\circ$  and b)  $\hat{\alpha} = 45^\circ$  for a simulated loop in CST MW with  $\alpha = 45^\circ$ . The green surface represents the difference between the phase and the fitting.

both modes are excited and a contribution of each is seen in the simulations. For the  $S_{21}$  parameter, excited modes can not be received at  $\alpha = 0^\circ$  or  $\alpha = 90^\circ$  due to the position of the loop regarding to the incident wave and the received probe. For this reason simulated E-fields corresponding to  $S_{21}$  have not been plotted in Fig. 3.41. Between  $\alpha = 0^\circ$  and  $\alpha = 90^\circ$ , the contribution of the two modes follows (3.31). So, by applying (3.32), the modes  $A_d$  and  $A_l$  can be isolated from each other. The mode that includes the tag ID ( $A_l$ ) is plotted in Fig. 3.42. By removing the dipole mode contribution, the loop mode can be found perfectly. It is also clear that the extracted curve is rotation independent (as long as  $\alpha$  is correctly estimated as it is the case in Fig. 3.42). The dipole mode  $A_d$  is plotted in Fig. 3.43 as an example. The dipole mode is clearly found, with some residual contributions of the loop mode around its resonance frequency due to numerical errors. The simulations are in good agreement with the theory, namely that it confirms the orthogonality of the two modes and therefore the possibility of separating them.

Fig. 3.39 illustrates the resolution approach to estimate the value of  $\alpha$ . The unwrapped phase of  $A_d$  is plotted versus frequency for several values of estimated  $\hat{\alpha}$ . By varying  $\hat{\alpha}$ , the criterion  $\alpha = \hat{\alpha}$  is verified when the loop mode and dipole mode are independent one of each other, i.e. when the  $A_d$  mode obtained after projection (3.32) is independent of the loop mode and therefore only the contribution of the dipole mode is present. For this reason, by looking at the phase of  $A_d$ , we know that the loop mode is not present if no non-regular variation of the phase around the resonance frequency of the loop mode is present. A numerical resolution consists of linear fitting the phase  $A_d$  near the  $A_l$  resonant frequency. The correct value of  $\hat{\alpha}$  is the one that minimizes the norm of the residues of the linear fitting. In Fig. 3.39 the loop resonator is placed with  $\alpha = 40^\circ$  and the only value

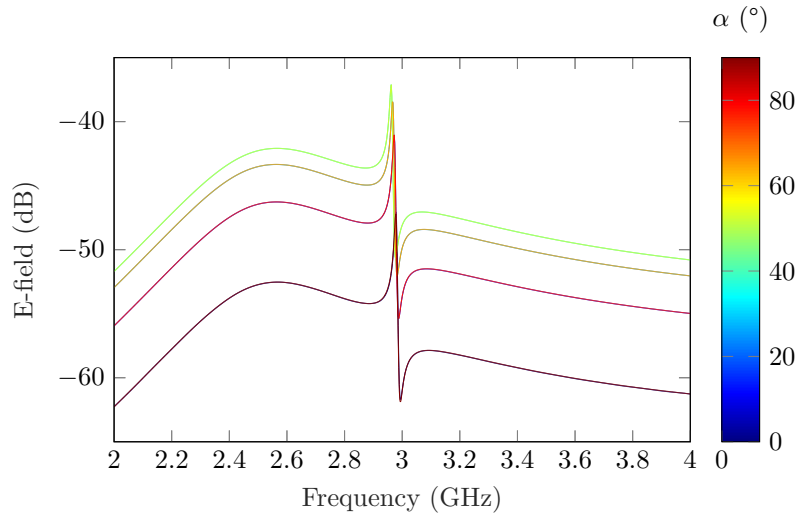


**Figure 3.41:** Simulated E-farfields corresponding to  $S_{21}$  parameter of a loop for different values of  $\alpha$ . The incoming E-field according to the resonator is shown in Fig. 3.35. The angle  $\alpha$  goes from  $0^\circ$  to  $90^\circ$  with  $10^\circ$  step.

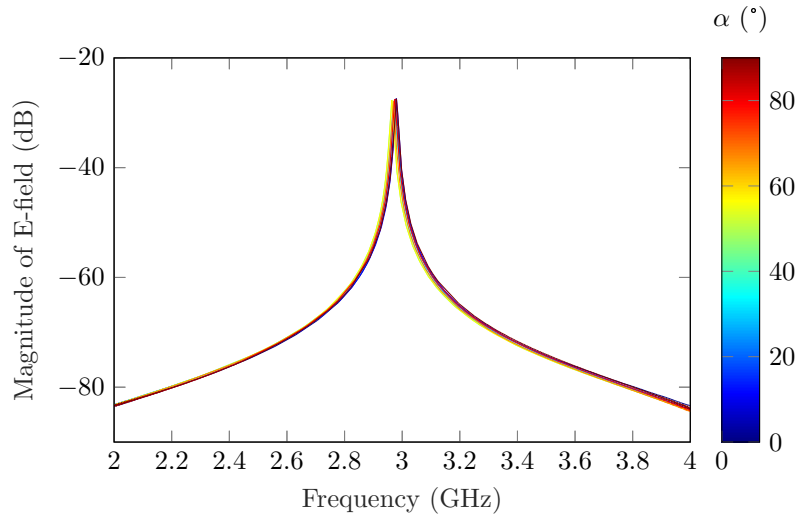


**Figure 3.42:** Extracted loop mode  $A_1$  using (3.32) for different values of  $\alpha$ .

of  $\hat{\alpha}$  that presents no phase variation on the estimated  $A_d$  is  $\hat{\alpha} = 40^\circ$ .

In general, the direction perpendicular to the loop axis, in addition to admitting the dipole resonance mode  $A_d$ , can also recover a parasitic field contribution reflected from the environment. This contribution negatively impacts the detection system. We can see that (3.32) allows to reduce this contribution, that can be considered as external noise. The reduction of these environment responses is not visible in the simulation since this effect is not taken into account in the simulator. However this significant effect will be seen in Section 3.3.5 and 3.3.6 on measurements in real environments.

For comparison with the introduced approach, time-gating (TG) technique will be applied to the loop resonator at  $\alpha = 45^\circ$ . In Fig. 3.44, the frequency response (backscattered E-fields obtained from

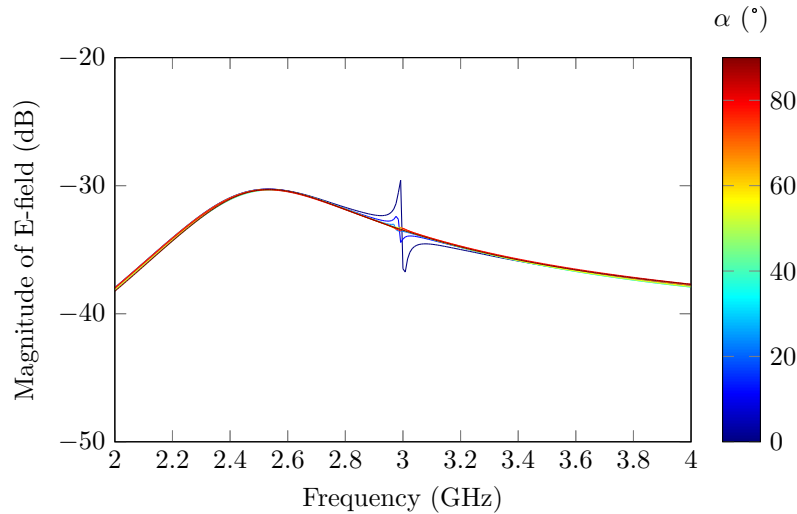


**Figure 3.43:** Extracted loop mode  $A_d$  using (3.32) for different values of  $\alpha$ .

a probe on CST with plane wave excitation, i.e. quantities similar in measurement to the parameters  $S_{11}$  and  $S_{21}$ ) of the simulated loop is presented along the extracted modes  $A_d$  and  $A_1$ . We can see that the mode of interest  $A_1$  is correctly extracted. If we look at the time domain representation of the E-fields in Fig. 3.45, we can see that it is difficult without any post processing to differentiate the different modes in the response. Now if we apply (3.32) on these time signals, we can compute the time response of each mode as illustrated in Fig. 3.46.

The mode  $A_1$  is resonating for a longer time than the mode  $A_d$  due to its higher Q-factor. From Fig. 3.46, to remove the response of  $A_d$  from the signal, a time-gating with a  $t_{\text{start}} = 7\text{ns}$  is needed. With such  $t_{\text{start}}$ , time-gated signals TG  $S_{11}$  and TG  $S_{21}$  are presented in Fig. 3.47. We can see that the  $A_1$  mode present in TG  $S_{11}$  and TG  $S_{21}$  is also partly removed hence the peak apexes of these two curves have lower amplitudes. Indeed, the time-gated signal is 8dB lower than the  $A_1$  mode. This is because the time-window 7ns on  $S_{11}$  or  $S_{21}$  also remove  $A_1$ 's signal as showed in its time response in Fig. 3.46. Furthermore, as said previously, it is difficult to estimate  $t_{\text{start}}$ . In practice, to limit the effect of the presence of the object on which the tag is fixed, one can choose to cut off the order of 1ns from the maximum of the time response signal (which here makes  $t_{\text{start}} = 4.5\text{ns}$  - see Fig. 3.46). In this case, the result that we would have is presented in Fig. 3.48. We can see that the time-gated signals are not as pure as the  $A_1$  signal. The problem in this case is that if for a given ID, another scatterer could resonate around 2.4 GHz, it would be impacted by the presence of the  $A_d$  mode. The peak amplitude is also lower than the  $A_1$  amplitude by 6dB. Since less signal was removed (2.5ns time-window difference), the amplitude difference with  $A_1$  is lower. Finally, if we compare the results between Fig. 3.47 and 3.48, we can say that the approach introduced here allows us to suppress the entire spurious mode. If we had tried to cut the spurious mode with time-gating (Fig. 3.47 or Fig. 3.48), we would have significantly degraded the useful signal, reducing the signal-to-noise ratio and thus the read range.

In summary, the proposed method allows to improve the reading robustness of the resonant scatterers. This approach can be advantageously used in combination with the time-gating method (see

section 3.3.8). It allows to isolated different resonance modes that time-gating can hardly separate.

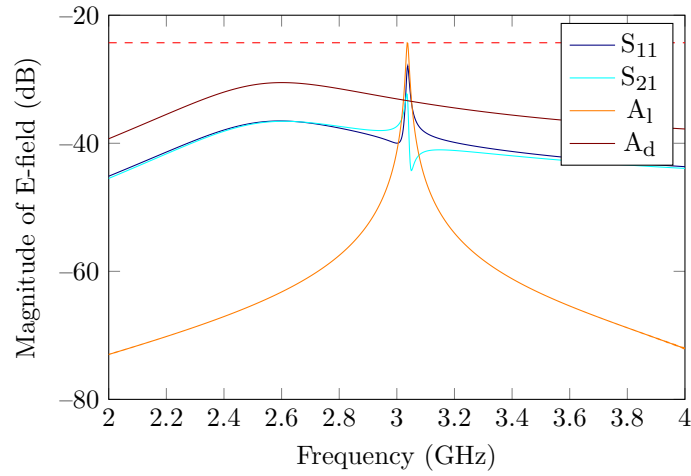


**Figure 3.44:** Frequency response of E-fields corresponding to S-parameters of a simulated loop at  $\alpha = 45^\circ$  along with  $A_d$  and  $A_1$  obtained with (3.32).

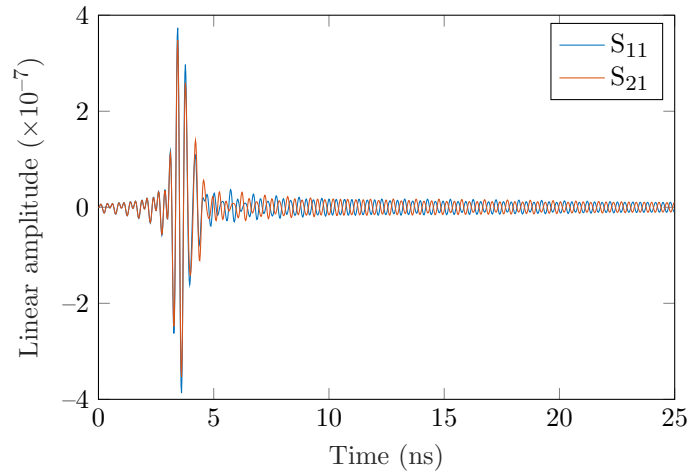


**Figure 3.45:** Time domain representation of E-fields corresponding to S-parameters plotted in Fig. 3.44 of a simulated loop at  $\alpha = 45^\circ$ .

### 3.3.4 Measurements

The test-bench setup is presented in Fig. 3.49. Experimental measurements are performed using a VNA (Agilent 5222A). The source power of VNA is equal to 0 dBm. The frequency sweep ranging from 2 to 3 GHz with 10001 points is used. A co-polarization bistatic configuration with Satimo (QH2000) quad ridged open boundary antennas (2–32 GHz) is used. The measurements are done in a real environment with people in close proximity. A first measurement is done without the resonator. After that the resonator is placed in front of the antenna and the first measurement is subtracted to the new measurements to remove the response of the environment. The loop resonator can rotate for different values of  $\alpha$  ( $\alpha = 0$  corresponds to the direction of Port 1). A spacer in polystyrene of 5 cm is

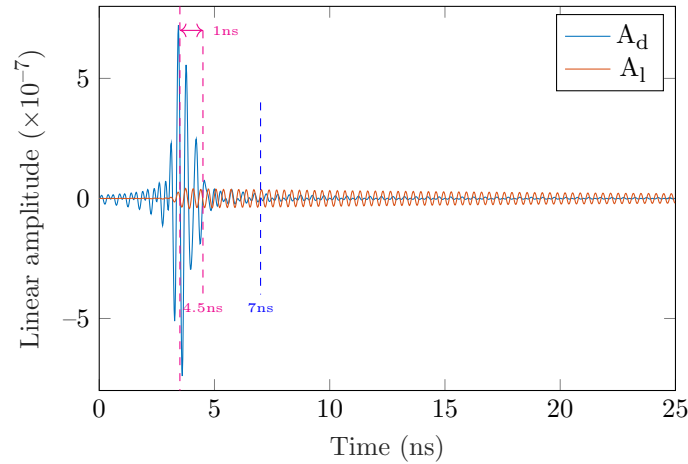


**Figure 3.46:** Time response of  $A_d$  and  $A_1$  obtained with (3.32) for a simulated loop at  $\alpha = 45^\circ$ .

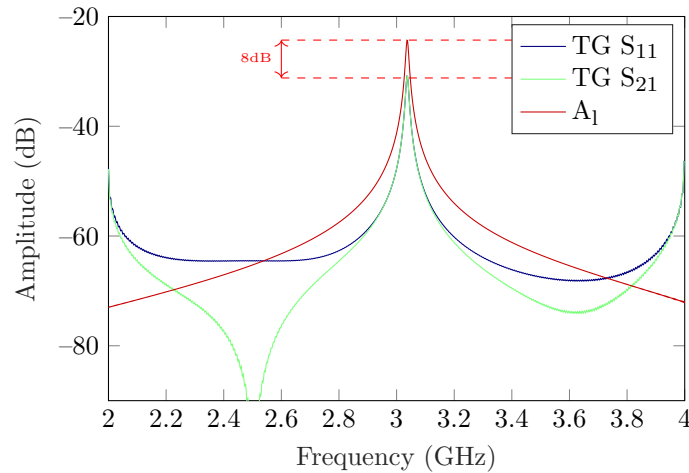


**Figure 3.47:** Comparison of time-gated S-parameters with  $t_{\text{start}} = 7\text{ns}$  and  $A_1$  obtained with (3.32).

used to separate the resonator from the antenna. A protractor is placed under the loop to measure  $\alpha$  as the resonator rotates.  $S_{11}$  and  $S_{21}$  measurements are done and plotted in Fig. 3.50 and Fig. 3.51 respectively.  $S_{11}$  are in good agreement with the simulation, but  $S_{21}$  presents a dip instead of a peak at the resonance frequency. This is due to a phase opposition between the resonator contribution and the environment (not considered in simulation). With these S-parameters and the dipole mode  $A_d$  phase,  $\alpha$  is estimated as previously explained. The angle value  $\alpha$  measured with the protractor can be compared with the estimated  $\hat{\alpha}$  and both values are listed in Table 3.7. The estimated and real angle values are in good agreement with a maximum difference of  $5^\circ$ . This shows that the method can also be used to determine the angle of the loop to the antenna. When  $\alpha$  is found, (3.32) is used to extract the loop mode  $A_1$  which is plotted in Fig. 3.52. Like in simulation (Fig. 3.42), we can see that the peak is more visible when (3.32) is applied but also that the peak does not change with  $\alpha$ . The noise is higher for the measurement at  $\alpha = 60^\circ$  which is also the measurement where the guessed  $\hat{\alpha}$  has the highest error of  $5^\circ$ . The dipole mode  $A_d$  is plotted in Fig. 3.53 for illustration.

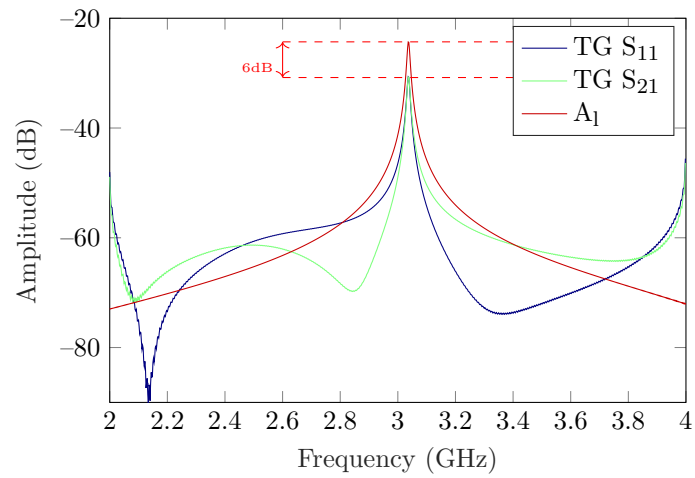


Figure 3.48: Comparison of time-gated S-parameters with  $t_{\text{start}} = 4.5\text{ns}$  and  $A_1$  obtained with (3.32).



Figure 3.49: Measurement setup.

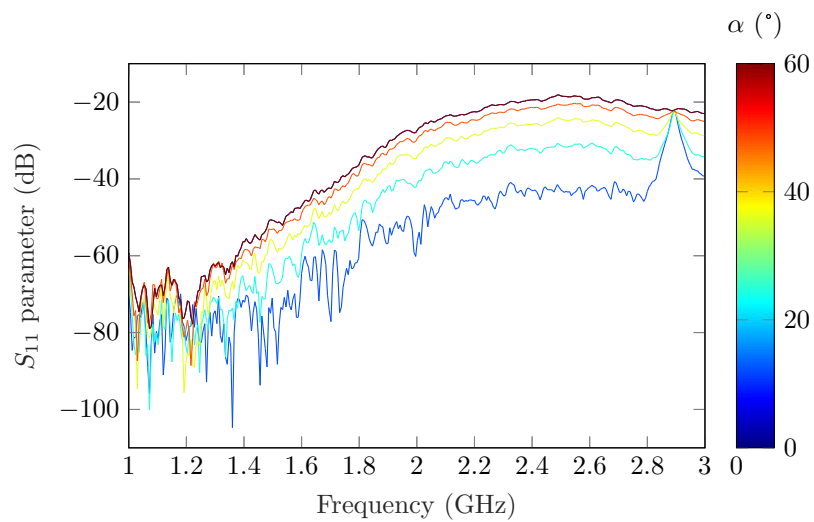
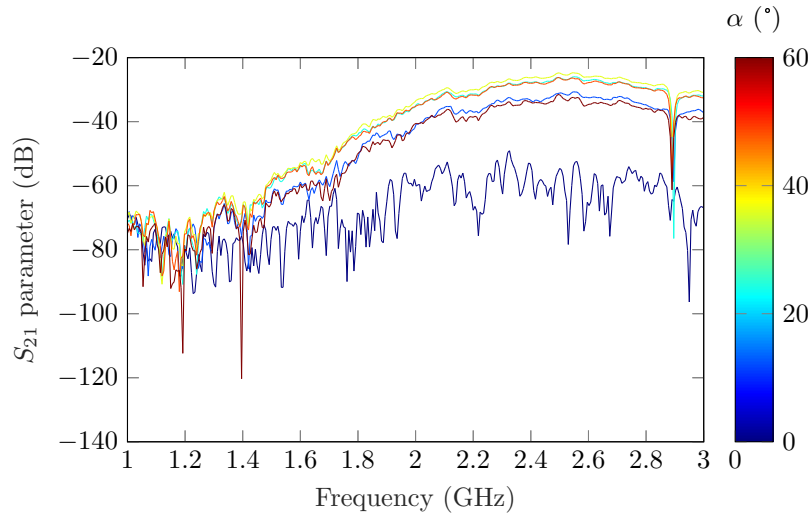
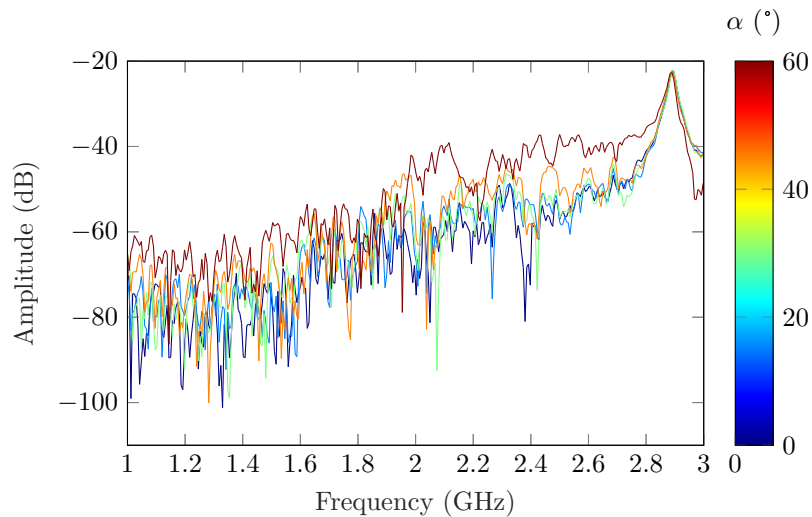


Figure 3.50: Measured  $|S_{11}|$  parameter of the loop for different rotation angles  $\alpha$ .





**Figure 3.51:** Measured  $|S_{21}|$  parameter of the loop for different rotation angles  $\alpha$ .



**Figure 3.52:** Extracted loop mode  $A_1$  (magnitude) for different rotation angles  $\alpha$  using (3.32) and the estimated  $\hat{\alpha}$ .

When a chipless RFID tag is composed of several loop resonators, the technique is still valid; it is even more efficient because the dipole mode of each loop can impact a loop mode of another loop. Also the possibility to remove it will increase the peaks prominence of each scatterer. This idea is presented in Fig. 3.54 where a tag of 4 loop resonators is placed at  $\alpha = 45^\circ$ . The raw measurement where the environment is subtracted with a first measurement gives the  $S_{11}$  parameters in orange where prominence of each resonator peak is quite low. Equation (3.32) is applied resulting in the improved ratio between the amplitude of loop modes and noise. The residual environment as defined in [23] is reduced by -12dB in minimum.

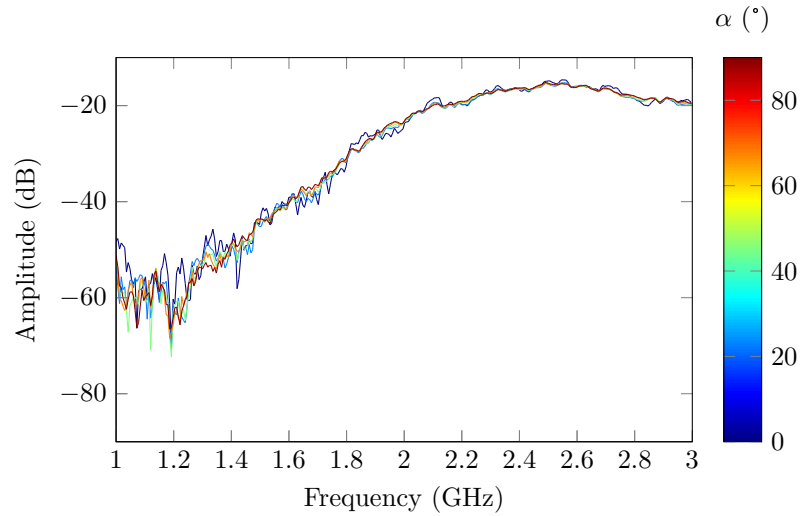


**Figure 3.53:** Extracted dipole mode  $A_d$  (magnitude) for different rotation angles  $\alpha$  using (3.32) and the estimated  $\hat{\alpha}$ .

**Table 3.7:** Real angle  $\alpha$  and estimated angle  $\hat{\alpha}$  using the phase of  $A_d$ .

Real angle $\alpha$	$0^\circ$	$15^\circ$	$30^\circ$	$45^\circ$	$60^\circ$
Estimated angle $\hat{\alpha}$	$0^\circ$	$14^\circ$	$30^\circ$	$45^\circ$	$65^\circ$

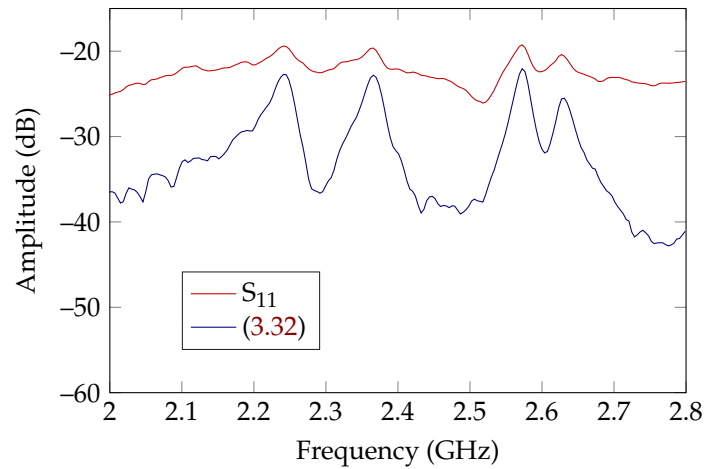


**Figure 3.54:** Comparison of the  $S_{11}$  measurement and the post-processing done with (3.32) on a tag composed of 4 loop resonators placed at  $45^\circ$ .

### 3.3.5 Impact of highly reflective environment

In this paragraph, we want to emphasize the improvement of the reading robustness of this approach according to the environment. The introduced method eliminates the total contribution of the environment and the tag oriented perpendicular to the preferred reading direction ( $E_1$ ). The measurement setup in this highly reflective environment is illustrated in Fig. 3.55. A metallic plane is placed below the loop resonator to increase the reflection of the incoming electromagnetic wave, introducing a

higher residual environment. A spacer of polystyrene is used to reduce the coupling effect between the loop and the metallic plane that would change the scatterer resonant frequency. The measured S-parameters of this configuration are presented in Fig. 3.56 when the resonator is placed at  $45^\circ$ . Raw S-parameters and S-parameters with an empty measurement (with the metallic plate) are compared in Fig. 3.56. Note that the peak corresponding to the resonance frequency is hardly visible for  $S_{11}$  and  $S_{21}$  with the metallic plane used as an empty measurement. If (3.32) is applied to the measured S-parameters with empty, the resonance frequency is easily observable with a peak prominence of 10dB. Time-Gating (TG) post processing is used for comparison with optimised  $t_{\text{start}} = 3\mu\text{s}$  and  $t_{\text{stop}} = 3.1973\mu\text{s}$ . Results are presented in Fig. 3.57. We can notice that (3.32) gives a better peak prominence than TG (10dB higher) because it is able to use 100% of the resonator useful signal (6dB) as well as it compensates for the resonator misorientation (4dB). Measurements have been achieved for different a priori unknown orientation angles  $\alpha$  of the resonator in front of the metallic plane. Extracted  $A_1$  modes using (3.32) are plotted in Fig. 3.58. We can see that the residual environment is always reduced while the resonator amplitude remains constant when the resonator rotates since the total energy is conserved during the post processing.

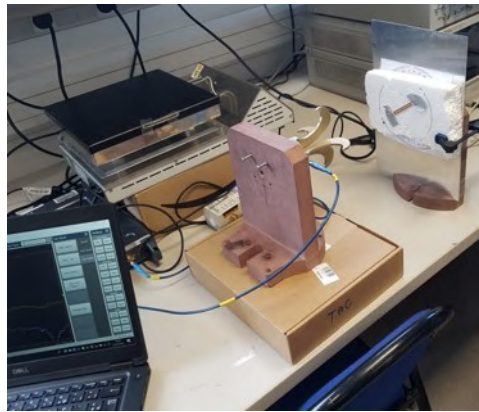


**Figure 3.55:** Measurement setup used to measure a loop resonator on a highly reflective support.

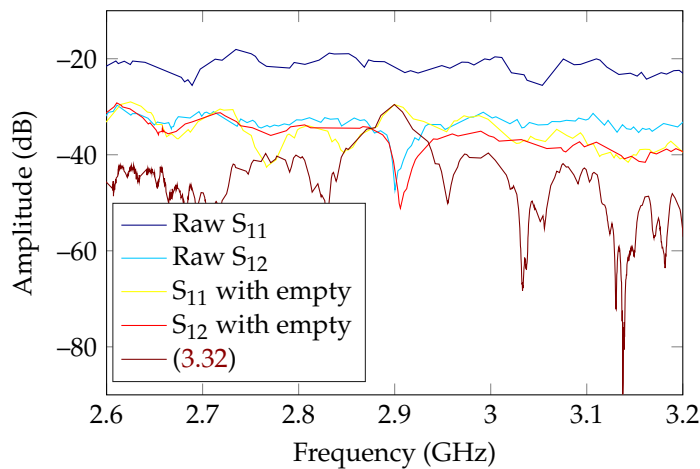


**Figure 3.56:** Measured  $S_{11}$  and  $S_{21}$  of the loop resonator at  $45^\circ$  in front of a metallic plane (see Fig. 3.55) compared with the use of (3.32).

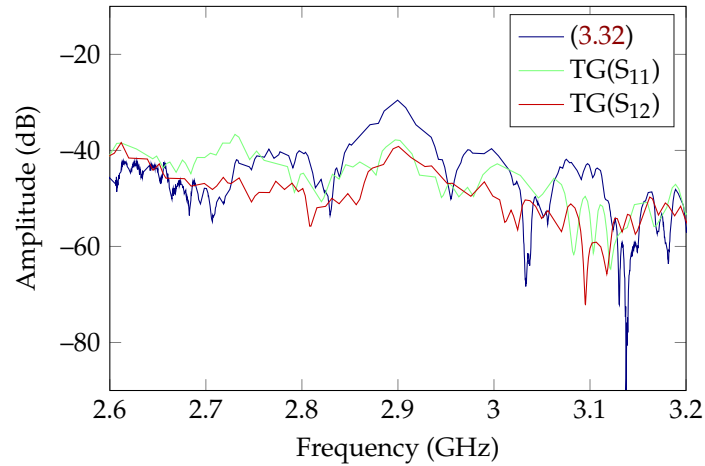


**Figure 3.57:** Extracted loop mode  $A_1$  of the loop resonator at  $45^\circ$  in front of a metallic plane (see Fig. 3.55) with (3.32) compared with the time-gating (TG) method. Angles are not apriori known.

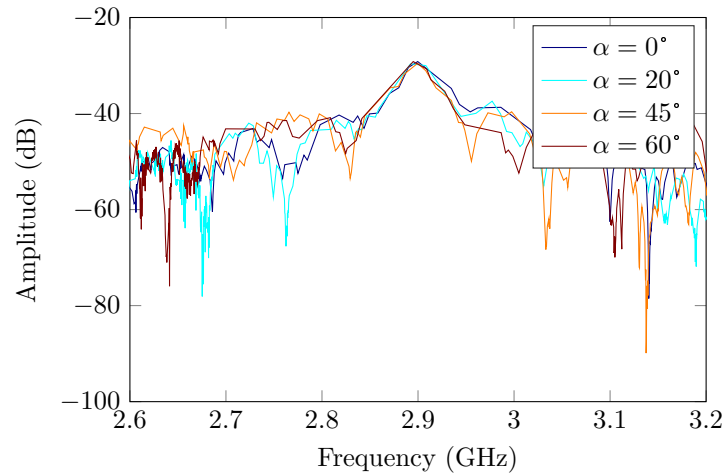


**Figure 3.58:** Extracted mode  $A_1$  of the loop resonator for different angles  $\alpha$  in front of a metallic plane (see Fig. 3.55) with (3.32).

### 3.3.6 Impact of the distance

A study of the readable distance of a chipless tag has been done. The test bench used for this measurement is illustrated in Fig. 3.59. The resonator is placed on a polystyrene support above the antenna. S-parameters are measured and then the distance between the antenna and the tag is increased from  $d = 1.5\text{cm}$  to  $84.5\text{cm}$  by adding a new polystyrene support. For each distance,  $S_{11}$  and  $S_{21}$  raw measurements are compared with the proposed approach (3.32) as well as with the  $S_{11}$  and  $S_{21}$  parameters where TG is applied. For each distance, TG parameters' ( $t_{\text{start}}$  and  $t_{\text{stop}}$ ) are deduced from the inverse Fourier transform of the S-parameters to maximized the accuracy of the response.

The loop resonator is placed at  $\alpha = 45^\circ$ . Comparisons for distances  $d = 1.5\text{ cm}$  and  $d = 20.5\text{ cm}$  are plotted as examples in Fig. 3.60 and Fig. 3.61 respectively. A quantitative criterion was chosen to consider if a loop resonator can be read or not. The criteria are the following : the peak prominence

should be +10dB or higher, the maximum amplitude in a frequency span of 0.15 GHz must be greater than -50dB (this must correspond to the amplitude of the resonance peak). This procedure is done using the *findpeak* function in Matlab. Results are presented in Table 3.8 where a “1” indicates that the peak is detected and a “0” when it is not, considering these criteria. We can see that for a loop resonator placed at 45°, these criteria are never valid for raw measurements of  $S_{11}$  and  $S_{21}$  because the +10dB peak criterion can not be met due to the presence of the  $A_d$  mode and the environment response. With the TG technique, it is possible to satisfy correctly this criterion up to 64,5 cm. After that, the signal amplitude goes below the -50dB threshold and the peak predominance of +10dB with the environment noise is not respected. The limitation of the TG approach is due to the fact that : some part of the useful signal will be removed hence deteriorating the peak signal. On the contrary, the idea introduced here is that when doing the projection with (3.32), we are retrieving 100% of the useful signal while reducing others parasitic signals, hence keeping a better peak prominence. By using (3.32), the peak is better marked as shown in Fig. 3.60 and Fig. 3.61 allowing an increase of 30 cm compared to the TG on a readability with a maximum distance of 84,5 cm.



**Figure 3.59:** Measurement setup used to study the readable distance of the resonator.

The tag is now composed of 4 resonators and is measured as a function of distance. The same tag configuration as the one presented in Fig. 3.54 is used. The same criteria as previously described are used with a frequency span of 0.65GHz for resonators between 2.2 GHz and 2.7 GHz (see Fig. 3.54). The number of peaks correctly detected up to 4 are plotted in Table 3.9. We can see that raw  $S_{11}$  and  $S_{21}$  never succeed to respect these criterion for the 4 resonant frequencies. Since the tag is now composed of 4 resonators, the post-processing to implement the TG approach is harder since higher resonant frequencies tend to attenuate sooner in time than lower frequencies. Choosing a lower  $t_{start}$  allows to capture more high frequency signal but also environment noise. For these reasons, the TG method is not able to respect the imposed criterion as soon as the distance is higher than 13 cm. However, the proposed approach allows to see the 4 peaks up to 34 cm. Notice that reading distance decreases because the tag composed of 4 resonators has resonators with a lower Q-factor than the resonator used alone (see Table II).

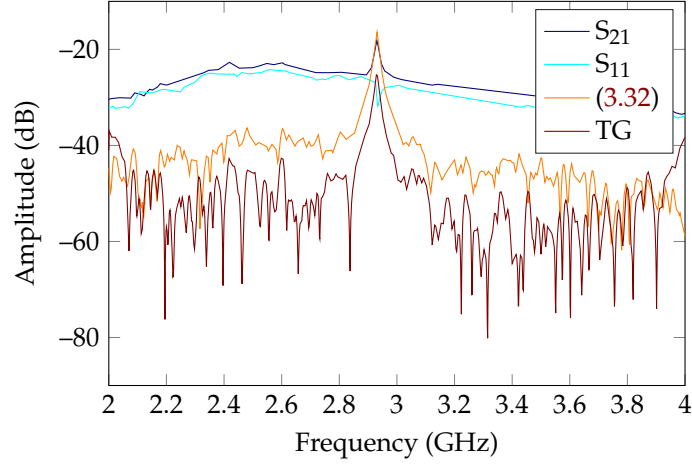


**Figure 3.60:** Raw S-parameters and post-processed S-parameters [with (3.32) and TG] for a distance between the resonator and the antenna of  $d=1.5$  cm.

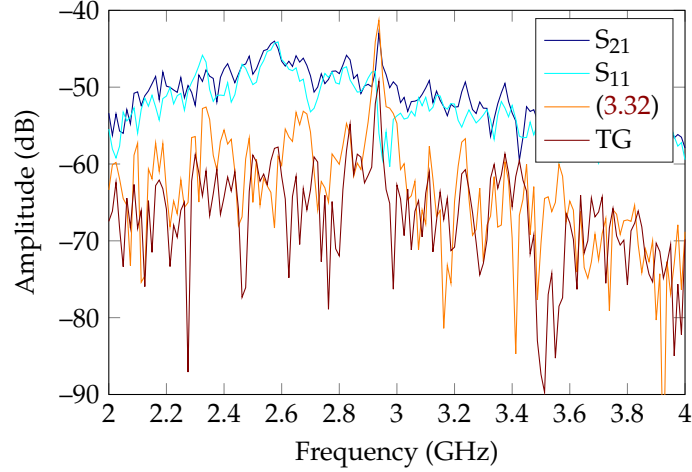


**Figure 3.61:** Raw S-parameters and post-processed S-parameters [with (3.32) and TG] for a distance between the resonator and the antenna of  $d=20.5$  cm.

### 3.3.7 Case of an antenna not placed in normal incidence with respect to the tag

In the previous cases, the loop resonator is rotated in the  $xOy$  plane and the antenna is placed in a plane parallel to the  $xOy$  plane. In a more general case, the antenna is aiming at the resonator not necessarily in a parallel plane. In this case, a spherical coordinate system can be attached to the loop to indicate the position of the antenna as illustrated in Fig. 3.62. The dual-port antenna will sense the fields along the axis  $\vec{\vartheta}$  and  $\vec{\varphi}$ . By noticing that :

$$\begin{cases} \vec{r} = \sin(\vartheta) \cos(\varphi)\vec{x} + \sin(\vartheta) \sin(\varphi)\vec{y} + \cos(\vartheta)\vec{z} \\ \vec{\vartheta} = \cos(\vartheta) \cos(\varphi)\vec{x} + \cos(\vartheta) \sin(\varphi)\vec{y} - \sin(\vartheta)\vec{z} \\ \vec{\varphi} = -\sin(\varphi)\vec{x} + \cos(\varphi)\vec{y} \end{cases} \quad (3.33)$$

**Table 3.8:** Research of the peak resonance (Prominence of +10dB on a frequency span of 0.15GHz around the resonance frequency and above -50dB of amplitude).

Distance (cm)	S <sub>11</sub>	S <sub>21</sub>	(3.32)	Time-Gating
1.5	0	0	1	1
13.5	0	0	1	1
20.5	0	0	1	1
27.5	0	0	1	1
39.5	0	0	1	1
44.5	0	0	1	1
49.5	0	0	1	1
54.5	0	0	1	1
59.5	0	0	1	0
64.5	0	1	1	1
74.5	1	1	1	0
79.5	0	0	1	0
84.5	1	0	1	0

**Table 3.9:** Number of peaks detected of +10dB on a frequency span of 0.65GHz and above -50dB of amplitude.

Distance (cm)	S <sub>11</sub>	S <sub>21</sub>	(3.32)	Time-Gating
3	1	1	4	4
13	1	1	4	2
23	0	0	4	2
34	0	2	4	2
44	0	1	3	0

The polarization of the loop resonator can be projected to the xOy plane using (3.33) and (3.32) can be applied. The scattered field for the loop polarization  $A_1$  can be estimated with :

$$A_1 = \frac{-E_\varphi \sin(\vartheta) - \tan(\alpha_y) [\cos(\varphi) \cos(\vartheta) E_\varphi + \sin(\varphi) E_\vartheta]}{\sin(\vartheta) \sin(\varphi)} \quad (3.34)$$

Notice in (3.33) that the loop resonator also radiates energy on the  $\vec{r}$  which is not measured by the antenna. For this reason, a constant amplitude of the estimated mode for varying values of  $\alpha_y$  is not verified there. Simulations have been done using CST MW with an antenna placed at  $\vartheta = \varphi = 80^\circ$  and results for a rotation of  $\alpha_y = 50^\circ$  is plotted in Fig. 3.63. We can see once again the utility of the approach with a residual environment reduced by 25dB in this example.

Measurement in a semi-anechoic chamber were done to validate (3.34). The measurement setup is shown in Fig. 3.64 and results in Fig. 3.65. We can see that the peak amplitude is increased by almost 5dB but most importantly, the dipole mode of the loop is reduced by almost 10dB hence confirming the approach.

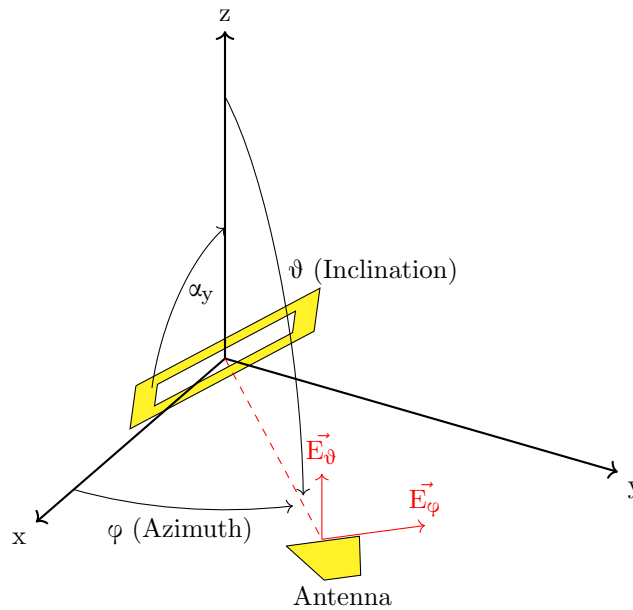


**Figure 3.62:** Loop scatterer, coordinate system and notations. The antenna is placed considering the angles  $\vartheta$  and  $\varphi$ . The resonator is placed in the  $xOz$  plane and rotates around the  $\vec{y}$  with an angle  $\alpha_y$ .

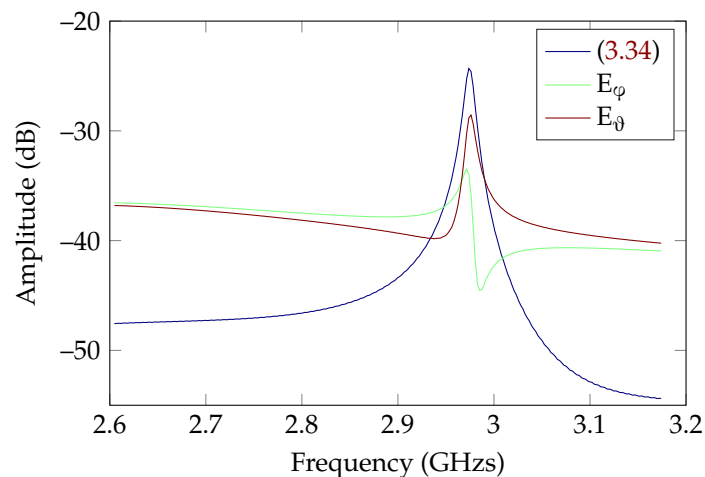


**Figure 3.63:** Simulated S-parameters on a loop resonator with  $\alpha_y = 45^\circ$  with an incoming wave excitation along  $E_\vartheta$  and  $\vartheta = \varphi = 80^\circ$ .

### 3.3.8 Example with other resonator's shapes

#### Example with other resonator's shapes

While a loop resonator was considered until now, this principle can be applied to other resonators shapes and types. In this section, resonators without ground plane illustrated in Fig. 3.66 will be used as different examples. These resonators can be found in different works such as in [69]. Simulations have been done as in Section 3.3.3. For the square loop, dimensions were  $l = 25\text{mm}$ ,  $w = 1.4\text{mm}$ . For the circular loop, the same  $l$  and  $w$  were kept. Results are displayed in Fig. 3.67 and Fig. 3.68



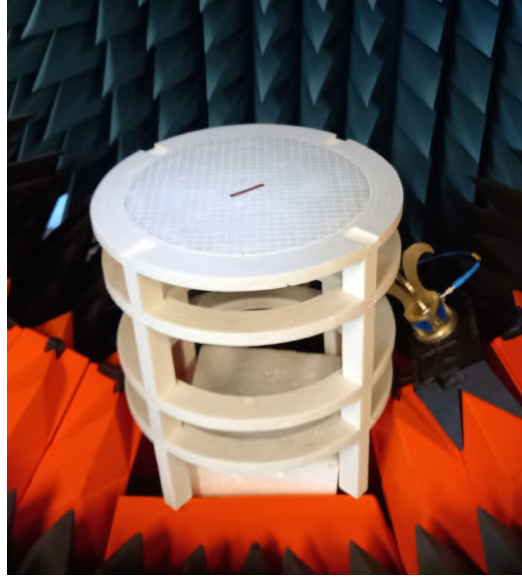


**Figure 3.64:** Measurement setup to validate (3.34). The antenna is placed at  $\vartheta = 90^\circ$  and  $\varphi = 80^\circ$ . The loop is rotated with  $\alpha_y = 45^\circ$ .

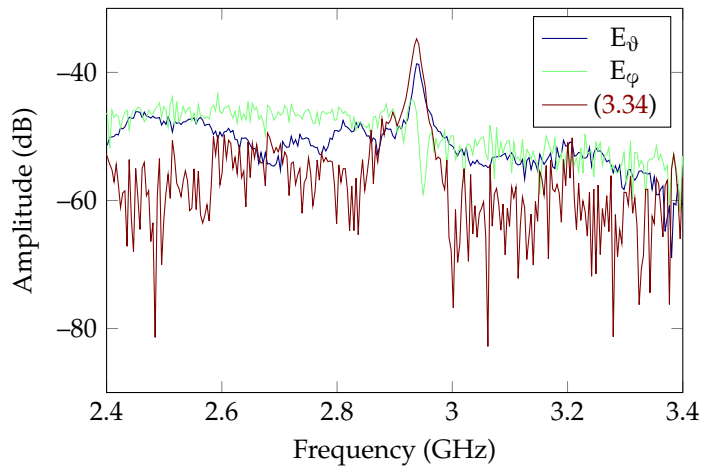


**Figure 3.65:** Measured S-parameters on a loop resonator with  $\alpha_y = 45^\circ$  with an incoming wave excitation along  $E_\theta$ .

respectively for the rectangular and circular resonators.

We can see that the highest Q-factor mode for these resonators' shape is well extracted, again with an amplitude higher than the one given by S-parameters. Once again, this shows the advantage of (3.32) over raw measurements. This method is straight-forward for resonators with no ground plane so the following section will discuss about resonators with ground plane where additional considerations have to be taken into account.

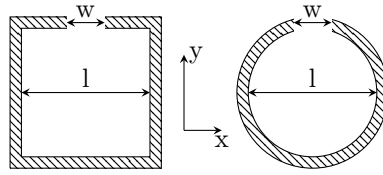


Figure 3.66: Square and circular resonator topology.

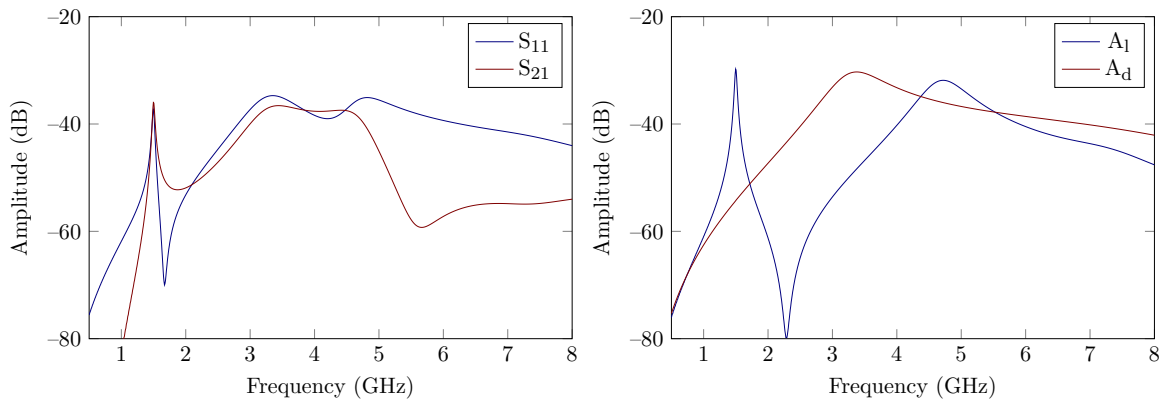


Figure 3.67: Square resonator topology frequency response for  $\alpha = 40^\circ$ .

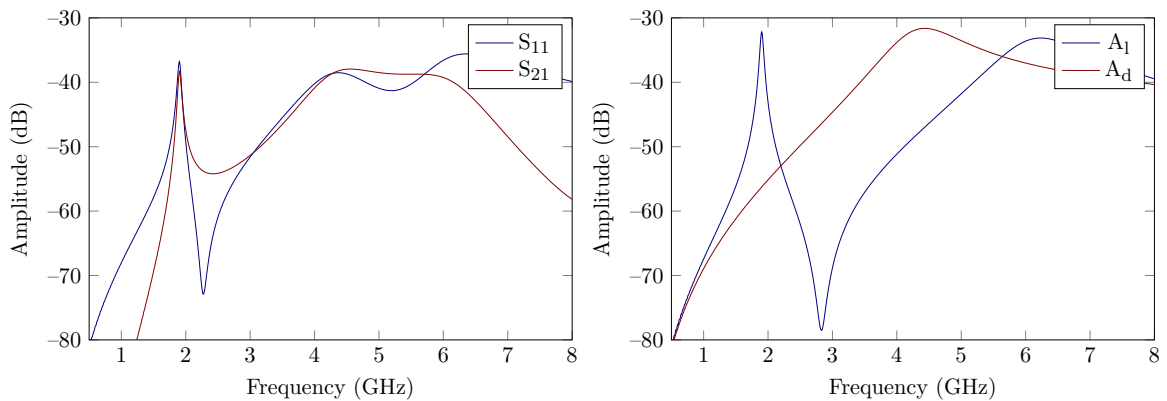


Figure 3.68: Circular resonator topology frequency response for  $\alpha = 50^\circ$ .

### Applications to resonators with ground plane

The same concept can be applied to different types of scatterers. In this section a resonant scatterer-based microstrip transmission-line (TL) is considered. In its simplest form, the scatterer is a metallic strip (a short-circuited dipole) above a ground plane. This scatterer can be considered as a TL terminated at both ends by an open circuit. This resonator is illustrated in Fig. 2.27.

These scatterers have a high Q-factor (around 120 at 3GHz) but due to the presence of the ground plane, these scatterers also exhibit a strong quasi-optic reflexion (comparable to the  $A_d$  mode discussed for the loop) making them hard to read. For this reason, this resonator is commonly placed at  $\alpha = 45^\circ$  and measured using cross-polarization ( $S_{21}$ ) to reduce the ground response contribution. As a consequence, the reading of such tag can only be done for a fixed orientation (limiting its usage

in real applications) but also the resonator signal backscattered on the co-polarization ( $S_{11}$ ) is not used. In Section 3.3.5, the highly reflective support was removed using an empty measurement of the metallic plate. This method being hard to implement in practice, in this section, the use of both (3.32) and TG jointly is presented to improve the measurements. The angle  $\alpha$  can still be known a priori or estimated as presented in Section 3.3.2. The TG will allow to remove the ground plane response and then (3.32) can be applied on the TG responses to retrieve more signal using both polarizations. CST MW simulations with the tag illustrated in Fig. 2.27 have been done and are plotted in Fig. 3.69.

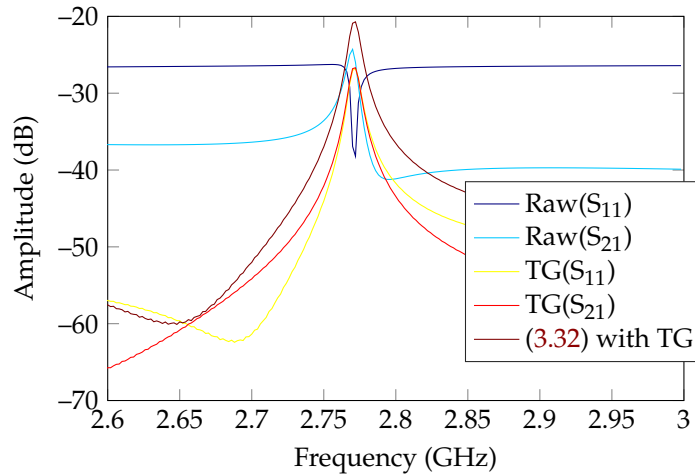


**Figure 3.69:** Simulated raw S-parameters and post-processed S-parameters [with TG and (3.32) with TG] for a microstrip resonator with  $\alpha_y = 45^\circ$ .

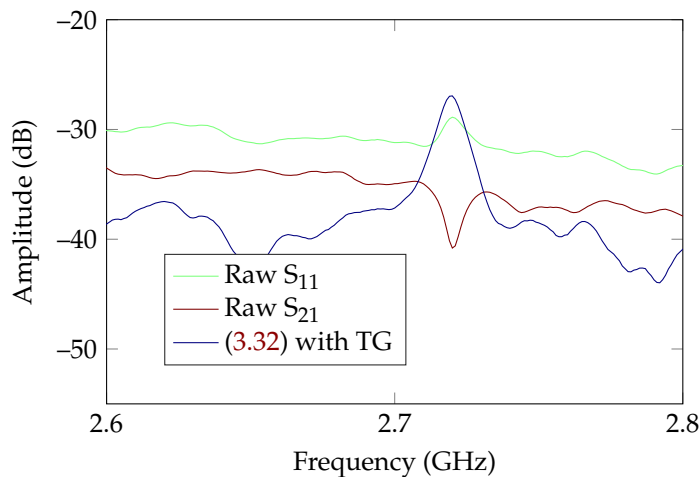


**Figure 3.70:** Measured raw S-parameters and post-processed S-parameters [(3.32) with TG] for a microstrip resonator with  $\alpha_y = 45^\circ$ .

We can see the presence of the ground plane on the raw S-parameters with the low prominence of the resonance peak. The responses of TG allowed to increase the peak prominence by removing successfully the ground plane response. Then when (3.32) is applied on TG, the peak amplitude is even higher by 6dB. Note that while the TG responses are dependent of the orientation of the

resonator, when (3.32) is applied on TG, the response is no longer orientation dependent as shown in previous section.

Measurements of the microstrip resonator of Fig. 2.27 are achieved using the same test-bench presented in Fig. 3.64. Raw measured S-parameters as well as (3.32) with TG are presented in Fig. 3.70. The TG window is  $t_{\text{start}} = 3.5e-9$  and  $t_{\text{stop}} = 6e-8$ .

### 3.3.9 Discussion

The method presented here allows by a projection to separate the useful signal (signal related to the loop mode) from the signal without information, namely the whole signal which is perpendicular to the excitation direction of the loop mode. It is now interesting to come back on the positioning of this method compared to the methods classically used in RFID chipless to read a tag, in particular the use of the background subtraction, the reading in cross-polarization and the time-gating. A general detailed comparison of these methods was made in the introduction of the article so the discussion here will focus on the link between these methods and the one introduced. We are interested in how these methods can interact with the introduced one in order to improve the chipless tag reading.

#### Link with the background subtraction

It is difficult in chipless to perform a tag reading without performing a background subtraction. This can be seen from the very limited number of articles on the subject, especially when the tag is positioned next to different objects [48]. Moreover, the use of background subtraction is not necessarily prohibitive for a real application. Indeed, it is similar to calibrating the device, once the system is started. However, it should be kept in mind that if the environment changes after this calibration measurement, the system must still be able to obtain accurately the identifier, so in this case it would be necessary to perform other calibration measurements over time when the tag is not present in front of the reader antennas. So, a background subtraction calibration is compatible with the practice, however, it can only take into account the fixed part of the environment of the system, like for example the effect of the antennas (matching, coupling), and part of the direct reflections on the walls, ceiling (supposedly fixed). Even if these contributions (background subtraction relative to the fixed part of the environment) are not sufficient to allow the reading of a tag without other dedicated techniques when adding objects to the scene, a very important part of the signal not related to the tag ID is subtracted. This is why it is still preferable to use background subtraction and this is what has been done in the article.

#### Link with cross polarization reading

The objective of the introduced method is to read a classical chipless tag whatever its orientation and in order to recover the whole useful signal. This is why we use both co-polarization and cross-polarization measurements ( $S_{11}$  and  $S_{21}$  in [4]). This method is different from a classical cross-polarization measurement and therefore cannot be combined together. Compared to a co-polarisation measurement, cross-polarization reading is still very efficient in that it reduces the signal by about 25 dB (to keep only the part containing the tag information). However, except for very special tag

designs (with a rotation invariant cross-polarization), the reader antennas must be oriented in a specific way with respect to the environment and similarly for the tag with respect to the antennas [45]. Furthermore, unlike the approach introduced here, a cross-polarization measurement only recovers a quarter of the power of the useful signal and this for an optimal orientation of the tag with respect to the antennas. Finally, we can see from the two examples presented here (rectangular loop and microstrip dipole) that the cross-polarization measurement alone is not sufficient. If we take the rectangular loop with an optimal position ( $45^\circ$ ) for this type of reading, according to (3.32) we have  $S_{21}$  equal to  $(A_d + A_1)/2$  which shows that we are not able to isolate the useful signal, namely  $A_1$ . Similarly, for the tag with microstrip dipole, the ground plane can have a cross-polarization reflection which will be visible on the  $S_{21}$  parameter. This is exactly what we have in Fig. 3.69, where the Raw  $S_{21}$  curve shows a dip (and not a peak) characteristic of the presence of a significant reflection not related to the resonance of the tag (quasi optic reflexion). In conclusion, we can say that the cross-polarization measurement is all the more interesting when used with time-gating. On its own, it does not provide an answer to all the problems of chipless reading, but it may prove indispensable in practice.

### Link with time-gating

What allows to read a tag in a very robust way (e.g. without background subtraction in a mobile environment or with objects near the tag that potentially move), is the use of time-gating combined with a tag with a high-quality factor (higher than 100). It is precisely this idea that has been implemented in [45] and that allowed to read tags without background subtraction. We show that we can temporally separate the quasi-optical reflections of the environment from the ones linked to the resonances of the tag which is spread over more than ten nanoseconds. By optimizing the time window on which the useful signal is recovered, it is possible to read some tags in mobile environments presenting various objects. Of course, the reading in cross polarization, as it is the case for the background subtraction, improves the reading when the environment is perfectly fixed and especially can be combined with the time-gating to further improve reading. However, time-gating cannot always be applied successfully, and the rectangular loop is a very good example. Indeed, for some angles, the dipole mode will be excited, and this mode is resonant (weakly resonant, but resonant all the same) which means that temporally, it will exist over several nanoseconds, which to eliminate it would lead to use a  $t_{start}$  of the same duration and thus cut off too much of the useful signal. From then on, it would no longer be possible to read the loop mode with a sufficiently high SNR and this for a distance greater than 20 cm. This example highlights one of the many interests of the proposed method. Indeed, it is quite possible to add to the described approach a time gating step (the time gating step can be performed on the raw signal as well as after the method described here, it is theoretically identical). The difference here is that the  $t_{start}$  to be considered will no longer be linked to the dipole mode (the latter will be eliminated by the method introduced in the article) but only to the environment, which means that it can be reduced to one nanosecond, for example, in order to eliminate the non-resonant part of the signal and thus keep only the part where the information is coded.

### 3.3.10 Conclusion of the section

In this section, a novel method based on polarization separation is presented to increase the peak prominence of the co-polarized chipless tag independently of the resonator orientation. The theory has been validated in simulations and with real-life measurement with both known and unknown orientations of the resonator. The presented results highlights the potential of the approach to increase the robustness of reading. In addition, this approach also allows the orientation of the tag to be determine, which provides additional information that can be used for sensor applications. The improvement was also quantified in terms of maximum reading distance. A comparison with the commonly used TG technique is presented as well as the jointly use of both methods to harsh environments.

## 3.4 Perspectives

As we have seen previously, it is possible to express the radiation pattern of a loop resonator, using antenna array theory, with the following formula :

$$E_s(f_0) = E_d \times AF_0 = k_0 T_0 \sin(\vartheta) \frac{\sin(\pi \sin(\vartheta) \cos(\varphi))}{\sin\left(\frac{\pi}{2} \sin(\vartheta) \cos(\varphi)\right)} \quad (3.35)$$

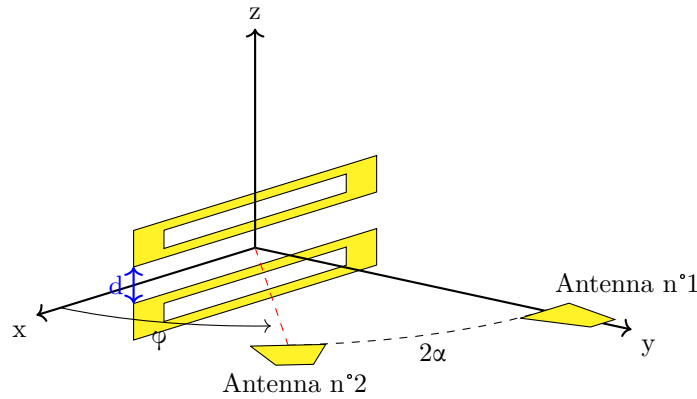


**Figure 3.71:** The coordinates system and notations. The angle under study  $\varphi$  is between the resonator and the receiving antenna. Emitting and receiving antennas are considered with the same angle  $\vartheta$  in our sensor application.

Once the radiation pattern of the loop is known, it is possible to reapply the antenna array theory to express the total radiation pattern of a tag consisting of several loops. Considering two loops as illustrated in Fig. 3.71, we obtain :

$$E_s(f_0) = E_d \times AF_x \times AF_z = k_0 T_0 \sin(\vartheta) \frac{\sin(\pi \sin(\vartheta) \cos(\varphi))}{\sin\left(\frac{\pi}{2} \sin(\vartheta) \cos(\varphi)\right)} \frac{\sin(kd(\cos(\vartheta) + \cos(\vartheta_i)))}{\sin\left(\frac{kd}{2}(\cos(\vartheta) + \cos(\vartheta_i))\right)} \quad (3.36)$$

where  $T_0$  is found with the same approach as Section 3.1.3 :

$$T_0 = \sin(\vartheta) \frac{\sin(\pi \sin(\vartheta_i) \cos(\varphi_i))}{\sin\left(\frac{\pi}{2} \sin(\vartheta_i) \cos(\varphi_i)\right)} \frac{\sin(kd \cos(\vartheta_i))}{\sin\left(\frac{kd}{2} \cos(\vartheta_i)\right)} \quad (3.37)$$

Fig. 3.72 shows the E-field radiated  $E_s(f_0)$  by two loops in the configuration presented in Fig. 3.71 in simulation compared to (3.36) for different spacing of  $d$ .

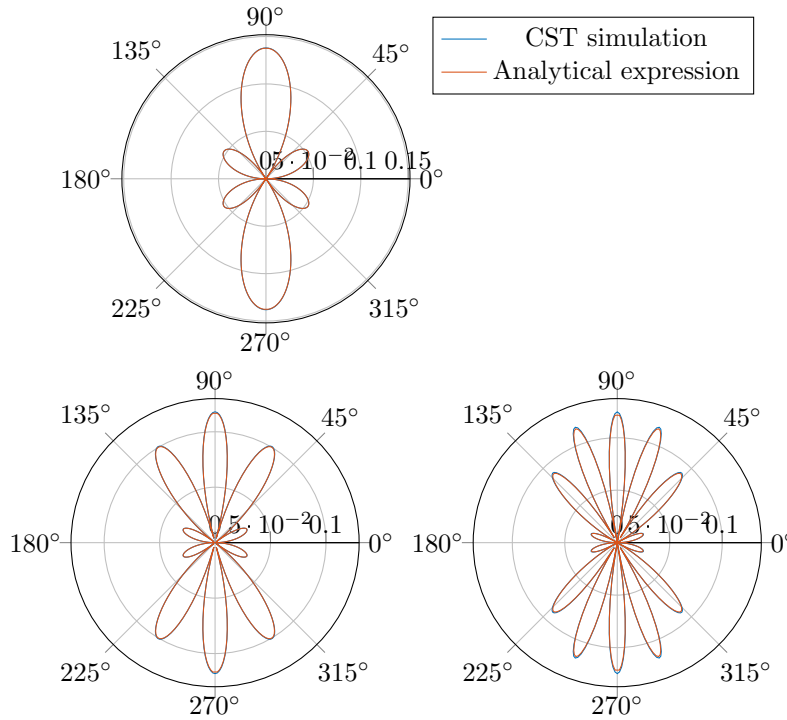


**Figure 3.72:** Magnitude of the E-field (V/m) radiated by two loops in the configuration presented in Fig. 3.71 at the fundamental frequency with  $\vartheta = \pi/2, \varphi \in [0^\circ; 360^\circ]$  and a)  $d = 90\text{mm}$ , b)  $d = 190\text{mm}$  and c)  $d = 290\text{mm}$ .

Contrary to a single loop radiation, as shown by (3.2), the two loops configuration is sensitive to the direction of the incident wave as stated by (3.36). Fig. 3.73 shows the E-field at fundamental frequency of two loops separated by  $d = 90\text{mm}$  and an incident wave at  $\vartheta = 60^\circ$ .

Equation (3.36) can be used to :

1. make a distance sensor. Indeed, following Section 3.1.3, the following equation can be written :

$$\begin{aligned} \frac{E(f_1)}{E(f_0)} &= 8 \sin\left(\frac{\pi}{2} \sin(\vartheta) \cos(\varphi)\right) \sin\left(\frac{\pi}{2} \sin(\vartheta_i) \cos(\varphi_i)\right) \\ &\times \sin\left(\frac{kd}{2}(\cos(\vartheta) + \cos(\vartheta_i))\right) \cot\left(kd(\cos(\vartheta) + \cos(\vartheta_i))\right) \\ &\times \sin\left(\frac{kd}{2} \cos(\vartheta_i)\right) \cot\left(kd \cos(\vartheta_i)\right) \end{aligned} \quad (3.38)$$

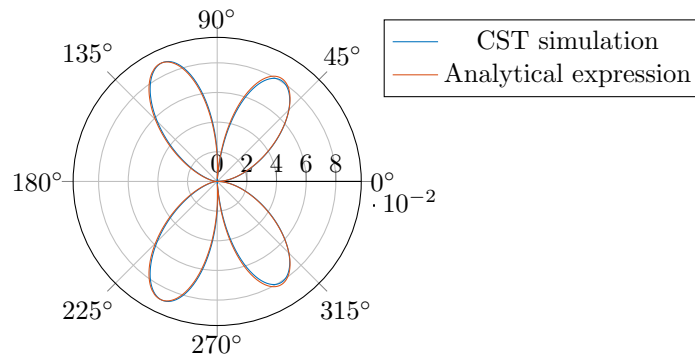


**Figure 3.73:** E-field at fundamental frequency of two loops separated by  $d = 90\text{mm}$  and an incident wave at  $\vartheta = 60^\circ$ .

Considering a known antenna position, (3.38) can be solved for the distance  $d$ . The estimated quantity is the distance between the resonators. Simulations were done using two approaches to break the periodicity of (3.38) and actually solve for  $d$ . Either a bi-static antenna configuration or a set of  $2 \times 2$  loops working at different frequencies can be used (as illustrated in Fig. 3.74). The first case introduces a diversity on  $(\vartheta, \varphi)$  with two positions of the antennas and the second a diversity on the value of  $k$ .

2. shape a wanted radiation pattern. Using (3.36) it is possible to radiate signal in direction where the single loop present no signal (see Fig. 3.5 and Fig. 3.72). It is also possible to find antenna position so the radiation pattern amplitude stays constant no matter the distance  $d$  ( $\varphi=60^\circ$ ,  $\vartheta_1=90^\circ$  and  $\vartheta=90^\circ$ ).

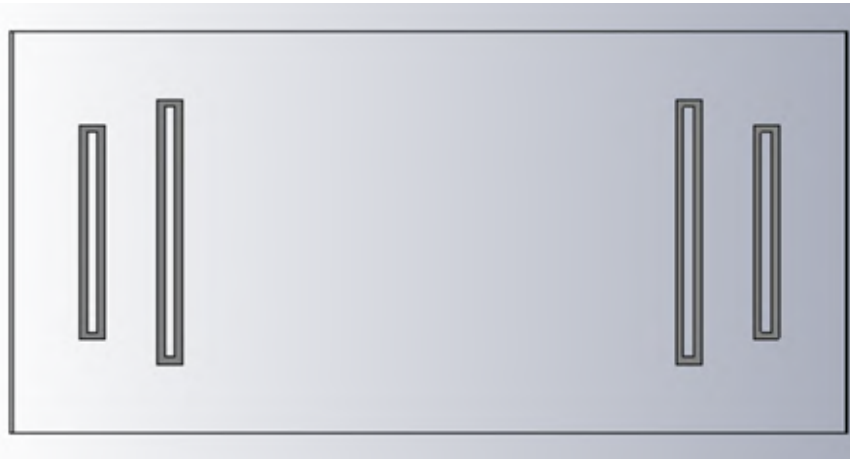


**Figure 3.74:** Set of  $2 \times 2$  loops working at different frequencies to achieve a distance sensing.

Perspectives on this chapter using the radiation pattern were presented in this section. These results have been validated using different simulations but no measurements have been done in practice.



### 3.5 Conclusion of the chapter

In this chapter, several chipless RFID sensors were presented. These sensors did not use the value of the resonance frequency to sense physical quantities but rather its amplitude. Indeed, the scattering parameters (radiation pattern of the loop resonator or polarization) were used to develop new approaches. Since the amplitude is less robust to the environment compared to the resonance frequency, each sensor was studied with Monte-Carlo simulations or with real-life measurements to exhibit its working application in real environments.

First, a model describing loop resonator radiation pattern is introduced. This radiation pattern was used to measure the loop rotation in 3-dimension. Contrary to already implemented chipless RFID angle sensors, the one introduced here allows the extraction of the tag rotation or the antenna position in 3D using a novel approach based on the resonator radiation pattern. An analytical model is developed to measure the tag orientation determining both the inclination and azimuthal angle of the tag in a spherical coordinates system for both mono-static and bi-static antenna configurations. This method was proven using MC to be robust but also calibration independent which is not the case of actual chipless RFID orientation sensors. This radiation pattern was also used to increase the capacity of RFID chipless tags. While the idea today is to make resonators more compact, this work was able to increase the coding capacity by allocating multiple resonance peaks in a single frequency slot without interfering together. It is based on the radiation pattern diversity of different resonators' topologies or different modes of resonance on the same resonator topology. Finally, the polarization of resonators was studied to improve RFID reading robustness. This approach was compared to state-of-art approaches such as time-gating. It was proven that this method allows obtaining a higher signal-to-noise ratio of resonators whose orientation with respect to the reader is unknown. With this principle, it is also possible to separate the resonance mode of the resonator that is connected to the identifier from other parasitic resonance modes that may appear due to possible misalignment between the tag and the antenna. Measurements in harsh environments, as well as comparisons with classical techniques such as time gating, were presented. A study of the improvement in the read range was achieved to highlight the potential of the proposed technique.

## Chapter 4

# Medium characterization using a radar approach

This chapter will present medium sensors. The first section suggests shows the possibility to detect the presence of grafted molecules on the surface of silicon nanowires thanks to a wireless RF radar approach based on the measurement of the backscattered signal of a resonant structure on which the nanowires are deposited. The measured resonance frequency allows the determination of the intrinsic properties related to temperature and humidity variations. Several functionalizations of nanowires have been realized and characterized. A RF approach allows the detection of significant differences related to the presence of grafted molecules on the surface of nanowires. The obtained results confirm the very good potential of the radar approach to identify the functionalization of nanowires. Also, discussions about the application of such functionalizations are made to increase the sensibility of sensors working using the radar approach.

Secondly, a method to characterize the complex permittivity of dielectric is presented. The back-scattered signal from a resonant scatterer placed in contact with the dielectric is used to estimate the quantities. This method is wireless, non-destructive, with no restriction on the sample thickness, and is done using a VNA and an antenna. Discussions on the geometry of the resonator as well as the calibration step are proposed to improve the sensing capability of the approach.

## 4.1 Wireless Detection of Surface modification of Silicon Nanowires

Nowadays silicon nanowires (SiNWs) are emerging as a promising solution for the development of practical devices thanks to their fascinating properties (high surface to volume ratio, one-dimensional semiconductor materials, easily modular surfaces) [165, 166]. Indeed, SiNWs-based devices are used for many applications such as catalysis, biology, lithium batteries, solar cells, or sensors [167]. For sensors applications, it was reported in [168] that the design requires a prior functionalization of silicon nanowires. Indeed, the functionalization of silicon nanowires especially by organic compounds could enhance their selectivity and their sensitivity leading thus to high-performance sensors. As an example, Chen et al. demonstrated that carboxylic acid-functionalized silicon nanowires improve the electron transfer conductivity [169]. They showed that the sensitivity was three times higher

compared to unmodified nanowires. There are several techniques for silicon nanowires functionalization. However, they can be grouped into two main categories. The first approach consists of modifying the native oxide surrounding the nanowires (SiO<sub>x</sub>/SiNWs). This includes silanization or the reaction of SiNWs with organophosphonates. The second one allows to modify directly the hydrogen terminated SiNW (hydrosilylation, arylation, halogenation or alkylation). The modified surface is usually thin. For more details about the functionalization methods, the readers can refer to [168] and [170].

#### 4.1.1 Classical methods for surface analysis

Surface analysis is an unavoidable step after surface modification. Indeed, it allows to verify the success of the surface modification, understand the provided benefits and ultimately improve its quality. A wide range of physical and chemical surface analysis techniques is available in the literature. They can be classified in two general viewpoints: those that measure the elemental composition or chemical species and those that make area topographic maps. In the first category, most of the tools used for the characterization of silicon nanowires involve spectroscopic methods [171, 172] especially infrared (IR) spectroscopy, energy-dispersive X-ray (EDX) and X-ray photoelectron spectroscopy (XPS).

IR is a powerful tool for chemical species, molecular structure, and defect determination. EDX is a technique of X-ray spectroscopy that is based on the collection and energy dispersion of characteristic X-rays. This analysis technique is usually associated with electron column instruments such as scanning electron microscopy (SEM). The sampling depth changed from 0.02 to 1  $\mu\text{m}$ . In addition, the XPS experiment is based on the ejection of electrons, of core levels, from an atom irradiated with a monoenergetic beam of soft X-rays. This technique provides information about elemental composition, chemical state, depth profiling and mapping. The sampling depth ranges from a few to several nm. XPS offers the advantage of being a non-destructive technique. Therefore, it is the most widely method for surface analysis [173].

For surface profile, scanning tunneling microscope (STM) and SEM are useful tools. STM offer the possibility to study the film thickness, make topographic imaging or topography, profilometry and identify the defects in thin films with a sampling depth of less than 0.05 nm. However, STM is based on tunneling current and works only with conducting and semiconducting materials. The main advantage of SEM is its ability to achieve very high magnification and resolution of a material surface. Also, SEM produces information about morphology, elemental composition, damages, imaging, or defects of the studied surface with a resolution varying from a few nm to a few  $\mu\text{m}$ .

On the whole, these techniques only give information on a small area. Regarding the characterization of surface modifications on nanowires, many approaches are currently used. They are most often specific physicochemical methods available in laboratories working on these topics. Here, we present an RF characterization approach, without contact allowing to detect the presence of grafting of the silicon molecules and even to differentiate the grafted molecules. The idea in principle is based on the measurement of a high-quality factor fully passive resonant scatterer designed on which the nanowires are deposited. The scatterer has an analytical model taking into account the surrounding temperature and humidity considered for this characterization approach. The principle used, and described in detail below, is a radar principle, i.e., we measure and analyze the field backscattered by

the resonator on which the surface-modified nanowires have been deposited. Based on this measurement, we are interested in determining the device response (resonator with nanowires) through the monitoring of the resonance frequency, as a function of temperature and humidity. It turns out that each molecule grafted on the nanowires interacts with the resonator and induces a different behavior when the temperature and humidity change. This behavior can be directly characterized by the measured resonance frequency which will vary differently depending on the grafted molecule. We show that the presence of these molecules which are significantly smaller than the wavelength used for the characterization (there are several orders of magnitude of difference) and therefore do not produce any measurable effect on the backscattered signal in the stationary case (constant temperature and humidity) will, however, have a quantifiable effect when temperature and humidity vary. This effect is highlighted in this section and will be used to differentiate the grafted molecules. These results open the way to the potential of RF using backscattering measurement approaches for chemical substances characterization such as surface functionalized nanowires. Indeed, it is a non-destructive wireless technique, adapted to smoother surfaces, and can measure areas over several centimeters. RF techniques have already been applied to characterize the humidity sensing properties of SiNWs [174]. We note that the proposed approach is very far from contact characterization approaches consisting in measuring electrical quantities such as voltages on electronic devices sensitive to the molecules attached to them. To the best of our knowledge, RF approaches have never been used to characterize functionalized silicon nanowires. In the present work, silicon nanowires have been modified using different organic groups. Upon exposure to various temperatures and relative humidity, we define a gaussian function that allows distinguishing the different end groups. In addition, we highlighted the effect of the functionalization on the temperature and humidity sensing capabilities.

## 4.1.2 Radio-frequency approach

### Principle of the radar approach

The measurement principle is based on a radar approach. Loop resonators are used but the approach can be used with other resonator shapes. When a loop resonator is illuminated by an incoming EM-field, the maximum energy backscattered at a temperature  $T$  and relative humidity  $RH$  occurs at its resonant frequency  $f$  defined by :

$$f = \frac{c}{2\sqrt{\epsilon_{\text{eff}}}L_0} \left( 1 - (\alpha_c + \frac{\alpha_p}{2})T - \frac{1}{2}[a' + \gamma RH] \right) \quad (4.1)$$

When these coefficients are unknown, (4.1) can be used to extract them with high accuracy as done in Section 2.3.4. In the case of silicon nanowires, the surface functionalization affects the thermal and humidity sensitivity of the radio-frequency response of the resonator [174] and different functionalizations introduce different unknown values for  $\alpha$  and  $\gamma$ . Thus, the identification of these coefficients by measurements will allow to distinguish the functionalization. The parameters  $\alpha$  and  $\gamma$  represent temperature and humidity impacts on the effective permittivity  $\epsilon_{\text{eff}}$ . The effective permittivity  $\epsilon_{\text{eff}}$  of the substrate (Rogers RO4003C will be used) and the superstrate which is the nanowires deposit [112]. For this reason, the same substrate have to be used with the different nanowires samples to only measure the functionalization impact.

Main information	Technique	Types of specimen	Main features	Depth of analysis
Elemental composition & chemical state	Infrared spectroscopy (IR)	Solid, liquid or gas	High scan speed, high sensitivity, non-destructive technique, unsuitable for sample containing water	10 nm to several micrometer
	Energy-dispersive X-ray (EDX)	Ultra-high vacuum compatible solids	High detector's efficiency, ease of use, able to scan areas ( $\sim 1 \text{ mm}^2$ ) and single spots, destructive analysis	0,02 to $1 \mu\text{m}$
	Photoelectron spectroscopy (XPS)	Ultra-high vacuum (UHV), compatible solids	Can detect almost all elements, most used technique, effective at identifying surface contaminants, samples must be compatible with high vacuum environment	From 5 to 10 nm
Morphology & imaging	Transmission electron microscope (TEM) or scanning electron microscopy (SEM)	Ultra-high vacuum compatible solids	Powerful magnification, high-quality images, very expensive and laborious sample preparation	From few nm to $\mu\text{m}$
	Scanning tunnelling microscope (STM)	All	3D profile of surface, operate in large range of temperature (from 0K to a few hundred degrees Celsius), versatile technique (can be used in air, UHV and water), fragile and expensive, not work with insulators	$< 0,03$ to $0,05 \text{ nm}$
	Atomic force microscope (AFM)	All	Not requires vacuum and any special treatments; 2D image, 3D surface profile, high resolution, slow scanning rate, single scan image size (order of micrometers)	$< 0,03$ to $0,05 \text{ nm}$
Conductivity & permittivity	Radio frequency	Planar surface, flat smooth films, conductors and semi-conductors	Non-destructive method, non-contact measurement, wide analysis surface (several centimeters), very reliable measurements, laborious sample preparation and expensive	—

### Extraction of the physical parameters

By considering  $f_{\text{ini}}$  as the first resonance frequency measured at time  $t_0$  and the coefficients  $a'$ ,  $\alpha$ ,  $\gamma$ , we can have [140] :

$$\frac{f}{f_{ini}} \simeq 1 - \frac{a'}{2} - \alpha T - \frac{\gamma}{2} RH \quad (4.2)$$

From (4.2) it is possible to extract the coefficients  $a'$ ,  $\alpha$  and  $\gamma$  by linear regression applied on measurement. Indeed, it is possible to measure the resonance frequencies corresponding to a set of different values of temperature and humidity.

Measurements in the climatic chamber with the controlled temperature and humidity profiles such as the one shown in Fig. 4.2 have been used to extract the three coefficients. Indeed, once the frequencies  $f$  were measured alongside the temperature  $T$  and humidity  $RH$ , a fit of all the realized measurements was done based on (4.2) to find the values of  $\alpha$ ,  $\gamma$  and  $a'$ .

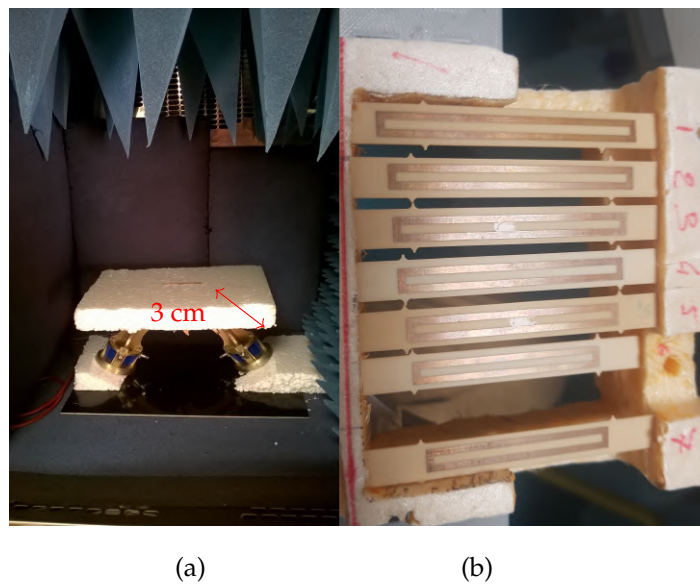


**Figure 4.1:** Photo of the measurement bench and tags. a) Setup inside the climatic chamber. b) Copper loop resonators on Rogers RO4003C substrates used for the measurements.

### 4.1.3 Measurements

Six resonators were measured in the same time. One resonator was without nanowires (Rogers) and used to make sure the measurement was done without incident. One resonator was impregnated with silicon nanowires and the four remaining resonators were impregnated with functionalized surface silicon nanowires (respectively Ethynyl, Pentacene, N3 and Octadecyl). In the different measurements, the nanowires deposit was swap between the resonators. A volume of  $5\mu\text{l}$  was deposited on the resonator using same concentration solution from the each functionalized nanowires.

The measurement setup and the fabricated tags used in practice are presented in Fig. 4.1. The nanowires were fabricated, functionalized and characterized prior by chemical approaches at the ICCF laboratory by external researchers. More informations can be found in Appendix A.

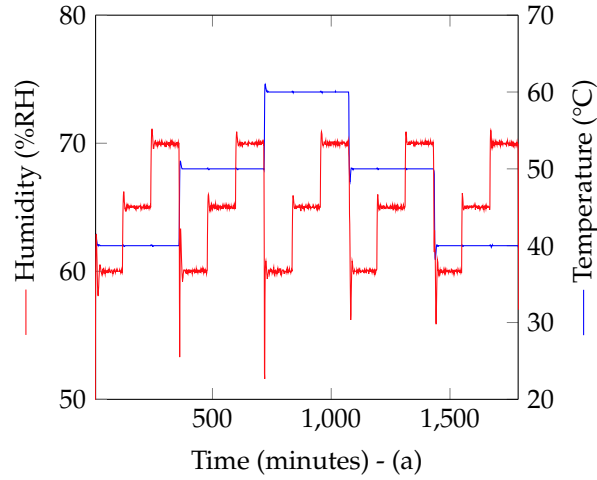


**Figure 4.2:** Temperature and humidity measured with an electronic sensor inside the climatic chamber during the measurements.

The climatic chamber was used to control both temperature and humidity. The temperature and humidity profile illustrated in Fig. 4.2 was achieved. The measurement protocol is the same as Section 2.1.4. An IF bandwidth of 10kHz was used during the measurements with the VNA.

This extraction was repeated several times. For each measurement, the entire test bench was disassembled and put back in place, the deposit of nanowires was re-done. Indeed,  $\alpha$  and  $\gamma$  have already been measured for this configuration (in Section 2.3.4) or can be calculated using provider's datasheet information [79, 140]. These values can be compared with the estimated one from a measurement. Temperature and humidity profile are such as presented in Fig. 4.2.

### Results and analysis

The measurement have been repeated ten times. As an example, the first 6 coefficients  $\alpha$  and  $\gamma$  extracted for the sample without nanowires are given in Table 4.1. These results show a good repeatability on the extracted coefficient as well as a good estimation compared to the analytical value for  $\alpha$  (see [79]). Frequency variations as a function of temperature or humidity are plotted in Fig. 4.3 and Fig. 4.4 respectively.

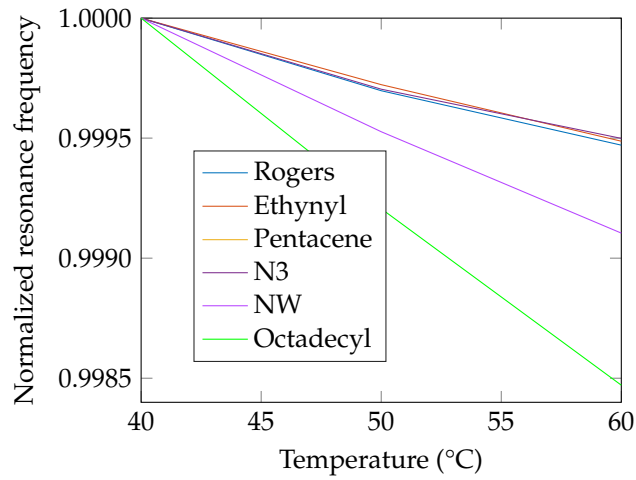
A 3-dimension representation has been chosen to ease the reading of the results. For each sample, the following Gaussian function  $g$  has been calculated :

$$g(\alpha, \gamma) = \exp \left( -\frac{(\alpha - \bar{\alpha})^2}{2\sigma_{\alpha}^2} - \frac{(\gamma - \bar{\gamma})^2}{2\sigma_{\gamma}^2} \right) \quad (4.3)$$

where  $\bar{x}$  denotes the mean of  $x$  and  $\sigma_x$  denotes its standard deviation. Gaussian functions for each sample are plotted in Fig. 4.5. Also the different values of  $\bar{x}$  and  $\sigma_x$  are given in Tab. 4.2. We can see that each functionalization introduces different coefficients  $\alpha, \gamma$  allowing thus to differentiate the samples. For a measured  $(\alpha_m, \gamma_m)$ , the likelihood of this sample being silicon nanowires functionalized from

**Table 4.1:** Extracted coefficients  $\alpha, \gamma$  using (4.2) for the resonator with no nanowires.

Measure n°	$\alpha (10^{-5})$	$\gamma (10^{-5})$
1	3.026	2.106
2	2.999	2.280
3	3.015	2.030
4	3.148	1.987
5	3.069	1.966
6	3.051	1.904
7	2.938	2.400
8	3.012	2.164
9	3.003	2.266
10	3.074	2.074

**Figure 4.3:** Normalized resonance frequencies for different temperatures at a constant humidity of RH=60%.

the j-sample is given by :

$$\text{likelihood}(j\text{-sample}) = \frac{g_j(\alpha_m, \gamma_m)}{\sum_{i=\text{all samples}} g_i(\alpha_m, \gamma_m)} \quad (4.4)$$

**Table 4.2:** Estimated coefficients  $\alpha$  and  $\gamma$  for the different functionalized nanowires.

	$\bar{\alpha} (10^{-5})$	$\bar{\gamma} (10^{-5})$	$\sigma_{\alpha} (10^{-7})$	$\sigma_{\gamma} (10^{-7})$
No nanowires	3.0335	2.1178	5.6193	15.821
Ethynyl functionalized	3.2834	2.2760	17.942	11.890
Pentacene functionalized	1.4711	1.145	10.654	39.312
N3 functionalized	2.7703	1.1726	2.8808	7.3588
Octadecyl functionalized	7.7328	2.8420	21.761	18.213
Pure nanowires	5.0758	2.9144	44.762	7.4154

The likelihood of the 6 samples is presented in Fig. 4.6.



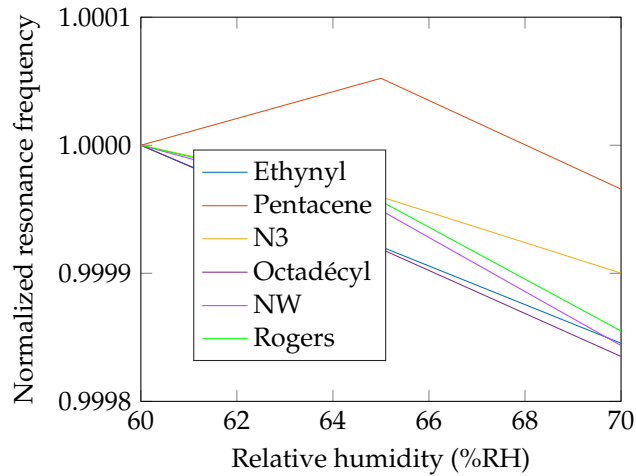


**Figure 4.4:** Normalized resonance frequencies for different temperatures at a constant temperature of  $T=40^{\circ}\text{C}$ .

Eq. (4.4) can be used to estimate the percentage of belonging of the measured sample to the different samples of the database. The highest probability is given by  $\max(\text{likelihood})$ . Eq. (4.3) can be used to compute the correctness of belonging of this sample to the guessed sample from database. In practice, both estimations should be used to have a correct estimation on the sample. For example, a measured  $(\alpha_m, \gamma_m) = (80 \times 10^{-5}, 10 \times 10^{-5})$  gives 100% likelihood to Octadécyl since it is the only functionalization with  $\alpha > 60 \times 10^{-5}$ . But if we look at Fig. 4.5, we can notice that for this value of  $\gamma_m$ , the sample might not be Octadécyl since  $g_{\text{Octadécyl}}(\alpha_m, \gamma_m)$  gives 0% of correctness. The computation of both quantities can give an additional indication such as indication on the quality of the measurement (if the likelihood is 100% and  $g$  is 0% the sample under test can be a new sample which is not from the database or that the measurements was dysfunctional).

From Tab. 4.2 and Fig. 4.5, we can see that it is possible to distinguish the different functionalization of silicon nanowires of our samples.

## Discussions

Other than the detection of the surface functionalization by a RF approach, Fig. 4.5 shows that the sensitivity of the RF response can strongly vary depending on the functionalization. Numerous sensor applications in the RF domain use the resonance frequency to measure quantities such as temperature or humidity [95, 96, 140, 118]. It has already been shown that nanowires can improve the sensitivity of such sensors by increasing the frequency shifts [174] but the functionalization of the nanowire was never studied. In Tab. 4.2, we can notice that the functionalized silicon nanowires by Pentacène is a bad candidate for such sensing application because  $\alpha, \gamma$  are smaller than the resonators used without nanowires. So, the frequency shifts will be smaller and harder to measure (see (4.1)) [79]. But SiNWs-py is a good option to reduce the environment response of temperature and humidity on a resonator and so improve its response stability towards these variations. On the opposite, SiNWs-OTS is a good candidate for sensors applications. Indeed, both the thermal and humidity sensitivities are improved compared to naked Rogers or Rogers with nanowires with no surface functionalization

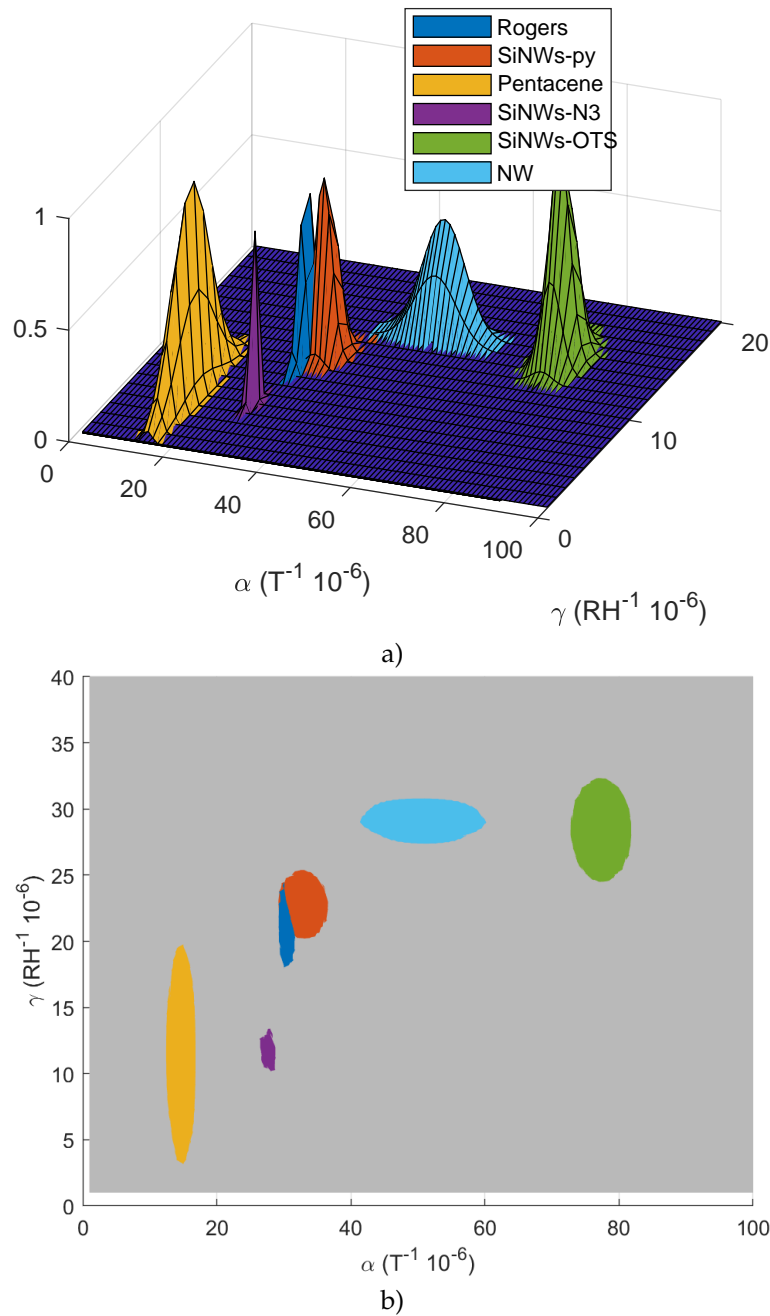


**Figure 4.5:** a) 3-dimension representation of the 6 samples measured in practice using the climatic chamber. b) Top-view of the gaussian representation.

making the frequency shifts bigger. This larger shift not only allow an easier measurement but also improves the accuracy of the sensor [79].

#### 4.1.4 Conclusion of the section

In this section we proposed a radar approach for the detection of the surface functionalization of silicon nanowires. The identification of the functionalization is done by depositing functionalized

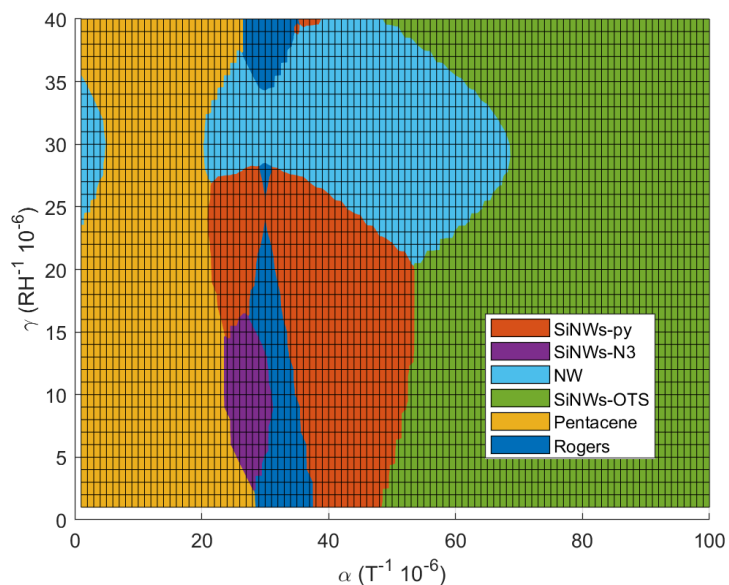


**Figure 4.6:** Likelihood representation of the 6 samples.

silicon nanowires on a loop resonator and monitoring its resonance frequency during temperature and humidity variations. Measurements were performed using a climatic chamber. The obtained results confirm the very good potential of the radar approach to identify the functionalization of nanowires. Indeed, each functionalization introduced a different response towards humidity and temperature. Also, discussions about the application of such functionalizations is made to increase the sensibility of sensors working using radar approach or in the opposite, reduce the environment impact on such resonators (by lowering  $\alpha$ ,  $\gamma$ , ...).

## 4.2 Complex permittivity sensing

Microwave sensors interest has increased over the last decades. Such sensors have been able to measure quantities such as temperature [79], humidity [175], gas [176], strain [93] without batteries or electronic chips. This wireless approach based on radio-frequency (RF) waves caught the curiosity for sensor applications due to its low-profile (often planar and single layer sensors), its accuracy, its price and finally its infinite life-time of operation due to the absence of electronic parts. The RF waves also provide advantages such as wireless measurements that allow the reading of multiple sensors at the same time, in real-time and even through obstacles [140]. Such RF approaches have also been developed to do metrology. We can cite for example the characterization of materials thermal dilatation [79] or the complex permittivity [177]. Concerning the complex permittivity measurements, numerous works can be found [178]. These methods can be divided in two categories : resonant and non-resonant approaches. In non-resonant approaches, coaxial measurements is commonly used and standardized [179]. The coaxial method consist in measuring the transmission and reflection coefficients of a coaxial filled with the dielectric under-test [180, 181]. The transmission/reflection idea is also transposed to other technique such as waveguide [182] or free-space measurements [183]. These techniques are simple to implement, works on wide frequency band but the major drawback is their low accuracy especially on the losses extraction. On the other hand, resonant methods permits to have higher accuracies and to measure lower losses but are restricted in the frequency response. We can cite cavity measurements [184, 185] or by means of an open resonator [186, 187]. Lastly, dielectric rod resonator short circuited at both ends by two parallel conducting plates can be used to measure the complex permittivity [188, 189]. For the solid dielectric materials which the present concern is exclusively concerned, a major problem is the accurate machining of a specimen of the material to fit closely into the resonator or waveguide. In the recent years, planar microstrip resonator using the under-characterization material as a substrate appeared [190, 78, 191] which do not have the machining drawback. These techniques allows a wireless measurement based on a radar principle. While in [190] the RF access lines conventionally used to connect a VNA [178] were replaced by antennas, [191] and [78] present an approach where only a resonant target is present without any antenna. In [78] the resonant target is realized as a PCB (open metal ring on a known dielectric substrate) where the material to be characterized is a small dielectric slab of a few mm length, positioned in the opening of the ring. The ease and cost to use such wireless test-benches (only one antenna and a VNA are needed), as well as the advantages (real-time and accurate measurements) make it a good solution for dielectric characterization. Contrary to [188, 189] the sample under test does not need to be precisely positioned in relation to the test bench (e.g. the distance between the antenna and the resonator can be changed without difficulty). In these works, the permittivity [191], or the complex permittivity [190, 78] is directly linked to the resonance with its frequency and its attenuation. However in [190, 78], measurements or simulations are used to fit a model which describes the resonance frequency behavior. In this section, the complex permittivity is related to the resonance with a theoretical approach and an analytical formula is obtained. In addition, to increase the characterization frequency band, it is sufficient to place different resonators operating at different frequencies. As in [191] the approach is based on the use of an independent metallic resonator which is attached to the dielectric plate to be measured and whose thickness is assumed to be known. However here a more general approach is introduced in order to have also access to the dielectric

losses. Compared to [78] the sensitivity is maximized by using no other dielectric than the one we want to characterize, we do not have to machine the dielectric, it is enough that its dimension largely covers the metallic resonator. Section II will introduced the equations that associate the resonance to the complex permittivity. Section III will focus on the complex permittivity extraction from radar measurements. Section IV and V will present simulations and measurements of several samples as well as discussions on the accuracy and sensitivity of the proposed approach. Finally Section VI will conclude the section.

### 4.2.1 Complex resonance frequency

Using the Singularity Expansion Method (SEM), it can be shown that in the time domain, the signal back-scattered  $u(t)$  by a resonator can be written as a exponentially damped sinusoidal as follows :

$$u(t) = Ae^{-\sigma(t-2\tau)} \cos(\omega(t-2\tau))\Gamma(t-2\tau) \quad (4.5)$$

where  $A$  is the amplitude of the back-scattered signal,  $\Gamma$  is the Heavyside function and  $\tau$  the propagation constant. Let define the complex resonance frequency  $s = \sigma + j\omega$  to analyze the radar response of a resonant target in terms of damping factor  $\sigma$  and angular frequency  $\omega$ . The back-scattered signal can be re-written as :

$$u(t) = A \times \text{Re} \left[ e^{-s(t-2\tau)} \right] \times \Gamma(t-2\tau) \quad (4.6)$$

where  $\text{Re}$  defines the real part. If we use a simple loop resonator (as illustrated in Fig.4.7) for our radar target, we have its resonance frequency  $f_0$  defined by [101]:

$$f_r = \frac{c}{2L\sqrt{1 + \frac{\epsilon_r - 1}{2}q}} \quad (4.7)$$

where  $c$  is the speed of light in vacuum,  $L$  the length of the resonant scatterer,  $q$  the filling factor which is a coefficient to take into account the support height [112] and  $\epsilon_r$  the permittivity of the dielectric under-test. For this reason, a resonator placed on a dielectric with no losses is associated at its resonance frequency to the variable  $s_r$  by :

$$s_r = \sigma_r + j\omega_r = \sigma_r + j2\pi \frac{c}{2L\sqrt{1 + \frac{\epsilon_r - 1}{2}q}} \quad (4.8)$$

When a dielectric presents RF losses, its permittivity can be written as  $\epsilon = \epsilon_r(1 - j \tan \delta)$  hence the complex resonance frequency can be introduced :

$$f_d = \frac{c}{2L\sqrt{1 + \frac{\epsilon_r(1 - j \tan \delta) - 1}{2}q}} \quad (4.9)$$

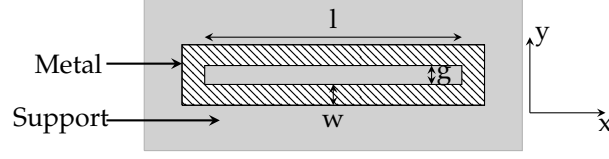


**Figure 4.7:** Loop resonator considered in this study. The support is the dielectric under-test defined by  $\varepsilon = \varepsilon_r(1 - j \tan \delta)$ .

which gives the complete expression of  $s_r$  :

$$s_d = \sigma_r + jB\varepsilon \frac{-j}{2} \tan \left( \frac{\tan \delta q \varepsilon_r}{2 + q(\varepsilon_r - 1)} \right) \quad (4.10)$$

where  $B = \frac{\omega_0}{\sqrt{1 + \frac{\varepsilon_r - 1}{2}q} \left( 1 + \left( \frac{\tan \delta q \varepsilon_r}{2 + q(\varepsilon_r - 1)} \right)^2 \right)^{1/4}}$ . For small losses, ( $\tan \delta \ll 1$ ) which is usually the case for RF substrates, we can expand and approximate the complex resonance frequency  $f_d$  with :

$$f_d = \frac{c}{2L \sqrt{1 + \frac{\varepsilon_r(1 - j \tan \delta) - 1}{2}q}} \quad (4.11)$$

$$\simeq F_0 \left( 1 - \frac{j}{2}X - \frac{3}{8}X^2 \right)$$

where  $F_0 = \frac{c}{2L \sqrt{1 + \frac{\varepsilon_r - 1}{2}q}} = \frac{f_0}{\sqrt{1 + \frac{\varepsilon_r - 1}{2}q}}$  and  $X = \frac{\tan \delta q \varepsilon_r}{2 + q(\varepsilon_r - 1)}$ . Therefore, the variable  $s_d$  at the complex resonance frequency  $f_d$  is now given by :

$$s_d = \sigma_d + j\omega_d = \left( \sigma_0 + \frac{1}{2}W_0X \right) + jW_0 \left( 1 - \frac{3}{8}X^2 \right) \quad (4.12)$$

where  $W_0 = 2\pi F_0$ . After identification, we get the damping factor and frequency at resonance for a dielectric with losses ( $\sigma_d, \omega_d$ ) can be expressed by :

$$\left\{ \begin{array}{l} \sigma_d = \sigma_0 + \frac{\omega_0}{2\sqrt{1 + \frac{\varepsilon_r - 1}{2}q}} \frac{\tan \delta q \varepsilon_r}{2 + q(\varepsilon_r - 1)} \end{array} \right. \quad (4.13a)$$

$$\left\{ \begin{array}{l} \omega_d = \frac{\omega_0}{\sqrt{1 + \frac{\varepsilon_r - 1}{2}q}} \left( 1 - \frac{3}{8} \left( \frac{\tan \delta q \varepsilon_r}{2 + q(\varepsilon_r - 1)} \right)^2 \right) \end{array} \right. \quad (4.13b)$$

Note that in (4.13b) only  $\varepsilon_r$  and  $\tan \delta$  are unknown. Indeed, ( $\sigma_0, \omega_0$ ) and ( $\sigma_d, \omega_d$ ) are the damping factor and the resonance frequency measured for a loop resonator with no support and with the dielectric under-test respectively. Note that the length  $L$  does not affect the measurement. Also, different length can be used to characterize the losses at different frequencies. The coefficient  $q$  can be

directly calculated using [112] or obtained through simulations as explained in Section IV. It is possible from the measurement of the back-scattered signal of a resonator to extract the values of damping factors and resonance frequencies. Several techniques allow the extraction of these coefficients from the backscattered electromagnetic signature of a resonant scatterer. We can cite approaches that are applied to the temporal representation of the signal [192] or to a frequency representation [153]. An example of time domain back-scattered signal (in simulation) from the loop illustrated in Fig. 4.7 is shown in Fig. 4.8.

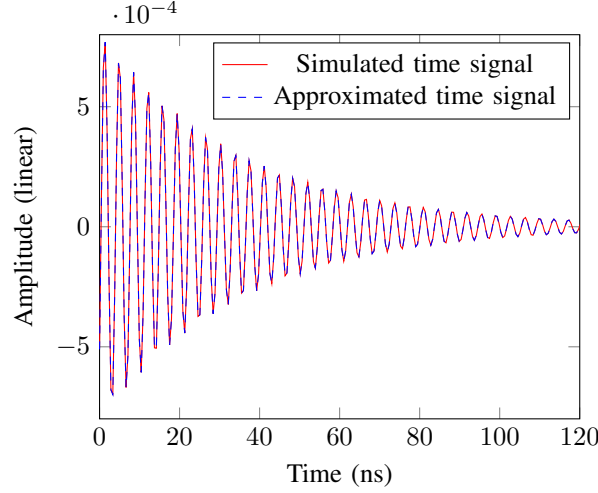


**Figure 4.8:** Time domain back-scattered signal from a loop resonator in simulation.

### 4.2.2 Permittivity extraction

Equation (4.13b) can be re-written as :

$$\begin{cases} \tan \delta = 2(\sigma_d - \sigma_0) \frac{\sqrt{1 + \frac{\epsilon_r - 1}{2} q} 2 + q(\epsilon_r - 1)}{\omega_0 q \epsilon_r} \\ \bar{\omega} \sqrt{1 + \frac{\epsilon_r - 1}{2} q} = 1 - \frac{3}{2} \bar{\sigma}^2 \left( 1 + \frac{\epsilon_r - 1}{2} q \right) \end{cases} \quad (4.14)$$

where  $\bar{\omega} = \frac{\omega_d}{\omega_0}$  and  $\bar{\sigma} = \frac{\sigma_d - \sigma_0}{\omega_0}$ . By letting  $Y = \sqrt{1 + \frac{\epsilon_r - 1}{2} q}$ , the second equation can be expressed as a quadratic equation  $aY^2 + bY + c$  with :

$$\begin{cases} a = \frac{3}{2} \bar{\sigma}^2 \\ b = \bar{\omega} \\ c = -1 \end{cases} \quad (4.15)$$

The real positive solution  $Y$  is :

$$Y = \frac{-\bar{\omega} + \sqrt{\bar{\omega}^2 + 6\bar{\sigma}^2}}{3\bar{\sigma}^2} \quad (4.16)$$

Then the real part of the permittivity  $\epsilon_r$  can be found using (4.16) with :

$$\begin{aligned} \epsilon_r &= 1 + 2 \frac{Y^2 - 1}{q} \\ &= 1 + \frac{2}{q} \left( \left( \frac{-\bar{\omega} + \sqrt{\bar{\omega}^2 + 6\bar{\sigma}^2}}{3\bar{\sigma}^2} \right)^2 - 1 \right) \end{aligned} \quad (4.17)$$

and the losses can be found using (4.13b) and (4.17) with :

$$\tan \delta = 4\bar{\sigma} \frac{\left( \frac{-\bar{\omega} + \sqrt{\bar{\omega}^2 + 6\bar{\sigma}^2}}{3\bar{\sigma}^2} \right)^{5/2}}{q + 2 \left( \frac{-\bar{\omega} + \sqrt{\bar{\omega}^2 + 6\bar{\sigma}^2}}{3\bar{\sigma}^2} - 1 \right)^2} \quad (4.18)$$

These formulas are used to extract  $\epsilon_r$  and  $\tan \delta$ . Indeed, as already said,  $(\sigma_0, \omega_0)$  and  $(\sigma_d, \omega_d)$  are the damping factor and the resonance frequency measured for a loop resonator with no support and with the dielectric under-test respectively. The coefficient  $q$  can be calculated using [112] or obtained through simulations as explained in Section V.

### 4.2.3 Simulations

Simulations have been carried out using CST MW to validate the introduced equations. The loop resonator configuration of Fig. 4.7 has been used. Dimensions are  $l = 50\text{mm}$ ,  $w = 1.4\text{mm}$  and  $g = 2\text{mm}$ . The metal is 1mm thick. The dielectric height is 1mm so  $q \simeq 0.58$  [112]. The excitation is a plane wave polarized along the  $\vec{y}$ -axis. The probe is placed 1 meter away from the resonator. The simulated back-scattered E-fields are plotted in Fig. 4.9.

Based on these simulations, the Matrix Pencil method [192] is used to extract the complex variable  $s = \sigma + j\omega$ . For each configuration the resonance frequency  $f = \frac{\omega}{2\pi}$  as well as the damping factor  $\sigma$  are plotted in Fig. 4.10. The correspondence between the values of the complex permittivity and the number (noted "Run ID") associated to the simulation is given in Table. 4.3. We can see that resonance frequency decreases with an increase on the real and but also with the imaginary part of the permittivity. The attenuation mostly increase with the imaginary part of the permittivity (losses). In Fig. 4.10 is also plotted (4.13b) which shows good agreements with the simulations. The characterization of the error obtained from (4.13b) will be done in the measurement section. Indeed in simulation, even if the structure is relatively simple, the error will be directly linked to the models used in the EM simulator to take into account the losses, which is not what we seek to characterize in this article.



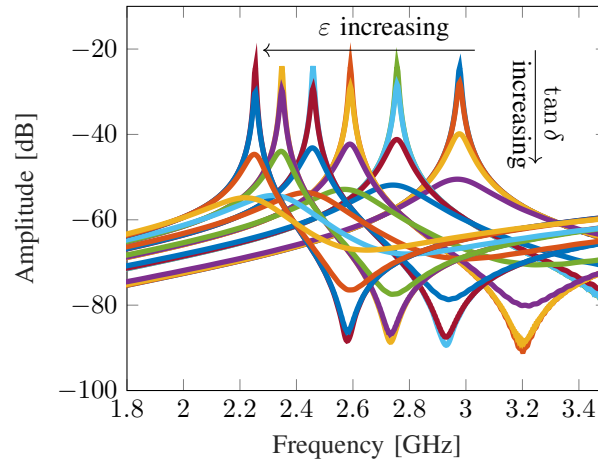


**Figure 4.9:** Simulated back-scattered E-field in amplitude for  $\epsilon_r = 1 : 0.5 : 3.5$  and  $\tan \delta \in [0, 0.005, 0.05, 0.2]$  for the loop resonator of Fig. 4.7 imprinted by a plan wave.

Proceeding from this results, the complex permittivity can be measured using (4.17) and (4.18). Estimated  $\epsilon_r$  and  $\tan \delta$  are plotted in Fig. 4.11. Again, we can notice that the extracted quantities are in good accord with the simulated values.

**Table 4.3:** Correspondence between simulations “Run ID” and  $(\epsilon_r, \tan \delta)$ .

Run ID	1	2	3	4	5	6	7	8	9	10	11	12	13	14	15	16	17	18	19	20	21	22	23	24
$\epsilon_r$	1	1	1	1	1.5	1.5	1.5	1.5	2	2	2	2	2.5	2.5	2.5	2.5	3	3	3	3	3.5	3.5	3.5	3.5
$\tan \delta$	0	0.005	0.05	0.2	0	0.005	0.05	0.2	0	0.005	0.05	0.2	0	0.005	0.05	0.2	0	0.005	0.05	0.2	0	0.005	0.05	0.2

A discussion will be made concerning the sensibility and accuracy of the proposed method based on the geometry of the resonant scatterer. As shown in (4.13b), the only external factor that impact the results is the coefficient  $q$ . Indeed, the higher is the value of  $q$ , the larger are the shifts in the signal amplitude or on the resonance frequency thus better results can be expected. To increase  $q$ , the loop geometry as well as the dielectric under-test thickness should be considered when designing the resonator [112]. A simulation with different gap for the loop, illustrated in Fig. 4.7, is presented in Fig. 4.12. We can see for example that a smaller gap induces a higher value for  $q$  and so higher shifts in the frequency response. Furthermore, in Fig. 4.13 is simulated the filling factor  $q$  for different dielectric height and different resonator’s metal thickness. We should notice that [112] works well only with very thin thickness of metal (the metal thickness is considered infinitely thin). When the resonator’s metal is thicker, [112] does not give the good value of  $q$ . For this reason, extracted value of  $q$  obtained from simulation are given in Fig. 4.13. Fig. 4.13 will be used in the section V according to the physical thickness of the resonators used in practice. Contrary to classical cavity method, this approach does not require thin dielectric sample to works. Indeed, as shown in Fig. 4.13, the thicker is the dielectric, the larger is the  $q$  factor hence improving the final estimation of the complex permittivity.

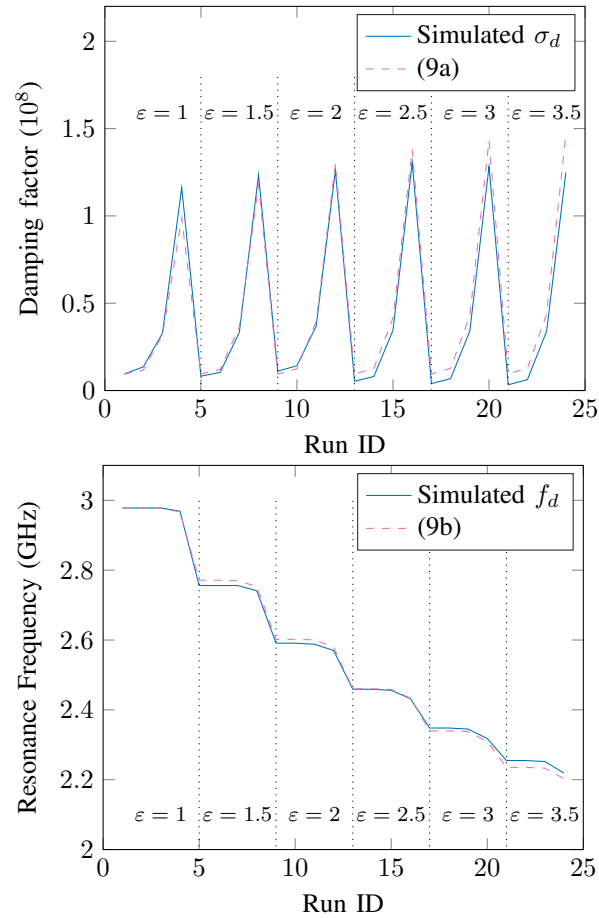


**Figure 4.10:** a) Simulated attenuation at the resonance frequency b) and resonance frequencies compared to the equations.

#### 4.2.4 Measurements

The proposed approach was then validated in practice using different sample. The different samples and dielectric heights evaluated in practice are given in Tab. 4.4. The "Red" sample was characterized using the cavity method for complex permittivity measurements (the Damaskos, Inc. Model 08 Thin Sheet Tester that measure the tangential component of dielectric constant of low loss materials over the approximate band of 800-4000 MHz in a non-destructive manner). The following protocol was used for the measurements : firstly, the loop resonator is measured in the air using a mono-static configuration inside an anechoic chamber (see Fig. 4.14). The VNA 5222A by Agilent was used. The source power of VNA is equal to 0 dBm. The frequency sweep ranging from 2 to 3 GHz with 4001 points is used. A mono-static configuration with Satimo (QH2000) quad ridged open boundary antennas (2–32 GHz) is used. Tape was used to suspend the loop in air (see Fig. 4.14a) to be as close as possible to a free space condition. Matrix Pencil is used on the S-parameters to evaluate  $(\sigma_0, \omega_0)$ . Secondly, the loop resonator was taped to the sample under-test as illustrated in Fig. 4.14. Matrix Pencil algorithm [192] is used once again on the S-parameters to evaluate  $(\sigma_r, \omega_r)$ . Finally, (4.17) and (4.18) are used to estimate the complex permittivity of the sample. The value of  $q$  is obtained based on the results presented in Fig. 4.13 for the corresponding dielectric height and for the 1mm metal

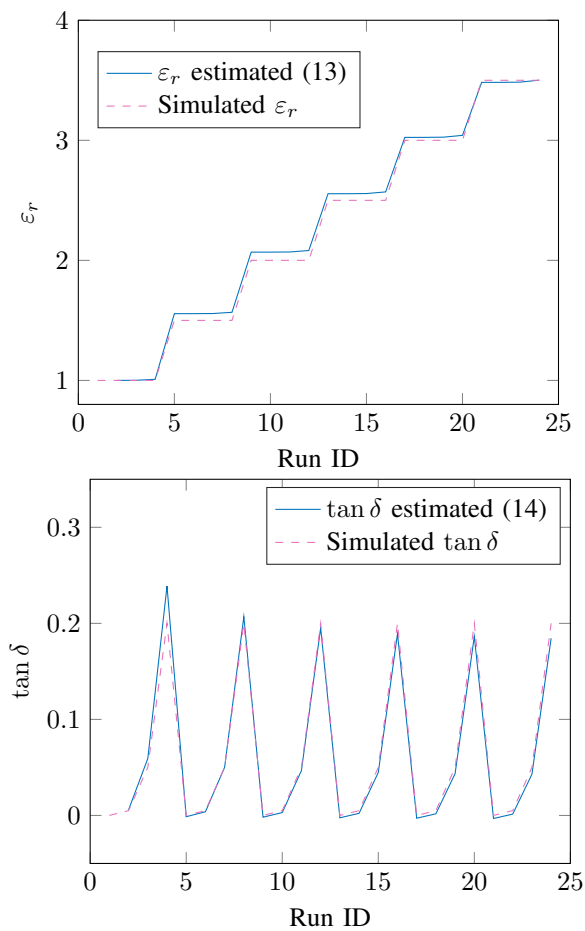


Figure 4.11:  $\tan \delta$  estimated with and without approximations (first order).

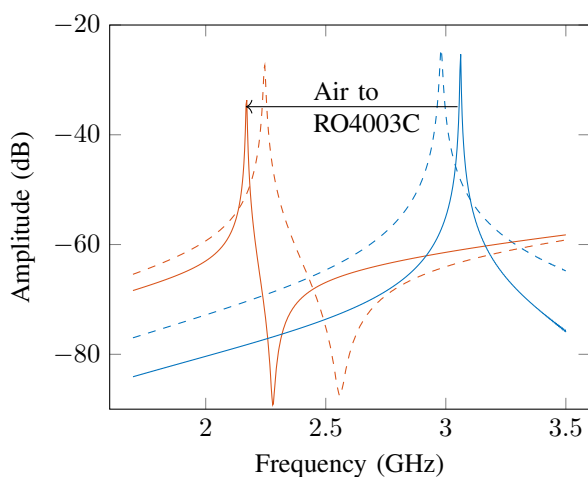
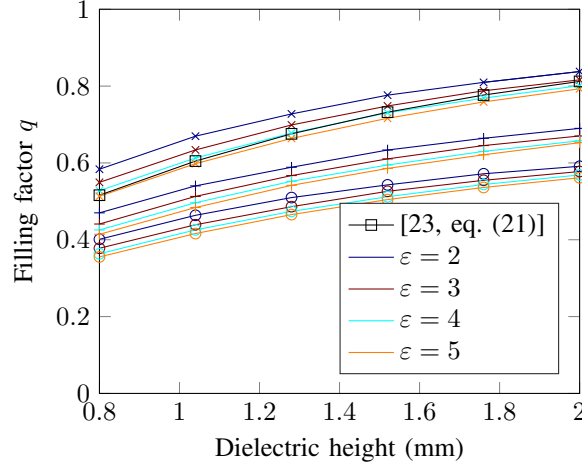


Figure 4.12: Influence of the gap  $g$  of the loop on the extraction of the complex permittivity: gap  $g = 0.5\text{mm}$  ( $q = 0.77$ ) [plain line] and  $g = 2\text{mm}$  ( $q = 0.6$ ) [dashed line]. The blue curves correspond to a permittivity of  $\epsilon = 1$  and the red ones to a permittivity of  $\epsilon = 3.55 - j0.007455$ .



**Figure 4.13:** Filling factor  $q$  as a function of the dielectric height and the metal thickness.  $\times$  markers correspond to a metal thickness of 0.01mm,  $+$  markers to a thickness of 0.5mm and  $\bigcirc$  markers to 1mm.  $\square$  is the  $q$  calculated using [112, eq. (21)].

thickness resonator used in practice. An example of measured S-parameters is given in Fig. 4.15 for the 0.7mm Rogers RO4003C substrate. For the different samples, the estimated values are given in Tab. 4.5. It is important to notice that these values are frequency dependent (especially  $\tan \delta$  in this frequency band). The proposed method allows to measure the complex permittivity at the resonance frequency of the scatterer when it is placed on the sample to estimate. For this reason, designing different resonator lengths is a solution to determine the complex permittivity at multiple frequencies. Scatterers were design to have their fundamental resonance frequency at 3GHz in the air. We can see that the estimated complex permittivity is close to the provider informations for the different samples and different dielectric thicknesses. The measured losses for the Duroid RT5880 (both heights) using the proposed approach grant losses  $\times 4$  times larger at 2.5GHz than the ones given by the provider at 10GHz.

Now that the approach is validated in practice, a second approach is presented in order to increase the accuracy of the method. When the resonator is taped to the dielectric, a small air gap is presented in between the resonator and the dielectric changing the effective permittivity seen by the resonator. Now, when resonators are taped several times to the same dielectric, it was seen that the resonance frequency does not vary a lot meaning that the air gap is constant between measurements. The improvement proposed here is to use a known dielectric for calibration to estimate the "in-air" resonator values. Then the estimate "in-air" value are used to characterized a second dielectric under-test. For a known dielectric and so its  $(\epsilon_{\text{cal}}, \tan \delta_{\text{cal}})$  permits to write :

$$\begin{cases} \omega_0 = \frac{w_{\text{cal}} \sqrt{1 + \frac{\epsilon_{\text{cal}} - 1}{2} q}}{\left(1 - \frac{3}{8} \left(\frac{\tan \delta_{\text{cal}} q \epsilon_{\text{cal}}}{2 + q(\epsilon_{\text{cal}} - 1)}\right)^2\right)} \\ \sigma_0 = \sigma_{\text{cal}} + \frac{\omega_0 \tan \delta_{\text{cal}} q \epsilon_{\text{cal}}}{2 \sqrt{1 + \frac{\epsilon_{\text{cal}} - 1}{2} q} (2 + q(\epsilon_{\text{cal}} - 1))} \end{cases} \quad (4.19)$$

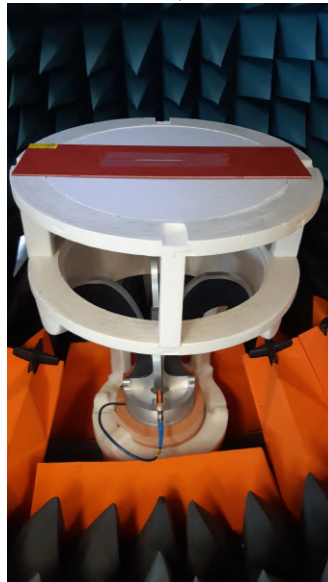
For this reason, the initial measurement in air can be replaced by a measurement on a fixed dielectric and (4.19) can be used to determine  $(\sigma_0, \tan \delta_0)$ . By using this procedure to estimate the RT5880 using the RO4003C as a calibration dielectric permits to measure  $\epsilon_{RT} = 2.32$  and  $\tan \delta_{RT} = 0.003$  @2.6GHz hence improving the results.

**Table 4.4:** Provider's informations for the under-test substrates

	$\epsilon_r$	$\tan \delta$	Thickness (mm)
Rogers RO4003C	3.55	0.0021 @2.5GHz	0.8 & 1.57
Duroid RT5880	2.33	0.0012 @10GHz	0.8 & 1.57
Red	4.25	0.0180 @3.1GHz	1.9548



a)



b)

**Figure 4.14:** Testbench used for the measurement. a) Initial measurement to evaluate  $(\sigma_0, \omega_0)$ . b) Measurement of the "Red" sample.

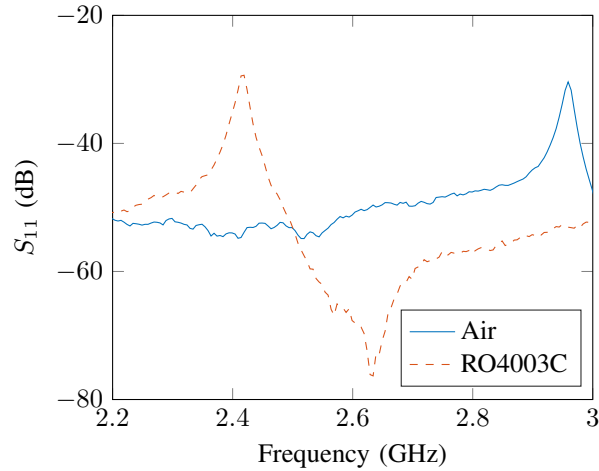


**Figure 4.15:**  $S_{11}$  parameters for a loop resonator in air (blue) and on a 0.7mm RO4003C Rogers's substrate.

**Table 4.5:** Comparison of the complex permittivity of the sample given by their provider and measured by this approach

	Thickness (mm)	$\epsilon_r$ (provider)	$\tan \delta$ (provider)	$\epsilon_r$ (this approach)	$\tan \delta$ (this approach)	$\epsilon_r$ (cavity method)	$\tan \delta$ (cavity method)
Rogers	0.7	3.55	0.0021 @2.5GHz	3.54	0.0024 @2.4GHz	3.72	0.0029 @2.5GHz
RO4003C	1.57	3.55	0.0021 @2.5GHz	3.59	0.0031 @2.2GHz	3.49	0.0014 @3GHz
Duroid	0.7	2.33	0.0012 @10GHz	2.31	0.004 @2.6GHz	2.29	0.0018 @2.5GHz
RT5880	1.59	2.33	0.0012 @10GHz	2.31	0.004 @2.5GHz	2.29	0.0018 @2.5GHz
Red	1.954	4.25	0.018 @3.1GHz	4.27	0.012 @2.2GHz	4.25	0.018 @3.1GHz

#### 4.2.5 Conclusion of the section

In this section, a method based on a radar approach to extract the complex permittivity of material is introduced. Tangential component of dielectric constant of low loss materials over the band of 2-3 GHz in a non-destructive manner is presented on slab dielectrics. A loop resonator is used to derive the expression from back-scattered signals. Simulations and measurements have been realised to validate the method. Discussions on the resonator and dielectric geometries have been done in order to improve the accuracy of the extraction. Also, additional calibration step using already known dielectric have been proposed and validated in practice to improve the estimations.

### 4.3 Conclusion of the chapter

In this chapter, the first section showed the possibility to detect the presence of grafted molecules on the surface of silicon nanowires thanks to a wireless RF radar approach based on the measurement of the back scattered signal of a resonant structure on which the nanowires are deposited. The measured resonance frequency allows the determination the intrinsic properties related to temperature and humidity variations. Several functionalizations of nanowires have been realized and characterized. A RF approach allows to detect significant differences related to the presence of grafted molecules on the surface of nanowires. The obtained results confirm the very good potential of the radar

approach to identify the functionalization of nanowires. Also, discussions about the application of such functionalizations is made to increase the sensibility of sensors working using radar approach.

In the second place, a method to characterize complex permittivity of dielectric was presented. The back-scattered signal from a resonant scatterer placed in contact with the dielectric is used to estimate the quantities. The proposed method was tested in simulation and validated in practice using different dielectric samples and different dielectric thicknesses. This method is wireless, non-destructive, with no restriction on the sample thickness and is done using a VNA and an antenna. Discussions on the geometry of the resonator as well as the calibration step is proposed in order to improve the sensing capability of the approach.

## Chapter 5

# Conclusion

This thesis manuscript was focused on the sensing assets of chipless RFID resonators. First, we have presented the history of RFID technology from the Thereminvox to today. A comparison between the barcode and RFID was presented to understand its assets and the enthusiasm around this new identification technology. The focus was done on chipless RFID to explain the context and the motivations behind this thesis work.

After that, temperature and humidity sensors were presented. This work started with the study of the thermal dilatation of metallic scatterers with no substrate. A method to characterize this dilatation using a contactless measurement was presented. This principle was then used in addition to permittivity thermal variations of resonators with a substrate to estimate temperature. Eventually, we noticed that the permittivity was also sensible to other physical quantities such as humidity. The material's permittivity (impacted by these two quantities) and dilatation (impacted only by the temperature) were taken into consideration to estimate these two physical quantities independently and simultaneously using two scatterers. Unlike previous works, the introduced model allows linking rigorously the variations of the measured resonance frequency with the temperature and humidity without any lookup table. The sensing limitation as well as the possibility of this approach to characterize the temperature and humidity dependencies of unknown materials were presented. Notice that no specific materials, i.e. particularly sensitive to the quantities to be measured, were used for ease of implementation.

In Chapter 3 the radiation pattern of a loop resonator was modeled using dipole antennas and antenna array-factor theory. The radiation pattern was used as a sensor to determine the position of the antenna in 3 dimensions. Since the sensor is based on the amplitude of the signal which is known to not be robust, uncertainties were studied with Monte-Carlo simulations. The radiation pattern was also used to encode multiple peaks of resonance on the same frequency slot without interfering together. This doubles the coding capacity without increasing the frequency band of operation. Lastly, a method to improve the readability of a chipless tag was presented. The proposed approach permits obtaining a higher signal-to-noise ratio and a better reading range (+30 cm). It also allows the separation of the resonance mode that is linked to the identifier from other parasitic resonance modes that may appear. This method will also be compared to state-of-art approaches and in harsh environments to highlight the potential of the proposed technique.



Lastly, Chapter 4 presented medium sensors. The first section suggested the possibility to detect the presence of grafted molecules on the surface of silicon nanowires by measuring the resonance frequency of loop resonators. Several functionalizations of nanowires have been realized and characterized. The obtained results confirm the very good potential of the radar approach to identify the functionalization of nanowires. Discussions about the application of such functionalizations were made to increase the sensibility of chipless RFID sensors. The second section presented a method to characterize the complex permittivity of dielectrics. The back-scattered signal from a resonant scatterer placed in contact with the dielectric was used to estimate the quantities. This method is wireless, non-destructive, with no restriction on the sample thickness, and is done using a VNA and an antenna. Discussions on the geometry of the resonator as well as the calibration step are proposed to improve the sensing capability of the approach.

Perspectives of future works were identified in the different chapters :

1. The characterization of thermal dilatation can be extended to dielectric materials while it is today restricted to metallic materials with the utilization of dielectric resonators.
2. The expression of the radiation pattern of the loop can be used to shape the scattered signals or to make new sensors such as the distance sensor presented in Section 3.4.
3. The test-bench presented in Section 4.1 used to characterize functionalized nanowires can be used to find functionalizations that improve the sensibility of chipless RFID sensors to temperature, humidity, gas, ...

## Appendix A

# Nanowires fabrication, functionalization and characterization

### A.1 Synthesis of silicon nanowires

Silicon nanowires growth was performed on quartz substrate using a horizontal low-pressure chemical vapor deposition (LPCVD) reactor at 600°C and total pressure of 3 Torr, using SiH<sub>4</sub> as precursor gas and Hydrogen (H<sub>2</sub>) as the carrier gas. First, the substrate was cleaned in acetone, rinsed with isopropanol and immediately followed by the deposition of a 2-nm-thick gold layer in a vacuum pressure of 10<sup>-6</sup> Pa. HCl gas was used to inhibit the gold diffusion and two-dimensional (2D) growth. Under such growth conditions, the nanowires exhibit p-type semiconductor behavior with an estimated density of ionized acceptors of the order of 10<sup>15</sup> cm<sup>-3</sup>.

### A.2 Silicon nanowires functionalization

In order to form organic silane monolayer covalently attached to silicon surface, a thin SiO<sub>2</sub> sheath surrounding the nanowires is required. Indeed, it facilitates silicon nanowires surface modification due to presence of hydroxyl groups and minimizes the interference from the current flow in analyte solution. Therefore, all the functionalization operations were carried out on freshly oxidized surfaces. The oxidation process was achieved by soaking the SiNWs (attached to quartz substrate) in 3:1 H<sub>2</sub>SO<sub>4</sub> / H<sub>2</sub>O<sub>2</sub> solution for 30 min at 80°C followed by copious rinsing with distilled water. Afterwards, the silicon nanowires were placed in oven at 70°C for 30 min.

#### A.2.1 Octadecyltrichlorosilane modified silicon nanowires (SiNWs-OTS)

The wafer was dipped in 20 µl OTS in 10 ml toluene at room temperature for 2h. After this period, the sample was washed with pure toluene, dried under a gentle stream of nitrogen, and placed in oven at 60°C for 20 min.

### A.2.2 Silicon nanowires functionalization with 3-azidopropyltriethoxysilane (SiNWs-N<sub>3</sub>)

The first step of this process is the preparation of 3-azidopropyltriethoxysilane. In 100 ml acetonitrile, 4g of 3-chloropropyltriethoxysilane, 2.16 g of sodium azide and 1.3 g of tetrabutylammonium bromide were added. The reaction mixture was placed under nitrogen atmosphere and stirred at reflux for 24 h. Then, the solvent was removed using a rotavapor under reduced pressure. The residue obtained was diluted in cyclohexane, filtered and washed with MgSO<sub>4</sub>. After removing the solvent afresh, we obtained a crude oil. The oxidized silicon nanowires were immersed in toluene (10 ml) containing 50  $\mu$ l of 3-azidopropyltriethoxysilane and heated at reflux for 24h. Afterwards, the sample was rinsed with pure toluene and placed in oven at 60°C for 20 min.

### A.2.3 Ethynylpyrene covalently attached to SiNWs (SiNWs-py)

The pyrene moieties were covalently attached to SiNWs via click chemistry reaction. First, in a solution of THF (10 ml) of ethynylpyrene (10 mg), we added 3 ml H<sub>2</sub>O containing 12 mg of ascorbic acid and 2 mg CuSO<sub>4</sub>·H<sub>2</sub>O. Then, the azide functionalized silicon nanowire was immersed in the mixture (in dark) for 24h. After that, the nanowires were rinsed carefully with pure THF in order to remove the unreacted ethynylpyrene and placed in oven at 60°C for 30 min.

## A.3 Results and discussion

We will describe hereafter the different analyses that have been implemented to ensure the presence of the different functional groups on the nanowires

### A.3.1 Characterization of SiO<sub>2</sub>-SiNWs

Basically, CVD synthesis method leads to high purity films and allows epitaxial growth of silicon wires [193]. However, the impurities (mainly from gold particules) incorporation into the nanowires were found to induce an anisotropic growth. That is why the pressure of the CVD reactor was lowered in order to reduce unwanted contamination and promoting the epitaxial growth of uniform silicon nanowires. Fig. A.1 shows the scanning electron microscopy (SEM) of the general morphology of oxidized P-type silicon nanowires. From the several pictures recorded (not shown), the length of SiNWs was found between 1 and 5  $\mu$ m, with an average value of 4  $\mu$ m. The short SiNWs ( $\leq 2 \mu$ m) occurred most probably when breaking the substrate. The core diameter of SiO<sub>2</sub>-SiNWs varied from 20-50 nm with average value of 30 nm. It should be also noted that the silicon nanowires exhibit different growth direction. This behaviour was already observed during silicon growth by CVD, especially for diameters smaller than about 50 nm [194]. Since silicon is known to oxidize easily when exposed at room temperature, we noticed that the SiO<sub>2</sub> thickness varied around 4 nm (inset).

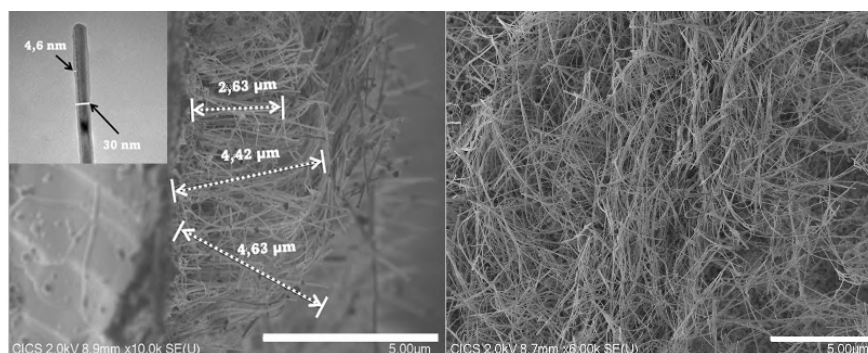


**Figure A.1:** Cross-sectional SEM image of P-type SiO<sub>2</sub>-SiNWs array. TEM image of SiNW (Inset). (insert top view picture)

### A.3.2 Octadecyltrichlorosilane modified silicon nanowires (SiNWs-OTS)

Oxidized silicon nanowires functionalized with chemically bonded alkyls end groups (OTS) were characterized by means of Fourier transform infrared (FTIR) spectroscopy (Fig. A.2). The spectrum shows a vibration band of Si-O-Si and Si-O-C between 1000-1250 cm<sup>-1</sup>. The presence of the monolayers indicated by two intense peaks obtained at 2850 and 2919 cm<sup>-1</sup> can be assigned to the symmetric and asymmetric C-H stretching vibrations of CH<sub>2</sub>, respectively. Finally, the small peak at ≈2960 cm<sup>-1</sup> can be assigned to the asymmetric C-H stretching vibration of the methyl end group. These results are in good agreement with the literature data [195]. It should be briefly recalled that according to theoretical simulations, increasing the length of the alkyl chain increases the van der Waals diameter and hinders the formation of dense alkyl packing [196]. The initial stages in the formation of alkyl layer involve the linkage between a silane and a hydroxyl group probably catalysed by traces of adsorbed surface water (physisorption) which is followed by a condensation reaction, via water consumption, to form a covalent bond (chemisorption). Note that, lateral interactions between long alkyl chains might occur during the physisorption step. A major drawback of long hydrocarbon chain is that they are able to reduce the thermal stability and change the mechanical properties, such as elasticity and hardness. Srinivasan et al. reported that the thermal stability of the OTS monolayer is 150 °C in ambient air and 450 °C in pure N<sub>2</sub> [197].

### A.3.3 Formation of Azide and pyrene terminated silicon nanowires surfaces

As described above, our approach for the preparation of azide-terminated silicon nanowires is based on silanization of azidopropyltriethoxysilane on oxidized silicon surfaces whereupon the pyrene moieties were covalently grafted via a chemical click reaction. The surface composition and the chemical environment were investigated with FTIR spectroscopy and XPS measurements. Fig. A.3 shows the different FTIR spectra, from unmodified nanowires to SiNWs-pyrene. The unmodified silicon nanowires (a) show only a vibrational peaks Si-O-Si between 1000-1200 cm<sup>-1</sup> owing to the surface oxidation during sample treatment. After silanization of azide group (b), we can clearly observe the appearance of a new peak at 2100 cm<sup>-1</sup>, characteristic of N<sub>3</sub>-vibration. The C-H stretching vibrations are located at 2855, 2876, 2930 cm<sup>-1</sup> [198]. Briefly recall that the click chemistry reaction is a cycloaddition reaction between an alkyne and azide groups [199]. The success of the reaction is

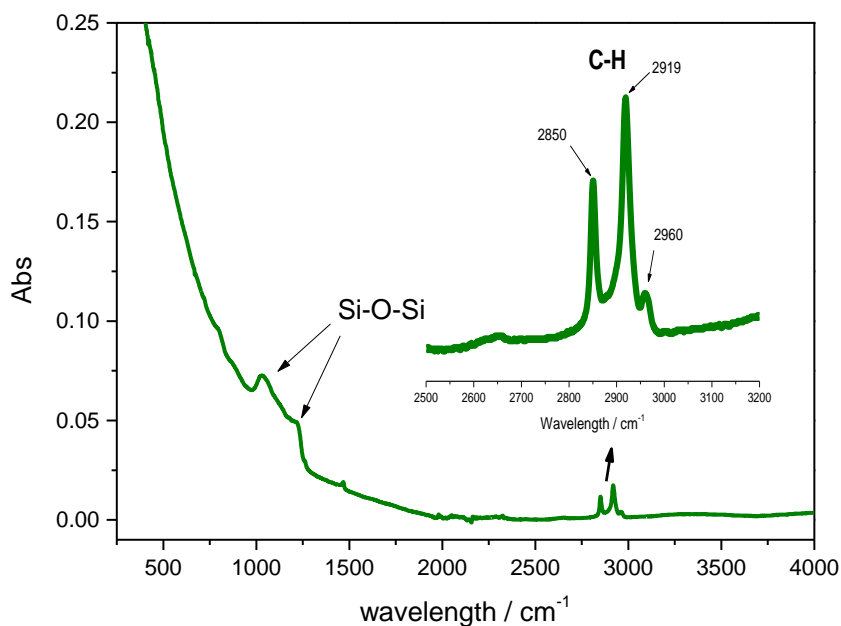


**Figure A.2:** Infrared spectrum of octadecyl functionalized silicon nanowire; C-H region (inset).

typically evidenced by the decrease or disappearance of  $N_3$ -vibration band after reaction completion [200]. Fig. A.3 shows a sharp decrease of azide peak at  $2100\text{ cm}^{-1}$  together with the appearance of new peaks at  $1612$ ,  $1362$  and  $1319\text{ cm}^{-1}$  typical of stretching modes of  $C=C$  and  $C-H$  of pyrene. This latter indicating the successful reaction.

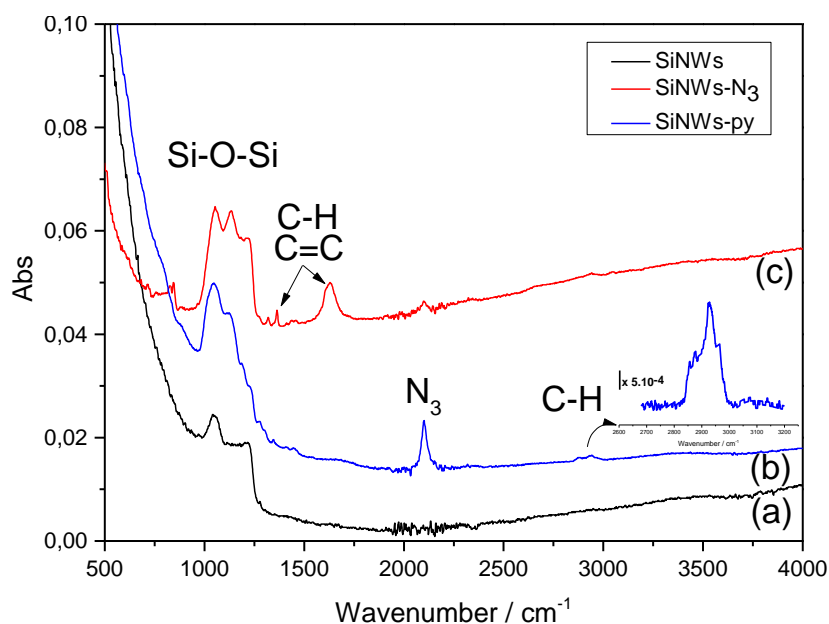


**Figure A.3:** Infrared spectrum of unmodified silicon nanowires (a), azide modified silicon nanowire (b), pyrene modified silicon nanowires (c).

XPS analyses were also performed in order to confirm the FTIR observations, especially the

incorporation of  $N_3$  function and pyrene portion on silicon nanowires surface. XPS survey spectrum of  $N_3$ -SiNWs indicate the presence of C 1s, O 1s, N 1s, Si 2s, Si 2p. We focus on the region of N1s core level (Fig. A.4). The peaks at 403,7 eV and 400 eV with ratio 2:1 are attributable respectively to the central electron-deficient nitrogen ( $-N=N=N$ ) and the two lateral nitrogen atoms ( $-N=N=N$ ) [201]. However, the same analysis performed, after the click reaction with ethynylpyrene, shown a one peak which can be fitted into bands at 401,3 and 400,1 eV attributed to the conversion in azide groups into the 1,2,3-triazole ring [202]. In addition, we observe an increase of intensity of carbon peak at 284.5 eV after the click chemistry reaction which is related to the presence of pyrene moiety on silicon nanowires surfaces.

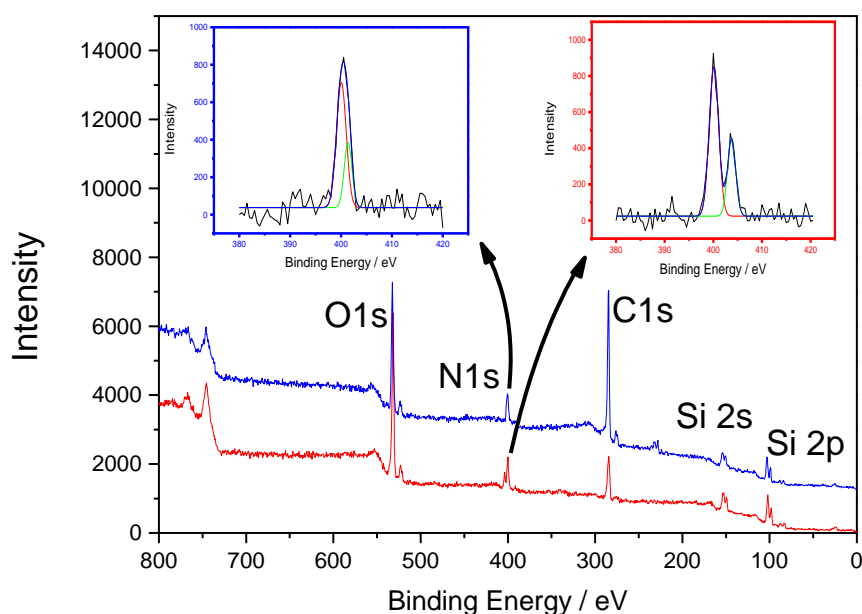


**Figure A.4:** XPS spectra recorded on silicon nanowire modified with azide (red curve) and pyrene groups (blue curve) including enlarged spectra of N1s before and after click chemistry.



## Appendix B

# Résumé en français

La RFID est une technologie d'identification nouvelle qui produit des étiquettes (tags) similaires au code à barres en adoptant une approche radar sans fil. Ces dernières années, cette technologie a subi un essor considérable que ce soit dans son utilisation mais également dans les efforts de recherche qui lui sont associés. De nombreuses familles RFID ont émergé en cherchant à répondre à de nouvelles problématiques. La RFID sans puce (ou chipless) en est un exemple ; l'objectif affiché est de réduire considérablement le prix du tag de manière à pouvoir concurrencer le code à barres. À défaut de pouvoir baisser indéfiniment le prix d'un tag sans puce pour égaler le code à barres, les fonctionnalités que ne possède pas son concurrent sont mises en avant. On retrouve les atouts liés à sa lecture par ondes radio mais aussi la possibilité d'ajouter des fonctionnalités capteurs directement dans le tag.

Cette thèse fait partie du projet "ScattererID" actuellement mené par Etienne PERRET. Il s'agit d'un projet financé par l'ERC. L'objectif de ce projet est de : *" de développer une nouvelle génération d'étiquettes d'identification par radiofréquence, sans puce, imprimables, recyclables et peu coûteuses. Contrairement aux codes à barres, elles peuvent être lues à travers des objets opaques ou à distance. Il est également possible d'implémenter de nouvelles fonctionnalités qui sont incompatibles avec la technologie des codes à barres. Enfin, comme ils ne comportent ni puce ni antenne, ils sont beaucoup moins chers que les étiquettes RFID. Avec des coûts comparables à ceux d'un code à barres, ces étiquettes devraient se démarquer en offrant plus de fonctionnalités que l'approche optique"*.

Cette thèse vise à tirer profit des applications capteurs possibles des étiquettes RFID sans puce pour apporter des avantages vis-à-vis des code à barres.

Il est important de noter que les applications de détection développées peuvent être mises en œuvre sur des étiquettes RFID sans puce déjà existantes, mais qu'elles peuvent également être utilisées indépendamment comme un capteur complet. Les avantages peuvent être trouvés dans la méthode de lecture sans fil, son coût, ses petites dimensions (planaire), sa durée de vie infinie, ou son utilisation dans un environnement dangereux où les capteurs à puce ne peuvent pas aller en raison de la présence d'électronique (température trop élevée, corrosif, ...).

La détection en plus de la fonctionnalité d'identification peut être utilisée dans l'exemple de la boutique Amazon. L'identification permet au magasin de savoir quels articles sont pris par le consommateur, de gérer les rayons et les dates d'expiration. La détection peut être ajoutée pour surveiller la température des aliments (protection de la chaîne du froid) et l'humidité (protection des appareils



ménagers) afin de contrôler la qualité des produits. Les magasins ne sont pas les seuls bénéficiaires potentiels. Il pourrait également être souhaitable d'avoir la protection d'infrastructures sensibles en détectant la présence d'eau dans les murs (fuite d'eau) en utilisant la planéité des tags ainsi que leur durée de vie infinie de fonctionnement sans maintenance. Enfin, de tels capteurs commencent à apparaître auprès du grand public avec par exemple des bracelets à des fins d'autorisation, des jouets, de la reconnaissance de gestes, du suivi de l'humain... La technologie RFID peut représenter le point d'inflexion pour le développement massif de l'IoT.

Ce manuscrit de thèse s'est concentré sur les atouts capteurs des résonateurs RFID sans puce. Dans un premier temps, nous avons présenté l'historique de la technologie RFID depuis le Theremin jusqu'à aujourd'hui. Une comparaison entre le code-barres et la RFID a été présentée afin de comprendre ses atouts et l'enthousiasme autour de cette nouvelle technologie d'identification. Un focus a été fait sur la RFID sans puce pour expliquer le contexte et les motivations de ce travail de thèse. Nous avons pu voir les principes physiques qui permettent à cette technologie de fonctionner en tant que système d'identification mais aussi concernant l'approche capteur associé.

Ensuite, les capteurs de température et d'humidité ont été présentés. Ce travail a débuté par l'étude de la dilatation thermique de résonateurs métalliques sans substrat. Une méthode permettant de caractériser cette dilatation par une mesure sans contact a été présentée offrant des avantages par rapport aux méthodes actuelles. Ensuite, nous avons étudié la détection de la température en incluant la variation de la permittivité sur la réponse du résonateur. Cette partie étudie la mesure de température, mais aussi son cas applicatif dans la vie réelle, avec une étude de la plage de lecture, de différents cas d'environnement réel possibles, ... Les équations ont également été étendues à différents résonateurs. Finalement, nous avons remarqué que la permittivité était également sensible à d'autres quantités physiques telles que l'humidité. La permittivité du matériau (impactée par ces deux quantités) et la dilatation (impactée uniquement par la température) ont été prises en compte pour estimer ces deux quantités physiques indépendamment et simultanément en utilisant deux résonateurs. Contrairement aux travaux précédents, le modèle introduit permet de relier rigoureusement les variations de la fréquence de résonance mesurée avec la température et l'humidité sans aucune table de correspondance. Cela permet non seulement de réaliser la multi-détection mais aussi de réduire les erreurs sur les quantités estimées (puisque elles ont toutes un impact sur la fréquence de résonance qui est la seule mesurande). Ces erreurs ont été caractérisées à l'aide de simulations numériques de Monte-Carlo. Un banc de mesure pour caractériser les dépendances en température et en humidité de matériaux inconnus a été présentées. Finalement, les équations ont été généralisées pour mesurer d'autre quantité physique qui pourraient impacter la fréquence de résonance du résonateur. Une mesure de température et d'humidité en simultanée est présentée Figure. B.1 à titre d'exemple.

Dans le chapitre 3, le diagramme de rayonnement d'un résonateur boucle a été modélisé à l'aide d'antennes dipôles et de la théorie de réseau d'antennes. Ce modèle de rayonnement a été utilisé pour mesurer la rotation de la boucle en 3 dimensions. Contrairement aux capteurs d'angle RFID sans puce déjà mis en œuvre, celui présenté ici permet d'extraire la rotation de l'étiquette ou la position de l'antenne en 3D en utilisant une nouvelle approche basée sur le diagramme de rayonnement du résonateur. Un modèle analytique est développé pour mesurer l'orientation de

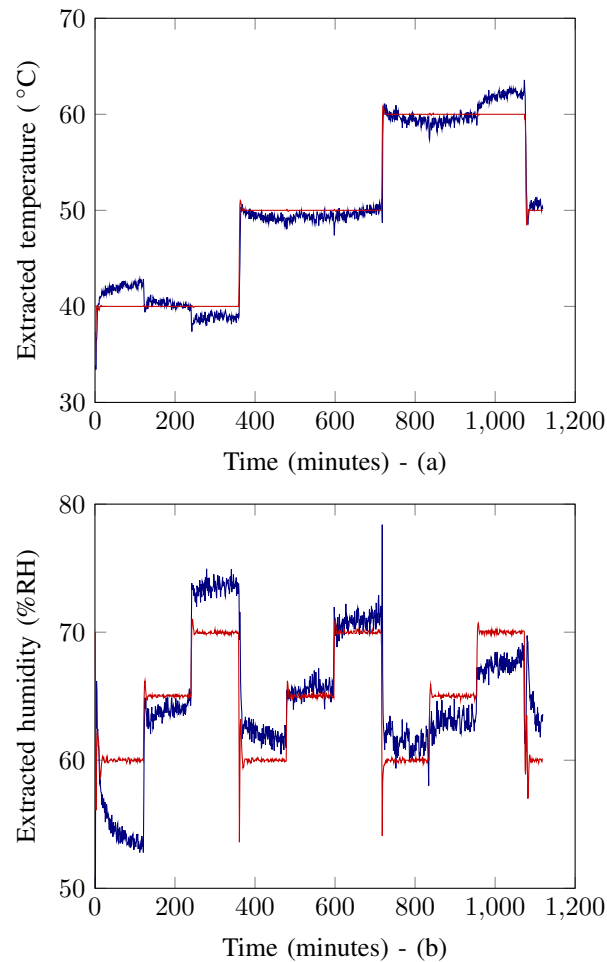


**Figure B.1:** a) Température estimée en bleu avec (2.38a) et température mesurée avec un capteur électronique en rouge. b) Humidité relative extraite avec (2.38b) en bleu et mesurée avec le capteur électronique en rouge.

l'étiquette en déterminant à la fois l'inclinaison et l'angle azimutal de l'étiquette dans un système de coordonnées sphériques pour les configurations d'antenne mono-statique et bi-statique. Cette méthode s'est avérée robuste et indépendante de la calibration, ce qui n'est pas le cas des capteurs d'orientation RFID sans puce. Ce modèle de rayonnement a également été utilisé pour augmenter la capacité des étiquettes RFID sans puce. Alors que l'idée aujourd'hui est de rendre les résonateurs plus compacts, ce travail a permis d'augmenter la capacité de codage en allouant plusieurs pics de résonance dans un seul créneau de fréquence sans interférer ensemble. Il s'appuie sur la diversité du diagramme de rayonnement de différentes topologies de résonateurs ou de différents modes de résonance sur la même topologie de résonateur. Enfin, la polarisation des résonateurs a été étudiée pour améliorer la robustesse de la lecture RFID. Cette approche a été comparée aux approches de l'état de l'art telles que le time-gating. Il a été prouvé que cette méthode permet d'obtenir un meilleur rapport signal/bruit des résonateurs dont l'orientation par rapport au lecteur est inconnue. Grâce à ce principe, il est également possible de séparer le mode de résonance du résonateur qui est connecté à l'identificateur des autres modes de résonance parasites qui peuvent apparaître en raison

d'un éventuel désalignement entre l'étiquette et l'antenne. Des mesures dans des environnements difficiles, ainsi que des comparaisons avec des techniques classiques telles que le time gating, ont été présentées. Une étude de l'amélioration de la portée de lecture a été réalisée pour mettre en évidence le potentiel de la technique proposée. Ces capteurs n'utilisent pas la valeur de la fréquence de résonance pour détecter des quantités physiques mais plutôt son amplitude. L'amplitude étant moins robuste à l'environnement que la fréquence de résonance, chaque capteur a été étudié à l'aide de simulations de Monte-Carlo ou de mesures réelles afin de démontrer son application dans des environnements réels. Le capteur d'orientation a été implémenté sur Matlab en temps réel. Une illustration de ces mesures est présentée Figure B.2. Les vidéos sont disponibles aux liens [137, 138].

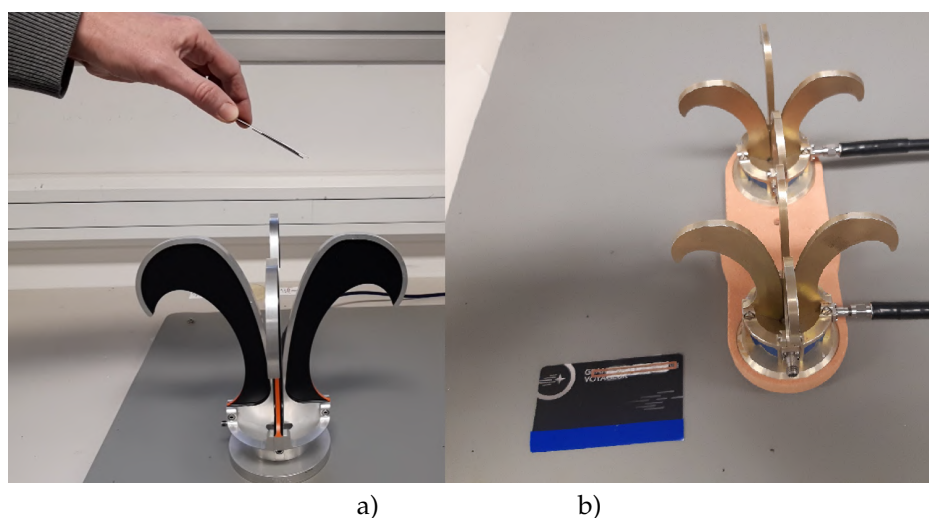


**Figure B.2:** Application temps réel : exemple de suivi angulaire. Au-dessus de l'antenne, un utilisateur tient le résonateur attaché à une carte plastique. L'équation (3.23) est utilisée pour extraire les angles à partir des mesures effectuées par le VNA connecté aux antennes. Le résultat est affiché en temps réel sur l'écran d'un ordinateur afin de visualiser les déplacements générés par l'utilisateur. a) Configuration monostatique, détection de l'angle d'azimut uniquement (vidéo : [137]), b) Configuration bi-statique, détection de l'élévation et de l'azimut (vidéo : [138]).

Enfin, le dernier chapitre a montré la possibilité de détecter la présence de molécules greffées à la surface de nanofils de silicium grâce à une approche radar RF sans fil basée sur la mesure du signal rétrodiffusé d'une structure résonante sur laquelle les nanofils sont déposés. La fréquence de résonance mesurée permet de déterminer les propriétés intrinsèques liées aux variations de température et d'humidité. Plusieurs fonctionnalisations de nanofils ont été réalisées et caractérisées. Une approche RF permet de détecter des différences significatives liées à la présence de molécules greffées à la surface des nanofils. Les résultats obtenus confirment le très bon potentiel de l'approche radar pour identifier la fonctionnalisation des nanofils. De plus, des discussions sur l'application de telles fonctionnalisations sont menées pour augmenter la sensibilité des capteurs fonctionnant avec l'approche radar. Un exemple de représentation en 3-dimensions de la caractérisation des nanofils permettant leur identification est présenté Figure B.3. En second lieu, une méthode pour caractériser la permittivité complexe d'un diélectrique a été présentée. Le signal rétrodiffusé par un diffuseur résonnant placé en contact avec le diélectrique est utilisé pour estimer les quantités. La méthode proposée a été testée en simulation et validée en pratique en utilisant différents échantillons diélectriques

et différentes épaisseurs de diélectrique. Cette méthode est sans fil, non-destructive, sans restriction sur l'épaisseur de l'échantillon et se fait à l'aide d'un VNA et d'une antenne. Des discussions sur la géométrie du résonateur ainsi que sur l'étape de calibration sont proposées afin d'améliorer la capacité de détection de l'approche.

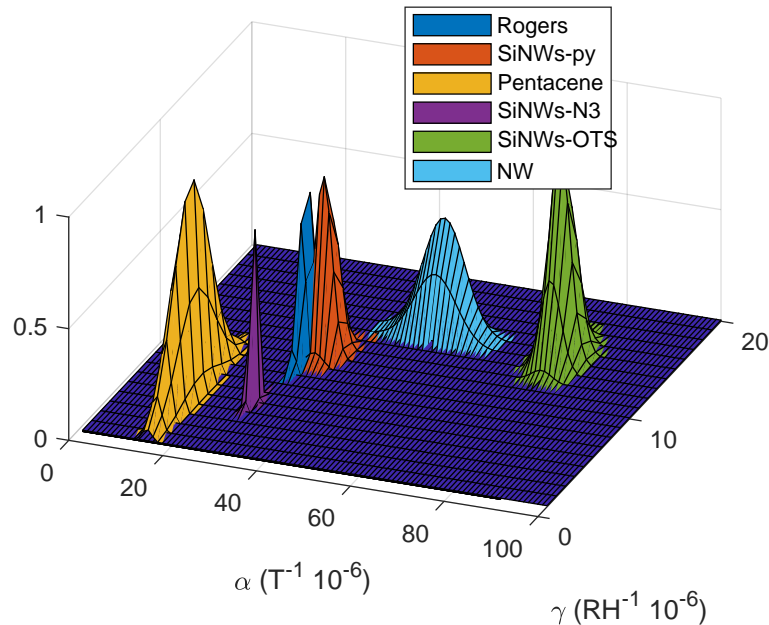


**Figure B.3:** Représentation tridimensionnelle des 6 échantillons de nanofils mesurés en pratique.

Les perspectives de travaux futurs ont été identifiées dans les différents chapitres :

1. La caractérisation de la dilatation thermique peut être étendue aux matériaux diélectriques alors qu'elle est aujourd'hui limitée aux matériaux métalliques avec l'utilisation de résonateurs diélectriques.
2. L'expression du diagramme de rayonnement de la boucle peut être utilisée pour mettre en forme les signaux diffusés ou pour fabriquer de nouveaux capteurs tels que le capteur de distance présenté dans la Section 3.4.
3. Le banc d'essai présenté dans la Section 4.1 utilisé pour caractériser les nanofils fonctionnalisés peut être utilisé pour trouver des fonctionnalisations (ou juste substrats) qui amélioreraient la sensibilité des capteurs RFID sans puce à la température, l'humidité, le gaz, ...

**Mot-clés :** RFID sans puce, capteur sans-fil, radar, code à barres.



# Bibliography

- [1] M. R. Rieback, B. Crispo, and A. S. Tanenbaum, "The evolution of RFID security," *IEEE Pervasive Computing*, no. 1, pp. 62–69, 2006.
- [2] P. Nikitin, "Leon Theremin (lev termen)," *IEEE Antennas and Propagation Magazine*, vol. 54, no. 5, pp. 252–257, 2012.
- [3] J. Landt, "The history of RFID," *IEEE potentials*, vol. 24, no. 4, pp. 8–11, 2005.
- [4] A. N. Nambiar, "RFID technology: A review of its applications," in *Proceedings of the world congress on engineering and computer science*, vol. 2. Citeseer, 2009, pp. 20–22.
- [5] RFID forecasts, players and opportunities 2018-2028 (idtechex) . [accessed 22 aug. 2022]. [Online]. Available: <https://www.idtechex.com/en/research-report/rfid-forecasts-players-and-opportunities-2018-2028/642>
- [6] P. Harrop and R. Das, *Printed and Chipless RFID Forecasts, Technologies & Players 2009-2029*. IDtechEx, 2010.
- [7] Allied market research. [accessed 20 jul. 2022]. [Online]. Available: <https://www.alliedmarketresearch.com/>
- [8] Just walk out (technology by amazon). [accessed 22 aug. 2022]. [Online]. Available: <https://justwalkout.com/>
- [9] G. L. Puerini, D. Kumar, and S. Kessel, "Transitioning items from a materials handling facility," Aug. 24 2021, uS Patent 11,100,463.
- [10] J. M. Purushothama, S. Lopez-Soriano, A. Vena, B. Sorli, I. Susanti, and E. Perret, "Electronically rewritable chipless RFID tags fabricated through thermal transfer printing on flexible PET substrates," *IEEE Transactions on Antennas and Propagation*, vol. 69, no. 4, pp. 1908–1921, 2020.
- [11] F. Costa, S. Genovesi, M. Borgese, A. Michel, F. A. Dicandia, and G. Manara, "A review of RFID sensors, the new frontier of internet of things," *Sensors*, vol. 21, no. 9, p. 3138, 2021.
- [12] Magicbands (disney). [accessed 22 aug. 2022]. [Online]. Available: <https://en.wikipedia.org/wiki/MagicBands>
- [13] Amiibo (nintendo). [accessed 22 aug. 2022]. [Online]. Available: <https://www.nintendo.co.uk/Hardware/amiibo-/About-amiibo/About-amiibo-932316.html>
- [14] A. Spielberg, A. Sample, S. E. Hudson, J. Mankoff, and J. McCann, "RapID: A framework for fabricating low-latency interactive objects with RFID tags," in *Proceedings of the 2016 chi conference on human factors in computing systems*, 2016, pp. 5897–5908.

- [15] H. Li, E. Brockmeyer, E. J. Carter, J. Fromm, S. E. Hudson, S. N. Patel, and A. Sample, "PaperID: A technique for drawing functional battery-free wireless interfaces on paper," in *Proceedings of the 2016 CHI Conference on Human Factors in Computing Systems*, 2016, pp. 5885–5896.
- [16] G. Marrocco, "RFID antennas for the uhf remote monitoring of human subjects," *IEEE transactions on antennas and propagation*, vol. 55, no. 6, pp. 1862–1870, 2007.
- [17] S. Amendola, R. Lodato, S. Manzari, C. Occhiuzzi, and G. Marrocco, "RFID technology for iot-based personal healthcare in smart spaces," *IEEE Internet of things journal*, vol. 1, no. 2, pp. 144–152, 2014.
- [18] C. Occhiuzzi, G. Contri, and G. Marrocco, "Design of implanted RFID tags for passive sensing of human body: The STENTag," *IEEE Transactions on Antennas and Propagation*, vol. 60, no. 7, pp. 3146–3154, 2012.
- [19] M. I. Skolnik, "Radar handbook second edition," *McGrawHill*, 1990.
- [20] C. E. Baum, "The singularity expansion method," *Transient electromagnetic fields*, pp. 129–179, 1976.
- [21] R. Rezaiesarlak and M. Manteghi, *Chipless RFID*. Springer, 2016.
- [22] S. Schelkunoff, "Representation of impedance functions in terms of resonant frequencies," *Proceedings of the IRE*, vol. 32, no. 2, pp. 83–90, 1944.
- [23] N. Barbot, O. Rance, and E. Perret, "Classical RFID versus chipless RFID read range: Is linearity a friend or a foe?" *IEEE Transactions on Microwave Theory and Techniques*, 2021.
- [24] N. Barbot, O. Rance, and E. Perret, "Differential RCS of modulated tag," *IEEE Transactions on Antennas and Propagation*, vol. 69, no. 9, pp. 6128–6133, 2021.
- [25] C. A. Balanis, "Advanced engineering electromagnetics, john wiley & sons," *Inc., New York*, 1989.
- [26] P. V. Nikitin, K. V. S. Rao, and S. Lazar, "An overview of near field UHF RFID," in *2007 IEEE International Conference on RFID*, Grapevine, TX, Mar. 2007, pp. 167–174.
- [27] A. Abdelnour, A. Hallet, S. B. Dkhil, P. Pierron, D. Kaddour, and S. Tedjini, "Energy harvesting based on printed organic photovoltaic cells for RFID applications," in *2019 IEEE International Conference on RFID Technology and Applications (RFID-TA)*, Pisa, Italy, Sep. 2019, pp. 110–112.
- [28] A. P. Sample, D. J. Yeager, P. S. Powledge, and J. R. Smith, "Design of a passively-powered, programmable sensing platform for UHF RFID systems," in *2007 IEEE International Conference on RFID*, Grapevine, TX, Mar. 2007, pp. 149–156.
- [29] K. V. S. Rao, P. V. Nikitin, and S. F. Lam, "Antenna design for UHF RFID tags: a review and a practical application," *IEEE Trans. Antennas Propag.*, vol. 53, no. 12, pp. 3870–3876, Dec. 2005.
- [30] U. Karthaus and M. Fischer, "Fully integrated passive UHF RFID transponder IC with 16.7-microW minimum RF input power," *IEEE J. Solid-State Circuits*, vol. 38, no. 10, pp. 1602–1608, Oct. 2003.

- [31] S. Thomas, J. Teizer, and M. Reynolds, "Smarthat: A battery-free worker safety device employing passive UHF RFID technology," in *2011 IEEE International Conference on RFID*, Orlando, FL, Apr. 2011, pp. 85–90.
- [32] A. Sharma, A. T. Hoang, F. Nekoogar, F. U. Dowla, and M. S. Reynolds, "An electrically small, 16.7 m range, ISO18000-6c UHF RFID tag for industrial radiation sources," *IEEE RFID J.*, vol. 2, no. 2, pp. 49–54, Jun. 2018.
- [33] T. H. Li, A. Borisenko, and M. Bolic, "Open platform semi-passive RFID tag," in *11th International Conference, ADHOC-NOW 2012*, Belgrade, Serbia, Jul. 2012, pp. 249–259.
- [34] S. J. Thomas and M. S. Reynolds, "A 96 Mbit/sec, 15.5 pJ/bit 16-QAM modulator for UHF backscatter communication," in *2012 IEEE International Conference on RFID (RFID)*, Orlando, FL, Apr. 2012, pp. 185–190.
- [35] D. De Donno, L. Catarinucci, and L. Tarricone, "A battery-assisted sensor-enhanced RFID tag enabling heterogeneous wireless sensor networks," *IEEE Sensors J.*, vol. 14, no. 4, pp. 1048–1055, Apr. 2014.
- [36] V. Pillai, H. Heinrich, D. Dieska, P. V. Nikitin, R. Martinez, and K. V. S. Rao, "An ultra-low-power long range battery/passive RFID tag for UHF and microwave bands with a current consumption of 700 nA at 1.5 V," *IEEE Trans. Circuits Syst. I*, vol. 54, no. 7, pp. 1500–1512, Jul. 2007.
- [37] S. Preradovic, I. Balbin, N. C. Karmakar, and G. F. Swiegers, "Multiresonator-based chipless RFID system for low-cost item tracking," *IEEE Trans. Microw. Theory Techn.*, vol. 57, no. 5, pp. 1411–1419, May 2009.
- [38] H. El Matbouly, S. Tedjini, K. Zannas, and Y. Duroc, "Chipless sensing system compliant with the standard radio frequency regulations," *IEEE RFID J.*, vol. 3, no. 2, pp. 83–90, Jun. 2019.
- [39] A. Vena, E. Perret, and S. Tedjini, "A depolarizing chipless RFID tag for robust detection and its FCC compliant UWB reading system," *IEEE Trans. Microw. Theory Techn.*, vol. 61, no. 8, pp. 2982–2994, Aug. 2013.
- [40] M. Garbati, R. Siragusa, E. Perret, A. Vena, and C. Halopé, "High performance chipless RFID reader based on IR-UWB technology," in *2015 9th European Conference on Antennas and Propagation (EuCAP)*, Lisbon, Portugal, Apr. 2015, pp. 1–5.
- [41] R. Tavares de Alencar, N. Barbot, M. Garbati, and E. Perret, "Practical comparison of decoding methods for chipless RFID system in real environment," in *2019 IEEE International Conference on RFID Technology and Applications (RFID-TA)*, Pisa, Italy, Sep. 2019, pp. 207–211.
- [42] A. Vena, E. Perret, and S. Tedjini, "Chipless RFID tag using hybrid coding technique," *IEEE Trans. Microw. Theory Techn.*, vol. 59, no. 12, pp. 3356–3364, Dec. 2011.
- [43] F. Costa, S. Genovesi, and A. Monorchio, "A chipless RFID based on multiresonant high-impedance surfaces," *IEEE Trans. Microw. Theory Techn.*, vol. 61, no. 1, pp. 146–153, Jan. 2013.



- [44] M. Khaliel, A. El-Awamry, A. Fawky, and T. Kaiser, "Long reading range chipless RFID system based on reflectarray antennas," in *2017 11th European Conference on Antennas and Propagation (EUCAP)*, Paris, France, Mar. 2017, pp. 3384–3388.
- [45] A. Ramos, E. Perret, O. Rance, S. Tedjini, A. Lázaro, and D. Girbau, "Temporal separation detection for chipless depolarizing frequency-coded RFID," *IEEE Transactions on microwave theory and techniques*, vol. 64, no. 7, pp. 2326–2337, 2016.
- [46] A. Vena, E. Perret, and S. Tedjini, "A depolarizing chipless RFID tag for robust detection and its FCC compliant UWB reading system," *IEEE transactions on microwave theory and techniques*, vol. 61, no. 8, pp. 2982–2994, 2013.
- [47] R. Rezaiesarlak and M. Manteghi, "Short-time matrix pencil method for chipless RFID detection applications," *IEEE Transactions on Antennas and Propagation*, vol. 61, no. 5, pp. 2801–2806, 2013.
- [48] A. T. Blischak and M. Manteghi, "Embedded singularity chipless RFID tags," *IEEE Transactions on Antennas and Propagation*, vol. 59, no. 11, pp. 3961–3968, 2011.
- [49] F. Costa, A. Gentile, S. Genovesi, L. Buoncristiani, A. Lazaro, R. Villarino, and D. Girbau, "A depolarizing chipless RF label for dielectric permittivity sensing," *IEEE Microw. Wireless Compon. Lett.*, vol. 28, no. 5, pp. 371–373, 2018.
- [50] M. Borgese, F. Costa, S. Genovesi, and G. Manara, "Depolarizing chipless tags with polarization insensitive capabilities," *Electronics*, vol. 10, no. 4, p. 478, 2021.
- [51] Z. Ali and E. Perret, "A simple RCS calibration approach for depolarizing chipless RFID tags," in *2021 IEEE MTT-S International Microwave Symposium (IMS)*. IEEE, 2021, pp. 165–168.
- [52] R. Nair, E. Perret, and S. Tedjini, "Temporal multi-frequency encoding technique for chipless RFID applications," in *2012 IEEE/MTT-S International Microwave Symposium Digest*. IEEE, 2012, pp. 1–3.
- [53] R. Nair, E. Perret, and S. Tedjini, "Novel encoding in chipless RFID using group delay characteristics," in *2011 SBMO/IEEE MTT-S International Microwave and Optoelectronics Conference (IMOC 2011)*. IEEE, 2011, pp. 896–900.
- [54] I. Jalaly and I. Robertson, "Capacitively-tuned split microstrip resonators for RFID barcodes," in *2005 European Microwave Conference*, vol. 2. IEEE, 2005, pp. 4–pp.
- [55] O. Rance, R. Siragusa, P. Lemaitre-Auger, and E. Perret, "Rcs magnitude coding for chipless RFID based on depolarizing tag," in *2015 IEEE MTT-S International Microwave Symposium*. IEEE, 2015, pp. 1–4.
- [56] I. Balbin and N. C. Karmakar, "Phase-encoded chipless RFID transponder for large-scale low-cost applications," *IEEE microwave and wireless components letters*, vol. 19, no. 8, pp. 509–511, 2009.
- [57] M. Zomorodi and N. C. Karmakar, "Novel mimo-based technique for em-imaging of chipless RFID," in *2015 IEEE MTT-S International Microwave Symposium*. IEEE, 2015, pp. 1–4.

- [58] M. Poepperl, J. Adametz, and M. Vossiek, "Polarimetric radar barcode: A novel chipless RFID concept with high data capacity and ultimate tag robustness," *IEEE Transactions on Microwave Theory and Techniques*, vol. 64, no. 11, pp. 3686–3694, 2016.
- [59] O. Rance, R. Siragusa, P. Lemaitre-Auger, and E. Perret, "Toward RCS magnitude level coding for chipless RFID," *IEEE Transactions on Microwave Theory and Techniques*, vol. 64, no. 7, pp. 2315–2325, 2016.
- [60] C. S. Hartmann, "A global SAW ID tag with large data capacity," in *2002 IEEE Ultrasonics Symposium, 2002. Proceedings.*, vol. 1. IEEE, 2002, pp. 65–69.
- [61] B. Shao, Q. Chen, Y. Amin, S. M. David, R. Liu, and L.-R. Zheng, "An ultra-low-cost RFID tag with 1.67 gbps data rate by ink-jet printing on paper substrate," in *2010 IEEE Asian Solid-State Circuits Conference*. IEEE, 2010, pp. 1–4.
- [62] A. El-Awamry, M. Khaliel, A. Fawky, M. El-Hadidy, and T. Kaiser, "Novel notch modulation algorithm for enhancing the chipless RFID tags coding capacity," in *2015 IEEE International Conference on RFID (RFID)*. IEEE, 2015, pp. 25–31.
- [63] E. Perret, *Radio Frequency Identification and Sensors: From RFID to Chipless RFID*. John Wiley & Sons, 2014.
- [64] A. Vena, E. Perret, and S. Tedjini, "A fully printable chipless RFID tag with detuning correction technique," *IEEE Microw. Wireless Compon. Lett.*, vol. 22, no. 4, pp. 209–211, 2012.
- [65] A. Vena, E. Perret, and S. Tedjini, "Chipless RFID tag using hybrid coding technique," *IEEE Transactions on Microwave Theory and Techniques*, vol. 59, no. 12, pp. 3356–3364, 2011.
- [66] C. Feng, W. Zhang, L. Li, L. Han, X. Chen, and R. Ma, "Angle-based chipless RFID tag with high capacity and insensitivity to polarization," *IEEE Transactions on Antennas and Propagation*, vol. 63, no. 4, pp. 1789–1797, 2015.
- [67] M. Zomorodi and N. C. Karmakar, "Cross-RCS based, high data capacity, chipless RFID system," in *2014 IEEE MTT-S International Microwave Symposium (IMS2014)*. IEEE, 2014, pp. 1–4.
- [68] S. Kofman, Y. Meerfeld, M. Sandler, S. Dukler, and V. Alchanatis, "Radio frequency identification system and data reading method," May 1 2012, uS Patent 8,167,212.
- [69] A. Vena, E. Perret, and S. Tedjini, "A compact chipless RFID tag using polarization diversity for encoding and sensing," in *2012 IEEE International Conference on RFID (RFID)*. IEEE, 2012, pp. 191–197.
- [70] Federal communications commission, "radio frequency devices," code of federal regulations, part 15. [accessed 28 oct. 2019]. [Online]. Available: [https://www.highfrequencyelectronics.com/Jan05/HFE0105\\_Tutorial.pdf](https://www.highfrequencyelectronics.com/Jan05/HFE0105_Tutorial.pdf)
- [71] E. Decision, "On the harmonized conditions for devices using ultra-wideband (uwb) technology in bands below 10.6 ghz," ECC, Tech. Rep., 2007.

- [72] W. Wiesbeck and D. Kahny, "Single reference, three target calibration and error correction for monostatic, polarimetric free space measurements," *Proceedings of the IEEE*, vol. 79, no. 10, pp. 1551–1558, 1991.
- [73] S. Preradovic, I. Balbin, N. C. Karmakar, and G. F. Swiegers, "Multiresonator-based chipless RFID system for low-cost item tracking," *IEEE Transactions on Microwave Theory and Techniques*, vol. 57, no. 5, pp. 1411–1419, 2009.
- [74] E. Perret, M. Hamdi, G. E. P. Tourtollet, R. Nair, F. Garet, A. Delattre, A. Vena, L. Duvillaret, P. Martinez, S. Tedjini *et al.*, "THID, the next step of chipless RFID," in *2013 IEEE International Conference on RFID (RFID)*. IEEE, 2013, pp. 261–268.
- [75] I. Jalaly and I. Robertson, "Capacitively-tuned split microstrip resonators for RFID barcodes," in *2005 European Microwave Conference*, vol. 2. IEEE, 2005, pp. 4–pp.
- [76] WISP platform. [accessed 22 aug. 2022]. [Online]. Available: <https://alansonsample.com/research/WISP.html>
- [77] K. Zannas, H. El Matbouly, Y. Duroc, and S. Tedjini, "Self-tuning RFID tag: A new approach for temperature sensing," *IEEE Transactions on Microwave Theory and Techniques*, vol. 66, no. 12, pp. 5885–5893, 2018.
- [78] B. D. Wiltshire, T. Zarifi, and M. H. Zarifi, "Passive split ring resonator tag configuration for RFID-based wireless permittivity sensing," *IEEE Sensors Journal*, vol. 20, no. 4, pp. 1904–1911, 2019.
- [79] F. Requena, M. Gilch, N. Barbot, D. Kaddour, R. Siragusa, F. Costa, S. Genovesi, and E. Perret, "Thermal modeling of resonant scatterers and reflectometry approach for remote temperature sensing," *IEEE Transactions on Microwave Theory and Techniques*, 2021.
- [80] F. Requena, N. Barbot, D. Kaddour, and E. Perret, "Modelling of the radiation pattern of a loop resonator for orientation sensing," *in review to IEEE Transactions on Antennas and Propagation*, 2022.
- [81] J. James, J. Spittle, S. Brown, and R. Evans, "A review of measurement techniques for the thermal expansion coefficient of metals and alloys at elevated temperatures," *Measurement science and technology*, vol. 12, no. 3, p. R1, 2001.
- [82] J. Neumeier, R. Bollinger, G. Timmins, C. Lane, R. Krogstad, and J. Macaluso, "Capacitive-based dilatometer cell constructed of fused quartz for measuring the thermal expansion of solids," *Review of Scientific Instruments*, vol. 79, no. 3, p. 033903, 2008.
- [83] G. R. Hyde, L. P. Domingues, and L. R. Furlong, "Improved dilatometer," *Review of Scientific Instruments*, vol. 36, no. 2, pp. 204–205, 1965.
- [84] E. G. Wolff, "Fundamentals of optical interferometry for thermal expansion measurements," in *Proceedings of the 27th International Thermal Conductivity Conference and the 15th International Thermal Expansion Symposium*, 2003, pp. 615–633.

- [85] G. Bianchini, M. Barucci, T. Del Rosso, E. Pasca, and G. Ventura, "Interferometric dilatometer for thermal expansion coefficient determination in the 4–300K range," *Measurement Science and Technology*, vol. 17, no. 4, p. 689, 2006.
- [86] C. G. Tseng and Y. S. Jiang, "Optical interference dilatometer," *Measurement Science and Technology*, vol. 16, no. 10, p. 2114, 2005.
- [87] R. Montanini and F. Freni, "Non-contact measurement of linear thermal expansion coefficients of solid materials by infrared image correlation," *Measurement Science and Technology*, vol. 25, no. 1, p. 015013, 2013.
- [88] Y. Okada and Y. Tokumaru, "Precise determination of lattice parameter and thermal expansion coefficient of silicon between 300 and 1500K," *Journal of applied physics*, vol. 56, no. 2, pp. 314–320, 1984.
- [89] "Standard test method for linear thermal expansion of solid materials with a vitreous silica dilatometer," E 228-95, annual book of astm standards, astm, 1995."
- [90] "Standard test method for linear thermal expansion of rigid solids with interferometry," E 289-99, annual book of astm standards, astm, 1999."
- [91] "Standard test method for linear thermal expansion of solid materials by thermomechanical analysis," E 831, annual book of astm standards, astm, 2000."
- [92] E. Perret, "Displacement sensor based on radar cross-polarization measurements," *IEEE Trans. Microw. Theory Techn.*, vol. 65, no. 3, pp. 955–966, 2017.
- [93] T. T. Thai, H. Aubert, P. Pons, G. DeJean, M. M. Tentzeris, and R. Plana, "Novel design of a highly sensitive RF strain transducer for passive and remote sensing in two dimensions," *IEEE Transactions on Microwave Theory and Techniques*, vol. 61, no. 3, pp. 1385–1396, 2013.
- [94] Z. Ali, N. Barbot, R. Siragusa, E. Perret, D. Hely, and F. Bernier, Maxime Garet, "Detection of minimum geometrical variation by free-space-based chipless approach and its application to authentication," *IEEE Microw. Wireless Compon. Lett.*, vol. 28, no. 4, pp. 323–325, 2018.
- [95] E. M. Amin and N. Karmakar, "Development of a chipless RFID temperature sensor using cascaded spiral resonators," in *SENSORS, 2011 IEEE*. IEEE, 2011, pp. 554–557.
- [96] T. T. Thai, F. Chebila, J. M. Mehdi, P. Pons, H. Aubert, G. R. DeJean, M. M. Tentzeris, and R. Plana, "Design and development of a millimetre-wave novel passive ultrasensitive temperature transducer for remote sensing and identification," in *The 40th European Microwave Conference*. IEEE, 2010, pp. 45–48.
- [97] J. Valentich, "A vitreous silica tube dilatometer for the measurement of thermal expansion of solids from -195 to 1000°C," *Journal of Materials Science*, vol. 14, no. 2, pp. 371–378, 1979.
- [98] M. Okaji and H. Imai, "A practical measurement system for the accurate determination of linear thermal expansion coefficients," *Journal of Physics E: Scientific Instruments*, vol. 17, no. 8, p. 669, 1984.

- [99] T. R. Touloukian YS, Kirby RK and D. PD, *Thermophysical Properties of Matter, Volume 12—Thermal Expansion, Metallic Elements and Alloys*. New York: IFI-Plenum, 1975.
- [100] Goodfellow.com. (2019). [accessed 28 oct. 2019]. [Online]. Available: <http://www.goodfellow.com/PDF/TAB004F.pdf>
- [101] O. Rance, R. Siragusa, P. Lemaître-Auger, and E. Perret, "Contactless characterization of coplanar stripline discontinuities by RCS measurement," *IEEE Trans. Antennas Propag.*, vol. 65, no. 1, pp. 251–257, 2016.
- [102] Vostch vc0018 manuel d'utilisation. [accessed 28 oct. 2019]. [Online]. Available: [shorturl.at/bgLP8](http://shorturl.at/bgLP8)
- [103] A. Petosa, A. Ittipiboon, Y. Antar, D. Roscoe, and M. Cuhaci, "Recent advances in dielectric-resonator antenna technology," *IEEE Antennas and Propagation Magazine*, vol. 40, no. 3, pp. 35–48, 1998.
- [104] C. Herrojo, F. Paredes, and F. Martín, "A new paradigm in chipless-RFID: all-dielectric permittivity contrast tags," in *2019 IEEE International Conference on RFID Technology and Applications (RFID-TA)*. IEEE, 2019, pp. 163–166.
- [105] A. S. Leger and C. Nwankpa, "OTA-based transmission line model with variable parameters for analog power flow computation," *International Journal of Circuit Theory and Applications*, vol. 38, no. 2, pp. 199–220, 2010.
- [106] V. Cecchi, A. S. Leger, K. Miu, and C. O. Nwankpa, "Incorporating temperature variations into transmission-line models," *IEEE Transactions on Power Delivery*, vol. 26, no. 4, pp. 2189–2196, 2011.
- [107] J. Virtanen, L. Ukkonen, T. Björninen, L. Sydänheimo, and A. Z. Elsherbeni, "Temperature sensor tag for passive UHF RFID systems," in *2011 IEEE Sensors Applications Symposium*. IEEE, 2011, pp. 312–317.
- [108] T. Noor, A. Habib, Y. Amin, J. Loo, and H. Tenhunen, "High-density chipless RFID tag for temperature sensing," *Electronics Letters*, vol. 52, no. 8, pp. 620–622, 2016.
- [109] S. Preradovic and N. Karmakar, "Chipless RFID tag with integrated sensor," in *SENSORS, 2010 IEEE*, vol. 11, no. 7, IEEE. IEEE, 2010, pp. 1277–1281.
- [110] A. Vena, L. Sydänheimo, M. M. Tentzeris, and L. Ukkonen, "A fully inkjet-printed wireless and chipless sensor for CO<sub>2</sub> and temperature detection," *IEEE Sensors J.*, vol. 15, no. 1, pp. 89–99, 2014.
- [111] B. Kubina, M. Schüßler, C. Mandel, A. Mehmood, and R. Jakoby, "Wireless high-temperature sensing with a chipless tag based on a dielectric resonator antenna," in *SENSORS, 2013 IEEE*. IEEE, 2013, pp. 1–4.
- [112] E. Chen and S. Y. Chou, "Characteristics of coplanar transmission lines on multilayer substrates: Modeling and experiments," *IEEE Trans. Microw. Theory Techn.*, vol. 45, no. 6, pp. 939–945, 1997.

- [113] O. Rance, E. Perret, R. Siragusa, and P. Lemaitre-Auger, *RCS synthesis for chipless RFID: theory and design*. Elsevier, 2017.
- [114] R. E. Collin, *Foundations for microwave engineering*. John Wiley & Sons, 2007.
- [115] Rogerscorp.com. (2021). [accessed 04 feb. 2021]. [Online]. Available: <https://rogerscorp.com/-/media/project/rogerscorp/documents/advanced-connectivity-solutions/english/data-sheets/ro4000-laminates-ro4003c-and-ro4350b---data-sheet.pdf>
- [116] Magneticsgroup. (2021). [accessed 04 feb. 2021]. [Online]. Available: <https://www.magneticsgroup.com/material/k/>
- [117] A. Vena, E. Perret, D. Kaddour, and T. Baron, "Toward a reliable chipless rfid humidity sensor tag based on silicon nanowires," *IEEE Transactions on Microwave Theory and Techniques*, vol. 64, no. 9, pp. 2977–2985, 2016.
- [118] E. M. Amin, M. S. Bhuiyan, N. C. Karmakar, and B. Winther-Jensen, "Development of a low cost printable chipless RFID humidity sensor," *IEEE Sensors J.*, vol. 14, no. 1, pp. 140–149, 2013.
- [119] M. Borgese, F. A. Dicandia, F. Costa, S. Genovesi, and G. Manara, "An inkjet printed chipless RFID sensor for wireless humidity monitoring," *IEEE Sensors J.*, vol. 17, no. 15, pp. 4699–4707, 2017.
- [120] S. Fan, T. Chang, X. Liu, Y. Fan, and M. M. Tentzeris, "A depolarizing chipless RFID tag with humidity sensing capability," in *2018 IEEE International Symposium on Antennas and Propagation & USNC/URSI National Radio Science Meeting*. IEEE, 2018, pp. 2469–2470.
- [121] J. G. Hester and M. M. Tentzeris, "Inkjet-printed flexible mm-wave van-atta reflectarrays: A solution for ultralong-range dense multitag and multisensing chipless rfid implementations for iot smart skins," *IEEE Transactions on Microwave Theory and Techniques*, vol. 64, no. 12, pp. 4763–4773, 2016.
- [122] F. Requena, N. Barbot, D. Kaddour, and E. Perret, "Contactless characterization of metals thermal expansion coefficient by a free-space RF measurement," *IEEE Transactions on Antennas and Propagation*, vol. 69, no. 2, pp. 1230–1234, 2020.
- [123] A. Vena, E. Perret, and S. Tedjini, "Chipless RFID tag using hybrid coding technique," *IEEE Transactions on Microwave Theory and Techniques*, vol. 59, no. 12, pp. 3356–3364, 2011.
- [124] Z. Ali, E. Perret, N. Barbot, and R. Siragusa, "Extraction of aspect-independent parameters using spectrogram method for chipless frequency-coded rfid," *IEEE Sensors Journal*, vol. 21, no. 5, pp. 6530–6542, 2020.
- [125] A. Vena, E. Perret, and S. Tedjini, "Design of compact and auto-compensated single-layer chipless RFID tag," *IEEE Trans. Microw. Theory Tech.*, vol. 60, no. 9, pp. 2913–2924, 2012.
- [126] dupont.com. (2021). [accessed 01 mar. 2021]. [Online]. Available: <https://www.dupont.com/content/dam/dupont/amer/us/en/products/ei-transformation/documents/EI-10142-Kapton-Summary-of-Properties.pdf>
- [127] C. A. Balanis, *Antenna theory: analysis and design*. John wiley & sons, 2016.

- [128] Y. Qin, Y. Fan, X. Liu, and M. M. Tentzeris, "A novel passive chipless RFID tag for angle sensor," in *2019 International Conference on Microwave and Millimeter Wave Technology (ICMMT)*, 2019, pp. 1–3.
- [129] A. Vena, E. Perret, and S. Tedjini, "A compact chipless RFID tag using polarization diversity for encoding and sensing," in *2012 IEEE International Conference on RFID (RFID)*, April 2012, pp. 191–197.
- [130] S. Genovesi, F. Costa, M. Borgese, F. A. Dicandia, A. Monorchio, and G. Manara, "Chipless RFID sensor for rotation monitoring," in *2017 IEEE International Conference on RFID Technology Application (RFID-TA)*, Sept. 2017, pp. 233–236.
- [131] S. Genovesi, F. Costa, M. Borgese, A. Monorchio, and G. Manara, "Chipless RFID tag exploiting cross-polarization for angular rotation sensing," in *2016 IEEE International Conference on Wireless for Space and Extreme Environments (WiSEE)*, Sept. 2016, pp. 158–160.
- [132] S. Genovesi, F. Costa, M. Borgese, F. A. Dicandia, and G. Manara, "Chipless radio frequency identification (RFID) sensor for angular rotation monitoring," *Technologies*, vol. 6, no. 3, 2018. [Online]. Available: <http://www.mdpi.com/2227-7080/6/3/61>
- [133] N. Barbot, O. Rance, and E. Perret, "Angle sensor based on chipless RFID tag," *IEEE Antennas Wireless Propag. Lett.*, vol. 19, no. 2, pp. 233–237, 2020.
- [134] P.-Y. Lyu, C.-C. Chang, and S.-F. Chang, "Detecting yaw and pitch change with single millimeter-wave CW radar," *IEEE Sensors Letters*, vol. 5, no. 8, pp. 1–4, 2021.
- [135] Datasheet - open boundary quad-ridge horns. MVG (2019). [accessed sep. 20, 2021.]. [Online]. Available: [https://www.mvg-world.com/sites/default/files/2021-04/Datasheet\\_Antennas\\_Open%20Boundary%20Quad-Ridge%20Horns\\_04\\_21\\_BD.pdf](https://www.mvg-world.com/sites/default/files/2021-04/Datasheet_Antennas_Open%20Boundary%20Quad-Ridge%20Horns_04_21_BD.pdf)
- [136] P. V. Nikitin and K. S. Rao, "Theory and measurement of backscattering from RFID tags," *IEEE Antennas and Propagation Magazine*, vol. 48, no. 6, pp. 212–218, 2006.
- [137] Video : real-time angle sensing using a chipless RFID resonator. [accessed 19 jan. 2022]. [Online]. Available: <https://bit.ly/3fIYmQy>
- [138] Video : real-time angle sensing using a chipless RFID resonator in 3D. [accessed 19 jan. 2022]. [Online]. Available: <https://bit.ly/3tGMwPh>
- [139] N. C. Karmakar, E. M. Amin, and J. K. Saha, *Chipless RFID sensors*. Wiley Online Library, 2016.
- [140] F. Requena, N. Barbot, D. Kaddour, and E. Perret, "Chipless RFID temperature and humidity sensing," in *2021 IEEE MTT-S International Microwave Symposium (IMS)*, IEEE. IEEE, 2021, pp. 545–548.
- [141] F. Costa, D. Brizi, S. Genovesi, A. Monorchio, G. Manara, F. Requena, and E. Perret, "Wireless detection of water level by using spiral resonators operating in sub-ghz range," in *2019 IEEE International Conference on RFID Technology and Applications (RFID-TA)*. IEEE, 2019, pp. 197–200.

- [142] A. M. J. Marindra and G. Y. Tian, "Chipless RFID sensor tag for metal crack detection and characterization," *IEEE Transactions on Microwave Theory and Techniques*, vol. 66, no. 5, pp. 2452–2462, 2018.
- [143] E. M. Amin, R. Bhattacharyya, S. Sarma, and N. C. Karmakar, "Chipless RFID tag for light sensing," in *2014 IEEE Antennas and Propagation Society International Symposium (APSURSI)*. IEEE, 2014, pp. 1308–1309.
- [144] J. Kracek, M. Svanda, and K. Hoffmann, "Scalar method for reading of chipless rfid tags based on limited ground plane backed dipole resonator array," *IEEE Transactions on Microwave Theory and Techniques*, vol. 67, no. 11, pp. 4547–4558, 2019.
- [145] M. Polivka, J. Havlicek, M. Svanda, and J. Machac, "Improvement in robustness and recognizability of rcs response of u-shaped strip-based chipless rfid tags," *IEEE Antennas and Wireless Propagation Letters*, vol. 15, pp. 2000–2003, 2016.
- [146] E. Perret, *Radio frequency identification and sensors: from RFID to chipless RFID*. John Wiley & Sons, 2014.
- [147] A. Ramos, Z. Ali, A. Vena, M. Garbati, and E. Perret, "Single-layer, flexible, and depolarizing chipless RFID tags," *IEEE Access*, vol. 8, pp. 72 929–72 941, 2020.
- [148] S. Hu, Y. Zhou, C. L. Law, and W. Dou, "Study of a uniplanar monopole antenna for passive chipless uwb-rfid localization system," *IEEE Transactions on Antennas and Propagation*, vol. 58, no. 2, pp. 271–278, 2009.
- [149] D. Girbau, A. Lázaro, and Á. Ramos, "Time-coded chipless rfid tags: Design, characterization and application," in *2012 IEEE International Conference on RFID-Technologies and Applications (RFID-TA)*. IEEE, 2012, pp. 12–17.
- [150] R. B. Green, *The general theory of antenna scattering*. The Ohio State University, 1963.
- [151] R. Rezaiesarlak and M. Manteghi, "Complex-natural-resonance-based design of chipless rfid tag for high-density data," *IEEE Transactions on Antennas and Propagation*, vol. 62, no. 2, pp. 898–904, 2013.
- [152] C. E. Baum, "On the singularity expansion method for the solution of electromagnetic interaction problems," AIR FORCE WEAPONS LAB KIRTLAND AFB NM, Tech. Rep., 1971.
- [153] Z. Ali, E. Perret, N. Barbot, and R. Siragusa, "Extraction of aspect-independent parameters using spectrogram method for chipless frequency-coded RFID," *IEEE Sensors Journal*, vol. 21, no. 5, pp. 6530–6542, 2020.
- [154] A. Vena, E. Perret, and S. Tedjini, "Design of compact and auto-compensated single-layer chipless rfid tag," *IEEE Transactions on Microwave Theory and Techniques*, vol. 60, no. 9, pp. 2913–2924, 2012.
- [155] F. Requena, M. Gilch, N. Barbot, D. Kaddour, R. Siragusa, F. Costa, S. Genovesi, and E. Perret, "Thermal modeling of resonant scatterers and reflectometry approach for remote temperature



- sensing," *IEEE Transactions on Microwave Theory and Techniques*, vol. 69, no. 11, pp. 4720–4734, 2021.
- [156] M. Polivka, J. Havlicek, M. Svanda, and J. Machac, "Improvement in robustness and recognizability of RCS response of u-shaped strip-based chipless RFID tags," *IEEE Antennas and Wireless Propagation Letters*, vol. 15, pp. 2000–2003, 2016.
- [157] M. Borgese, S. Genovesi, G. Manara, and F. Costa, "Radar cross section of chipless RFID tags and BER performance," *IEEE Transactions on Antennas and Propagation*, vol. 69, no. 5, pp. 2877–2886, 2020.
- [158] M. Khaliel, A. El-Awamry, A. Fawky, M. El-Hadidy, and T. Kaiser, "A novel co/cross-polarizing chipless RFID tags for high coding capacity and robust detection," in *2015 IEEE international symposium on antennas and propagation & USNC/URSI national radio science meeting*. IEEE, 2015, pp. 159–160.
- [159] N. Barbot, O. Rance, and E. Perret, "Chipless RFID reading method insensitive to tag orientation," *IEEE Trans. Antennas Propag.*, 2020.
- [160] S. Genovesi, F. Costa, F. A. Dicandia, M. Borgese, and G. Manara, "Orientation-insensitive and normalization-free reading chipless RFID system based on circular polarization interrogation," *IEEE Transactions on Antennas and Propagation*, vol. 68, no. 3, pp. 2370–2378, 2019.
- [161] O. Rance, N. Barbot, and E. Perret, "Design of planar resonant scatterer with roll-invariant cross polarization," *IEEE Transactions on Microwave Theory and Techniques*, vol. 68, no. 10, pp. 4305–4313, 2020.
- [162] R. Olivier, B. Nicolas, and P. Etienne, "Comparison between cross-polarization and circular polarization interrogation for robust chipless rfid reading," *51th European Microwave Conference (EuMC 2021)*, 2021.
- [163] C. A. Balanis, *Antenna theory: analysis and design*. John wiley & sons, 2015.
- [164] E. F. Knott, J. F. Schaeffer, and M. T. Tulley, *Radar cross section*. SciTech Publishing, 2004.
- [165] L. Luo, J. Jie, W. Zhang, Z. He, J. Wang, G. Yuan, W. Zhang, L. C. M. Wu, and S.-T. Lee, "Silicon nanowire sensors for Hg 2+ and Cd 2+ ions," *Applied Physics Letters*, vol. 94, no. 19, p. 193101, 2009.
- [166] X. Zhou, J. Hu, C. Li, D. Ma, C. Lee, and S. Lee, "Silicon nanowires as chemical sensors," *Chemical Physics Letters*, vol. 369, no. 1-2, pp. 220–224, 2003.
- [167] M. Shao, D. D. D. Ma, and S.-T. Lee, "Silicon nanowires—synthesis, properties, and applications," *European Journal of Inorganic Chemistry*, vol. 2010, no. 27, pp. 4264–4278, 2010.
- [168] S. Ahoulou, E. Perret, and J.-M. Nedelec, "Functionalization and characterization of silicon nanowires for sensing applications: A review," *Nanomaterials*, vol. 11, no. 4, p. 999, 2021.
- [169] W. Chen, H. Yao, C. H. Tzang, J. Zhu, M. Yang, and S.-T. Lee, "Silicon nanowires for high-sensitivity glucose detection," *Applied physics letters*, vol. 88, no. 21, p. 213104, 2006.

- [170] Y. Coffinier and R. Boukherroub, "Surface modification of semiconducting silicon nanowires for biosensing applications," in *Semiconducting silicon nanowires for biomedical applications*. Elsevier, 2014, pp. 26–61.
- [171] K. Miyoshi *et al.*, "Surface characterization techniques: an overview," *Mechanical tribology: materials, characterization, and applications. Part*, vol. 2, pp. 1–46, 2002.
- [172] G. Gillberg, "Polymer surface characterization: an overview," *The Journal of Adhesion*, vol. 21, no. 2, pp. 129–154, 1987.
- [173] D. W. Dwight, T. J. Fabish, H. R. Thomas *et al.*, *Photon, electron, and ion probes of polymer structure and properties*. American Chemical Society, 1981.
- [174] A. Vena, E. Perret, D. Kaddour, and T. Baron, "Toward a reliable chipless RFID humidity sensor tag based on silicon nanowires," *IEEE Transactions on Microwave Theory and Techniques*, vol. 64, no. 9, pp. 2977–2985, 2016.
- [175] Y. Feng, L. Xie, Q. Chen, and L.-R. Zheng, "Low-cost printed chipless RFID humidity sensor tag for intelligent packaging," *IEEE Sensors Journal*, vol. 15, no. 6, pp. 3201–3208, 2014.
- [176] L. Yang, R. Zhang, D. Staiculescu, C. Wong, and M. M. Tentzeris, "A novel conformal RFID-enabled module utilizing inkjet-printed antennas and carbon nanotubes for gas-detection applications," *IEEE Antennas and Wireless Propagation Letters*, vol. 8, pp. 653–656, 2009.
- [177] R. A. Alahnomi, Z. Zakaria, Z. M. Yussof, A. A. Althuwayb, A. Alhegazi, H. Alsariera, and N. A. Rahman, "Review of recent microwave planar resonator-based sensors: Techniques of complex permittivity extraction, applications, open challenges and future research directions," *Sensors*, vol. 21, no. 7, p. 2267, 2021.
- [178] J. Krupka, "Frequency domain complex permittivity measurements at microwave frequencies," *Measurement Science and Technology*, vol. 17, no. 6, p. R55, 2006.
- [179] UTE, "Mesure de la permittivite et de la permeabilite de materiaux homogenes et isotropes a pertes dans le domaine des micro-ondes. methode de mesure en guide coaxial circulaire," (*Union Technique de l'Electricite et de la Communication*), 1999.
- [180] A. Nicolson and G. Ross, "Measurement of the intrinsic properties of materials by time-domain techniques," *IEEE Transactions on instrumentation and measurement*, vol. 19, no. 4, pp. 377–382, 1970.
- [181] J. Baker-Jarvis, E. J. Vanzura, and W. A. Kissick, "Improved technique for determining complex permittivity with the transmission/reflection method," *IEEE Transactions on microwave theory and techniques*, vol. 38, no. 8, pp. 1096–1103, 1990.
- [182] S. Bakhtiari, S. I. Ganchev, and R. Zoughi, "Open-ended rectangular waveguide for nondestructive thickness measurement and variation detection of lossy dielectric slabs backed by a conducting plate," *IEEE Transactions on Instrumentation and Measurement*, vol. 42, no. 1, pp. 19–24, 1993.

- [183] F. I. Shimabukuro, S. Lazar, M. R. Chernick, and H. B. Dyson, "A quasi-optical method for measuring the complex permittivity of materials," *IEEE transactions on microwave theory and techniques*, vol. 32, no. 7, pp. 659–665, 1984.
- [184] S. Li, C. Akyel, and R. G. Bosisio, "Precise calculations and measurements on the complex dielectric constant of lossy materials using tm/sub 010/cavity perturbation techniques," *IEEE Transactions on Microwave Theory and Techniques*, vol. 29, no. 10, pp. 1041–1048, 1981.
- [185] S. Dmowski, J. Krupka, and A. Milewski, "Contactless measurement of silicon resistivity in cylindrical TE<sub>01n</sub> mode cavities," *IEEE Transactions on Instrumentation and Measurement*, vol. 29, no. 1, pp. 67–70, 1980.
- [186] A. L. Cullen and P. Yu, "The accurate measurement of permittivity by means of an open resonator," *Proceedings of the Royal Society of London. A. Mathematical and Physical Sciences*, vol. 325, no. 1563, pp. 493–509, 1971.
- [187] T. M. Hirvonen, P. Vainikainen, A. Lozowski, and A. V. Raisanen, "Measurement of dielectrics at 100 ghz with an open resonator connected to a network analyzer," *IEEE transactions on instrumentation and measurement*, vol. 45, no. 4, pp. 780–786, 1996.
- [188] B. Hakki and P. D. Coleman, "A dielectric resonator method of measuring inductive capacities in the millimeter range," *IRE Transactions on Microwave Theory and Techniques*, vol. 8, no. 4, pp. 402–410, 1960.
- [189] Y. Kobayashi and M. Katoh, "Microwave measurement of dielectric properties of low-loss materials by the dielectric rod resonator method," *IEEE Transactions on Microwave Theory and Techniques*, vol. 33, no. 7, pp. 586–592, 1985.
- [190] H. Lobato-Morales, A. Corona-Chávez, J. L. Olvera-Cervantes, R. A. Chávez-Pérez, and J. L. Medina-Monroy, "Wireless sensing of complex dielectric permittivity of liquids based on the RFID," *IEEE Transactions on Microwave Theory and Techniques*, vol. 62, no. 9, pp. 2160–2167, 2014.
- [191] E. Perret, "Permittivity characterization based on radar cross measurements," in *2016 URSI International Symposium on Electromagnetic Theory (EMTS)*. IEEE, 2016, pp. 457–460.
- [192] T. K. Sarkar and O. Pereira, "Using the matrix pencil method to estimate the parameters of a sum of complex exponentials," *IEEE Antennas and Propagation Magazine*, vol. 37, no. 1, pp. 48–55, 1995.
- [193] N. M. Hwang, W. S. Cheong, D. Y. Yoon, and D.-Y. Kim, "Growth of silicon nanowires by chemical vapor deposition: approach by charged cluster model," *Journal of crystal growth*, vol. 218, no. 1, pp. 33–39, 2000.
- [194] V. Schmidt, S. Senz, and U. Gösele, "Diameter-dependent growth direction of epitaxial silicon nanowires," *Nano letters*, vol. 5, no. 5, pp. 931–935, 2005.
- [195] A. Schmohl, A. Khan, and P. Hess, "Functionalization of oxidized silicon surfaces with methyl groups and their characterization," *Superlattices and Microstructures*, vol. 36, no. 1-3, pp. 113–121, 2004.

- [196] M. Y. Bashouti, T. Stelzner, S. Christiansen, and H. Haick, "Covalent attachment of alkyl functionality to 50 nm silicon nanowires through a chlorination/alkylation process," *The Journal of Physical Chemistry C*, vol. 113, no. 33, pp. 14 823–14 828, 2009.
- [197] U. Srinivasan, M. R. Houston, R. T. Howe, and R. Maboudian, "Alkyltrichlorosilane-based self-assembled monolayer films for stiction reduction in silicon micromachines," *Journal of Microelectromechanical Systems*, vol. 7, no. 2, pp. 252–260, 1998.
- [198] Y. Cao, E. Galoppini, P. I. Reyes, and Y. Lu, "Functionalization of nanostructured ZnO films by copper-free click reaction," *Langmuir*, vol. 29, no. 25, pp. 7768–7775, 2013.
- [199] Z. P. Demko and K. B. Sharpless, "A click chemistry approach to tetrazoles by Huisgen 1, 3-dipolar cycloaddition: synthesis of 5-sulfonyl tetrazoles from azides and sulfonyl cyanides," *Angewandte Chemie International Edition*, vol. 41, no. 12, pp. 2110–2113, 2002.
- [200] M. Abdelhameed, D. R. Martir, S. Chen, W. Z. Xu, O. O. Oyeneye, S. Chakrabarti, E. Zysman-Colman, and P. A. Charpentier, "Tuning the optical properties of silicon quantum dots via surface functionalization with conjugated aromatic fluorophores," *Scientific reports*, vol. 8, no. 1, pp. 1–10, 2018.
- [201] A. Gouget-Laemmel, J. Yang, M. Lodhi, A. Siriwardena, D. Aureau, R. Boukherroub, J.-N. Chazalviel, F. Ozanam, and S. Szunerits, "Functionalization of azide-terminated silicon surfaces with glycans using click chemistry: XPS and FTIR study," *The Journal of Physical Chemistry C*, vol. 117, no. 1, pp. 368–375, 2013.
- [202] N. Vilà, J. Ghanbaja, and A. Walcarius, "Clickable bifunctional and vertically aligned mesoporous silica films," *Advanced Materials Interfaces*, vol. 3, no. 2, p. 1500440, 2016.